Durham University

Durham E-Theses

Microfabricated liquid density sensors using polyimide-guided surface acoustic waves

Andrew Charles Turton

How to cite:

Turton, Andrew Charles (2006) Microfabricated liquid density sensors using polyimide-guided surface acoustic waves. Doctoral thesis, Durham University.

Use policy

The full-text may be used and/or reproduced, and given to third parties in any format or medium, without prior permission or charge, for personal research or study, educational, or not-for-profit purposes provided that:

- a full bibliographic reference is made to the original source
- a https://etheses.durham.ac.uk/id/eprint/2605/ is made to the metadata record in Durham E-Theses
- the full-text is not changed in any way

The full-text must not be sold in any format or medium without the formal permission of the copyright holders.

Please consult the full Durham E-Theses policy for further details.

Academic Support Office, The Palatine Centre, Durham University, Stockton Road, Durham, DH1 3LE
e-mail: e-theses.admin@durham.ac.uk Tel: +44 0191 334 6107
https://etheses.durham.ac.uk

Microfabricated liquid density sensors using polyimide-guided surface acoustic waves

The copyright of this thesis rests with the author or the university to which it was submitted. No quotation from it, or information derived from it may be published without the prior written consent of the author or university, and any information derived from it should be acknowledged.

Andrew Charles Turton M.Sci

School of Engineering

University of Durham

A thesis submitted to the University of Durham for the Degree of Doctor of Philosophy

2006

0 1 JUN 2006

Acknowledgements

I would like to acknowledge my supervisor, Prof. David Wood, for his outstanding and continued support and encouragement throughout this study. I also thank Index Instruments UK for sponsoring this project and EPSRC for their additional financial support.

No acknowledgement would be complete without a mention for John Gibson whose extensive technical assistance was invaluable. The practical support of other members of technical staff, and the input and assistance from the other members of the microsystems technology group have also been greatly appreciated!

I finally thank my family and friends for their support.

Declaration

I declare that no material in this thesis has previously been submitted for a degree at this or any other university.

The copyright of this thesis rests with the author. No quotation from it should be published in any format, including electronic and the Internet, without the authors prior written consent. All information derived from this thesis must be acknowledged appropriately.

Microfabricated liquid density sensors using polyimide-guided surface acoustic waves.

Andrew Charles Turton

Abstract

The simultaneous measurements of liquid density and refractive index on the same liquid sample are desirable. This thesis investigates the development of a micro-fabricated liquid density sensor that can be integrated into existing refractometers. A discussion of density sensing techniques and review of suitable sensors is given, leading to the choice of a Love mode surface acoustic wave (SAW) device.

Love modes are formed by focussing the acoustic energy in a thin waveguide layer on a surface acoustic wave device. The horizontal-shear wave motion reduces attenuation in liquid environments, and the high surface energy density theoretically gives the highest sensitivity of all SAW devices. This study follows the development of a Love mode liquid density sensor using a polyimide waveguide layer. The novel use of polyimide offers simple and cheap fabrication, and theoretically gives a very high sensitivity to surface loading due to its low acoustic velocity.

Love mode devices were fabricated with different polyimide waveguide thicknesses. The optimum thickness for a compromise between low loss and high sensitivity was 0.90 – 1.0 μm. These devices exhibited a linear shift in frequency with the liquid density-viscosity product for low viscosities. The response was smaller for high viscosities due to non-Newtonian liquid behaviour.

Dual delay-line structures with a smooth 'reference' and corrugated 'sense' delay-lines were used to trap the liquid and separate the density from the density-viscosity product. A sensitivity up to 0.13 $\mu gcm^{-3}Hz^{-1}$ was obtained. This is the highest density sensitivity obtained from an acoustic mode sensor.

Experimental results show a zero temperature coefficient of frequency is possible using polyimide waveguides. These are the first Love mode devices that demonstrate temperature independence, highlighting the importance of polyimide as a new waveguide material.

Table of contents

Table of contents ..... **ii**

List of figures ..... **vi**

List of tables ..... **xiv**

List of abbreviations ..... **xv**

Nomenclature ..... **xvii**

1 Introduction – microsystems technology **1**
1.1 Small is beautiful 2
1.2 Microfabrication 3
1.3 Micromachining 4
1.4 The MST market 7
1.5 Aims of this study 10

2 Liquid density sensing **11**
2.1 Introduction 12
2.2 Liquid density 13
2.3 Hydrometer 13
2.4 Resonating tube densitometer 15
2.4.1 Resonance 15
2.4.2 Resonating tube 15
2.5 Review of alternative sensors 17
2.5.1 Ultrasonic sensing 17
2.5.2 Resonating cantilevers 18
2.5.3 Micromachined resonating tube 19
2.5.4 Quartz crystal microbalance 21
2.5.5 Acoustic plate mode sensors 23
2.5.6 Love mode surface acoustic wave sensor 24
2.6 Conclusions 26

3 Surface acoustic waves and devices **29**
3.1 Rayleigh waves 30
3.1.1 Theory of Rayleigh waves 31
3.2 SAW Excitation 33
3.2.1 Interdigitated transducers 33
3.2.2 Electrical excitation – delta function model 34
3.3 Surface acoustic wave device substrates 36
3.3.1 Elastic properties 36
3.3.2 Piezoelectric properties 37
3.3.3 Piezoelectric equations 38
3.3.4 Quartz substrates 40
3.3.5 Quartz structure 41
3.3.6 Quartz piezoelectric constants 42
3.3.7 Substrate manufacture and orientation 42
3.4 SAW devices 44
3.4.1 Electronics devices 44

3.4.2 SAW oscillators 46
3.4.3 Sensors 47
3.4.4 Wireless passive sensing 48
3.4.5 Temperature sensors 49
3.4.6 Stress and strain sensors 49
3.4.7 Mass loading sensors 51
3.4.8 Sensor conclusions 52
3.4.9 SAW actuators 52
3.5 Love modes 53
3.5.1 Love mode formation 54
3.5.2 Surface perturbations of Love modes 57
3.5.3 Mass loading 61
3.5.4 Viscous coupling 62
3.5.5 Application to the dual delay-line liquid density sensor 64
3.5.6 Love mode sensitivity 66
3.5.7 Waveguide materials 67
3.5.8 Attenuation of Love modes 69
3.5.9 Love mode conclusions 72

4 Experimental procedures 73
4.1 Process flows 74
4.1.1 IDT fabrication 74
4.1.2 Polyimide waveguide devices 75
4.1.3 SiO_2 waveguide devices 76
4.1.4 Multilayer waveguide devices 77
4.2 Wafer preparation 78
4.3 Photolithography 78
4.3.1 In-house mask fabrication and design 78
4.3.2 Commercial masks 79
4.3.3 Photoresist 81
4.3.4 Mask aligning and exposure 81
4.3.5 Development 84
4.4 Metal deposition and patterning 85
4.4.1 Evaporation 85
4.4.2 Aluminium deposition and patterning 87
4.4.3 Chrome and gold deposition and patterning 89
4.5 CVD SiO_2 deposition and patterning 90
4.6 Polyimide deposition and patterning 92
4.6.1 Adhesion promoter 93
4.6.2 Polyimide spin coating and wet-etching 93
4.6.3 Polyimide Curing 94
4.7 Reactive ion etching 96
4.7.1 Organics 97
4.7.2 Inorganics 98
4.8 Inspection 99
4.8.1 Scanning electron microscope 99
4.8.2 Optical microscopes 99
4.8.3 Profiling 100
4.9 Device preparation 100
4.9.1 Dicing 100
4.9.2 Wire bonding and packaging 100

4.10 Electrical measurements 101
4.11 Temperature measurements 102

5 Device characterisation 104
5.1 Physical inspection 105
5.1.1 Quartz substrate 105
5.1.2 Polyimide waveguide devices 106
5.1.3 SiO_2 waveguide devices 110
5.2 Electrical characteristics – uncoated SAW devices 112
5.2.1 Transducer layout 112
5.2.2 Interdigitated transducer design parameters 114
5.2.3 Substrate orientation 116
5.3 Polyimide waveguide Love mode characterisation 117
5.4 SiO_2 waveguide Love mode characterisation 124
5.5 Multilayer waveguide Love mode characterisation 126
5.6 Temperature dependence 129
5.6.1 Substrate temperature dependence 129
5.6.2 Waveguide temperature dependence 131
5.6.3 Surface topology temperature dependence 133
5.7 Summary 134

6 Results and analysis of liquid sensing 137
6.1 Sensitivity 138
6.2 Corrugations 141
6.3 Sucrose measurements 146
6.3.1 Polyimide waveguide device response 147
6.3.2 SiO_2 device response 153
6.4 Commercial spirits and liqueurs 156
6.5 Solvents 161
6.6 Summary 165

7 Device simulation 168
7.1 Device modelling 169
7.2 Microsystems simulation 169
7.3 Piezoelectric modelling 170
7.3.1 ATILA 170
7.3.2 Trial simulation 170
7.3.3 ATILA simulation results 172
7.3.4 Conclusions on ATILA 172
7.4 Electrical SAW device modelling 175
7.5 Transducer simulation with TRES2 175
7.5.1 Delay line simulation 176
7.6 SAW Resonator sensors 179
7.6.1 Resonator design 181
7.6.2 Resonator modelling 182
7.6.3 Resonator conclusions 186

8 Liquid sensor packaging 188
8.1 Packaging requirements for sensors 189
8.2 Electronics packaging 189
8.3 Liquid density sensor package requirements 191
8.4 Initial ideas 193

8.4.1 Modifying conventional headers 193
8.4.2 Backside contacts 195
8.5 Prototype package 198
8.6 Flexible PCB Package 201
8.7 Commercial packaging solutions 203
8.7.1 Oil dipstick sensor 203
8.7.2 Fingerprint sensors 204
8.7.3 Open cavity liquid sensor package 206
8.8 Summary 208

9 Conclusions 210
9.1 Initial aims 211
9.2 Results 211
9.3 Limitations 212
9.4 Integration into refractometer 213
9.5 Future work 214

Appendices 215

A Publications and conference presentations 216

B Dispersion – transverse resonance 217

C Bulk waves in SAW devices 219

D Fresnel's equations 220

References 221

List of figures

Figure 1-1. Miniature motor produced to claim the Feynman prize. The object in the background is a pinhead. (Courtesy of the Archives, California institute of Technology). 2

Figure 1-2. Examples of surface and bulk micromachining. 5

Figure 1-3. Micromachined devices from SANDIA National Laboratories. (a) – Three cylinder steam engine. (b) – Mirror and actuation mechanism. (c) – Gear mechanism. (d) – Electrostatic comb-drive. 6

Figure 1-4. Summary of NEXUS predictions 1996 – 2002. 7

Figure 1-5. Summary of NEXUS predictions 2000 – 2005. 8

Figure 1-6. Total turnover forecast for the RF MEMS market. 8

Figure 1-7. Micrograph of Analog Devices accelerometer showing suspended central mass, produced using surface micromachining. 10

Figure 2-1. Schematic of resonating tube structure. The side view (bottom) shows a bending resonant mode. 16

Figure 2-2. (a) – Simple pulse echo densitometer using a single reflector [21]. (b) – More advanced bi-directional transducer using a reference path [22]. 18

Figure 2-3. Micro fabricated resonating silicon tube densitometer [25-28]. 20

Figure 2-4. Fabrication process of silicon resonating tube structure. The tube halves are first anisotropically etched into silicon, and then the wafers bonded to create the tube. The entire device is packaged in a glass cavity incorporating electrodes for capacitive measurement [25-28]. 20

Figure 2-5. Resonating tube structure using a CMOS based process. The tube is fabricated in CMOS dielectrics using a sacrificial aluminium structure to define the hole. The tube is released using anisotropic silicon etching [30, 31]. 21

Figure 2-6. Schematic of a quartz crystal microbalance. The oscillator circuit is connected to the upper and lower electrodes. The horizontal hatched lines indicate the particle displacement. 22

Figure 2-7. Schematic of the acoustic plate mode sensor presented by Martin et al [38]. The enlarged diagram shows the structure of the membrane and transducers. 24

Figure 2-8. Love mode density sensor developed by Hermann et al [40]. 25

Figure 2-9. Schematic showing the Love mode density sensor with liquid flow cell [42, 43]. The serpentine component marked 15 is a temperature dependent resistor to monitor the surface temperature. 26

Figure 3-1. Rayleigh wave displacement with elliptical particle motion. 30

Figure 3-2. Rayleigh waves on an infinite half-space propagating in the z-direction with wave motion in the y-z sagittal plane. 31

Figure 3-3. Comb transducer. 33

Figure 3-4. Delay line composed of transmit and receive IDTs. 34

Figure 3-5. Uniform IDT showing 3dB power in each direction. 34

Figure 3-6. Theoretical |sinc| frequency response from uniform IDT. 36

Figure 3-7. Equilibrium (a), compression (b) and tension (c)..... 38

Figure 3-8. Alpha quartz bond structure. 41

Figure 3-9. Quartz crystal..... 41

Figure 3-10. *Y*-cut Quartz plate rotated θ around the *x*-axis. 43

Figure 3-11. Quartz wafer diagram showing the flat specifying the *x*-direction, and the central seed crystal area that cannot be used for devices. 43

Figure 3-12. Apodised filter operation, showing uniform input IDT with impulse, apodised output IDT, and the time varying output *h(t)*..... 45

Figure 3-13. Chirp filter with uniform input IDT, and wavelength varying output IDT. 45

Figure 3-14. Photo of commercial filter showing IDTs, reflectors, and contacts. The metallisation is light, and the clear substrate dark. The large metallised areas are bus bars and contact pads, and gold wire connections are shown at each end. The diagonal defect on the right hand side is a crack through the substrate arising from de-packaging. 46

Figure 3-15. Delay line oscillator using external feedback..... 47

Figure 3-16. Reflective gate oscillators..... 47

Figure 3-17. Dual delay line configuration. 48

Figure 3-18. Torque sensor with perpendicular delay lines on an axle..... 49

Figure 3-19. SAW Pressure sensor with a single delay line on a membrane..... 50

Figure 3-20. Tyre pressure monitoring device using three SAW delay lines (Transense Technologies PLC). 50

Figure 3-21. Hand-held gas analyser (Microsensor Systems Inc). 51

Figure 3-22. Schematic of SAW motor [65]. 53

Figure 3-23. Love mode shear motion. 53

Figure 3-24. Shear waves in a waveguide of thickness *h*, with losses into the substrate. 54

Figure 3-25. Love mode dispersion curves for $h = 1$. Copied from Auld [67]. 56

Figure 3-26. Harmonic Love modes [69]. Insertion loss (squares) and resonant frequency (triangles) for a device operated at the fundamental frequency as a function of waveguide thickness. 57

Figure 3-27. A cross section of the dual delay line density sensor showing the smooth and corrugated delay lines. Taken from [40]. 64

Figure 4-1. Photo reduction of transparency onto glass plate. 79

Figure 4-2. Comparison between Photronics e-beam (left) and JD Phototools LCD projection (right) masks. The Photronics mask shows 10μm IDTs. The JD Phototools mask shows a resolution test pattern. 80

Figure 4-3. Exposure variation across wafer due to grey mask regions. Over-exposure (a), correct exposure (b), and under-exposure (c). 83

Figure 4-4. Newton's rings in Al following etching. They appear here mainly confined in the propagation path between IDTs. 83

Figure 4-5. Variation in feature size with exposure time and development time (A-C), and contact method (D). 85

Figure 4-6. Schematic of 12-inch thermal Al evaporator 86

Figure 4-7. Electron beam evaporation source 87

Figure 4-8. (a) Completely removal of the Al on the un-annealed sample and (b) only partial removal due to improved adhesion with annealing. 88

Figure 4-9. Al spots resulting from H_2 bubbles forming during Al etching, causing short-circuits 89

Figure 4-10. Cr - Au patterning process 89

Figure 4-11. Schematic of PECVD chamber showing gas inlets and vacuum port. RF is applied between the anode and substrate. 92

Figure 4-12. Process gases SiH_4 and N_2O react in the plasma 'A' and 'B' at the substrate surface, and migrate along the surface to nucleate forming a thin conformal film 92

Figure 4-13. Experimentally derived spin deposition characteristics for PI2545 and thinned PI2545/T9039 compared with manufacturer's data. 93

Figure 4-14. Polyimide cure temperature ramping for programmable furnace. 95

Figure 4-15. Schematic of the programmable furnace tube. 95

Figure 4-16. Temperature profile along the programmable furnace tube. Temperature set to 350°C. 96

Figure 4-17. Reactive ion etcher process chamber showing large ground electrode (chamber lid) and small driven electrode (substrate stage) 97

Figure 4-18. Detail of etching process. Directional ions attack the material anisotropically through a resistant mask layer (black) 97

Figure 4-19. S-parameters for a two-port device. 102

Figure 4-20. Photograph of the temperature control module. 103

Figure 5-1. Micrograph showing seed crystal hole, with flat crystallographic planes visible. The faint line around the hole edge (passing through "×1.5 k ") is the Al electrode metallisation edge. 105

Figure 5-2. End of corrugations etched 0.5 μm into polyimide, showing vertical sidewalls and smooth trough base 106

Figure 5-3. View of corrugations 2mm along the device etched 0.5 μm into polyimide, showing increased roughness. 107

Figure 5-4. View of corrugations half way along the device etched 0.5 μm into polyimide, showing poor etch quality with peak-like structures partially filling the liquid traps 108

Figure 5-5. Wider view of figure 5-4 showing consistency of the poor etch process. The sharp sidewalls are still evident. 108

Figure 5-6. Surface topology of polyimide over IDT fingers measured using an Alphastep profilometer. 109

Figure 5-7. Corrugations etched 0.9 μm into SiO_2, with uneven spacing due to poor photoresist adhesion, and undercut sidewalls. 110

Figure 5-8. Close-up of previous image showing undercut sidewall profile. 111

Figure 5-9. Conformal SiO_2 deposition with corrugations (0.5 μm deep) from bottom-left to top-right and the underlying IDT fingers perpendicular. 111

Figure 5-10. Alterative transducer layouts showing a common grounded busbar (top) and separate grounded busbars diagonally opposite (bottom). 112

Figure 5-11. Representation of the common busbar IDT structure acting as a high-pass RC filter 113

Figure 5-12. Band-pass characteristics of a common busbar delay line. The horizontal scale is 20 MHz / division and the vertical scale 10 dB / division. 113

Figure 5-13. SAW ripple (≈ 7 dB amplitude) in a common busbar delay line. The horizontal scale is 500 kHz / division. 113

Figure 5-14. Response after common busbar removal, reducing direct RF feedthrough, and preventing RC filter – like behaviour. The horizontal scale is 2 MHz / division and the vertical 10 dB / division. 114

Figure 5-15. Delay line response with varying IDT and propagation path lengths. All devices are on AT-quartz substrates. 115

Figure 5-16. Frequency response from Y-AT and Y-ST delay lines with 80 λ IDTs and 40 λ propagation paths. 116

Figure 5-17. Comparison of uncoated SAW and Love mode device responses, showing a reduction in frequency and loss with the addition of a waveguide layer. 118

Figure 5-18. Response reproducibility from three identical delay lines with h = 0.80 μm polyimide. 119

Figure 5-19. Frequency response characteristics for different polyimide waveguide thicknesses. 120

Figure 5-20. Frequency dependence on polyimide waveguide thickness for device set A. 121

Figure 5-21. Insertion loss dependence on polyimide waveguide thickness for device set A. 122

Figure 5-22. Frequency comparison between set A (mean) and set B 123

Figure 5-23. Insertion loss comparison between set A (mean) and set B. 123

Figure 5-24. Frequency dependence on SiO_2 waveguide thickness. Data is shown for more than one device at each thickness. 124

Figure 5-25. Insertion loss dependence on SiO_2 waveguide thickness. Data is shown for more than one device at each thickness 125

Figure 5-26. Typical response from a SiO_2 waveguide Love mode device, with h = 2.35 μm. 126

Figure 5-27. Frequency dependence on polyimide thickness (horizontal axis) and SiO_2 thickness (data sets) for multilayer devices. 127

Figure 5-28. Insertion loss dependence on polyimide thickness (horizontal axis) and SiO_2 thickness (data sets) for multilayer devices. 128

Figure 5-29. Frequency temperature dependence for Y-AT and Y-ST uncoated devices. 130

Figure 5-30. Insertion loss temperature dependence for Y-AT and Y-ST uncoated devices. 131

Figure 5-31. Love mode frequency temperature dependence for different polyimide thicknesses on Y-ST substrates. 132

Figure 5-32. Love mode temperature coefficient of frequency (TCF) dependence on polyimide waveguide thickness. 133

Figure 5-33. Smooth and corrugated surface temperature dependence for polyimide h = 0.90 μm on Y-ST substrates. Data is plotted for temperature ramp up and ramp down. The corrugations are 0.5 μm deep, 2.5 μm wide, and spaced by 20 μm. . 134

Figure 6-1. DI water sensitivity for single layer polyimide, SiO_2 and multilayer smooth waveguide devices. 138

Figure 6-2. IPA sensitivity for single layer polyimide, SiO_2 and multilayer smooth waveguide devices. 139

Figure 6-3. Frequency shift versus insertion loss change for DI water and IPA samples on smooth single layer polyimide and SiO_2, and multilayer waveguide devices. 140

Figure 6-4. Sensitivity of polyimide devices to DI water and IPA as a function of waveguide thickness. 141

Figure 6-5. Effect of corrugations on the frequency response with DI water and IPA samples for 0.91 μm polyimide. Smooth surface – 0%. *cor2.5/20(0.5)* – 11%. *cor2.5/2.5(0.5)* – 50 %. *cor5.0/2.5(0.5)* – 67%. Three devices are shown for 0 %, and 2 devices for 11 %, 50 % and 67 % corrugations. 142

Figure 6-6. Effect of corrugations on the insertion loss change with DI water and IPA samples for 0.91 μm polyimide. 144

Figure 6-7. Effective permittivity ε_{eff} for polyimide waveguide layers with DI water and IPA samples, and with no sample in air. 145

Figure 6-8. Effective permittivity ε_{eff} for polyimide waveguide layers with DI water and IPA samples, and in air. The permittivity difference between the trough regions and smooth regions is highlighted for water loading. 146

Figure 6-9. Sucrose solution density and viscosity dependence on concentration. 147

Figure 6-10. Frequency shift with increasing sucrose concentration (described in terms of density and viscosity). The error bounds are $(\Delta f / f) = \pm 8 \times 10^{-5}$. 148

Figure 6-11. Insertion loss change with increasing sucrose concentration (in terms of viscosity). 149

Figure 6-12. Difference in relative frequency shift between corrugated and smooth delay lines with sucrose solution density. The error bounds are $(\Delta f / f) = \pm 1.6 \times 10^{-4}$. 152

Figure 6-13. Frequency shift with increasing sucrose concentration for SiO_2 and polyimide waveguide layers. The error bounds are $(\Delta f / f) = \pm 8 \times 10^{-5}$. 153

Figure 6-14. Insertion loss change with increasing sucrose concentration for SiO_2 and polyimide waveguide layers. 154

Figure 6-15. Difference in relative frequency shift between corrugated and smooth delay lines with sucrose solution density for SiO_2 and polyimide waveguide layers. The error bounds are $(\Delta f / f) = \pm 1.6\times10^{-4}$. 155

Figure 6-16. Frequency response to commercial spirits and liqueurs. 156

Figure 6-17. Frequency dependence on alcoholic beverage $\sqrt{(\rho\eta)}$. The error bounds are $(\Delta f / f) = \pm 8\times10^{-5}$. 157

Figure 6-18. Insertion loss dependence on alcoholic beverage viscosity. 158

Figure 6-19. Difference in relative frequency shift between corrugated and smooth delay lines with alcoholic beverage density. The error bounds are $(\Delta f / f) = \pm 1.6\times10^{-4}$. 159

Figure 6-20. Difference in relative frequency shift between corrugated and smooth delay lines for Famous Grouse and Bushmills whisky solutions. The error bounds are $(\Delta f / f) = \pm 1.6\times10^{-4}$. 160

Figure 6-21. Frequency shift of smooth and corrugated polyimide devices (h = 0.95 μm) with solvent and water samples. The error bounds are $(\Delta f / f) = \pm 8\times10^{-5}$. 162

Figure 6-22. Insertion loss response of smooth and corrugated polyimide devices (h = 0.90 μm) with solvent and water samples. 163

Figure 6-23. Difference in relative frequency shift between corrugated and smooth delay lines with solvent and water samples. The error bounds are $(\Delta f / f) = \pm 1.6\times10^{-5}$. 164

Figure 6-24. Difference in relative frequency shift between corrugated and smooth delay lines for three trials with the same device and samples. The error bounds are $(\Delta f / f) = \pm 1.6\times10^{-5}$. 165

Figure 7-1. Unit structure of SAW simulation. (a) Shows the solid model with two electrodes on a piezoelectric substrate, and (b) shows the meshed model. 171

Figure 7-2. ATILA results - Resonant responses at two nodes positioned between electrode fingers. 173

Figure 7-3. ATILA results - Regional displacements at 141 MHz and 179 MHz (note change in scales). 174

Figure 7-4. Acoustic and electrical ports on an arbitrary electrode structure. 176

Figure 7-5. Simulated band pass shape with different reflection coefficients. 177

Figure 7-6. Comparison in band pass shape of 0.84 μm polyimide Love, mode device with simulated responses of 0.0060 and 0.0080 reflectivity. 178

Figure 7-7. Close-up of previous figure showing the peak detail. 179

Figure 7-8. Synchronous resonator structure. 181

Figure 7-9. Simulated resonator response with variations in IDT length reflective grating length, 5.0 λ central spacing and 200 strips in each grating. 183

Figure 7-10. Simulated resonator response with variations in number of grating strips, 5.0 λ central spacing and 40 periods in each IDT. 184

Figure 7-11. Simulated resonator response with variations in cavity length, 40 period IDTs and 200 strips in each grating. 185

Figure 7-12. Resonator frequency response for identical transducer structures on ST quartz and $LiTaO_3$, 40 period IDTs and 200 strips in each grating. 186

Figure 7-13. Optimum resonator design on ST-X quartz, with 40 period IDTs, 400 strip gratings and a 4.8 λ central cavity length. 187

Figure 8-1. Plastic moulded packages. The diagram on the left shows the dies wire bonded to the lead frame before encapsulation and the cross section on the right shows the finished package. 190

Figure 8-2. Ceramic package cross-section 190

Figure 8-3. Metal can package cross-section. 190

Figure 8-4. Refractometer sample chamber. The stainless steel bowl with the central window region is positioned towards the bottom of the picture, and the lid with the central stub is in the vertical open position. The UK one-penny coin has a diameter of 20 mm for comparison. 192

Figure 8-5. Cross-section of sample chamber, showing stainless bowl, lid and stub, window and sample liquid. 192

Figure 8-6. Method of sealing electrical contacts using a metal lid and ceramic base. The ceramic package is based on the electrical header illustrated in figure 8-2... 193

Figure 8-7. Alternative method of sealing using sealant or epoxy 194

Figure 8-8. Encapsulated test devices using a Kyocera ceramic header (left), and a metal 'bath-tub' header (right). Araldite Rapid epoxy has been used for encapsulation. 194

Figure 8-9. Basic process to produce contact vias through substrate using etching and electroplating. 196

Figure 8-10. Backside contact arrangement using SMD ceramic header upside down with sensor die inside. The hole through the header base (now top) allows sample contact. 197

Figure 8-11. Backside contact arrangement using SMD ceramic header upside down with sensor die bonded to outside. The hole through the header allows wire bonds to be made to the die. The outline of the header and die can be identical. 197

Figure 8-12. Ball Grid Array (BGA) type package. Contacts made between die and Au plated pins with solder. 198

Figure 8-13. Cross-section schematic of prototype package. The detail shows the electrical contact method and liquid sealing. 199

Figure 8-14. Component parts of prototype package. The sensor die is positioned in the case, surrounded by 8 spring-loaded pins. The copper tracks on the PCB allow contact between the pins and contact pads on the die. 199

Figure 8-15. All parts in position showing the open chip area. 200

Figure 8-16. Prototype package in sample chamber. The pins would locate in a socket in the lid. 200

Figure 8-17. The proposed shape of a package incorporating flexible PCBs. The contacts are sealed under the protected covers. The chip surface (shaded area) can

be easily cleaned with a continuous surface at each end of the delay lines. The corrugations (indicated by lines in the picture) are also aligned in this direction.201

Figure 8-18. Cross section through flexible PCB package. A machined case with silicone sealant is illustrated, although a moulded case could be used.....202

Figure 8-19. Plan view of package. The right side is shown at sensor surface level and the shading on the left shows the raised protective region. The PCBs become narrower for the lead-outs.....202

Figure 8-20. Perspex liquid cell clamped to the surface of a SAW sensor. The SAW device is dark, with the inlet and outlets directed at the propagation path between the IDTs [88, 130].....204

Figure 8-21. Dip-stick viscometer using a SAW device for oil quality measurements [129].....204

Figure 8-22. Fingerprint sensors manufactured by UPEK Inc. The large open sensor surface is orange / yellow, encapsulated in the black moulded package. Electrical contacts are on the reverse of the package.....205

Figure 8-23. Packaging encapsulation method patented by AuthenTec [132].....206

Figure 8-24. Liquid sensor in an open cavity sealed package by Eurasem [133].....207

Figure 8-25. Cross section through Eurasem open cavity package [134]. Note the smooth rounded join at the cavity periphery.....207

Figure B-1. Shear wave on a plate of thickness *h* reflecting off upper and lower boundaries.....217

Figure C-1 Propagation of bulk waves into substrate from multiple point sources. 219

List of tables

Table 2-1. Example hydrometer ranges and resolutions. 14

Table 2-2. Comparison of different density sensors (values in italics are estimates based on research publications). 28

Table 3-1. The eighteen piezoelectric constants 40

Table 3-2. Relative operating regimes for bulk and surface wave resonators 46

Table 3-3. Waveguide relative properties for glassy and polymer materials. 69

Table 6-1. Properties of IPA and DI water at 20°C [18]. 143

Table 6-2. Corrugation geometry of polyimide devices used with sucrose samples {values in brackets are measured values} 148

Table 6-3. Physical properties of the solvent (and DI water) samples. Values are taken from manufacturers or other published data. 162

List of abbreviations

General abbreviations

AFM	Atomic force microscope
APM	Acoustic plate mode
BGA	Ball grid array
CMOS	Complementary metal-oxide-semiconductor
CVD	Chemical vapour deposition
DI	De-ionised
ETWI	Electrical through wafer interconnect
FBAR	Film bulk acoustic resonator
IC	Integrated Circuit
IDT	Interdigitated transducer
IL	Insertion loss
MEMS	Micro Electro-Mechanical Systems
MST	Microsystems Technology
PCB	Printed circuit board
PECVD	Plasma enhanced CVD
QCM	Quartz crystal microbalance
RF	Radio Frequency
RIE	Reactive ion etch
SAW	Surface acoustic wave
SEM	Scanning electron microscope
SH-SAW	Shear horizontal SAW
SMD	Surface Mount Device
SSBW	Surface skimming bulk wave
TCF	Temperature coefficient of frequency
TOT	Turnover temperature
TSM	Thickness shear mode
VNA	Vector network analyser
Y-AT	Quartz orientation 36°
Y-ST	Quartz orientation 42.75°

Materials

Al	Aluminium
Al_2O_3	Aluminium oxide
Au	Gold
$C_2H_4O_2$	Acetic acid
CF_4	Carbon tetrafluoride
Cr	Chrome
HF	Hydrofluoric acid
HNO_3	Nitric acid
H_2O_2	Hydrogen peroxide
H_3PO_4	Orthophosphoric acid
H_2SO_4	Sulphuric acid
I	Iodine
IPA	Isopropyl alcohol
$K_3Fe(CN)_6$	Potassium hexacyanoferrate

KI	Potassium iodide
KOH	Potassium hydroxide
$LiNbO_3$	Lithium Niobate
$LiTaO_3$	Lithium tantalate
N_2	Nitrogen
NaOH	Sodium hydroxide
N_2O	Nitrous oxide
NH_4F	Ammonium fluoride
O_2	Oxygen
PMMA	Polymethyl methacrylate
Si	Silicon
SiC	Silicon carbide
SiH_4	Silane
Si_3N_4	Silicon nitride
SiO_2	Silicon dioxide
TMAH	Tetramethyl ammonium hydroxide
ZnO	Zinc oxide

Nomenclature

A	Amplitude
$A(\omega)$	Array factor (of a finger in an IDT)
B	Constant (trapping factor)
C	Capacitance
D	Constant (in delta function model of IDT)
d	Depth of trough
E_s	Shear stiffness
f	Frequency
f_0	Resonant frequency
h	Waveguide thickness
h_m	IDT metallisation thickness
k	Spring constant
k_t	Wavevector – transverse
k_{ts}	Wavevector – transverse shear
k_l	Wavevector – longitudinal
k_{ls}	Wavevector – longitudinal shear
L_c	Cavity length (of a SAW resonator)
l	Length (propagation path in ultrasonic sensor)
M	Resonating tube mass
N	Number of periods in an IDT
n	Mode number (of Love mode)
P	Average power flow of wave per unit width
Q	Quality factor
r_s	Reflection coefficient of single IDT
S	Sensitivity
S_f	Sensitivity (in terms of frequency)
s	Spacing of troughs
s_l	Slip coefficient
t	Layer thickness
t	Time
v_D	Driving voltage (of an IDT)
v_s	Shear particle velocity
V_g	Group velocity
V_l	Acoustic velocity – longitudinal
V_{ph}	Phase velocity
V_R	Rayleigh velocity
V_s	Shear acoustic velocity – in waveguide
V'_s	Shear acoustic velocity – in substrate
V_t	Acoustic velocity – transverse
W	Width of IDT (IDT aperture)
w	Length of individual finger in IDT
w	Width of trough
Z_l	Acoustic impedance – liquid
Z_{ref}	Acoustic impedance – reference
Z_s	Shear acoustic impedance – in waveguide
Z'_s	Shear acoustic impedance – in substrate

(continued overleaf)

α	Attenuation constant wavevector
β	Phase constant wavevector
χ	Wave amplitude (from point source in IDT)
ε	Electrical permittivity
ϕ	Normalised permittivity difference
Γ	Reflectivity
γ	General propagation constant ($\gamma = \alpha + i\beta$)
η	Viscosity
λ	Wavelength
μ_∞	High frequency shear modulus
ρ	Density
ρ_s	Density (QCM substrate)
σ	Induced stress
υ	Partial wave solution
ω	Angular frequency

Piezoelectricity nomenclature

d_{hi}	Piezoelectric strain constants
e_{hi}	Piezoelectric stress constants
E_x, E_y, E_z	Applied electric field
P_x, P_y, P_z.	Induced Polarisation
X, Y, Z	Crystallographic axes
X_x, Y_y, Z_z, Y_z, Z_x, X_y	Stress in crystallographic axes
X_1, X_2, X_3, X_4, X_5, X_6	Stress in crystallographic axes (alternative notation)
x_x, y_y, z_z, y_z, z_x, x_y	Strain in crystallographic axes
x_1, x_2, x_3, x_4, x_5, x_6	Strain in crystallographic axes (alternative notation)

1 Introduction – microsystems technology

1.1 Small is beautiful

Miniaturisation has always been a driving force in man-made devices and objects. 'Small is beautiful' is often applied to aesthetically pleasing objects such as an item of jewellery, but can also describe the attractiveness of a machine in terms of its compactness and complexity, whether a watch movement or an internal combustion engine. Miniaturisation enables the production of more powerful, compact and cost-effective machines.

The historic paper *'There's plenty of room at the bottom'*, presented by Feynman in 1959 to the American Physical Society, discussed the need for miniaturisation, and predicted current research areas such as nanotechnology, with the aim of manipulating atoms and molecules at a fundamental level to produce miniature 'machines' [1]. Feynman claimed that by using a system of encoding at an atomic level, the entire stock of volumes contained in the world's libraries could fit in a cube of material of dimension one two-hundredth of an inch (125 μm) wide. The manipulation of materials at this scale would require a new set of 'miniature tools', which could be produced in stages using a series of pantogram-type apparatus. A prize of US $1000 was offered to the first person that could manufacture an operating electric motor fitting into a cube of side 1/64 inch, and a Caltech graduate constructed a working motor using conventional engineering techniques in 1960 to claim the prize (figure 1-1).

Figure 1-1. Miniature motor produced to claim the Feynman prize. The object in the background is a pinhead. (Courtesy of the Archives, California institute of Technology).

1.2 Microfabrication

The terms 'microengineering' or 'micromachine' are often used to describe small intricate machines, such as the Feynman prize-winning motor, which are built using standard engineering techniques on a miniature scale. The motor was constructed with small-scale components using fine tweezers, under a microscope. The method of fabrication was identical to that used for a large electric motor, just using smaller scale tools.

However, the term 'microfabrication' encompasses a range of processes, techniques, and tools far removed from traditional methods. This has enabled the emergence of microsystems technology 'MST' (often used in Europe) or micro electro-mechanical systems 'MEMS' (used in US).

The origins of microfabrication lie in the electronics industry. The semiconductor revolution was started in 1947 by the invention of the point contact transistor by Bardeen and Brattain [2], followed by Shockley's work on the *p-n* junction and bipolar transistor in 1949 [3], leading to the first 'modern' MOSFET in 1960 [4]. During the 1950s, in parallel to the development of these new devices, a range of fabrication techniques and tools were also being developed, allowing the fabrication of the first monolithic integrated circuit (IC) in 1960 [5]. Since this first IC, the growth of the microelectronics industry has been relentless, with the first Intel 4004 microprocessor containing 2250 transistors developed in 1971, and the present day Intel Itanium 2 microprocessor containing 410 million transistors. This is a perfect example of where miniaturisation has enabled the fabrication of more powerful and complex, but cheaper, devices. The increase in the number of transistors is described by Moore's law, which states that the transistor density on an IC will double about every two years. This has been facilitated by a reduction in feature size, improved circuit layout and design, and an increase in the IC area.

The fundamental processes of microfabrication are the deposition and selective removal of materials on a substrate. The deposition takes a variety of forms including the evaporation and sputtering of metals, diffusion, and ion implantation, and the removal is usually in the form of wet chemical or dry plasma etching.

The cornerstone of all microfabrication is lithography, which defines the regions of material addition and subtraction. There is typically one lithography stage for every patterned layer, with a modern microprocessor having over 30 different layers. The

lithography techniques define the smallest feature size making the development of high-resolution lithography processes the main driving force in the IC industry. The origins of lithography lie in the 18th Century and helped form the basis of photography, but the techniques were first applied to the semiconductor industry in 1957 for pattern transfer. The process essentially consists of selectively exposing a light sensitive resist through a patterned mask. Development removes the exposed resist (positive process) to leave the pattern, which defines the areas for deposition or etching. The requirement for ever smaller features has necessitated the need for more advanced mask making techniques and shorter wavelength light to combat diffraction. The current 90 nm technology used by Intel uses 193 nm UV wavelength lithography and phase shift masks, and further development of extreme UV (EUV) lithography down to 13.4 nm wavelength could allow the fabrication of features below 50 nm [6]. This will allow the further miniaturisation of edifices allowing the production of more powerful and complex ICs. More detailed descriptions of lithographic processes are given in chapter 4.

1.3 Micromachining

Unlike the Feynman 'micro-motor', micromachined MST or MEMS devices use a variety of microfabrication techniques borrowed from the IC industries, and some newly developed micromachining techniques and tools. The origins of micromachining lie in the 1960s, with experiments in wet crystallographic etching of silicon to produce trenches in ICs [7] enabling the fabrication of 3-dimensional structures in silicon. The first micromachined devices were piezoresistive silicon membrane pressure sensors developed by Honeywell in 1962 [8] using bulk etching of silicon. Possibly the most commercially important micromachined device was the ink-jet printer head developed by IBM in 1977 [9], which used the emerging technology to fabricate structures that were previously impossible to make.

The two basic approaches to micromachining are surface and bulk fabrication as shown in figure 1-2. As its name suggests, surface micromachining consists of the deposition, patterning, and release of materials on the surface of a substrate, allowing structures such as cantilevers and membranes to be produced. Bulk micromachining is where the substrate material forms the structures, achieved through using wet crystallographic etching techniques. Figure 1-2 shows the examples of a surface cantilever, and a mass on the end of a beam.

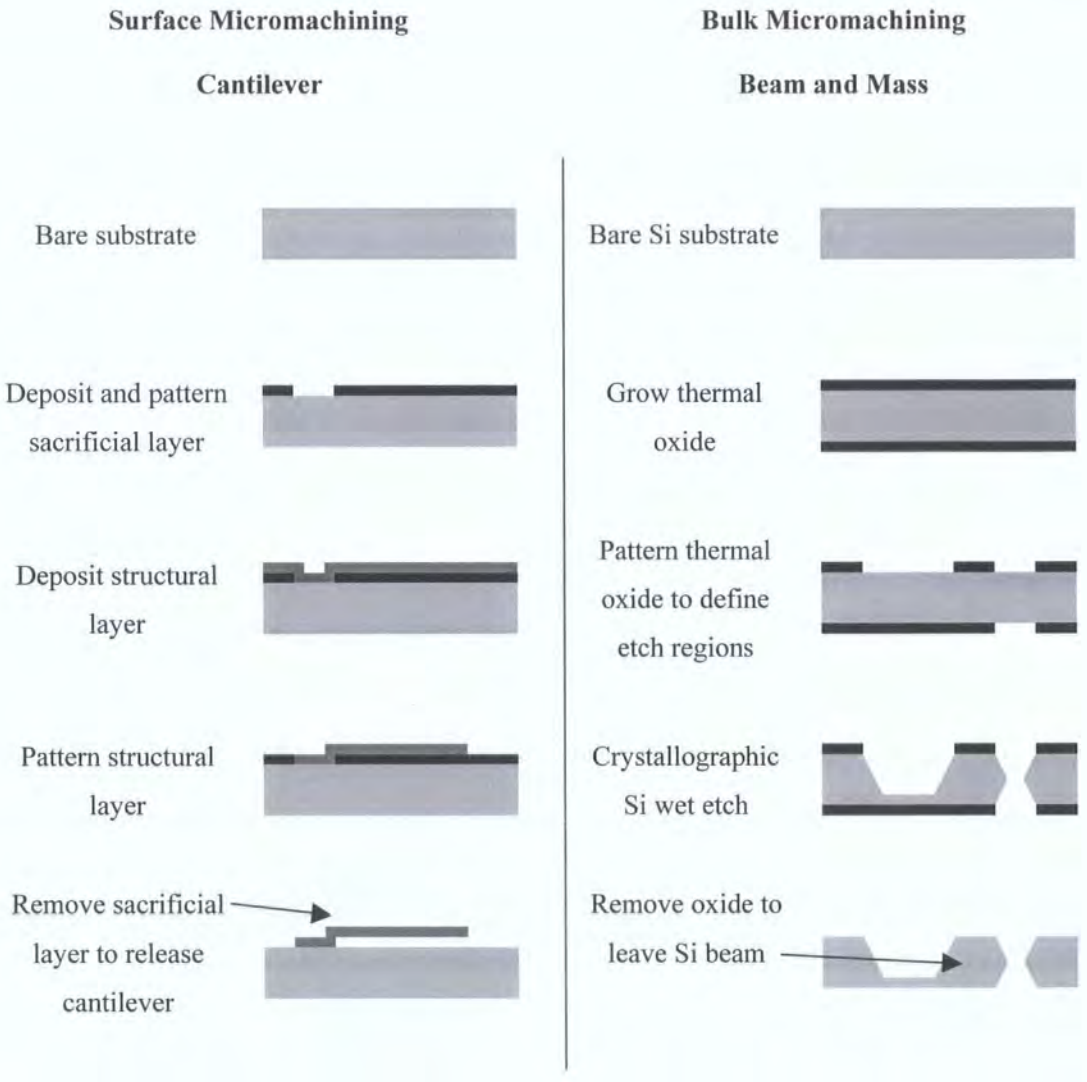

Figure 1-2. Examples of surface and bulk micromachining.

Surface and bulk techniques can be used together on the same device, if the processes will permit, to produce complex structures. The process techniques also allow the integration of electronic circuits onto a device chip so that a sensor or actuator and all the drive electronics and information processing can be combined.

New processes, tools, and materials developed for micromachining allow the construction of thicker structures to escape from the planarity of the standard microelectronics fabrication techniques. These include the LIGA process, a combination of X-ray lithography, moulding, and electro-deposition, which allows deep high-aspect ratio structures to be built [10]. A true 3-dimensional structure is difficult to achieve due to the 2-dimensional nature of lithography, and most devices are in

essence an extruded 2-dimensional structure. However some devices can self-assemble to build structures, such as the mirror shown in figure 1-3.

Devices developed at, for example, SANDIA National Laboratories (figure 1-3) illustrate the potential of micromachining, with the possibility of miniaturising conventional 'machines' such as steam engines, turbines, and gear trains.

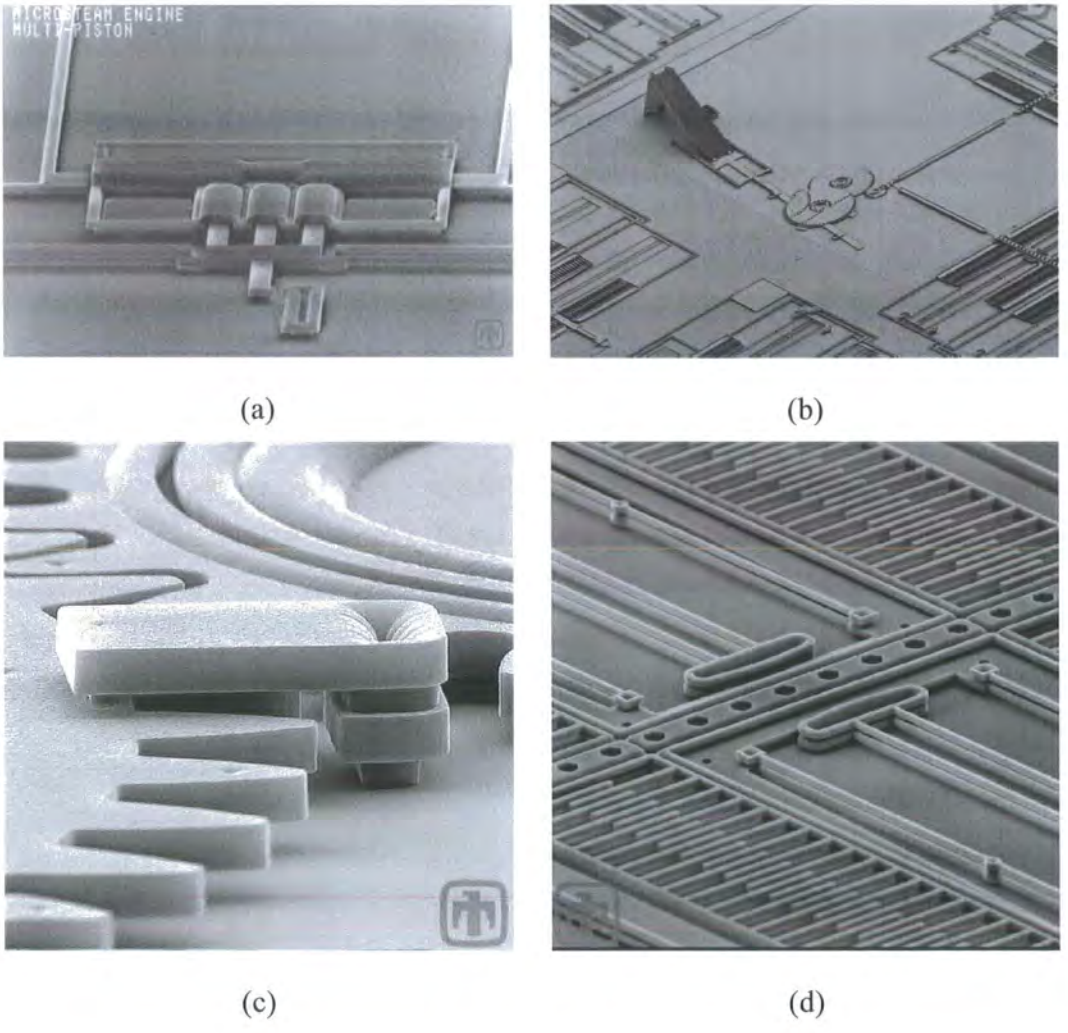

Figure 1-3. Micromachined devices from SANDIA National Laboratories.
(a) – Three cylinder steam engine. (b) – Mirror and actuation mechanism.
(c) – Gear mechanism. (d) – Electrostatic comb-drive.

Many of these 'mechanical' devices have limited uses at present and only demonstrate the possibilities, but they could be used for example in future mechanical logic devices (such as password encryption) and in-vitro drug delivery systems. They highlight a current problem with the microsystems area: the initial micromachining development for pressure sensors (Honeywell) and ink-jet printer heads (IBM) was

driven by the industrial pull for the new technology; but there is now a technical push to find new markets and applications for devices.

1.4 The MST market

The first NEXUS (The Network of Excellence in Multifunctional Microsystems) task force report predicted a world market growth in microsystems from US $14 billion in 1996 to $38 billion by 2002 [11]. The individual applications are shown in figure 1-4, with the largest growth in IT peripherals, covering display technology, printing technology and hard-disk read/write heads.

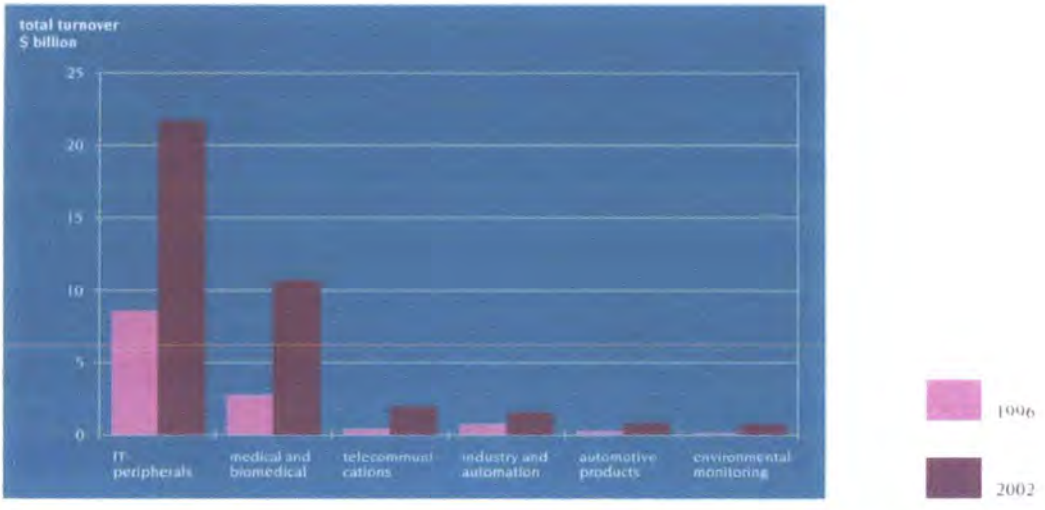

Figure 1-4. Summary of NEXUS predictions 1996 – 2002.

The subsequent review predicted a market increase from US $30 billion in 2000 to $68 billion by 2005, showing the rapid increase in new devices and markets as shown in figure 1-5 [12]. This report introduced new applications including household, and possibly most importantly telecommunications.

The optical communications industry was seen as a large growth industry in the late 1990s and early 2000s with large-scale research and development of optical MEMS (MOEMS). These integrated mechanical, electrical and optical functions onto single chips producing systems containing lasers and detectors, optical waveguides and mechanical mirror switching mechanisms. However the virtual collapse of the optical telecommunications industry in 2001 led to a massive reduction in this area.

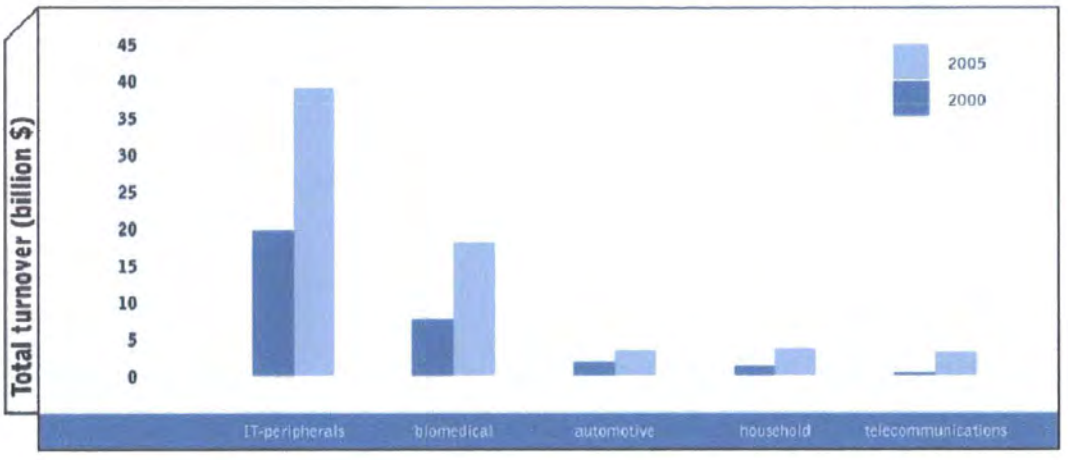

Figure 1-5. Summary of NEXUS predictions 2000 – 2005.

RF-MEMS is currently a rapid growth area due to the expansion of the mobile phone network and security devices such as RF-ID tags (figure 1-6) [13]. Micromachining techniques allow the production of high frequency devices and circuits incorporating variable capacitors, inductors, high-speed switches, and miniature antennas.

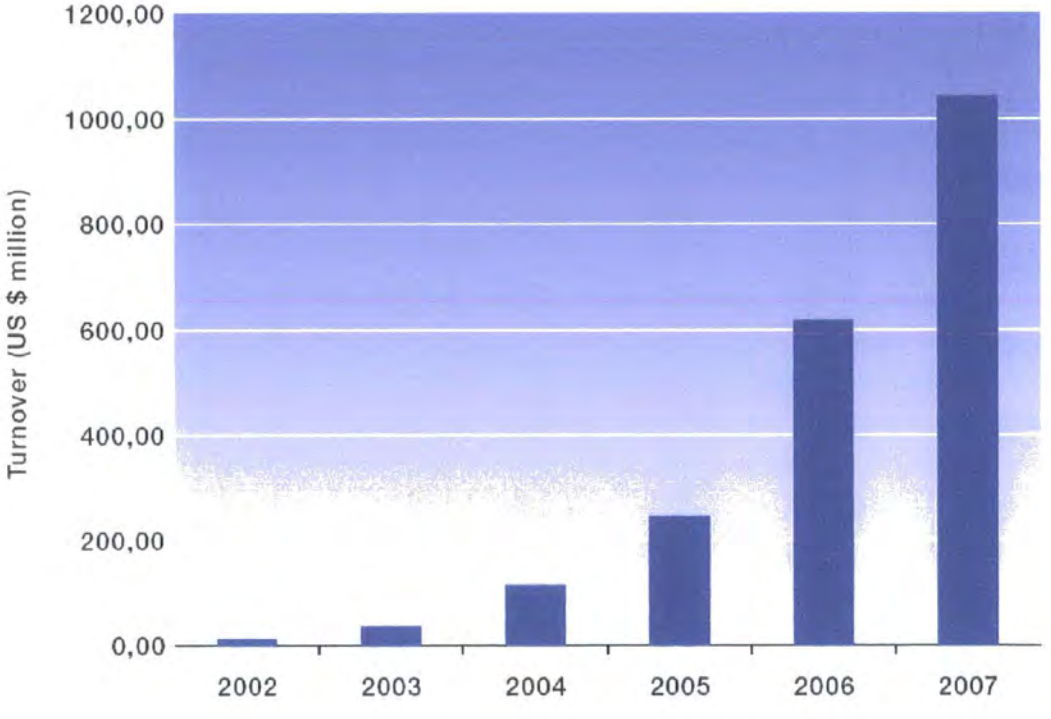

Figure 1-6. Total turnover forecast for the RF MEMS market.

Ink-jet printer heads are widespread with one or more in many homes and offices, and technological advances have enabled companies such as Epson to produce micromachined heads using electrostatically actuated pumps capable of producing 20 picolitre drops of ink [14]. Strategic marketing by introducing printer heads with a limited lifetime and making them a consumable item, combined with the rapid growth in home printing and digital photography (40% growth in 2004 [15]) has created a strong market. Hewlett Packard alone sold 14 million printers (including laser printers) during the last quarter of 2004 and supplies revenue grew by 8% [16].

The automotive market represents a large growth area for sensing with many opportunities for MST devices. Micromachined gyroscopes allow sophisticated suspension control preventing body roll and improving handling, whilst other devices such as gas and oil quality sensors can be incorporated into fuel and exhaust systems to control combustion and emissions. Bosch GMBH is one of the largest producers of automotive sensors, with 40 % of the devices produced using MST [17]. A modern car contains up to 100 sensors, with the number growing with advances in safety, braking, stability control, security, navigation systems, and emissions regulations. The first mainstream MST device incorporated into vehicles was the micromachined accelerometer by Analog Devices USA, used to sense sudden deceleration to trigger safety airbags. The sensor consists of a floating released membrane mass supported on spring structures at the edges. Movement of the membrane caused by acceleration is measured capacitively using comb structures, and electronic circuitry incorporated onto the device processes the response. The accelerometers are typically SMD packaged with external dimensions approximately 5 mm square, and offer significant improvements in reliability, cost, size, and sensitivity over the existing traditional mechanical devices. Figure 1-7 shows a micrograph of the central mass, springs and capacitive sensing mechanism.

Sensing perhaps represents the largest growth area, where micromachining techniques have significant advantages over the traditional engineering technologies, as amply illustrated by the accelerometer. The applications for sensors are almost limitless, with potential competitive solutions for most situations given by MST devices. The automotive industry has already been discussed, but other areas being exploited include household applications, environmental monitoring, and medical sensing with the possibility of in-vitro machines.

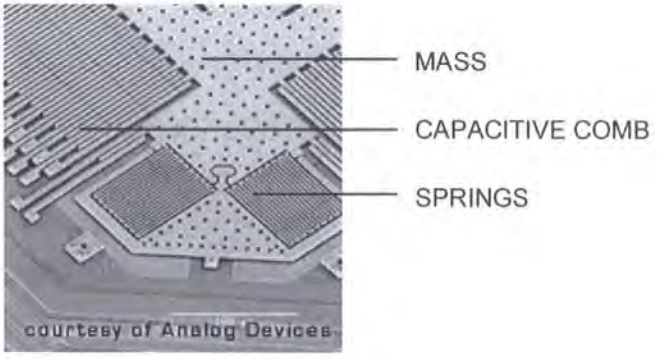

Figure 1-7. Micrograph of Analog Devices accelerometer showing suspended central mass, produced using surface micromachining.

1.5 Aims of this study

This study explores the use of MST for measuring the density of a liquid. An MST device could have the potential to significantly reduce the complexity and size of current liquid densitometers by enabling the production of a small, reliable and cost effective sensor. The study is presented with the following structure:

- Review of existing and current liquid density sensing techniques leading to the choice of a suitable method
- Outline of the theory and technology of chosen method
- Description of experimental procedures and techniques used in the fabrication of devices
- Results from the characterisation and testing of devices
- Discussion of ancillary aspects such as integration and packaging
- Conclusions

2 Liquid density sensing

This chapter outlines the requirements for the density sensor, and the desired specifications to allow commercial competition with other current systems. A brief discussion of the measurement of density is given. Different potential sensor designs are discussed, and their merits and disadvantages analysed. Finally, the conclusions lead to the choice of a suitable sensor type, which could be used as a basis for a liquid density sensor.

2.1 Introduction

Index Instruments UK manufactures a range of liquid refractometers and approached the University of Durham with the idea of developing a small liquid density sensor which could be integrated in the existing instrumentation. The successful integration of a density sensor into their refractometers would give them a unique market position and superior product.

The combined measurement of density and refractive index is desirable in many industries including food and drink, petrochemicals and cosmetics. The separate values or combined measurements can be used for a variety of quality control and analysis applications such as sucrose concentration, salinity, or alcohol content. By comparing the measured results with standard tables such as those published by the Chemical Rubber Company [18], the solution properties can be accurately determined.

Anton Parr, Mettler-Toledo, and K2 Analytical all offer combined systems that measure both properties simultaneously [19]. However, the equipment is made from separate modules for density and refractive index, and essentially offers a 'combined' solution through the use of shared sample filling and control, rather than a truly integrated instrument. Integration of a density sensor into the refractometer sample chamber would allow simultaneous measurements on the same sample volume without increasing the operation time due to filling and cleaning two instruments. Combination of the instruments could also reduce the number of components, overall footprint and cost.

A combined instrument should fulfil the following operational specifications:

- Single sample filling and removal
- Small sample size (< 1 ml)
- Short measurement time (a few seconds)
- Easy cleaning
- Short time span between measurements (< 1 minute)

The density sensor should offer technical specifications comparable to those of the current market leader Anton Parr GmbH:

- Range: $0 - 3\ gcm^{-3}$

- Accuracy: 5×10^{-6} gcm^{-3}
- Repeatability: 1×10^{-6} gcm^{-3} (standard deviation)

Other less critical technical specifications of the Anton Parr machine are a temperature range of 0 – 90 °C and a pressure range of 0 – 10 bar.

2.2 Liquid density

The density ρ of a liquid is defined as the mass per unit volume as given in equation (2-1) and is measured in kilograms per cubic metre.

$$\rho = \frac{mass}{Vol} \qquad (2\text{-}1)$$

The mass of one cubic centimetre of water was originally defined as a gram, giving a density 1 gcm^{-3}. The ratio of the density of a substance to that of water is called the **specific gravity**, and the magnitude of this is given in kgl^{-1}.

When mineral oil and water are mixed, the oil rises to the surface – this is because the specific gravity of the oil is about 0.87, and experiences less of a force due to gravity than the water. The buoyancy of a solid object in a liquid gives an indication of the object's mean density. Ice has a specific gravity of about 0.92, and thus a lump of ice (e.g. an iceberg) floats in water with 92% of its volume beneath the surface. This equilibrium occurs due to the iceberg's overall mass equalling the displaced water mass as stated by Archimedes' principle:

"A body immersed in a fluid is buoyed up by a force equal to the weight of the displaced fluid."

This example shows that by measuring the proportion of an object submerged in a liquid of known mass (assuming the object is less dense than the liquid and doesn't sink), the specific gravity of the object can be calculated.

2.3 Hydrometer

The hydrometer is the simplest instrument used to measure liquid specific gravity and is based on the buoyancy principle stated above. The device consists of a float with a mass at the bottom, and a scale up the side. The float remains vertical when placed in a sample liquid due to the mass, and floats at a level determined by the buoyancy. The

buoyancy (float level) depends on the sample liquid specific gravity, which can be read off the scale.

The hydrometer is a simple and cheap device with no moving parts. For this reason it is used extensively in many areas such as brewing, where the specific gravity of a brew solution indicates the sugar concentration (Brix rating). Hydrometers are manufactured for many purposes with measuring ranges suited to their test liquid range.

There are many limitations to using hydrometers as a general measuring system. The sample volume is typically large (10 – 100 ml), and size reductions would reduce buoyancy movement and the corresponding resolution. The major drawback is the narrow range of operation. If the hydrometer float is too light it will float on the surface of a dense liquid giving no reading. Similarly, if too heavy, it will sink in the sample. The solution is to have different mass hydrometers, each covering a finite range. For each hydrometer to cover an adequate range of specific gravities, the resolution of the scale may be relatively poor, thus another set of reduced range/increased resolution hydrometers are required to "zoom in". Combination hydrometers consisting of many floats in a partially sealed vessel can be used to overcome this but they still offer limited resolution. Table 2-1 shows the specifications of some hydrometers costing in the region of £10 each from BDH laboratory supplies.

Table 2-1. Example hydrometer ranges and resolutions.

Type	Range / specific gravity	Resolution / specific gravity
'Less sensitive'	1.100 – 1.200 1.200 – 1.300	0.002
'More sensitive'	1.150 – 1.200 1.200 – 1.250	0.001
Combination	0.700 – 2.000	0.01

2.4 Resonating tube densitometer

The resonating tube densitometers, such as those made by Anton Parr GmbH, are currently the standard method of high quality liquid density measurements. They operate using resonance to measure the physical properties of the liquid.

2.4.1 Resonance

All objects have a resonant frequency which is a direct measure of the physical properties such as mass, and stiffness or elasticity. External forces acting on a resonator also affect the resonance by damping or changing the resonant frequency. By configuring the resonator in the correct manner, these physical properties can be directly measured.

The quality factor, Q, of a resonator is defined as "the total energy stored in the structure divided by the sum of energy losses from the vibrating element per cycle" [20]. A strong Q factor implies a structure with low losses and energy dispersion, operating at a narrow bandwidth, giving the alternative definition of Q (2-2):

$$Q = \frac{f_0}{\Delta f_{3dB}} \tag{2-2}$$

where f_0 is the resonant frequency and Δf_{3dB} the bandwidth at 3 dB loss. A narrow frequency response with high Q allows straightforward control electronics with a low loss signal. The stability of high frequency resonators and the independence of frequency from noise and attenuation make them an ideal choice for many applications. Q factors in excess of 1000 are easily achieved by good design.

Resonators come in many forms including micromachined cantilevers and diaphragms, bulk piezoelectric resonators and acoustic wave resonators. The piezoelectric resonators have transformed frequency electronics by enabling high frequency and high stability sources as used in 'quartz' watches.

2.4.2 Resonating tube

The resonating tube densitometer consists of a U-shaped vibrating tube usually made out of glass or stainless steel with a bore of about 1 mm (figure 2-1). A sample

liquid filling the tube increases its mass and reduces the frequency by Δf in proportion to ρ.

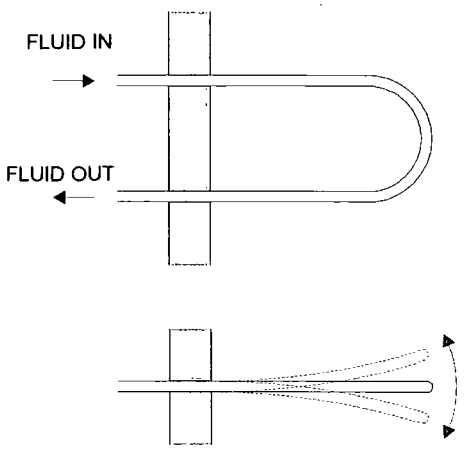

Figure 2-1. Schematic of resonating tube structure. The side view (bottom) shows a bending resonant mode.

The resonance of a tube of mass M and spring constant k is (2-3):

$$f_0 = \frac{1}{2\pi}\sqrt{\frac{k}{M}} \tag{2-3}$$

Insertion of a liquid into the tube volume *Vol* increases the effective mass to $M + \rho\ Vol$. Rearranging (2-3) we get:

$$\rho = \frac{k}{\left(2\pi f_{filled}\right)^2 Vol} - \frac{M}{Vol} \tag{2-4}$$

where the new resonant frequency is directly related to ρ. The tube vibration can be measured by various methods including capacitance (one fixed electrode and one moving on the tube), piezoelectric, or optical (photo-detector or interferometry) [20]. Non-contact methods are required to reduce damping of the structure.

The specifications in section 2.1 are for an Anton Parr DMA 5000 which requires a small sample volume of about 1 ml, although a larger volume, typically 2 – 3 ml, is required to effectively fill the tube without bubbles. The resonating tube densitometers are also expensive and complex. Inter-sample times can be long with different sample types to allow cleaning of the tube, a process which consists of flushing with two or more cleaning liquids followed by blowing air through with an in-built fan. The tubes

are susceptible to air bubbles distorting the result and careful filling is required. The small bore of the tube also makes filling with highly viscous liquids difficult. Such a system would be impossible to incorporate into a refractometer using the same liquid sample, due to its size, complexity, and nature of use.

2.5 Review of alternative sensors

2.5.1 Ultrasonic sensing

The density ρ is given by the ratio of the liquid acoustic impedance Z_l to the acoustic velocity V_l :

$$\rho = \frac{Z_l}{V_l} \tag{2-5}$$

The simplest form of liquid sensor consists of a piezoelectric ultrasonic transducer, a reference material, a liquid sample cavity and an acoustic reflector as shown in figure 2-2a [21]. The transducer operates in pulse echo mode, sending a pulse A_0 through the reference material, and measuring the reflected echoes from the reference material - liquid interface (A_1), and from the liquid – reflector interface (A_2). The ratio of amplitudes A_1 / A_0 give the reflectivity Γ at the reference material – liquid interface allowing calculation of the liquid impedance with knowledge of the reference material impedance Z_{ref}.

$$Z_l = Z_{ref} \frac{1+\Gamma}{1-\Gamma} \tag{2-6}$$

The time difference between the two received echoes directly gives V_l allowing direct calculation of ρ from (2-5). This method has no reference path thus variations in temperature, transducer response, and reference material properties require frequent calibration.

An improved variation uses a piezoelectric disk transducer using waves generated on both faces as shown in figure 2-2b [22]. Reference material is fixed on one side of length l_1, and another piece of reference material on the other side l_2 with $l_1 < l_2$, followed by a liquid cavity and a receiver. The difference in lengths of the reference material parts allows accurate determination of the material acoustic velocity v_{ref}. The reflection and time measurements to calculate ρ are based on differential measurements

between the two sides and not absolute measurements as in the earlier study, reducing the need for frequent calibration.

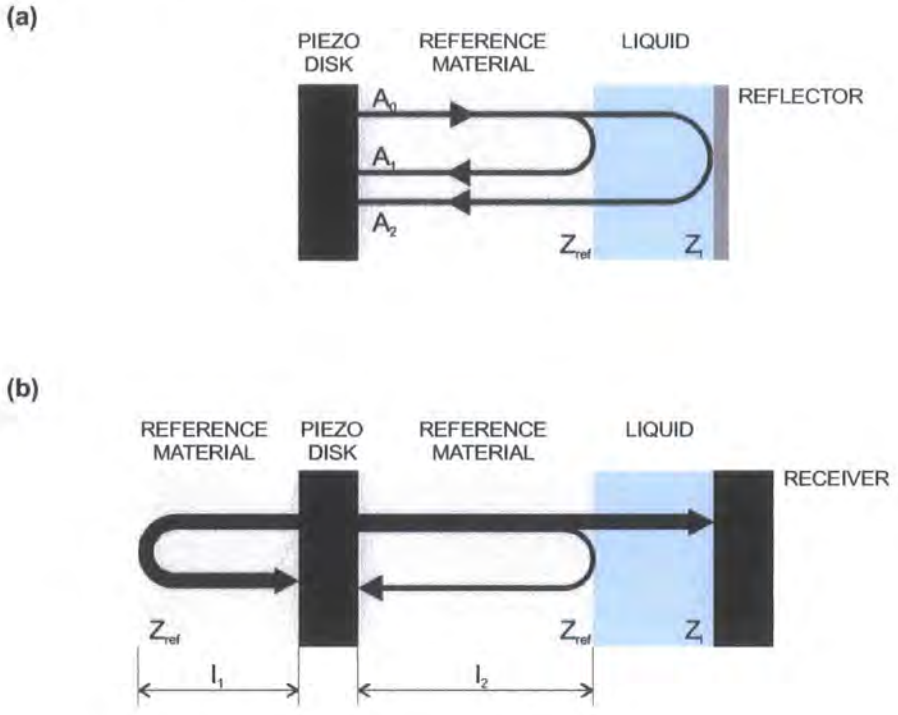

Figure 2-2. (a) – Simple pulse echo densitometer using a single reflector [21]. (b) – More advanced bi-directional transducer using a reference path [22].

No sensitivity information is provided on the devices, although this is presumably dependent on the quality of the control and analysis electronics including the analogue to digital converter [22]. The signal to noise ratio needs to be kept to 72 dB requiring careful design to avoid diffraction and spurious responses [22]. The overall device is large at around 80 mm diameter and produced using traditional engineering techniques, although possibly it could be reduced in size using higher frequency transducers and microfabrication. The liquid cavity is not open, and so has many of the disadvantages of the resonating tube.

2.5.2 Resonating cantilevers

The simplest liquid sensor consists of immersing a resonating structure in the liquid and measuring the change in resonant frequency and damping. Resonating cantilevers can be used to measure ρ and viscosity η of a liquid. The study in ref. [23] uses stainless steel cantilevers 4.95 × 0.6 × 0.1 mm coated with two PZT electrodes to drive

and sense the resonance. The cantilever is firmly clamped at one end, and the other end partially immersed. By simply modelling the system as a sphere on a spring, the resonance frequency is shown to be proportional to the effective mass of the cantilever and induced mass due to the liquid, allowing determination of ρ. The damping of the cantilever is proportional to the mass terms and the intrinsic and induced damping, with the latter directly proportional to η.

Experimental results with a small range of samples show good correlation with the theory, however the large losses prevent measurements of more viscous liquids than 75% glycerol. The resonance modes measured are all below 2.09 kHz in air, with a maximum drop to 190 Hz for the first mode in 75% glycerol. The given Q values range from 53 in water to 8 in 75% glycerol. The low operating frequencies and poor Q values suggest the device has a low sensitivity and resolution, and is only suitable for low viscosity liquids. The immersion depth of the cantilever would be difficult to control accurately, and this also affects the change in resonance along with the surface tension of the sample liquid.

Microfabricated cantilevers based on atomic force microscope tips operate in a similar manner to the stainless steel cantilever, but at higher frequencies up 106 kHz [24]. Different tips used are silicon bar, triangular silicon nitride, and triangular silicon. The resonance is measured using the AFM optical feedback and Fourier transformed into the frequency domain. The higher operating frequencies should give a greater sensitivity and resolution, with a Q value in air of more than 100. However the viscous damping reduces the Q to around 6 due to peak broadening and a logarithmic frequency decrease with glycerol concentration.

2.5.3 Micromachined resonating tube

A microfabricated silicon tube resonator developed by Enoksson et al shown in figure 2-3 miniaturises the existing resonating tube densitometer, whilst keeping the same principle of operation [25-28]. The structure is formed by anisotropic etching of silicon in KOH, by first etching half of each tube channel on the surface of separate wafers as in figure 2-4. The wafers are then bonded to form a complete channel, with further anisotropic etching to release the tubes. The device consists of two tube loops supported in the centre and operating in a balanced torsion mode as indicated in figure 2-3. The resonance was first electrostatically actuated and optically detected, with later

designs using capacitive detection. The entire device measures 14 × 23 × 1.85 mm (not including fluid inlets) and uses a sample size of 0.035 ml [28]. The $1/f^2$ frequency response is linear with ρ, with a resonance in air of 16.5 kHz and high Q values of 3400 (in air) and 1700 (water filled) resulting in a frequency sensitivity of $-2.6\ \mathrm{Hzkg^{-1}m^3}$. Similar devices from another research group show comparable responses, and also incorporate temperature control and sensing mechanisms to create a small hand-held unit for field use [29].

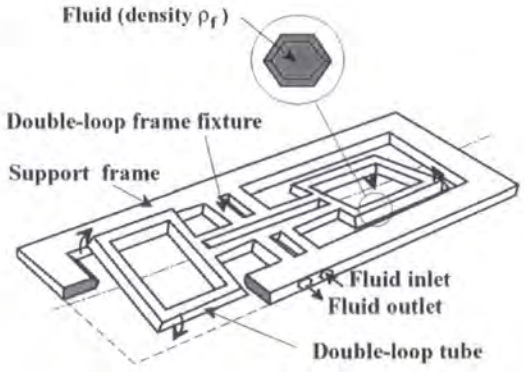

Figure 2-3. Micro fabricated resonating silicon tube densitometer [25-28].

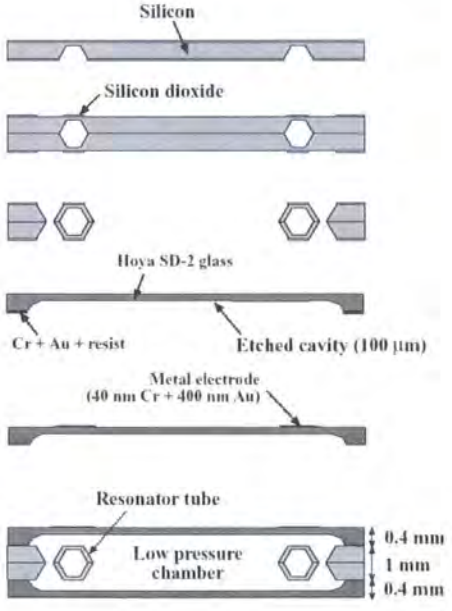

Figure 2-4. Fabrication process of silicon resonating tube structure. The tube halves are first anisotropically etched into silicon, and then the wafers bonded to create the tube. The entire device is packaged in a glass cavity incorporating electrodes for capacitive measurement [25-28].

Complicated fabrication for the bulk silicon resonating tubes in refs [25–29] has been overcome through surface micromachining techniques using sacrificial aluminium for compatibility with other CMOS processes [30, 31]. The tube structure is produced on the surface of the silicon wafer using CMOS dielectrics, and the tube cavity defined with a sacrificial aluminium structure that is subsequently etched, as shown in figure 2-5. The final process is an anisotropic silicon etch to release the entire tube structure. The operating frequency is around 150 kHz with similar Q values to the bulk silicon devices of around 2000. The frequency sensitivity given is $-5.7\ \mathrm{Hzkg^{-1}m^3}$.

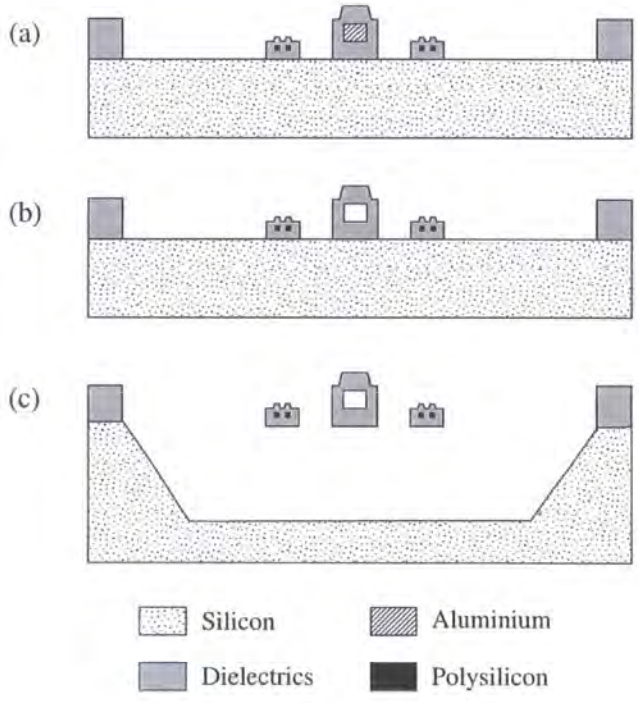

Figure 2-5. Resonating tube structure using a CMOS based process. The tube is fabricated in CMOS dielectrics using a sacrificial aluminium structure to define the hole. The tube is released using anisotropic silicon etching [30, 31].

2.5.4 Quartz crystal microbalance

The quartz crystal microbalance (QCM) is a well-established sensing technique for a variety of applications. The basic device consists of a thin piezoelectric quartz disc with electrodes deposited on either side connected to an oscillator circuit. For liquid sensing the disk resonates with a thickness shear mode (TSM) as indicated in figure 2-6. The crystal thickness determines the frequency, typically around 6 MHz.

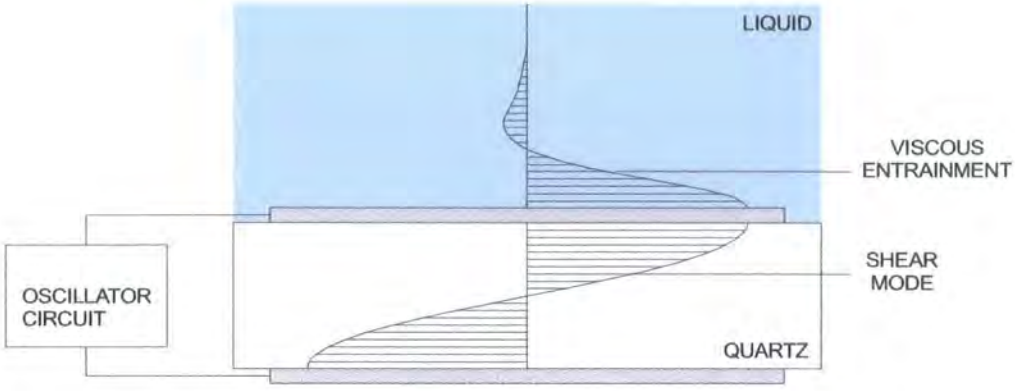

Figure 2-6. Schematic of a quartz crystal microbalance. The oscillator circuit is connected to the upper and lower electrodes. The horizontal hatched lines indicate the particle displacement.

It can be shown from [32] that the change in frequency of a QCM for mass loading with a thin solid layer is proportional to the layer density ρ_{layer}:

$$\frac{\Delta f}{f} = -\frac{2f\rho_{layer}t}{\sqrt{E_s\rho_s}} \tag{2-7}$$

where t is the layer thickness, and μ_s and ρ_s the shear stiffness and density of the quartz substrate. This relation is due to the stress induced in the QCM by the application of a mass loading layer with mass per unit area $\rho_{layer}t$.

Similarly liquid loading also shifts the frequency with the response dependent on the liquid viscosity η as shown in (2-8) [33]:

$$\frac{\Delta f}{f} = -\sqrt{\frac{f\rho_{liquid}\eta}{\pi\rho_s E_s}} \tag{2-8}$$

The frequency response is thus proportional to the square root of the density-viscosity product $\sqrt{(\rho\eta)}$. Equations (2-7) and (2-8) indicate that the density of a liquid cannot be sensed directly, but by altering the interaction between the liquid and the surface using surface patterning, the liquid can also be treated as a mass loading layer [34]. On a smooth surface the liquid is viscously entrained with the TSM causing a frequency change given by (2-8). Liquid trapped in a textured surface acts as a mass loading layer giving the mass response in (2-7) in addition to the viscous response in

(2-8). The difference in response between these two frequency changes removes the viscous component leaving the density.

Martin et al achieved this differential response using two QCMs mounted next to each other, one with a smooth surface and the other with surface texturing [34, 35]. The sensitivity is about –3.9 $Hzkg^{-1}m^3$ calculated from the data provided. By measuring the motional resistance of the QCMs through the oscillator circuit, the liquid η can also be deduced. The QCM type sensor offers the significant advantage over all the other sensors reviewed so far of having no sample cavity or fragile parts, but a single surface which allows quick and easy deposition and removal of the sample liquid.

2.5.5 Acoustic plate mode sensors

Acoustic plate mode (APM) sensors propagate a wave across a thin piezoelectric membrane, using interdigitated metal transducers to produce a periodic deformation. They are suitable for liquid sensing due to the phase velocity of the wave in the substrate being less than the acoustic velocity of the liquid. This helps prevent radiative losses into the liquid allowing efficient operation with low damping [36-39]. The sensor presented in [38] consists of a 0.7 μm zinc oxide (ZnO) layer deposited on top of a 2 μm silicon nitride layer on silicon. The transducers are patterned in aluminium on the ZnO layer. Removal of the Si behind the device with anisotropic etching forms the membrane with a cavity in the Si for the sample liquid. By placing the liquid in the etched cavity, the electrodes are protected by the membrane reducing electrical effects. A schematic is shown in figure 2-7.

The research initially assumes that the liquid density will mass load the device causing a frequency change Δf, and viscous damping will attenuate the wave. This response is given for low viscosity liquids, but with an increased Δf for higher viscosities. This is due to an additional viscous effective-mass loading, fitting well with theoretical predictions. The sensitivity in the linear response region is –1315 $Hzkg^{-1}m^3$ due to the increased operating frequency of 37.1 MHz, higher than the other devices discussed. The plate mode sensor has the ease of use advantages of the QCM but the membrane would be fragile in an open sensing environment.

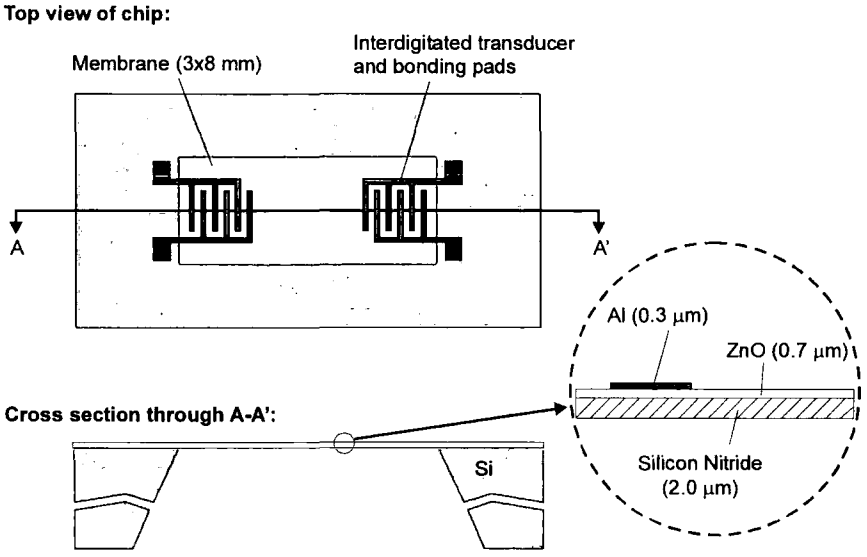

Figure 2-7. Schematic of the acoustic plate mode sensor presented by Martin et al [38]. The enlarged diagram shows the structure of the membrane and transducers.

2.5.6 Love mode surface acoustic wave sensor

Surface acoustic waves (SAWs) propagate along the surface of a material, unlike the bulk waves of the QCM and APM. The wave propagation is independent of the substrate thickness (which can be considered as a semi-infinite half space) and so there are no material limitations to the wave frequency in terms of crystal, or membrane, thickness.

Waves are generated with interdigitated transducers (identical to those described for the APM) patterned on the surface of a piezoelectric substrate, the period of the fingers determining the frequency. Love modes are formed by depositing a thin waveguide layer on the substrate surface, into which the SAW energy is confined. The focussing effect increases the acoustic energy at the surface giving a high sensitivity to surface perturbations, measurable by frequency and insertion loss changes.

The Love-mode density sensor presented by Herrmann et al consists of two sets of SAW transducers on the same substrate [40, 41]. The waveguide layer is made of chemical vapour deposition (CVD) of silicon dioxide (SiO_2) 2.2 μm thick. The surface of the waveguide layer over one set of transducers is corrugated, with vertical-sided troughs 0.59 μm deep made using a dry plasma etch. Figure 2-8 shows the basic components of the sensor.

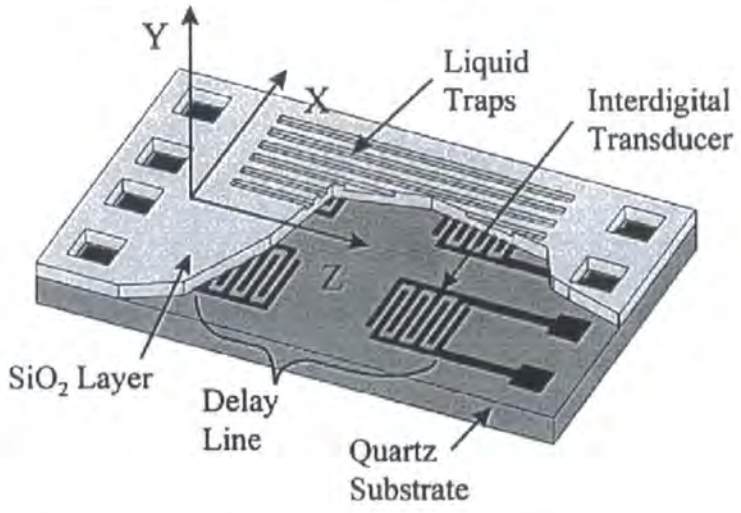

Figure 2-8. Love mode density sensor developed by Hermann et al [40].

The sensing mechanism is similar to the QCM based density sensor in ref. [34]. The Love waves have a horizontal motion in the surface plane, and the sample liquid is viscously entrained. On the smooth SAW device, this produces a frequency change proportional to $\sqrt{(\rho\eta)}$ as given in (2-8). On the corrugated side is an additional frequency change due to the mass loading effect of the trapped liquid given in (2-7). The difference in relative frequency change between the two SAW devices is thus proportional to ρ. The device operates around 125 MHz, the highest frequency of all the devices presented here. This high frequency combined with the large acoustic energy density near the surface give the device a sensitivity of up to –478 $Hzkg^{-1}m^3$. The insertion loss of the two SAW responses can also be used as a sensing mechanism. Once ρ has been measured, then η can subsequently be calculated, allowing simultaneous measurements on the same sample.

Patents on the sensor illustrate schematically the final device as shown in figure 2-9 [42, 43]. A liquid cell sealed to the chip surface with inlet and outlet ports confines the liquid to the region over the SAW devices. This, combined with the testing of diesel oils and an integrated temperature sensor (shown in figure 2-9), suggests in-line use, such as in an engine fuel system. Whilst this would make the patented sensor unsuitable for the refractometer sample chamber, there is no reason why the sensor could not be operated without the cell, leaving an open surface. This would make for simple sample loading and cleaning like the QCM and APM, but without the disadvantage of the two separate QCM crystals, or the fragile membrane of the APM.

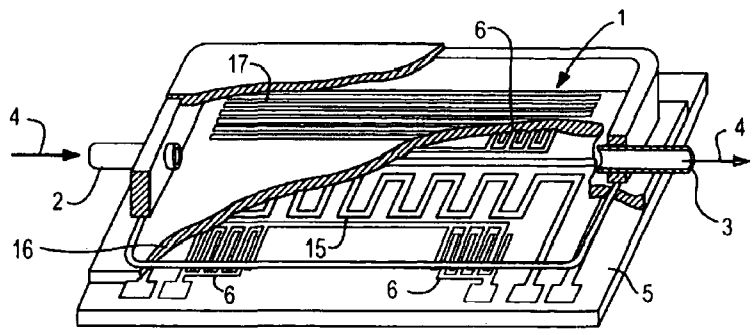

Figure 2-9. Schematic showing the Love mode density sensor with liquid flow cell [42, 43]. The serpentine component marked 15 is a temperature dependent resistor to monitor the surface temperature.

2.6 Conclusions

Table 2-2 compares the characteristics of the different designs discussed. All the devices apart from the ultrasonic sensor consist of a resonant system. The resonance is measured by monitoring the natural frequency, which can be used to directly calculate ρ and/or η. Frequency is a desirable sensing mechanism since it is dependent upon the fundamental device design and loading, and not affected by subsequent processing or electrical losses, unlike the insertion losses. The ultrasonic detector requires extensive signal processing to measure the signal time delays, with the possibility of errors and noise. This would probably be the most complex of the sensors to control.

Integration of a sensor into a refractometer sample chamber requires a small device which is easy to access and clean. The large size of the ultrasonic sensor combined with a semi-closed sample chamber precludes its use. The sensor could be miniaturised, but the complex construction, control, and enclosed chamber would still remain. The micromachined resonating tube structures are small, but the problems associated with the existing resonating glass tube densitometer are compounded. Their small size would make filling difficult with a lower limit on the sample viscosity and higher filling pressure. Most importantly, cleaning the tubes between samples would be very difficult, requiring multiple flush and drying processes, increasing the inter-sample time. The resonating cantilevers combine a potentially small size with no sample cavity. However the control could be expensive and complex (as with the AFM based cantilever) and the small cantilevers would be fragile and difficult to clean in an open

chamber. The large losses resulting from viscous drag on the cantilevers also lower their Q to less than 10 reducing their sensitivity and resolution.

The three acoustic mode sensors, the QCM, APM and Love mode sensor, all have similar attributes. They all make use of propagating acoustic waves in a piezoelectric substrate, with the sample liquid placed on the device surface. The devices are thus planar with no sample chamber enabling simple cleaning. They are relatively small allowing integration into the refractometer sample chamber, and simple to fabricate. The APM sensor and Love mode sensor exhibit the highest sensitivities to density of all the sensors discussed, with the APM 2.75 times more sensitive than the Love mode sensor. They are around 500 and 180 times more sensitive than the QCM respectively. Whilst the APM sensor is the most sensitive, it is potentially fragile and more difficult to fabricate than the Love device.

The open surface and simplicity of the acoustic mode sensors make them the obvious candidates for integration into the refractometer. Whilst the QCM sensors are well established commercially, the requirement for two sensors (one smooth and one patterned) would make the entire device relatively large. The Love mode sensor operates in a similar manner to the QCMs with smooth and corrugated sensing elements, whilst having a sensitivity 180 times larger and a smaller size. The Love devices are robust, with the option of using relatively thick substrates, and are simple to fabricate using surface micromachining. For these reasons, the Love mode density sensor is the most promising solution for the intended application.

Table 2-2. Comparison of different density sensors (values in italics are estimates based on research publications).

	Anton Parr Resonating Tube	**Ultrasonic [21,22]**	**Cantilever [23,24]**	**Micro tube [25 - 31]**	**QCM [34,35]**	**APM [36 - 39]**	**Love [40 - 43]**
Size	440 × 315 × 220 mm (entire machine)	98 mm ∅ × 85 mm	*< 5 × 2 mm (AFM Tip)*	14 × 23 × 1.85 mm	*≈ 10 mm ∅ × 1 mm* 2 required	*≈ 10 × 10 × 0.5 mm*	*≈ 10 × 10 × 0.5 mm*
Sensitivity	-	-	-	–2.6 $Hzkg^{-1}m^3$	*–3.9 $Hzkg^{-1}m^3$*	–1315 $Hzkg^{-1}m^3$	–478 $Hzkg^{-1}m^3$
Accuracy	0.005 kgm^{-3}	0.1%	-	-	-	-	-
Resolution	-	-	-	4 kgm^{-3}	-	-	-
Density Range	0 – 3000 $kg^{-1}m^3$	-	-	-	-	-	-
Viscosity Range	Limited by filling	-	-	Limited by filling	-	-	-
Fabrication method	Traditional engineering	Traditional engineering	Traditional engineering / microfabrication	Bulk / surface microfabrication	Surface microfabrication	Bulk / surface microfabrication	Surface microfabrication
Sample volume	≥ 1 ml	*≈ 38 ml*		0.035 ml	*≤ 1 ml*	*≤ 1 ml*	*≤ 1 ml*
Sample contact method	Tube ≈ 1 mm ∅	Semi-open cavity	Open	Tube ≈ 0.5 mm ∅	Smooth surface	Open cavity / smooth surface	Smooth surface
Ease of use / cleaning	Flush tube - difficult	Rinse and flush - moderate	Rinse clean. Fragile	Flush tube – very difficult	Wipe clean - easy	Wipe clean - easy	Wipe clean - easy
Control	Optical pickup. Frequency processing.	Signal monitoring in time domain.	Optical, piezo-resistive pickup. Frequency processing.	Optical, capacitive. Frequency processing.	Direct frequency via oscillator feed-back circuit.		

3 Surface acoustic waves and devices

This chapter describes the principles and theory of surface acoustic waves, and methods of generation using inter-digitated transducers and piezoelectric substrates. A review of electrical SAW devices followed by examples of SAW sensors is given. The final section introduces Love mode devices, finishing with a detailed description of device theory and materials.

3.1 Rayleigh waves

The English mathematician Lord Rayleigh first proposed surface acoustic waves (SAWs) in 1885 [44]. He showed how an acoustic mode could propagate along the boundary of an elastic material with a rarefied medium such as a vacuum or gas, i.e. at the surface of the material. Rayleigh's initial theory based around seismic waves was thought to be of limited importance, and in the 1920s his prediction that SAWs were a major component of earthquakes was confirmed with analysis carried out by the newly invented seismographs. During the mid 20th century, the same theory was applied at a smaller scale to piezoelectrically driven SAW devices, now produced in the billions.

'Rayleigh waves' contain longitudinal and vertical shear components with an ellipse-like particle motion into the surface (figure 3-1). The amplitude decays exponentially with depth into the propagation material, with the wave energy typically contained within one wavelength λ of the surface. The scale over which SAWs can occur is large, with wavelengths ranging from a few microns to many kilometres.

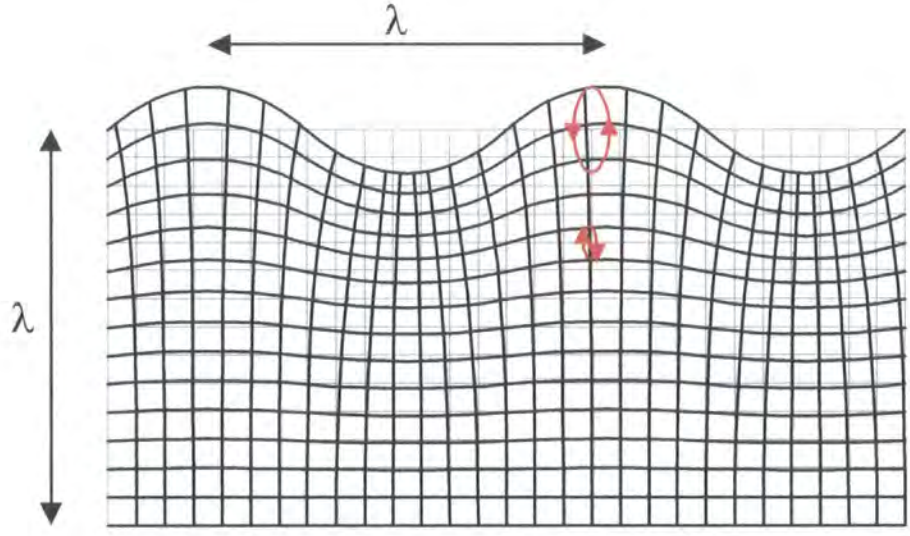

Figure 3-1. Rayleigh wave displacement with elliptical particle motion.

Acoustic wave modes of particular interest here are shear horizontal SAWs (SH-SAW). These have a longitudinal mode (like Rayleigh SAWs) and a horizontal mode with sideways particle motion in the surface plane, and discussed in more detail later. Other acoustic modes are often included in SAW discussions due to their similarities. These include surface skimming bulk waves (SSBW) which will be discussed later in this study (see Appendix **C**), and Lamb waves which are formed when the Rayleigh

wave substrate is approximately one wavelength thick causing the Rayleigh mode to degenerate into a plate mode.

3.1.1 Theory of Rayleigh waves

Consider an infinite half-space described by x and z lying on the surface, and y normal with the surface at $y = 0$ (figure 3-2). A surface wave propagates in the z-direction, with longitudinal and transverse partial wave components. The wave motion is confined to the y-z plane, known as the sagittal plane. There is no variation of the wave in the x-direction which lies parallel to the wave fronts.

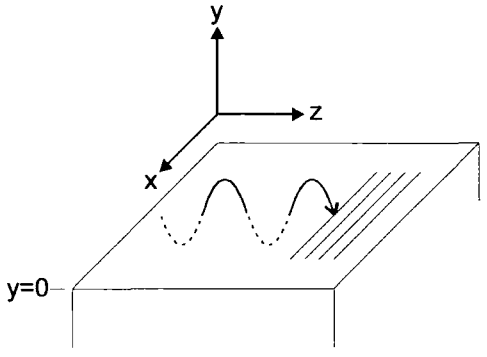

Figure 3-2. Rayleigh waves on an infinite half-space propagating in the z-direction with wave motion in the y-z sagittal plane.

The wave is described by its transverse (k_t) and longitudinal (k_l) wavevectors [45] where V_t and V_l are the transverse and longitudinal acoustic velocities and ω the circular frequency:

$$|k_t|^2 = \left(\frac{\omega}{V_t}\right)^2 \qquad |k_l|^2 = \left(\frac{\omega}{V_l}\right)^2 \tag{3-1}$$

The wave motion is confined to the sagittal plane and therefore k_t and k_l both lie in this plane with no x component. Omitting the time varying factor $\exp(i\omega t)$, the wave motion can be described as $\exp(-i\beta z)$ with the Rayleigh wavevector, β, defined as ω/V_R where V_R is the Rayleigh wave velocity. β is equal to the z-components of k_t and k_l.

The shear components of k_t and k_l are :

$$k_{ts}^{\ 2} = \left(\frac{\omega}{V_t}\right)^2 - \beta^2 \qquad k_{ls}^{\ 2} = \left(\frac{\omega}{V_l}\right)^2 - \beta^2 \tag{3-2}$$

With a full set of wavevectors to describe the wave, the transverse and longitudinal wave displacements υ_t and υ_l can be defined:

$$\upsilon_t = A \ \exp - i(\beta z - k_{ts} y) \tag{3-3}$$

$$\upsilon_l = B \ \exp - i(\beta z - k_{ls} y) \tag{3-4}$$

where A and B are constants, and the sum of the partial waves is $\upsilon = \upsilon_t + \upsilon_l$.

A property of Rayleigh waves is the exponential decrease in displacement from the surface ($y < 0$). For $y < 0$, both k_{ts} and k_{ls} need to be positive and imaginary for $\exp(ik_{ts}y)$ or $\exp(ik_{ls}y)$ to decay. From (3-2), $\beta > \omega/V_t$ and $\beta > \omega/V_l$, for k_{ts}^2 and k_{ls}^2 to be negative, thus the Rayleigh wave velocity is less than both the transverse and longitudinal velocities:

$$V_R < V_t \tag{3-5}$$

$$V_R < V_l \tag{3-6}$$

The wave displacements υ_t and υ_l can be solved in a modified form of the wave equation [45] which includes stress terms based on the elasticity of the material. The relationship is found where V_R/V_t is dependent upon V_l/V_t. Thus the Rayleigh wave velocity can be calculated for any isotropic medium with knowledge of V_l and V_t.

The resultant displacements upon solving are [45]:

$$\upsilon_z = \gamma \exp(a\beta y) - \exp(b\beta y) \tag{3-7}$$

$$\upsilon_y = i\left[\gamma a \exp(a\beta y) - b^{-1} \exp(b\beta y)\right] \tag{3-8}$$

where $a = -i\dfrac{k_{ls}}{\beta}$ $\quad b = -i\dfrac{k_{ts}}{\beta}$ $\quad \gamma = \dfrac{\left(2 - V_R^{\,2}/V_t^{\,2}\right)}{2ab}$

The displacement equations for υ_z and υ_y describe an elliptical wave motion, where the vertical axis is almost double the horizontal axis [44]. The horizontal motion vanishes about 0.2 λ into the substrate, where the direction of motion is reversed as indicated by the change in direction of the arrows in figure 3-1. The wave motion is typically contained within λ of the surface due to the real exponential terms in the

displacements, but theoretically, there is no finite depth where vertical particle motion becomes zero.

3.2 SAW Excitation

3.2.1 Interdigitated transducers

A SAW device consists of a piezoelectric substrate along whose surface the wave can propagate, a transducer to generate the wave, and possibly another transducer to detect the resultant wave. Mechanical comb transducers (figure 3-3) were initially used to generate the waves, where the teeth spaced at the desired wavelength are pressed on to the piezoelectric substrate with a periodic force at the wave frequency. The resultant induced strain propagates across the substrate.

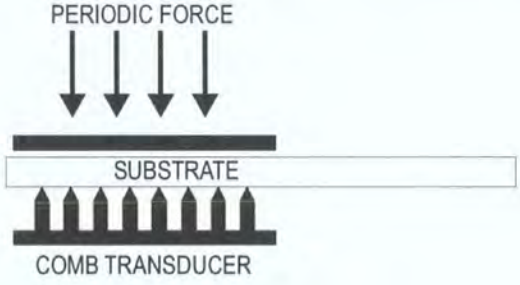

Figure 3-3. Comb transducer.

The modern SAW device was born in 1965 with the development of the 'interdigitated transducer' (IDT) [46], a periodic electrode structure patterned onto the piezoelectric substrate, to which an RF voltage is applied. Interlocking fingers connected by bus bars create a periodic electric field resulting in substrate deformations that propagate as SAWs. The waves are detected and generate an output RF voltage at a receive IDT, or are received at the transmit IDT after reflection. The IDT finger period is equal to the SAW wavelength, with the finger width and spacing usually being equal at $\lambda/4$ (a 'metallisation ratio' of 50%). The most basic SAW device made up of separate transmit and receive IDTs is known as a delay line, as shown in figure 3-4.

The fundamental advantage of IDTs is the 2-dimensional nature of their coupling to a piezoelectric material, allowing manipulation of the SAW over the actual substrate surface (this is mentioned further in section 3.4.1). IDT based devices are cheap and simple to produce using standard IC-based lithographic techniques. They can replace a variety of multi-component systems in the electronics field, and are small and robust.

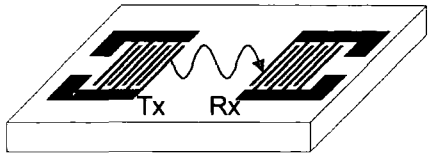

Figure 3-4. Delay line composed of transmit and receive IDTs.

Each IDT can transmit and receive surface waves from both ends, half the power in each direction, giving a single IDT an insertion loss of 3 dB, as shown in figure 3-5. A dual delay line structure thus has a minimum insertion loss of 6 dB.

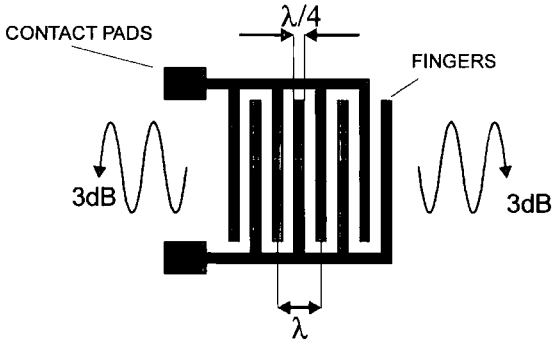

Figure 3-5. Uniform IDT showing 3dB power in each direction.

The length W of the IDT fingers must be large enough to avoid diffraction spreading of the wave as it propagates from the transducer. The finger lengths determine the overlap between the two ports of the transducer, and thus the IDT capacitance. With correct length, it is possible to electrically match the transducer to the external electronics controlling the device if required. Typical lengths are in the range 20 – 100 λ.

3.2.2 Electrical excitation – delta function model

The delta function model describes electrical excitation by an IDT as a number of point sources in each inter-electrode gap, resulting from the electric field between adjacent fingers [45]. Each independent source contributes to the SAW formation, and the model assumes each wave source is unaffected by other electrodes. The electrodes do in fact reflect and perturb the wave, but for weak piezoelectric coupling, and to reduce the analysis complexity, this is omitted here.

The wave amplitude (ignoring time variation) from a single finger (or single source) positioned at a point x_n along the IDT is:

$$\chi_s(x) = Dv_D C_n \exp[ik(x - x_n)] \tag{3-9}$$

where D is a constant, v_D is the driving voltage over the IDT, $C_n = \pm 1$ depending upon the direction of the field in between the fingers, and k is the wavevector.

The individual source factor is given:

$$A(\omega) = \sum_{n=1}^{N} C_n \exp(-ikx_n) \tag{3-10}$$

where $A(\omega)$ is known as the 'array factor', determined by electrode positions and polarities and N is the total number of fingers in an IDT. The total amplitude is:

$$\chi_s(x) = Dv_D A(\omega)\exp(ikx) \tag{3-11}$$

If we express $C_n = \pm 1$ using $C_n = C_1\exp(-in\pi)$, and replace x_n with $\lambda n/2$, the array factor becomes:

$$A(\omega) = C_1 \sum_{n=1}^{N} \exp\left[-in\left(k\lambda/2 - \pi\right)\right] \tag{3-12}$$

A Taylor expansion of (3-12) gives:

$$|A(\omega)| = \left|\frac{\sin N\theta/2}{\sin \theta/2}\right| \tag{3-13}$$

where $\theta = \pi(\omega - \omega_0) / \omega_0$. We are principally interested in the characteristics around the operating frequency, i.e., when $\omega \rightarrow \omega_0$. The approximation with $\theta \rightarrow 0$ is:

$$|A(\omega)| \approx N\left|\frac{\sin N\theta/2}{N\theta/2}\right| \tag{3-14}$$

Equation (3-14) describes the fundamental shape of the generated SAW as a $|\text{sinc}|$ function, with a large central response, and smaller side lobes. The first two minima each side of ω_0 occur at $\omega = \omega_0 \pm 2\omega_0 / N$, giving a 4 dB bandwidth of $\Delta\omega = 2\omega_0 / N$. By making N large, it is possible to excite a strong SAW with a large

amplitude ($A \propto N$), and with a narrow bandwidth ($\Delta\omega \propto 1/N$), ideal properties for a SAW sensor.

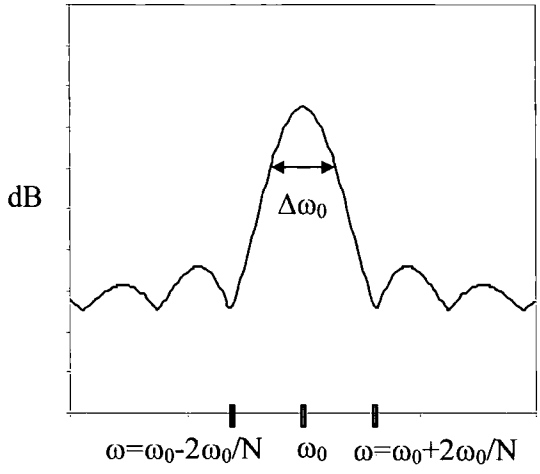

Figure 3-6. Theoretical |sinc| frequency response from uniform IDT.

IDT reception can be modelled in an identical manner to transmission, taking into account the IDT geometry, and summing the response from each finger. A length factor w/W is used for apodised transducers (see section 3.4.1), where w is the length of an individual finger, and W the width of the transmitting transducer.

3.3 Surface acoustic wave device substrates

3.3.1 Elastic properties

An orthogonal XYZ co-ordinate system that maps onto the crystallographic XYZ axes is used to describe the stresses, strains and piezoelectric constants.

The stress induced in a crystal is the force per unit area applied to a plane. Six components of stress, are labelled X_x, Y_y, Z_z, Y_z, Z_x and X_y, the first letter indicating the force direction, and the subscript the surface normal direction on which the force acts. The first three terms represent the material being **compressed** along the principal axis, and the last three terms are **shearing** stresses. An alternative notation is X_1, X_2, X_3, X_4, X_5 and X_6. A capital letter will always be used for stress. A positive stress indicates compression and a negative stress indicates extension.

The strain in a crystal is defined as the 'ratio of the change in length to the original length' when the crystal is deformed. Similarly to stress, there are three longitudinal

strains and three shearing strains labelled x_x, y_y, z_z, y_z, z_x and x_y, or alternatively x_1, x_2, x_3, x_4, x_5 and x_6. A positive strain indicates an extension, and therefore is comparable with a negative stress. Stress is often used when describing the applied mechanical force to induce a polarisation, and the result of applying an electric field is often given in terms of strain.

Stress and strain are related by the elastic constants c_{ik}:

$$X_k = -\sum_{i=1}^{6} c_{ik} x_i \tag{3-15}$$

In all there are 21 elasticity coefficients due to the relation $c_{ik} = c_{ki}$.

3.3.2 Piezoelectric properties

The piezoelectric effect (piezo – Greek "to press") was discovered by the brothers Pierre and Jacques Curie in 1880. They applied pressure to plates cut from crystals including quartz, and using tin foil electrodes found that electrical charges accumulated on some of the crystal faces when the crystals were compressed in particular directions. The charge on the faces was proportional to the compressional force and the process was reversible with all the charges disappearing when the forces were removed. This is the **direct** piezoelectric effect. The **converse** effect where an applied electric field induces a stress and, consequently, a deformation in a crystal, was subsequently demonstrated theoretically (Lippmann) and then experimentally (Curies).

To exhibit piezoelectricity, the crystal must be non-centrosymmetric, i.e., it must not have inversion symmetry. By applying a force, deformation of the atomic structure displaces the charged atoms causing dipole formation. Figure 3-7 illustrates this effect showing a crystal structure in equilibrium (a), under compression (b) and in tension (c). With certain crystal orientations, compression induces a polarisation parallel to the direction of compression (**longitudinal** effect) as shown in figure 3-7, and also perpendicular to the compression axis (**transverse** effect).

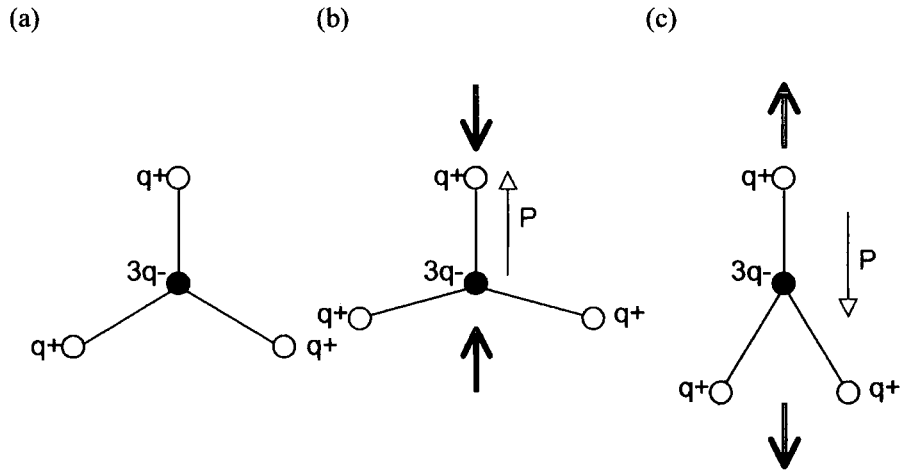

Figure 3-7. Equilibrium (a), compression (b) and tension (c).

Lippmann's theory on piezoelectricity can be expressed as follows: a piezoelectric material is subjected to a mechanical stress X whilst being placed in an electric field E, resulting in a polarisation P, and induced strain x, in the crystal [47]. If the stress and field are changed by dX and dE respectively, then the total change in energy can be expressed as $dU = PdE - xdX$. Assuming the process is reversible, we can write:

$$\left(\frac{\partial P}{\partial X}\right)_E = -\left(\frac{\partial x}{\partial E}\right)_X \tag{3-16}$$

The process is linear so:

$$\frac{\partial P}{\partial X} = -\delta \tag{3-17}$$

$$\frac{\partial x}{\partial E} = \delta \tag{3-18}$$

where δ is the piezoelectric strain constant. The induced polarisation can now be expressed in terms of the applied stress multiplied by a constant, and likewise the induced stress in a material in terms of the applied electric field multiplied by the same negative constant.

3.3.3 Piezoelectric equations

The fundamental piezoelectric equations describing all possible states of stress/strain, and electric field/polarisation can now be stated. Eighteen piezoelectric

constants are required, due to the 6 different states of stress or strain, X_h and x_h, for each of the three components of applied electric field, E_x, E_y, E_z, or induced polarization P_x, P_y, P_z.

For the direct effect, the piezoelectric equations in terms of stress are:

$$P_h = \sum_{h=1}^{3} \sum_{i=1}^{6} d_{hi} X_i \tag{3-19}$$

which expands to give:

$$\begin{aligned} P_x &= d_{11}X_1 + d_{12}X_2 + d_{13}X_3 + d_{14}X_4 + d_{15}X_5 + d_{16}X_6 \\ P_y &= d_{21}X_1 + d_{22}X_2 + d_{23}X_3 + d_{24}X_4 + d_{25}X_5 + d_{26}X_6 \\ P_z &= d_{31}X_1 + d_{32}X_2 + d_{33}X_3 + d_{34}X_4 + d_{35}X_5 + d_{36}X_6 \end{aligned} \tag{3-20}$$

where d_{hi} are the piezoelectric strain constants. The same equations are written in terms of the piezoelectric stress constants by exchanging X_i with x_i, and d_{hi} with e_{hi}.

For the converse effect, the equations (in terms of stress) are simply:

$$X_i = -\sum_{h=1}^{3} \sum_{i=1}^{6} e_{hi} E_h \tag{3-21}$$

which again can be expanded:

$$\begin{aligned} -X_1 &= e_{11}E_x + e_{21}E_y + e_{31}E_z \\ -X_2 &= e_{12}E_x + e_{22}E_y + e_{32}E_z \\ -X_3 &= e_{13}E_x + e_{23}E_y + e_{33}E_z \\ -X_4 &= e_{14}E_x + e_{24}E_y + e_{34}E_z \\ -X_5 &= e_{15}E_x + e_{25}E_y + e_{35}E_z \\ -X_6 &= e_{16}E_x + e_{26}E_y + e_{36}E_z \end{aligned} \tag{3-22}$$

Substitutions can likewise be made to give the equations in terms of strain.

All of these relations are summarised in table 3-1. L and T indicate longitudinal and transverse effects respectively, with a subscript s representing a shear mode. The piezoelectric properties of any material can thus be described using the 18 stress (or strain) coefficients. Only the Triclinic class 1 crystallographic group has all of the coefficients non-zero, essentially meaning that the piezoelectric effect will occur in all

directions through the crystal. For the other 19 groups, only certain coefficients take a value giving the crystals piezoelectric activity in certain directions only.

Table 3-1. The eighteen piezoelectric constants.

Stress (Strain) / Polarisation		1	2	3	4	5	6
		X_x (x_x)	Y_y (y_y)	Z_z (z_z)	Y_z (y_z)	Z_x (z_x)	X_y (x_y)
1	P_x	L d_{11} (e_{11})	T d_{12} (e_{12})	T d_{13} (e_{13})	L_s d_{14} (e_{14})	T_s d_{15} (e_{15})	T_s d_{16} (e_{16})
2	P_y	T d_{21} (e_{21})	L d_{22} (e_{22})	T d_{23} (e_{23})	T_s d_{24} (e_{24})	L_s d_{25} (e_{25})	T_s d_{26} (e_{26})
3	P_z	T d_{31} (e_{31})	T d_{32} (e_{32})	L d_{33} (e_{33})	T_s d_{34} (e_{34})	T_s d_{35} (e_{35})	L_s d_{36} (e_{36})

3.3.4 Quartz substrates

Although the cause of much scientific research and curiosity, the piezoelectric effect was only first applied during the First World War, when quartz plates were used as transmitters and receivers of underwater high frequency sound waves in rudimentary sonar systems.

Present day applications of piezoelectricity range from sonar and other ultrasonic uses to high voltage generators such as the domestic gas lighter. The greatest impact of piezoelectric materials is in the field of electronics where precision quartz resonators are used in a large variety of devices, from early radio sets, to the modern digital clock.

The widespread use of quartz is perhaps surprising due to its relatively low piezoelectric response, with the coefficients being only 1% of many other materials such as Rochelle salt. However, quartz is very robust, totally inert, and in great abundance naturally. The requirement for high quality electrical grade quartz for military electronics systems has made it a vitally important resource. Natural quartz

was used up to 1971, but increasing demand for perfect crystals led to the development of cultured, or synthetic quartz, which is grown around a natural 'seed' crystal. National stockpiles exist of natural quartz, with the US National Defense Stockpile (NDS) containing over 107,000 kg at the end of 1995 [48].

3.3.5 Quartz structure

Quartz is made up from tetrahedral groups of oxygen around a central silicon atom and formed from the crystallisation of silica at low pressures. The crystal is composed of SiO_2 molecules, which are bonded in a hexagonal structure, and X-ray diffraction gives structure constants of a = 4.90 Å and c = 5.39 Å [49]. Quartz exists in both a low and high state, α-quartz (figure 3-8) and β-quartz respectively. An irreversible phase change exists when α-quartz is heated above 573 °C to form β-quartz and this temperature should thus not be exceeded when processing quartz.

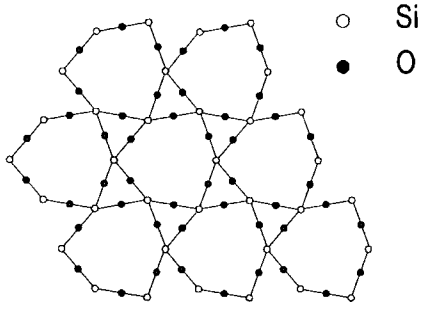

Figure 3-8. Alpha quartz bond structure.

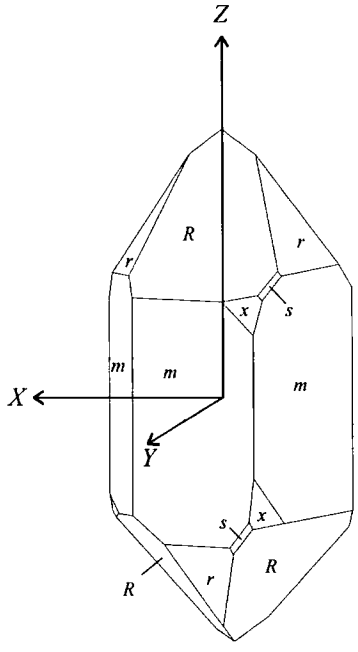

Figure 3-9. Quartz crystal.

α-quartz exists in right (figure 3-9) and left handed forms, the direction determined by the position of the crystal faces, *s* and *x*. The *Z*-axis (principal axis) lies vertically down the centre of the crystal in the *c* – direction, its positive end determined by the orientation of the *s* and *x* faces. The *Y*-axis and *X*-axis lie perpendicularly from the

Z-direction, the Y-direction normal to the m faces, and the X-direction lying at the join of two m-faces. Positive directions are again defined by the s and x faces. Three co-ordinate sets are obtained by rotating the structure 120° around Z.

By knowing angles between the faces, the geometrical relationships between the axis and the faces can be calculated. Face Miller indices are used to orientate a lump of quartz in terms of its X, Y and Z–directions with x-ray diffraction techniques. For example, m-faces have indices $[2\bar{1}\bar{1}]$ corresponding to the Y-axis, and R-faces have indices [100] and lie 38°13' to the m-faces [47].

3.3.6 Quartz piezoelectric constants

The complete piezoelectric properties of α-quartz can be described by just two strain coefficients, $d_{11} = 2.3\times10^{-12}$ mV^{-1} and $d_{14} = -0.67\times10^{-12}$ mV^{-1}:

$$\begin{pmatrix} d_{11} & -d_{11} & 0 & d_{14} & 0 & 0 \\ 0 & 0 & 0 & 0 & -d_{14} & -2d_{11} \\ 0 & 0 & 0 & 0 & 0 & 0 \end{pmatrix} \qquad (3\text{-}23)$$

Different values are obtained depending on test conditions [50]. It can be seen by comparing this matrix with table 3-1 that two normal modes exist, one longitudinal, and one transverse, whilst there are also three shear modes, two longitudinal, and one transverse.

3.3.7 Substrate manufacture and orientation

Quartz is the most common substrate material due to its robustness, inertness, and its strong basis in the field of electronics, which has led to the commercialised growth and characterisation of cultured quartz. The quartz is grown hydrothermally using an autoclave [51]. The synthetic quartz is grown around seed crystals, which are either cultured or natural, at a rate of up to 1 mm a day in the Z-direction.

When the crystal has reached an adequate size, blanks are sawn in the required orientations, which are then cut to size and lapped to the required thickness. For surface acoustic wave substrates, the thickness is arbitrary, with the waves being confined to the surface layer only. The device side of the wafer is polished, whilst the reverse side is left rough to help reduce bulk wave reflections.

Accurate substrate orientations allow exploitation of different piezoelectric properties, such as the temperature dependence of the quartz in certain directions. The development of x-ray diffraction orientation techniques has allowed plates to be cut with orientation accuracies of less than 1 arc minute. SAW quartz substrate orientation is specified by two parameters – the initial surface-normal orientation in terms of the *X*, *Y*, or *Z*-axes followed by a rotation around another axis (and sometimes a second rotation). For example, a *Y*-cut wafer has the positive *Y*-axis as a normal to the polished face (figure 3-10a). A *Y*-cut 36° orientation is a wafer initially with the *Y*-axis as a normal to the plane, then rotated 36° around the *X*-axis (figure 3-10b), such that the *Y*-axis is still perpendicular to the plane in the *Z*-direction, but at an angle of 36° to the normal. These cuts make use of the X_y shear stress components shown in (3-23).

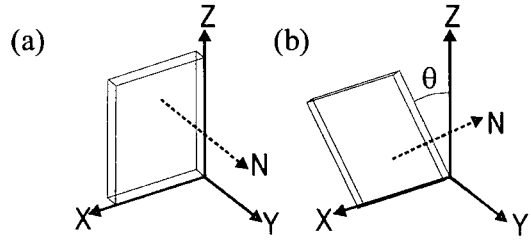

Figure 3-10. *Y*-cut Quartz plate rotated θ around the *x*-axis.

Different standard cuts are available designed for different purposes, many with abbreviated names. Some of the most common orientations for quartz SAW substrates are *Y*-cut with rotations around the *X*-axis varying between 30° and 45°. Names are given such as 'AT-cut' (36°) and the 'ST-cut' (42.75°).

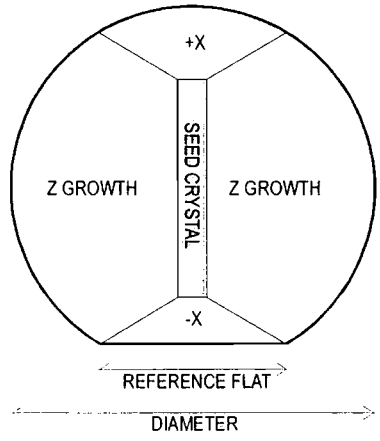

Figure 3-11. Quartz wafer diagram showing the flat specifying the *x*-direction, and the central seed crystal area that cannot be used for devices.

Wafers are available in a large range of shapes and sizes (typically 100 mm diameter maximum). Surface orientation is specified via flats (on circular) or long sides (on rectangular) wafers. Figure 3-11 illustrates a typical circular wafer indicating the seed area and the culture growth around the outside of the seed. Defects in the form of twinning or impurities prevent the use of the seed area for functioning devices. Twinning takes various forms, but essentially is caused by mixed regions of right and left handed crystals. The piezoelectric properties are altered, or even cancelled in certain circumstances. Seed free wafers are available and are cut from the cultured regions either side of the seed.

3.4 SAW devices

3.4.1 Electronics devices

SAW devices form a major constituent of modern electronics for signal processing. The majority of television tuner modules contain a SAW filter, whilst their use in the telecommunications industry is rapidly expanding. They also have a long established use in radar applications for signal compression and filtering.

The widespread use of SAW devices is due to one fundamental characteristic of the waves: **the acoustic wave velocity is approximately 10^5 times slower than electromagnetic radiation in a vacuum**. In a basic interpretation, this means SAW devices can delay signals, and they are used for this purpose in communications satellites where a small integrated SAW 'chip' can replace many metres of co-axial cable. The main advantage of this 'slowing down' is that many wavelengths can be contained on a small device, and the wave (up to about 2 GHz with current photolithography) can be manipulated on the device surface by changing the electrode design.

Apodised IDTs are used to control the frequency response in SAW filters, by having fingers of varying length, thus varying overlap, which have an amplitude output proportional to their overlap. As a short burst of wave energy from a uniform IDT transmitter passes over the apodised receiver, the output response changes in amplitude as a function of time (figure 3-12). This response, $h(t)$, is the Fourier transform of the frequency response $H(f)$. Thus if we have a certain frequency specification for a filter, an inverse Fourier transform will give the IDT shape.

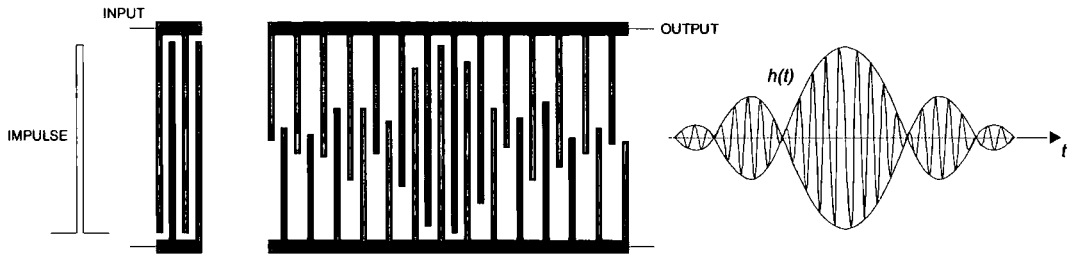

Figure 3-12. Apodised filter operation, showing uniform input IDT with impulse, apodised output IDT, and the time varying output *h(t)*.

Chirp filters (figure 3-13) increase or decrease the wavelength along the receive IDT from λ_1 to λ_2, giving a varying frequency output f_1 to f_2. The output from one chirp filter can be fed into another (this time f_2 to f_1) and a short compressed pulse will occur when the waveforms match. This pulse compression is used in radar systems to remove signal noise.

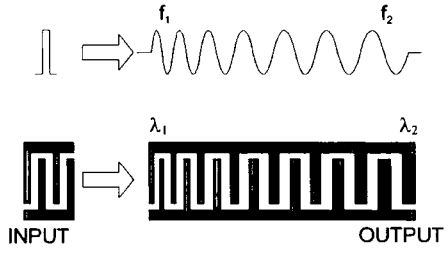

Figure 3-13. Chirp filter with uniform input IDT, and wavelength varying output IDT.

Other effects are possible using 'passive electrodes'. Reflection gratings are made up from unconnected electrode strips at $\lambda/2$ intervals and reverse the wave direction. The same effect can be made using grooves etched into the substrate instead of metal reflector gratings.

Figure 3-14 shows a typical commercial SAW filter from VI Telefilter, Germany, designed to operate around 82.2 MHz with a bandwidth of 0.05 MHz. The SAW is transmitted, reflected and received by one set of IDTs, shown in the top half of the photo. The signal is then passed through a second identical stage shown in the bottom half of the photo.

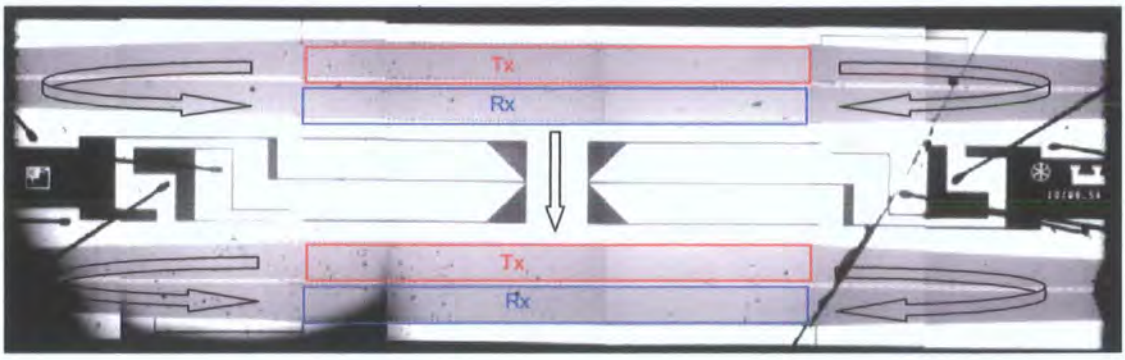

Figure 3-14. Photo of commercial filter showing IDTs, reflectors, and contacts. The metallisation is light, and the clear substrate dark. The large metallised areas are bus bars and contact pads, and gold wire connections are shown at each end. The diagonal defect on the right hand side is a crack through the substrate arising from de-packaging.

3.4.2 SAW oscillators

Crystal oscillators are the principle use of piezoelectric materials in electronics. Bulk-wave oscillators appear in many electronics applications, including radio tuners, and perhaps most commonly the 'quartz' watch movement, where a small accurate oscillator replaces a complex mechanical mechanism. The frequency of the oscillator is controlled by the size (typically thickness) of the crystal, with thinner crystals required for higher frequencies. Above a few MHz, traditional bulk wave devices become impractical with the crystal becoming thin and fragile, or even impossible to fabricate using traditional techniques (although microsystems fabrication techniques can produce smaller higher frequency devices such as the film bulk acoustic resonator or FBAR). In opposition, SAW devices would be impractical at these lower frequencies with the large wavelengths making the devices huge, but can work up to approximately 2 GHz with standard lithography techniques. Table 3-2 summarises these properties:

Table 3-2. Relative operating regimes for bulk and surface wave resonators.

Range	Bulk-wave	SAW
kHz < f < 50 MHz	Good	Large λ makes devices too large
50 MHz < f < low GHz	Plate thickness becomes thinner and fragile	Good up to photolithography limits

The two basic SAW oscillators are the delay line oscillator, and the reflective gate oscillator. The former is a simple SAW delay line with separate Tx and Rx IDTs connected through an amplification feedback circuit as shown in figure 3-15. The feedback gain exceeds any losses in the delay line allowing the loop to oscillate at the SAW centre frequency, f_0.

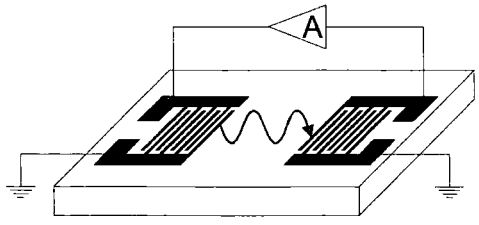

Figure 3-15. Delay line oscillator using external feedback.

The reflective gate oscillator uses reflectors to create an oscillation cavity on the device surface. 'Single port' oscillators use a single IDT for Tx and Rx with signal pulses. A more conventional 'two-port' resonator uses separate Tx and Rx IDTs with a continuous signal (figure 3-16). Reflective gate oscillators give high Q-values, up to 10,000 [45], whilst the delay line oscillator allows frequency tuning with external phase control. Both types of oscillator are extremely stable and can be designed using temperature independent substrate orientations.

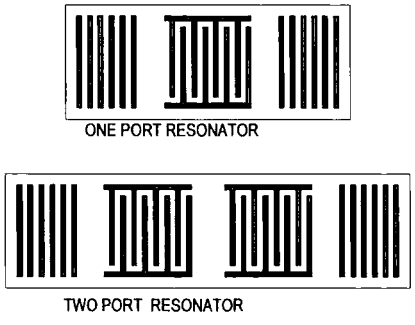

Figure 3-16. Reflective gate oscillators.

3.4.3 Sensors

Surface acoustic wave devices have revolutionised many aspects of RF electronics, and show similar potential in the area of sensing [52-54]. The confinement of the wave to the substrate surface allows external perturbations to heavily influence the wave, altering its phase velocity, and thus frequency. The high energy density near the surface

ensures that a large proportion of the wave energy is coupled to the perturbation leading to high sensitivity devices. Typical operating frequencies of 100 MHz allow significant frequency changes giving high resolution sensing.

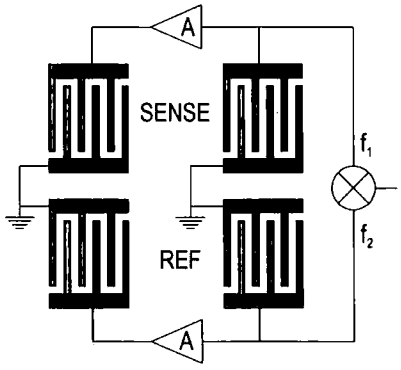

Figure 3-17. Dual delay line configuration.

A typical SAW sensor is made up of a 'dual delay-line' structure (figure 3-17). One delay line acts as the sensor with resonant frequency f_1, whilst the other propagation path is somehow protected and unaltered, acting as a reference with frequency f_2. This arrangement can be used to remove unwanted effects such as temperature variance, or to allow multiple parameter sensing. Depending on the sensor, f_1 and f_2 can be monitored individually, or calculations performed such as $\Delta f = f_1 - f_2$ using mixing techniques. Calibration allows the change in frequency, Δf, to give the magnitude of the external influence.

The basis of all SAW sensors is the SAW delay line, but by changing various parameters different sensors can be produced.

3.4.4 Wireless passive sensing

One major advantage of SAW sensors over existing solutions is their ability to be operated wirelessly in a passive nature. This permits simple operation in difficult environments where wire contacts or powered sensors are not suitable. The first wireless SAW operation was for RFID tags in 1972 [55]. These operate on a similar principle to bar codes, with one unique IDT of varying period giving an output waveform unique to the device [56].

Passive devices typically consist of a single port oscillator with the IDT connected to an antenna [57, 58]. A burst of RF power from a transmitter module (e.g. - in car) is

received by the sensor antenna (e.g. - in car tyre), and activates the IDT producing a SAW. The resultant reflected signal is transmitted from the sensor to the controller and analysed. The sensor is immune to noise problems and theoretically should operate forever, with no power requirements.

3.4.5 Temperature sensors

Piezoelectric substrates used for SAW devices have propagation path lengths and phase velocities dependent upon the ambient temperature [54, 59, 60]. The temperature coefficient of frequency (TCF) resulting from these effects varies with the substrate orientation, with some cuts showing large variations and others being independent of temperature. This effect allows temperature sensing with a simple delay line on a suitably orientated substrate. The high Q-factors of SAW resonators allow high sensitivity and temperature resolution.

These sensors require hermetically sealed packaging to prevent mass loading of the sensor surface. They are suitable for harsh environments and operate from -196°C to approximately 500°C, packaging often being the limiting factor [54].

3.4.6 Stress and strain sensors

Stressing the substrate of a SAW delay line results in wave propagation changes by biasing the elastic and piezoelectric constants. The resultant frequency change can therefore be calibrated to measure the stress or strain in a material to which the device is firmly attached.

Torque gauges using two SAW delay lines at right angles to each other have been developed [61] for drive shafts, etc. By placing the device such that both delay lines are at 45° to the axis of the shaft, both tension and compression can be measured with the resultant torque calculated (figure 3-18). The response from both devices can also be used to monitor the shaft temperature.

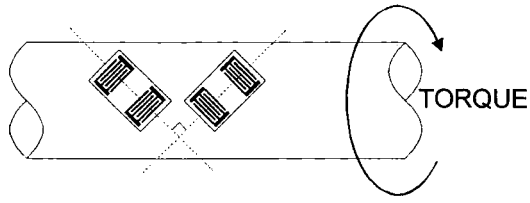

Figure 3-18. Torque sensor with perpendicular delay lines on an axle.

Pressure sensors use a SAW strain sensor placed on a membrane forming part of a hermetically sealed cavity (figure 3-19). A change in ambient pressure causes the membrane to deform, thus applying a measurable strain to the SAW delay line resulting in a frequency change. A large potential market for these sensors is for in-tyre pressure monitoring for the automotive market [54]. Transense Technologies PLC have developed both in-tyre pressure sensors (figure 3-20), and torque sensors for steering component monitoring for commercial use, with many more automotive applications in the process of development for suspension and braking control, etc. These sensors are operated passively.

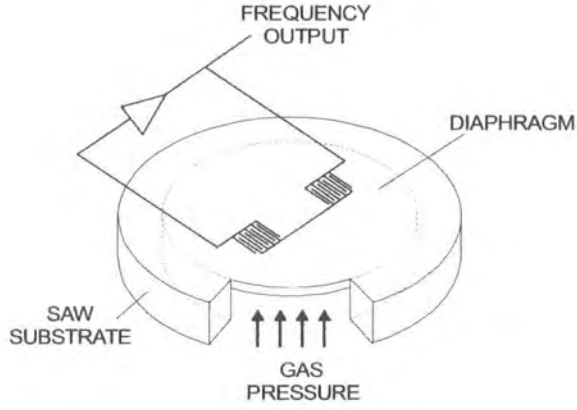

Figure 3-19. SAW Pressure sensor with a single delay line on a membrane.

Figure 3-20. Tyre pressure monitoring device using three SAW delay lines (Transense Technologies PLC).

3.4.7 Mass loading sensors

Bulk wave mass loading piezoelectric sensors are well established, with an appropriate example being the film thickness monitor crystal in vacuum deposition equipment as discussed in section 2.5.4. Material deposition onto the crystal changes the plate's thickness and overall density, and thus resonant frequency, allowing thickness measurement. SAW sensors work in an identical way, but can operate at much higher frequencies than bulk wave devices because their resonant frequencies are dependent upon IDT design and not limited by the plate thickness. Loading the SAW propagation path with another material changes the surface wave propagation velocity, thus device frequency.

Chemical SAW sensors rely on a chemically sorptive coating over the delay line that absorbs the vapour of interest [62-64]. The device senses using physical changes to the waveguide layer with absorption altering the propagation characteristics, and also dielectric changes influencing the IDTs. By combining many sensors with different selective coatings to produce an array, it is possible to produce a 'chemical nose', which can detect a variety of vapours and match the response in software to a particular chemical. Microsensor Systems Inc. have developed a range of chemical sensors including small hand-held systems (figure 3-21) which are suitable in the field for military applications.

Figure 3-21. Hand-held gas analyser (Microsensor Systems Inc).

Biosensors operate in a similar manner to chemical sensors, but use selective coatings on which the desired biological agents are attracted. One important difference

with biosensors is the use of Love mode SAWs for use in a liquid environment as discussed later in section 3.5.

3.4.8 Sensor conclusions

A variety of mechanisms can be used to adapt a simple dual delay line SAW device for different sensing applications. With careful design, it is possible to use one device for different purposes; for example, a wireless passive in-tyre pressure sensor can also monitor the tyre temperature, all because of the basic SAW propagation physics.

SAW sensors have many potential advantages over other technologies:

- High Q-factor allowing high resolution and sensitivity measurements with fairly simple control electronics
- Robust – no moving or separate parts
- Simple and cheap fabrication
- Adaptable for many applications
- Small size

3.4.9 SAW actuators

Whilst we are principally engaged in the design of sensors, SAWs also have limited applications as transducers. A SAW linear motor [65] demonstrates the power contained in a Rayleigh wave. The motor consists of a basic 40 μm wavelength delay line with the Tx and Rx IDTs spaced about 6 mm on a $LiNbO_3$ substrate (figure 3-22). A silicon slider with etched 'microlens projections' to reduce friction and increase localised pressure is placed on the propagation path and loaded with a neodymium magnet attracted to a steel plate under the device, giving a load of 200 mN. A 0.3 ms^{-1} velocity and 13 mN output force were obtained, demonstrating the power confined to the surface in the Rayleigh wave and the interaction it has with the half-space above the substrate.

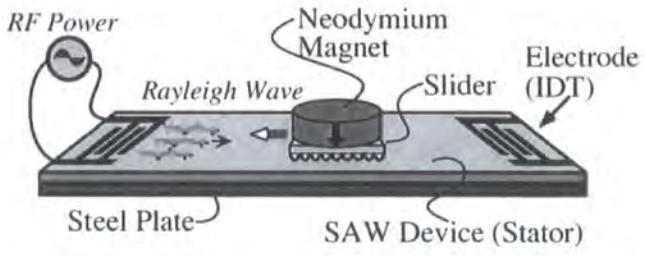

Figure 3-22. Schematic of SAW motor [65].

3.5 Love modes

The use of Rayleigh waves is well established in SAW sensors, but the large compressional acoustic losses caused by damping the vertical wave component means they are of little use for sensing liquids. By changing the piezoelectric substrate orientation such that the piezoelectric coefficients cause a sideways shear movement with applied electric field, a SAW is generated in the horizontal plane. Love modes are a particular sub-set, formed by focussing SH-SAW and SSBW modes in a thin waveguide layer deposited on the substrate. They were first demonstrated for acoustic mode sensors by Gizeli et al [66]. Love modes exhibit virtually no compressional losses into the liquid due to the absence of the vertical component. However the liquid is still coupled to the wave propagation via viscous coupling and is thus entrained across the sensor surface. Figure 3-23 illustrates the shear motion of Love modes.

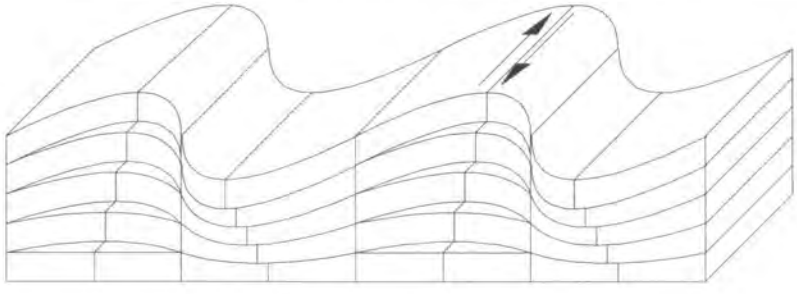

Figure 3-23. Love mode shear motion.

The material physical properties and thickness of the waveguide layer are critical to the device performance. With correctly chosen parameters, Love devices give a high sensitivity to liquid loading. One important by-product of the sensor structure is the protection offered by the waveguide layer, acting as a barrier between the sample and the electrodes.

3.5.1 Love mode formation

Love modes were initially considered in the context of seismic waves propagating through the earth's crust, which can be modelled as an isotropic plate (the crust) with different material properties to the half-space (the earth's magma) on which it lies. Love modes are the simplest solution to wave propagation in this type of waveguide structure.

The dispersion curves for Love modes can be derived by considering the incident and reflected waves in the waveguide, and the transmitted wave into the substrate [67]. Consider a plate of thickness h with a surface normal y such that the plate extends from $-h/2 < y < +h/2$ as shown in figure 3-24:

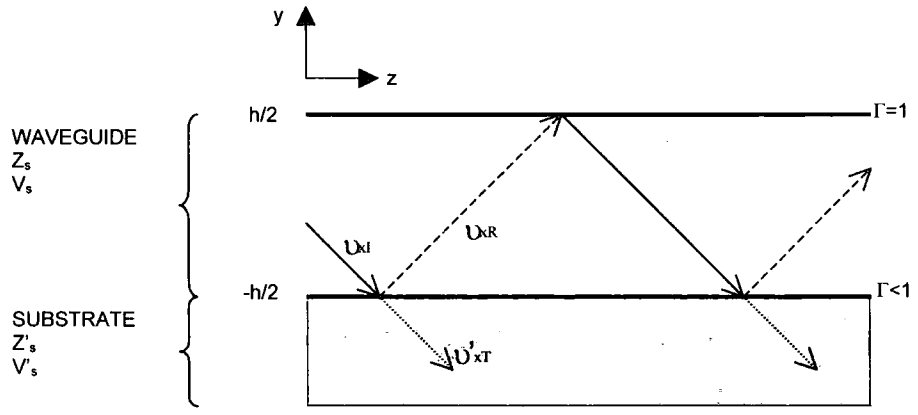

Figure 3-24. Shear waves in a waveguide of thickness h, with losses into the substrate.

The plate has shear acoustic impedance and shear wave velocity of Z_s and V_s, and lies on a half space with properties Z'_s, V'_s (the subscript 's' denotes shear). Shear waves with wave motion parallel to the surface propagate through the plate in the z-direction by reflecting off the upper and lower boundaries. The upper boundary has a reflection coefficient of $\Gamma=1$, whilst at $y = -h/2$, $\Gamma<1$, such that waves are transmitted into the half space at the lower boundary. The incident, reflected and transmitted waves are:

$$\begin{aligned} \upsilon_{xI} &= A\exp -i(-k_{ts}y + \beta z) \\ \upsilon_{xR} &= B\exp -i(k_{ts}y + \beta z) \\ \upsilon'_{xT} &= B'\exp -i(-k'_{ts}\, y + \beta z) \end{aligned} \tag{3-24}$$

Solving the waves with Fresnel's equations (Appendix D) at the upper and lower boundaries with the reflection coefficients stated, we get the transverse resonance condition:

$$\tan k_{ts}h = \frac{V'_s Z'_s \alpha'_{ts}}{V_s Z_s k_{ts}} \tag{3-25}$$

where $-i\alpha'_{ts} = k'_{ts}$ is the transmitted wavevector describing the exponential decay into the substrate of υ'_{xT} (3-24). For $\exp(-i\,k'_{ts})$ in (3-24) to describe exponential decay into the substrate, k'_{ts} is imaginary negative, thus α'_{ts} is real positive.

The transverse partial dispersion relations obtained from substituting wave solutions into the wave equation for the waveguide and substrate are:

$$k_{ts}^{\,2} = \left(\frac{\omega}{V_s}\right)^2 - \beta^2 \tag{3-26}$$

$$\alpha'^{\,2}_{ts} = \beta^2 - \left(\frac{\omega}{V_s'}\right)^2 \tag{3-27}$$

Eliminating β from (3-26) and (3-27) gives:

$$\alpha'^{\,2}_{ts} = \omega^2\left(\frac{1}{V_s^{\,2}} - \frac{1}{V_s'^{2}}\right) - k_{ts}^{\,2} \tag{3-28}$$

From (3-28), trapping of the Love modes can only occur when $V_s' > V_s$, i.e., the velocity of the wave in the plate is less than the velocity of the wave in the substrate. If this condition is not met, α'_t is real positive and energy is lost into the substrate. By plotting (3-25) and (3-28) against $\alpha'^{\,2}_{ts}$ and $k_{ts}^{\,2}$, graphical solutions can give the values of k_t^2 and ω at which the modes are trapped. Using the transverse resonance condition (Appendix B), the solutions for k_{ts} are $n\pi/h$ where n is the mode number taking the values 0,1,2,3,....N.

With this information, it is possible to draw the Love mode dispersion curves (figure 3-25) showing the relation between the frequency ω and the wave vector, β. The modes are shown trapped between the substrate velocity, $\omega/\beta = V_s'$, and the waveguide velocity $\omega/\beta = V_s$. The phase velocity $V_{ph} = \omega/\beta$ and group velocity $V_{gr} = \partial\omega/\partial\beta$ are different, except for waveguide thickness extremes: very thin layers when V_{ph} and V_{gr} approach the substrate velocity V_s', and for thick layers when V_{ph} and V_{gr} approach the waveguide layer velocity V_s. This describes the basic behaviour of the Love mode. With very thin waveguide layers, the majority of the acoustic energy remains in the substrate, and the mode velocities V_{ph} and V_{gr} approach the substrate velocity V_s'. As the thickness increases, V_{ph} reduces, and approaches the waveguide velocity V_s for thick layers. The group velocity $\partial\omega/\partial\beta$ shows a minima below V_s' (smaller gradient) and then increases to approach V_s' [68].

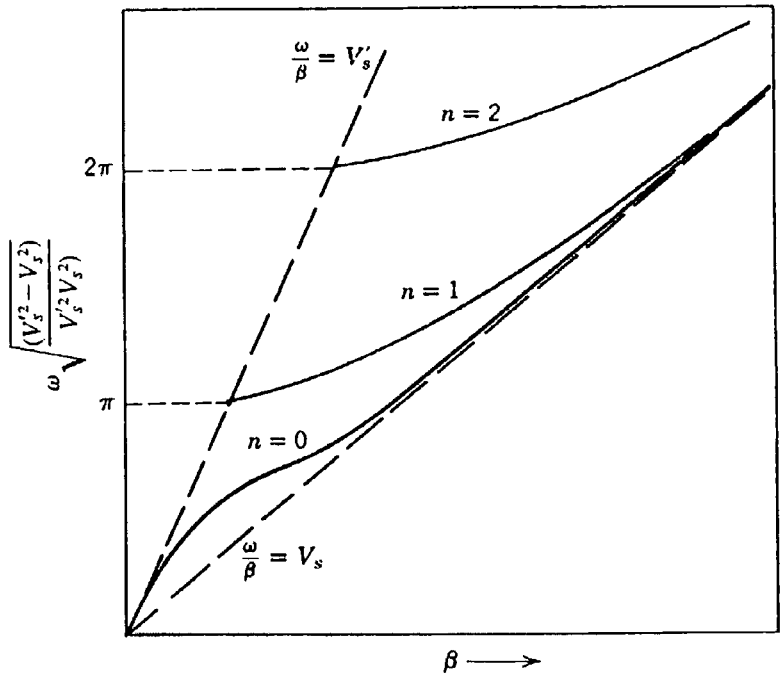

Figure 3-25. Love mode dispersion curves for h = 1. Copied from Auld [67].

Experimental studies of Love mode dispersion by McHale et al [69, 70] show mode confinement with waveguide thickness for the first few modes (figure 3-26). The peaks in the insertion loss correspond to the optimum thickness in terms of energy confinement, indicating minimal losses into the substrate and minimum absorption in the waveguide. The frequency (or phase velocity) starts high for each mode (when

wave velocity $\approx V_s$') and then reduces with an increasing gradient. No data is shown for the lower frequencies of each mode, presumably due to a lack of experimental results.

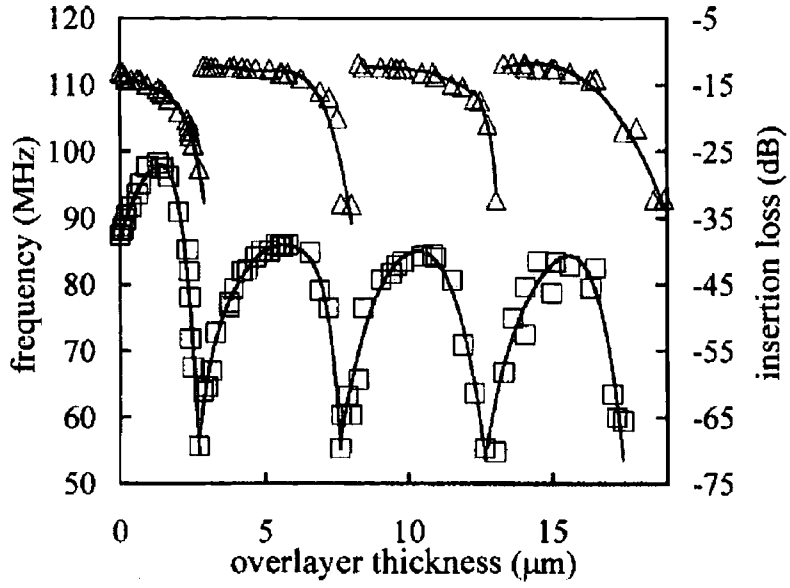

Figure 3-26. Harmonic Love modes [69]. Insertion loss (squares) and resonant frequency (triangles) for a device operated at the fundamental frequency as a function of waveguide thickness.

3.5.2 Surface perturbations of Love modes

Love mode sensors operate by enabling the external medium which is being sensed to bias the mechanical properties of the waveguide, and thus perturb the wave which is contained within the waveguide layer. When an external force is applied to the waveguide surface, the additional force induces a stress in the waveguide material thus changing the elastic properties. The waveguide velocity is directly dependent on the material elastic properties as shown:

$$V_s = \sqrt{\frac{E_s}{\rho}} \tag{3-29}$$

where ρ is the density of the material and E_s the shear stiffness. Thus by stressing the waveguide and changing the shear stiffness of the waveguide surface, the wave shear velocity is changed. A simple way of analysing this change is to describe the propagation properties of the waveguide in terms of acoustic impedance. From (2-5)

the acoustic impedance of a material is defined as $Z = \rho V$ and combining with (3-29) the impedance is directly related to the shear stiffness:

$$Z = \sqrt{E_s \rho} \tag{3-30}$$

The additional force resulting in a change to the elastic characteristics could be due to mass loading, where a material deposited on the waveguide of density ρ and thickness t loads the surface per unit area by applying a force $\rho g t$ (where g is acceleration due to gravity). When the mass loading film has viscous properties, such as with liquid loading, an additional drag force is exerted on the surface of the waveguide and this produces a further change in the elastic properties and thus acoustic impedance Z.

Analytical solutions for these perturbations are not always possible and a commonly used approximation is provided by using 'perturbation theory'. The derivation of the perturbation theory relation is complex and beyond the scope of this thesis, and a full description can be found in Auld, Chapter 12 [67]. The following description gives the fundamental stages of perturbation theory applied to a structure with shear horizontal waves being loaded by non-viscous and viscous materials.

Consider a general wave propagation constant, γ, used to describe the Love mode contained within the waveguide:

$$\gamma = \alpha + i\beta \tag{3-31}$$

where α is the attenuation constant describing real losses and β the phase constant describing the time dependent lossless wave component.

The perturbation theory describes a change in the phase propagation constant by determining the wave solutions for an unloaded (unperturbed) waveguide, and for a loaded (perturbed) waveguide which has stresses induced by the external force. The change in the phase propagation constant due to the perturbation is therefore:

$$\Delta\beta = \beta_{perturbed} - \beta_{unperturbed} \tag{3-32}$$

The analysis in [67] leads to a generalised form of the perturbation for mechanical surface perturbations on a waveguide, where only the upper surface is loaded and the interface between the substrate and waveguide remains un-perturbed:

$$\Delta\beta = \frac{-iv_s\sigma}{4P} \tag{3-33}$$

In this equation the shear particle velocity at the interface v_s is the same for both the layered loading material and the waveguide material, i.e, the wave function is continuous. σ is the induced stress in the surface of the waveguide material, and P is the average power flow of the wave in the unperturbed waveguide per a unit width along the x-direction (as defined in figure 3-24). This is the power contained within the shear particle motion described by v_s.

The stress induced in the waveguide can expressed as a function of the particle velocity of the unperturbed wave at the waveguide surface, v_s, and the acoustic impedance of the perturbed waveguide, Z:

$$\sigma = -Zv_s \tag{3-34}$$

and substituting (3-34) in (3-33), the change in wave propagation due to a surface perturbation can be expressed in terms of the impedance as given in (3-35):

$$\Delta\beta = \frac{iv_s^{\,2}Z}{4P} \tag{3-35}$$

In the application of sensors, we are interested in the fractional change in propagation allowing $\Delta\beta$ / β to be measured. Using the relation $\beta = \omega / V_{ph}$, (3-35) becomes:

$$\frac{\Delta\beta}{\beta} = \frac{iv_s^{\,2}ZV_{ph}}{4P\omega} \tag{3-36}$$

The example in Auld [67] 'Example 1 – Mechanical Perturbation by a Thin, Lossless Isotropic Overlay – equation (12.15)' provides a solution to the induced stress in the z-y plane, σ_{zy} (this plane is defined in figure 3-24). The shear component of the stress applicable to the Love wave is:

$$\sigma_{zy} = i\omega h v_s\left(\rho - \frac{E_s''}{V_{ph}^{\,2}}\right) \tag{3-37}$$

The superscript " denotes properties of the surface loading layer, and ρ is the density of the perturbing layer. Substituting this stress component into (3-33) and expressing the change in propagation as a fractional change the following expression is obtained to describe the perturbation of a Love wave with mass loading:

$$\frac{\Delta\beta}{\beta} = -\frac{v_s^{\,2} V_{ph} t}{4P}\left(\rho - \frac{E_s''}{V_{ph}^{\,2}}\right) \tag{3-38}$$

Using the relation in (3-30) and the fact that ρt is the loaded mass per unit area, m / A, the following expression is obtained:

$$\frac{\Delta\beta}{\beta} = -\frac{v_s^{\,2} V_{ph} m}{4PA}\left(1 - \left(\frac{V_s''}{V_{ph}}\right)^2\right) \tag{3-39}$$

Thus the perturbation of the Love mode, can be described by using the mass, m, and acoustic velocity properties, V_s", of the loading material causing the perturbation.

The relative change in propagation is described as the function of impedance, Z, and sensitivity, S:

$$\frac{\Delta\beta}{\beta} = -SZ \tag{3-40}$$

and from (3-39) the sensitivity term for Love mode device is:

$$S = -\frac{v_S^{\,2} V_{ph}}{4P}\left(1 - \left(\frac{V_s''}{V_{ph}}\right)^2\right) \tag{3-41}$$

If the mass loading layer is highly elastic and it supports acoustic waves with a large shear velocity such that $V_s" \geq 0$, then the factor in the brackets becomes small and the sensitivity of the device is reduced. However for a sample material which has a low elasticity, and/or is not a continuous material such that it can't support acoustic waves effectively, then $V_s" < V_{ph}$, then this factor is unity and the sensitivity is not dependent on the sample material.

If the impedance of the sample material / loading layer is not purely imaginary, then some real losses will occur in the form of attenuation of the acoustic wave. In this case

the propagation constant β changes as before (with a fractional change Δβ / β) but the attenuation constant, α will also change. Because the overall change in propagation, Δγ, scales with phase as the above discussion shows, a general form of (3-40) is:

$$\frac{\Delta\gamma}{\gamma} = \frac{\Delta\alpha}{\beta} + i\frac{\Delta\beta}{\beta} = -SZ \tag{3-42}$$

and this expression can be used to describe perturbations due to both real and imaginary impedances.

3.5.3 Mass loading

If we consider a sample loaded onto the waveguide surface which is perfectly elastic with no viscous properties the impedance is purely imaginary and proportional to the loaded mass [77]. By comparing (3-36), (3-39) and (3-41) the impedance for a mass loading layer can be deduced:

$$Z = -i\omega\frac{m}{A} \tag{3-43}$$

For the mass loading case where the impedance is purely imaginary, the attenuation is purely imaginary and the damping term Δα/β is therefore zero. Combining (3-42) and (3-43) the change in propagation due to mass loading is given:

$$\frac{\Delta\beta}{\beta} = S\omega\frac{m}{A} \tag{3-44}$$

Love modes are dispersive (see section 3.5.1) and when the group velocity and phase velocity are not equal, a conversion factor of V_{ph} / V_{gr} is used to express the propagation constant change in terms of frequency change. This is required for sensors where the frequency is the principal measurement technique. The change in frequency with mass loading then becomes:

$$\frac{\Delta f}{f} = -\left(\frac{V_{ph}}{V_{gr}}\right)\left(\frac{\Delta\beta}{\beta}\right) \tag{3-45}$$

$$\frac{\Delta f}{f} = S_f\omega\frac{m}{A} \tag{3-46}$$

where S_f is the sensitivity in terms of frequency. This is different to S and includes the dispersion conversion factor. Equation (3-46) shows that the relative frequency shift due to a perturbation is directly proportional to the mass, and therefore density, of the loading or sample material. This relation is known as the Sauerbrey equation [32] and is fundamental to this thesis.

3.5.4 Viscous coupling

If the sample which is in contact with the waveguide surface is not perfectly elastic and contains a viscous component, an additional drag is introduced to the perturbation. This acts as a damper between the acoustic mode in the waveguide and the shear particle motion in the sample, and results in attenuation of the acoustic energy. Thus attenuation means that both the phase constant β and the attenuation constant α are perturbed and the change in propagation contains both these terms as given in (3-42).

The surface impedance due to mechanical loading by a viscous material is given by [77]:

$$Z = -\sqrt{i\omega\eta\rho} \tag{3-47}$$

where η is the viscosity of the sample liquid. The change in propagation and attenuation are both therefore proportional to the square root of the density-viscosity product, √(ρη):

$$\frac{\Delta\alpha}{\beta} = \frac{\Delta\beta}{\beta} = S\sqrt{\frac{\omega\eta\rho}{2}} \tag{3-48}$$

Using the dispersion conversion, (3-48) can be expressed in terms of relative frequency change:

$$\frac{\Delta f}{f} = S_f\sqrt{\frac{\omega\eta\rho}{2}} \tag{3-49}$$

This relation was first shown by Kanazawa and Gordon [33] and is the second fundamental equation used in this study.

The introduction of a viscous component can greatly increase the complexity of the interaction between the sample and the waveguide surface, for example introducing

mechanisms such as slip. However the most important effect is the change in the behaviour of viscous properties at high frequencies. Equation (3-49) assumes that the liquid acts in a purely viscous manner (a Newtonian liquid) with a real η. If we consider the Maxwellian model of viscosity, where η has real and imaginary parts to allow for a liquid's elastic behaviour at high frequencies [78], then η takes the the frequency dependent form:

$$\eta(\omega) = \frac{\eta_0}{1 + i\omega\left(\eta_0 / \mu_\infty\right)} \tag{3-50}$$

The high frequency shear modulus μ_∞ is large, estimated at 2×10^7 Nm^{-2} by Jakoby et al [78] and thus in the low frequency-viscosity regime, the propagation change for α and β remains directly proportional to the viscosity similar to the Newtonian model. At high frequencies however, the denominator increases, reducing the effective viscosity $\eta(\omega)$. This reduced the effective impedance and therefore reduced the change in α and β. This has the effect of reducing the sensitivity of the device to the liquid loading, not because of changes to the properties of the device, but because the sample behaves in an 'unusual' manner.

The two fundamental equations covered so far are:

The Sauerbrey equation (3-46)

$$\frac{\Delta f}{f} = S_f \omega \frac{m}{A}$$

The Kanazawa and Gordon equation (3-49)

$$\frac{\Delta f}{f} = S_f \sqrt{\frac{\omega \eta \rho}{2}}$$

3.5.5 Application to the dual delay-line liquid density sensor

The principle of operation of the dual delay line liquid density sensor is directly dependent on the two fundamental equations stated above.

The sensor consists of a smooth delay line and a corrugated delay line as illustrated in figure 3-27. These surface topologies allow the different properties of equations (3-46) and (3-49) to be exploited.

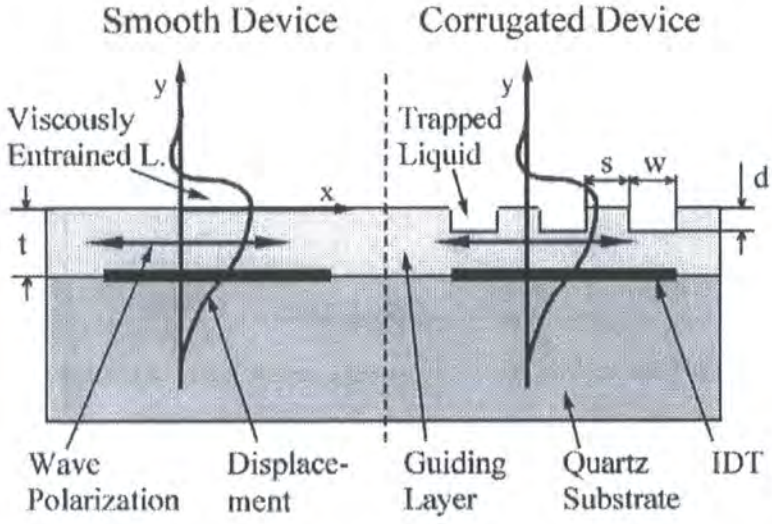

Figure 3-27. A cross section of the dual delay line density sensor showing the smooth and corrugated delay lines. Taken from [40].

The corrugated delay line has vertical sided troughs with a depth d, a width w and a spacing s (the spacing is the length of surface between the corrugations and not the pitch of the corrugations). By trapping liquid in these corrugations, the shear motion of the liquid is reduced and the device response is made up from a viscous loading perturbation AND a mass loading perturbation. The mass of the trapped liquid in the corrugations per unit area is given by:

$$\frac{m}{A} = \frac{w}{w+s}\rho d \tag{3-51}$$

Substituting this into (3-46) we get the frequency shift relation to the mass loading component on the corrugated delay line:

$$\left(\frac{\Delta f}{f}\right)_M = S_f \omega \rho d \frac{w}{w+s} \tag{3-52}$$

and the total shift on the corrugated delay line including the viscous loading effects is given by the sum of both components:

$$\left(\frac{\Delta f}{f}\right)_C = \left(\frac{\Delta f}{f}\right)_V + \left(\frac{\Delta f}{f}\right)_M \tag{3-53}$$

where the subscript C denotes 'corrugated', V 'viscous' loading, and M 'mass' loading.

The viscous loading component of perturbation on the corrugated delay line, and the perturbation on the smooth delay line is directly given by (3-49), i.e, the relative change in frequency is proportional to the square root of the liquid density-viscosity product. The relative frequency change on the smooth delay line is simply this viscous component:

$$\left(\frac{\Delta f}{f}\right)_S = \left(\frac{\Delta f}{f}\right)_V \tag{3-54}$$

where the subscript S denotes 'smooth'.

From inspection of (3-53) and (3-54) in combination with (3-46) and (3-49) it is clear that the liquid density cannot be discriminated from the density-viscosity product using a single delay line as the frequency shift is always dependent on these two parameters combined. However, the difference in relative frequency shift between the two delay lines can be used to separate out the sample density as shown:

$$\left(\frac{\Delta f}{f}\right)_C - \left(\frac{\Delta f}{f}\right)_S = -\left(\frac{v_g}{v_{ph}}\right) S_f \omega \rho d \frac{w}{w+s} \tag{3-55}$$

and rearranging to get density:

$$\rho = \left[\left(\frac{\Delta f}{f}\right)_S - \left(\frac{\Delta f}{f}\right)_C\right]\left[\left(\frac{v_{ph}}{v_g}\right)\frac{w+s}{w}\frac{1}{S_f d \omega B}\right] \tag{3-56}$$

B is a constant and reference [40] suggests a value around 0.38 to enable the results to coincide with the theoretical shifts. The exact cause of this variation is unknown, but

is thought to be due to the trapping efficiency of the corrugations, thus B is known as the 'trapping factor'.

Equations (3-55) and (3-56) are fundamental to the understanding of the dual delay line density sensor operation and the principle of taking the difference in frequency shift between the two delay lines is discussed in the results sections of this thesis.

3.5.6 Love mode sensitivity

Love waves theoretically have the highest sensitivity of all surface wave modes [71]. Rayleigh waves are typically contained within one wavelength of the surface, for example 40 μm in a typical device, giving relatively weak energy density at the surface. By focussing the energy in the thin waveguide, typically 0.14 λ thick for SiO_2 waveguides [72], the acoustic energy density is increased. This gives greater coupling with surface perturbations and thus a higher sensitivity.

The dispersion curves can be used to determine the sensitivity of the Love mode to mass loading [68, 73]. The dispersion relations show that an increase in normalised thickness results in a reduction in phase speed. The optimum device sensitivity occurs where the gradient of phase velocity to thickness is a maximum. This is the point where a standard increment in thickness produces the largest change in phase velocity. If the increase in thickness is thought of as extra mass loading (albeit the same material as the waveguide), then the increase in frequency is the sensitivity to this mass loading.

The dispersion analysis shows that Love mode trapping only occurs when $V_s' > V_s$. The difference in velocities determines the normalised thickness, h/λ, and thus the device's sensitivity. Materials are chosen which fulfil this condition, i.e. substrates with high velocities and waveguides with relatively low velocities. Y-rotated quartz substrates have a V'_s of around 5000 – 5100 ms^{-1} for rotations between 30 and 40° respectively [74, 75], ideal for Love mode devices. The shear acoustic velocity of a material is can be evaluated using (3-29)

By maximising the difference in shear velocities such that V_s / V_s' is small, the waveguide thickness is reduced. This produces a higher acoustic energy density within the layer leading to a higher sensitivity.

The maximum sensitivity and the corresponding optimum waveguide thickness h_{opt} can be determined by using perturbation theory [76]. For the lowest mode (n = 0) with $V_s' >> V_s$ the optimum thickness is simply:

$$h_{opt} \approx \frac{1}{4}\frac{V_s}{f} = \frac{\lambda}{4}\frac{V_s}{V'_s} \tag{3-57}$$

where f is the operating frequency. The optimum thickness of the waveguide is thus inversely proportional to the waveguide-substrate shear velocity ratio.

The maximum sensitivity to mass loading in terms of frequency change is $S_{f\max}$:

$$S_{f\max} = \frac{-1}{\rho h} \approx \frac{-4f}{\rho V_s} = \frac{-4}{\rho'\lambda'}\frac{V_s'}{V_s}\frac{\rho'}{\rho} = \frac{-4}{\rho'\lambda'}\sqrt{\frac{E'\rho'}{E\rho}} \tag{3-58}$$

where E and E' are the shear stiffness, and ρ and ρ' the density of the waveguide and substrate materials respectively. The device sensitivity is thus dependent on the density and stiffness ratios of the waveguide and substrate. To produce a high sensitivity device, we require $E' >> E$, and ρ' >> ρ.

3.5.7 Waveguide materials

The theoretical discussion shows how the formation of the Love mode and sensitivity to loading is dependent on the physical characteristics of the waveguide material. A number of materials are used for Love mode waveguides depending upon the sensor's application and specifications. Physical limitations are that the material has to be uniformly deposited in thin (<λ) layers, with strong adhesion to the substrate and electrode materials. In some applications, the material must be robust allowing contact with a range of chemicals, and abrasion resistant for cleaning purposes.

The early studies into Love mode sensors by Gizeli et al used PMMA guiding layers [66, 79]. Deposition of the layer improved the insertion loss by 8 dB over the uncoated device by reducing losses into the substrate. The results show a highest sensitivity for 1.6 μm thick layers at 45 μm wavelength, giving $h/\lambda = 0.036$. No results are shown for thicker layers, perhaps due to the large losses mentioned. Other studies using PMMA include those by Cernosek et al [80, 81] who found the optimum thickness to be between $h/\lambda = 0.05$ and 0.0575 corresponding to $h = 2.0$ to 2.3 μm at $\lambda = 40$ μm. The soft nature of polymers gives them low stiffness values, typically $2 - 3\times10^9$ Nm^{-2}, and

combined with the density of PMMA around 1.2×10^3 kgm^{-3}, the shear velocities are in the range 1290 – 1580 ms^{-1}.

The experimental studies by McHale and Newton et al use spin-coated photoresist as a waveguide layer [68-70]. Whilst not suitable for use in an open environment due to susceptibility to abrasion and solvent attack, the material allows extensive studying of the Love mode dispersion through the use of many different thicknesses. Figure 3-26 shows the results looking at higher order mode propagation.

The use of sputtered or CVD SiO_2 layers has been extensively studied. The most prominent group is that of Jakoby and Vellekoop [60, 77, 78, 82-84]. Other groups include Du and Harding [72, 85, 86], and Herrmann et al [40, 41, 59, 75, 87]. A typical density for SiO_2 is 2.2×10^3 kgm^{-3} but this varies with the deposition process. The Young's modulus also varies with values of $E_s = 5.0\times10^{10}$ Nm^{-2} [40] and $E_s = 1.74\times10^{10}$ Nm^{-2} [77]. These figures give a shear velocity of between $V_s = 2812$ ms^{-1} and $V_s = 4767$ ms^{-1}. The V_s values are close to the substrate shear velocity V'_s, and so from (3-57) h_{opt} is relatively large resulting in relatively low sensitivities. Experimentally obtained values of h_{opt} are around 0.14, corresponding to 5.5 μm at $\lambda = 40$ μm [72]. The same study shows minimum insertion losses are obtained between $h = 2.0$ to 2.5 μm suggesting that operation of the devices with maximum sensitivity and minimum loss is not achievable. SiO_2 film thicknesses of 2.2 μm were used by Herrmann et al for the Love mode liquid density sensor [40, 41]. This design may have traded optimum sensitivity for low loss, to make it suitable for a liquid environment.

SiO_2 has the positive attributes of chemical and abrasion resistance, making it ideal for use in an open environment. The material is compositionally similar to quartz, and therefore has good adhesion to the substrate. However, deposition of thick layers can be difficult with stress causing the layers to peel and crack. Pinholes can also form during CVD deposition, and the physical properties of density and stiffness are heavily dependent on the process parameters. Silicon carbide (SiC) is a similar glassy material to SiO_2 and was used in the study by Leidl et al [88]. The material is ideal as a passivation layer with a high hardness and resistance to chemicals. However, the density and stiffness are both large at $\rho = 3.21\times10^3$ kgm^{-3} and $E_s = 46.6\times10^{10}$ Nm^{-2} giving $V_s = 12048$ ms^{-1} (data taken from Rohm and Haas Advanced Materials, USA).

This is larger than the substrate velocity, and suggests that the device presented is operating as a non-Love device with the layer functioning as a protective surface.

The above discussion examines the properties of two different materials, each suited to Love mode sensor guiding layers. There are glassy materials such as SiO_2 with high stiffness values, giving large shear velocities, and thus thicker less sensitive layers. The soft polymer materials have low stiffness values which consequently give thinner, more sensitive layers, but with greater acoustic absorption. Table 3-3 summarises the properties of the two materials and their relative merits.

Fabricating a multilayer structure can use the relative merits of both materials. The experimental work by Du and Harding has investigated the use of a dual layer waveguide consisting of a SiO_2 base layer, and a PMMA surface layer, on ST quartz [85, 86]. SiO_2 thicknesses of 2.2 and 3.2 μm were used with a range of PMMA thicknesses. The results showed that thicker PMMA layers could be used in the multilayer structure than was possible with a single layer PMMA structure, due to the lower insertion losses. This allows operation closer to the optimum thickness, and thus optimum sensitivity, where insertion losses of single layers would prevent oscillation in water.

Table 3-3. Waveguide relative properties for glassy and polymer materials.

Property	Glassy	Polymer
Shear Stiffness / E_s	High	Low
Density / ρ	-	-
Shear velocity / $V=\sqrt{(E_s/\rho)}$	High	Low
Thickness / $h \propto V_s$	Thick	Thin
Sensitivity / $S \propto h^{-1}$	Low	High
Losses	Low (Good)	High (Poor)

3.5.8 Attenuation of Love modes

Whilst we are principally interested in the frequency response of devices, the attenuation or 'insertion loss' of a device is also critical to its performance. Attenuation

of acoustic energy in Love mode devices can be due to a range of mechanisms, and the following discussion aims to outline some of the principle causes.

The insertion loss of an optimised Love mode device is less than for the basic shear horizontal wave device (no waveguide layer) on which it is based. The SH-SAW / SSBW device contains acoustic energy primarily at the surface, but also components propagating in to the substrate. Absorption in the substrate material can result in relatively high losses. The addition of a surface waveguide removes the acoustic energy from the substrate and confines it within the waveguide, thus reducing the intrinsic insertion loss.

Losses within the waveguide occur through absorption in the waveguide material. For materials with high elasticity (for example the glassy materials such as SiO_2), these losses are relatively low, but for the softer less elastic materials such as polymers, the absorption is greater as described in section 3.5.7. In addition a component of the Love mode is transmitted across the waveguide-substrate interface as illustrated in figure 3-24 and this results in further losses.

When a Love-mode device is loaded with a sample, a number of mechanisms exist which can increase attenuation of the wave. Equation (3-44) describes the change in propagation due to mass loading as purely imaginary. However, no materials are truly lossless and there will be some propagation losses through the attenuation loss of acoustic energy within the sample material and waveguide. When the sample is viscous (such as when a liquid is being measured), this effect is greater due to the entrainment of the liquid with the shear motion, and the resultant dragging/damping effect of the liquid viscosity. This is described by (3-48). Kovacs et al [77] provide a relation to describe the attenuation per a wavelength in terms of the measured insertion loss:

$$\frac{\Delta\alpha}{\beta} = \frac{\ln(10)}{40\pi(l/\lambda)}\Delta IL \approx 1.47\times10^{-4}\Delta IL \qquad (3\text{-}58)$$

If we substitute this into (3-48) then the insertion loss per a wavelength can be expressed in terms of the sample material density and viscosity:

$$\Delta IL = \frac{40\pi}{\ln(10)}\frac{\Delta\alpha}{\beta} = \frac{40\pi}{\ln(10)}S\sqrt{\frac{\omega\eta\rho}{2}} \qquad (3\text{-}59)$$

Thus the measured insertion loss due to perturbations shows a similar response to the frequency change.

Rayleigh wave devices are not used for liquid sensing due to their shear component being in the *y-z* plane, i.e., normal to the substrate surface. This vertical component causes compressional waves to form in the liquid which propagate out into the body of the sample. This energy is all lost and can result in almost zero transfer of the wave along the delay line. A principal benefit of Love modes is the shear horizontal motion which prevents the compressional losses into the liquid body. However, under practical conditions, there is still the possibility of this occurring. In this study, the corrugated delay line has vertical sided corrugations which could cause horizontally orientated compressional waves to form in the liquid contained within the troughs. To prevent this the trough's widths are designed to be less than the compressional wavelength, thus preventing this loss. This relies on the sidewalls being perfectly vertical, and compressional waves could form off the sidewalls if they allow a component to be propagated into the body of the liquid, caused by sloping sidewalls and / or rounded profiles. The effect of these is discussed in the results sections.

The above losses all arise due to mechanical effects where the attenuation is due to the physical material acoustic propagation properties. Another substantial cause of attenuation in devices can be due to electrical effects. All SAW devices using IDTs have an electrical impedance determined by the capacitance of the transducers, which are in essence, comb-like parallel plate capacitors. The coating of a waveguide material over these transducers can alter their capacitance due to the addition of a material with different dielectric properties. This change in impedance will change the power of the transmitted propagated wave and also the efficiency of the receive IDT. If the IDT capacitance is increased by introducing a waveguide layer with dielectric constant larger than air, the impedance is reduced (impedance $Z = 1 / (i\omega C)$), and the power radiated from the IDT is less resulting in increased insertion loss for the delay line.

The dielectric properties of the sample liquid can also have a similar effect on the IDTs. Unless the waveguide layer is thick enough to buffer the IDTs from electric loading from the sample, the effective permittivity of the sample will change the electric field between the IDT fingers and thus the IDT capacitance. For example, the inclusion of a sample with a large dielectric constant such as water can increase the capacitance of the IDTs dramatically and cause a large increase in insertion loss. These issues are

investigated in the results and described in more detail. A key point to note is that whilst methods are available to screen the IDTs from the sample electric properties, these methods themselves can increase the IDT capacitance and therefore insertion loss [82].

3.5.9 Love mode conclusions

Love mode formation and sensitivity is strongly dependent on the waveguide structure and materials. Glassy layers such as SiO_2 with high stiffness values require thicker layers for optimum guiding, and thus exhibit relatively low sensitivity, but with low insertion losses. On the other hand, softer polymer materials with lower stiffness values can achieve higher sensitivities with thinner layers, but with large absorptive losses. The multilayer structure can make use of both these merits by enabling the use of thicker polymer layers operating closer to the optimum guiding thickness, but with lower losses due to the underlying glassy SiO_2 layer.

This study will investigate the use of both glassy and polymer materials for the guiding layer of the Love mode liquid density sensor. CVD SiO_2 and polyimide will be used in both single and multilayer structures. Operation in a liquid requires low insertion losses to allow oscillation. The sensitivity needs to be high to compete with existing densitometer performance.

Polyimides are used in a variety of industrial applications due to their mechanical strength, and high temperature and chemical resistance. Their low stiffness and density should produce a low shear velocity and thus high sensitivity with thin layers. Polyimide is a well-established material for microfabrication and can be wet etched and dry etched allowing conventional processing techniques to be used. The material offers cheap and simple fabrication through spin coating and curing.

4 Experimental procedures

This chapter describes all the experimental procedures used for the study. The chapter is split into three sections: the first covers the process flows for the device, the second covers the fabrication techniques required, and the final part describes the fundamental measurement and test techniques.

4.1 Process flows

The process flows illustrate the fabrication steps for the four types of device built:

- SH-SAW / SSBW device with no guiding layer
- Love mode device with polyimide guiding layer
- Love mode device with SiO_2 guiding layer
- Multilayer Love mode device with SiO_2 / polyimide guiding layer

The individual processes are explained in detail later in this chapter.

4.1.1 IDT fabrication

This process outline illustrates the deposition of the aluminium (Al) and subsequent patterning to produce the IDTs.

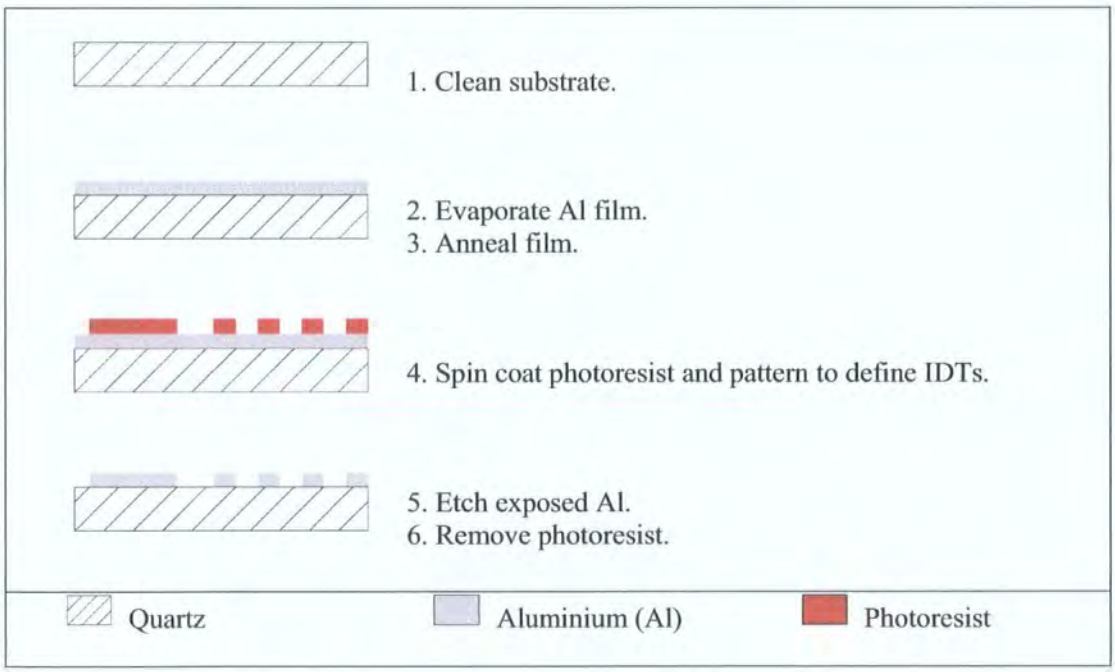

4.1.2 Polyimide waveguide devices

This process outline shows the deposition and patterning of polyimide to produce single layer polyimide waveguide Love mode devices with contact vias and surface corrugations.

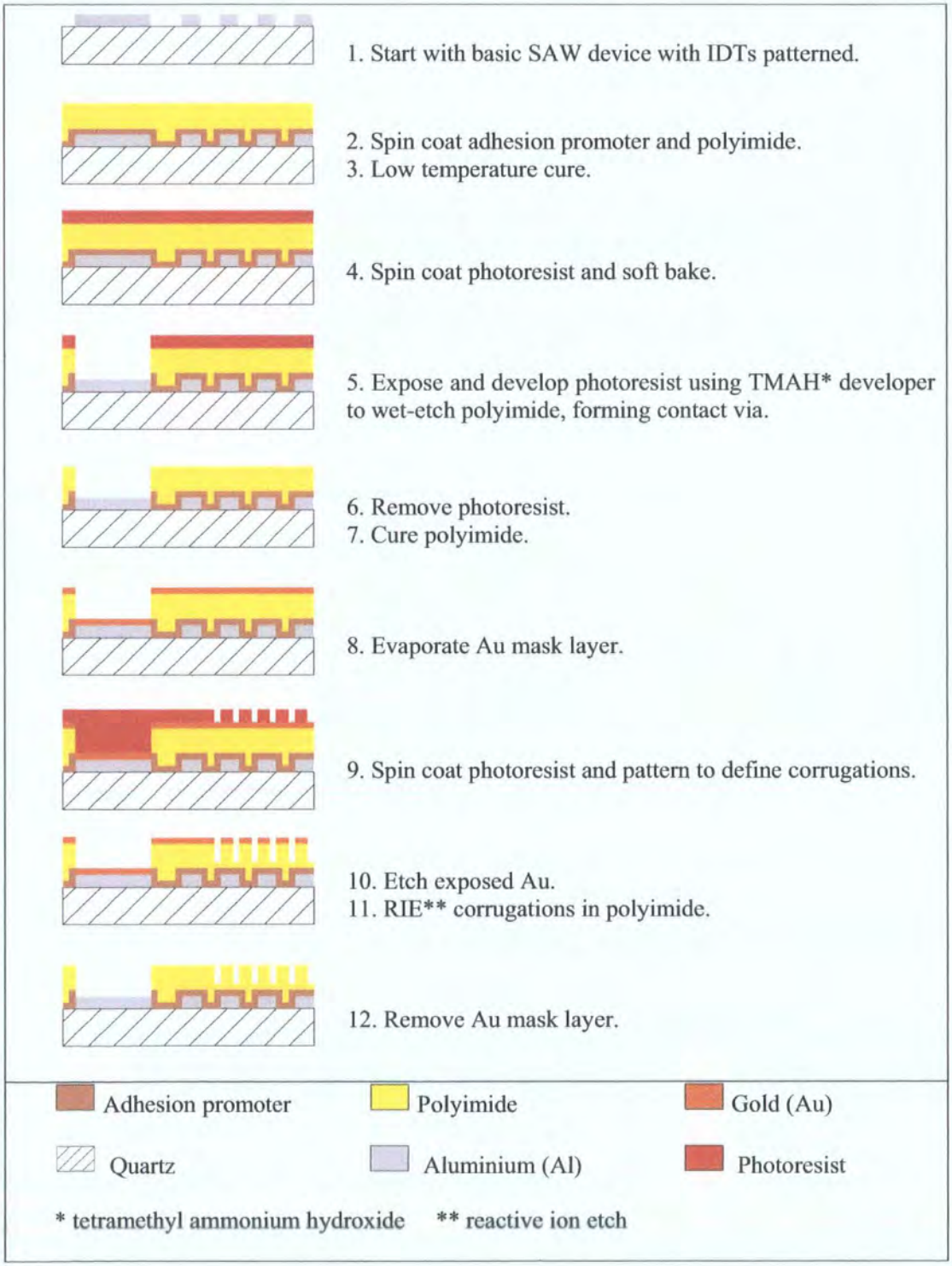

4.1.3 SiO_2 waveguide devices

This process outline shows the deposition and patterning of plasma enhanced chemical vapour deposition (PECVD) SiO_2 to produce single layer SiO_2 waveguide Love mode devices with contact vias and surface corrugations.

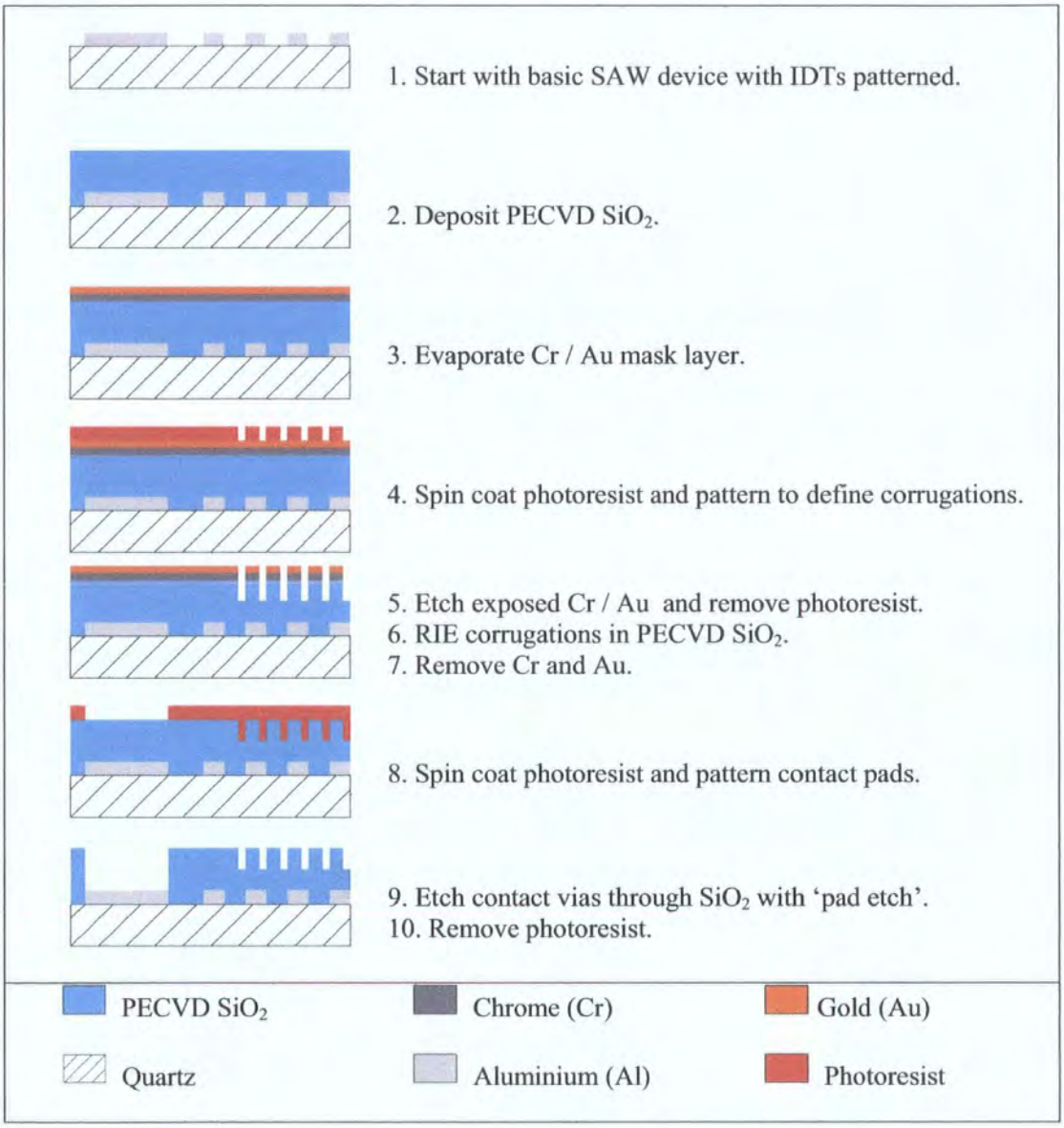

4.1.4 Multilayer waveguide devices

This process outline shows the deposition and patterning of PECVD SiO_2 and polyimide to produce multilayer devices.

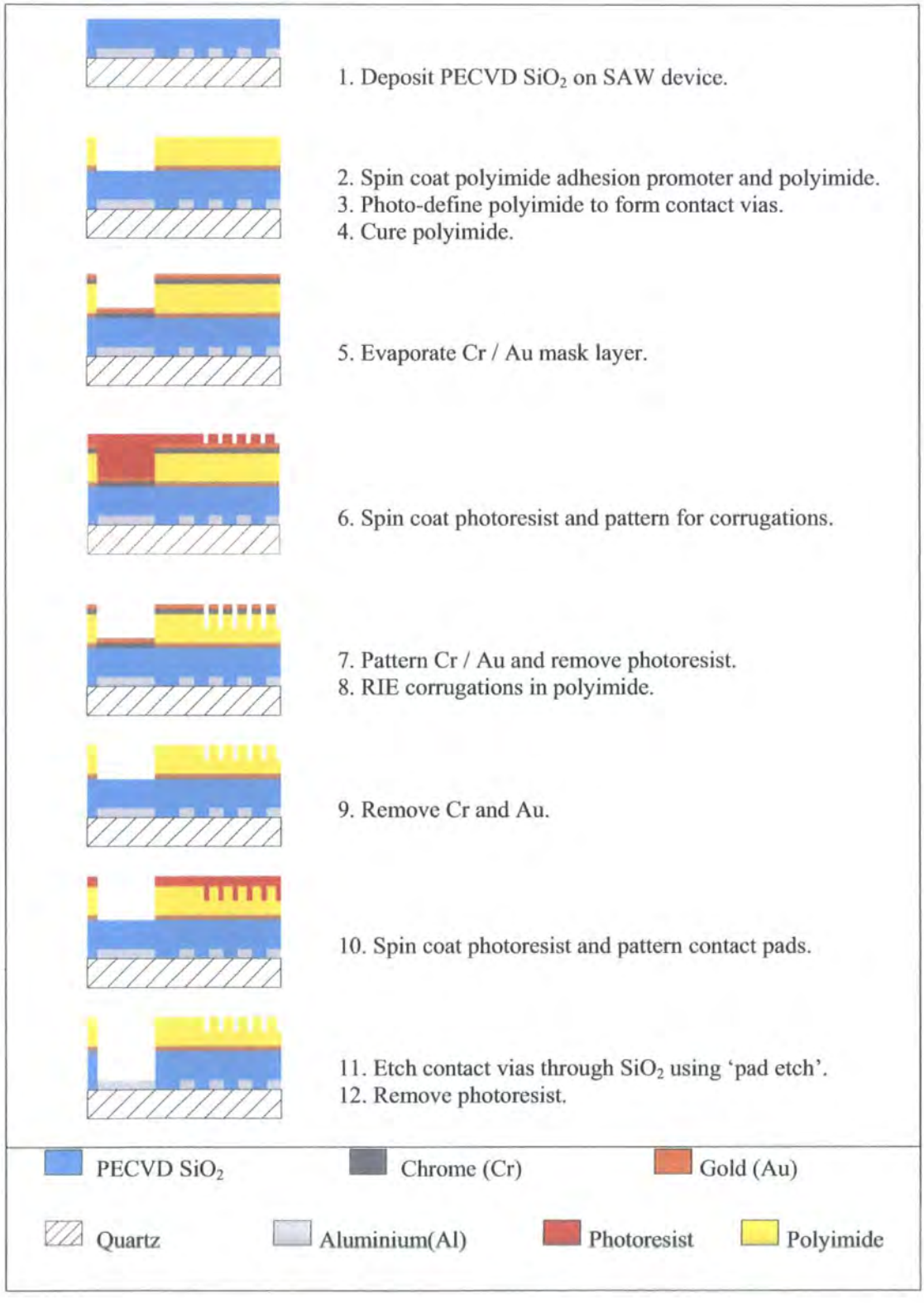

4.2 Wafer preparation

The quartz wafers are ultrasonically rinsed in two baths of isopropyl alcohol (IPA) followed by a 30 minute clean in 'bomb', consisting of equal parts sulphuric acid (H_2SO_4) and hydrogen peroxide (H_2O_2). After removal from the bomb, they are rinsed three times in de-ionised water (DI water) using an ultrasonic bath, and spin-dried.

4.3 Photolithography

Photolithography is the fundamental stage defining where additive or subtractive processes occur to build a device. Whilst there are some 'direct write' processes such as electron beam patterning (used extensively for mask manufacture) and laser/water jet etching such as the Synova Laser Microjet, virtually all patterning uses photolithography in one form or another. The driving force of greater integration and smaller feature sizes has resulted in sophisticated lithography techniques such as phase shift masks, but the basic principle is the same at any scale.

4.3.1 In-house mask fabrication and design

An in-house photo-mask fabrication process has been developed allowing the production of masks registering features down to approximately 10 μm. The mask design is drawn in negative in Corel Draw 10 times larger than required. The design is then printed on a high quality transparency film using an Epson 1290 inkjet printer set at high resolution (1440 dpi or 2880 dpi), allowing features down to 100 μm to be accurately printed. For repetitive designs of small features such as the IDT fingers, the design is drawn with 'points' as the base unit in Corel Draw. The printer stepper motor resolution is based on points, causing banding to occur in the print on regularly spaced features when using any other scale.

The transparency print is then transferred onto a high resolution photographic glass plate using a flat-field camera from a light box. Agfa Millimask and Slavich VRP-M plates were used, offering a relatively low sensitivity, but very high resolution. The plates are 2.5 inch (63.5 mm) square allowing approximately 50 mm square useable exposure area. The light box is mounted at one end of a frame (or on the base of a copy stand in a later set-up) and the camera at the other end (or pillar of the copy stand). The whole structure is rigid to prevent vibrations causing a relative movement between the two, as illustrated in figure 4-1. The distance between the light box and focal plane of

the camera is adjustable, but typically set for a 10 times reduction. Exposures around 4.5 minutes were adequate to produce opaque dark regions, and prevent fogging of the clear regions. Focussing is achieved at maximum aperture using a focusing screen in place of the dark slide, and the aperture stopped down to f16 for exposure to increase the depth of field and reduce aberrations. The plates are developed in Agfa G282C reversal developer, and fixed in Agfa G333c rapid fixer, followed by a rinse in DI water and an ultrasonic bath for 10 minutes.

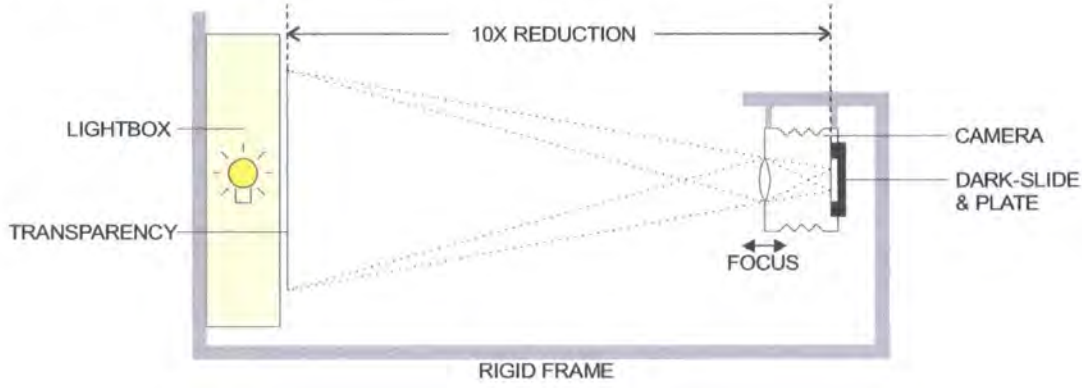

Figure 4-1. Photo reduction of transparency onto glass plate.

The quick and cheap fabrication is ideally suited to the research and development process allowing frequent design changes. These masks were used for some initial patterning of SAW devices, but it soon became clear that the resolution limit and edge contrast would not be adequate for accurate patterning of IDTs at 10 μm or less. Grey fringing over 5 μm around the perimeter of features also made reproducibility of exposure difficult. As a result, commercial masks were eventually used for small-scale patterning, and homemade masks for some larger patterning such as contact pads, and reworking.

4.3.2 Commercial masks

Three principle methods of commercial mask fabrication are LCD projection, laser writing and e-beam writing. LCD projection is the cheapest route, where the mask design is projected from an LCD display to a light sensitive mask plate, either emulsion or Cr, which offers greater contrast. J. D. Photo-Tools (UK) offers this service with a minimum specified feature size of 5 μm. Figure 4-2 shows part of a mask with 10 μm IDTs. The poor definition and large number of defects suggest that the 5 μm minimum size is actually the minimum registerable feature, with the practical limit many times

larger. The poor resolution makes this mask process unsuitable for accurate patterning of IDTs.

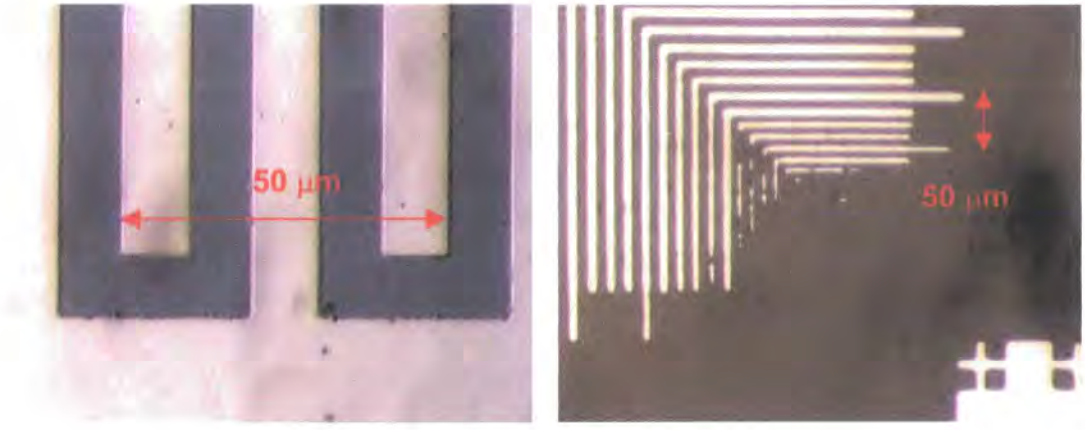

Figure 4-2. Comparison between Photronics e-beam (left) and JD Phototools LCD projection (right) masks. The Photronics mask shows 10μm IDTs. The JD Phototools mask shows a resolution test pattern.

Laser writing offered by companies such as Deltamask (Netherlands) exposes photoresist on a Cr-coated glass plate to a highly focused laser. The photoresist is developed and Cr etched, to leave the pattern in the Cr. Minimum feature sizes of 1.5 μm are possible (Deltamask specifications), with the quality mainly determined by the focusing quality. These masks would be suitable for IDT patterning.

Electron beam write is the principle mask production method, using an e-beam to expose polymethyl methacrylate resist (PMMA) on a Cr-coated glass plate. The PMMA is developed and Cr etched to leave the pattern in Cr. Long write times make the masks expensive and contact copies are used for working, with the masters being kept for future copies or re-working. E-beam masks offer a very low number of defects (typically less than 1 dot of 1 μm size per square inch), an important feature when working with large area devices such as SAWs. A standard minimum feature size of 0.5 μm is available, with a small error on the contact copies. A sample is shown in figure 4-2.

All commercial masks in this study were made by Photronics (UK) using the e-beam write method. The designs were made in Corel Draw and later converted into the standard GDSII format used by the manufacturer.

4.3.3 Photoresist

Photoresist is an organic polymer solution containing a sensitising agent that reacts to UV radiation. Throughout this study, Shipley 1813 photoresist is used for most patterning giving a thickness around 1.3 μm with standard spin (approximately 3700 rpm). AZ4562 photoresist is used where a thicker resist was required, giving thicknesses of 6.2 μm. All work using photoresist until completion of development is performed in yellow lighting with the blue end of the spectrum removed to prevent 'fogging'.

The photoresist is spin coated onto the prepared substrates using a vacuum chuck spinner with digital controller. The spin speed controls the photoresist thickness. The photoresist is dropped on the substrate whilst static with a pipette. An initial spin of 180 rpm is used to spread the resist over the entire substrate for 10 s, followed by the final spin for 30 s at the required speed. Particulate contamination control is vital to prevent radial 'striations' forming, where a particle obstructs the resist during spinning.

A pre-exposure bake following spinning evaporates the solvents, leaving a tough UV sensitive polymer. The pre-bake conditions can be critical for subsequent processing, especially where high-aspect ratio features in thick photoresist are required, such as in the formation of electroplating moulds [89]. If too little bake is used, exposed and unexposed resist may be removed during development, due to the presence of the unwanted solvents. Too much baking causes the resist to become desensitised to UV, and less easily removed in developer. Pre-exposure bakes of 90°C for 15 minutes on a non-vacuum hotplate, or 2 minutes with a vacuum hotplate were used for S1813 photoresist. This gives steep sidewalls and short exposure times, whilst not leaving the resist sticky causing adhesion to the mask.

4.3.4 Mask aligning and exposure

A mask aligner is used to expose the photoresist to UV light through the lithographic mask. A basic aligner consists of a mechanism to accurately align the wafer and mask relative to each other, whilst observing through optics. Once correctly aligned, the mask and wafer are brought into contact, and exposed to UV for a specified time or energy.

The earlier work was performed on a Karl Suss MJB3 contact aligner, with the later work on an EVG620 aligner. The Karl Suss is a basic machine using multi-line UV and

limited to wafers of 2 inch size, masks of 2.5 inches, and an exposure area of approximately 1.5 inches, greatly limiting the number of devices which can be patterned on a single wafer. The machine is fully manual with wafer thickness control and wafer movement for alignment achieved with micrometer style adjusters. The wafer and mask are brought into contact by moving a lever, which requires critical adjustment of the thickness micrometer to achieve good contact. The alignment optics are brought forward to cover the mask area with the UV optics for exposure. An exposure of around 10 s was used for the emulsion masks, and 2 - 2.5 s for the commercial Cr masks, although this varied with the age of the mercury-arc bulb, requiring constant calibration.

Alignment was difficult on the Karl Suss machine due to the narrow field of the single field optics. A mechanical lateral shift of the wafer stage of up to 20 μm when bringing the wafer and mask into contact made accurate alignment somewhat of a guess! However, this was not a major issue with no critical alignment required on subsequent stages of the device fabrication.

Two major exposure problems were experienced with the Karl Suss aligner. Firstly, when using emulsion masks, correct exposure time is critical with small features due to the grey regions around the feature's edges - the amount of exposure determines where in the grey region the edge of the exposed photoresist will be. The UV intensity varies across the exposure area of the aligner, so even with correct exposure over one part of the mask a different region might have larger or smaller feature sizes as shown in figure 4-3. With IDTs designed at 20 μm finger width, this effect resulted in sizes between 15 and 25 μm across the wafer, and was one of the principle reasons for the utilisation of high contrast commercial Cr masks early in the project.

Secondly, the basic mask-wafer contact method combined with the aluminium's high reflectivity cause interference effects, with Newton's rings forming during contact due to reflections between the Al and mask. The ring pattern resulting from the UV exposure is different to that in the yellow cleanroom lighting, but the same effect produces ring-like patterns in partially exposed and developed photoresist, superimposed on the devices as shown in figure 4-4. Trials using Brewer Science XL-20 antireflective coating, spin coated before the photoresist, partially improved the problem. However the extra processes involved with spinning and curing the coating and changes to exposure makes it undesirable. A more effective method eradicating the

problem is a short low power RIE O_2 etch for 90 s, thinning all of the developed photoresist, and completely removing the thinner rings. A bonus of this process is de-scumming - removal of development residue.

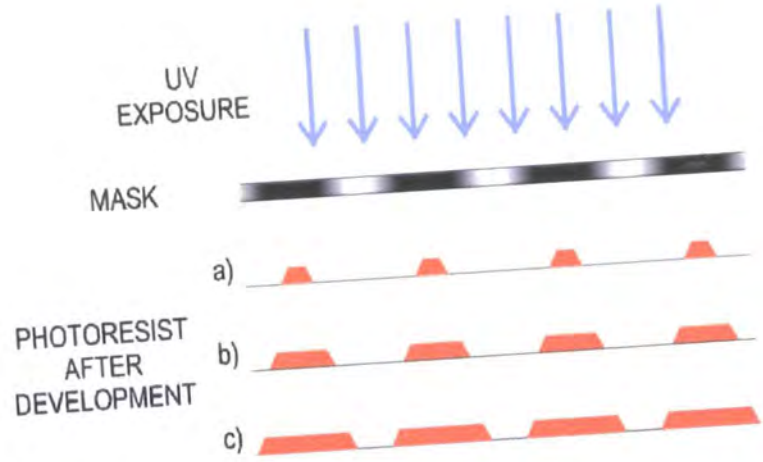

Figure 4-3. Exposure variation across wafer due to grey mask regions. Over-exposure (a), correct exposure (b), and under-exposure (c).

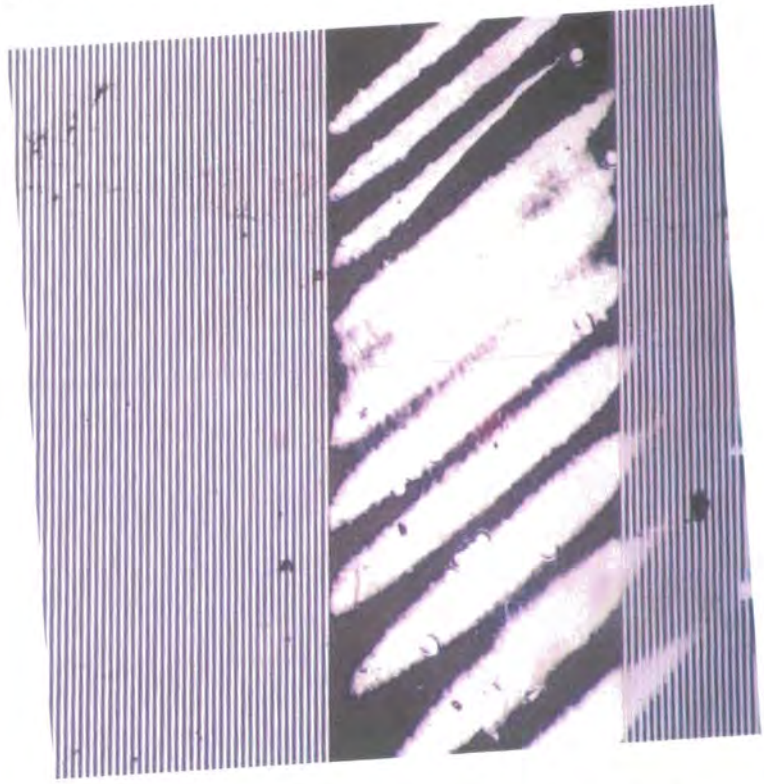

Figure 4-4. Newton's rings in Al following etching. They appear here mainly confined in the propagation path between IDTs.

The EVG620 aligner used later in the project is a modern semi-automated machine, capable of taking wafers up to 6 inches, and masks up to 7 inches square. In essence, the machine is very similar to the Karl Suss, but has the capability to print much smaller features due to higher quality exposure optics and a more advanced contact mechanism. This allows soft contact (mechanical pressure bringing the wafer and mask together), hard contact (compressed air applied to the underside of the whole wafer), vacuum contact (a vacuum applied between the mask and wafer) or both hard and vacuum. Tests on the aligner showed uniform intensity across the exposure area, and none of the exposure problems encountered on the Karl Suss exist on the EVG.

4.3.5 Development

The exposed photoresist is developed with 1 part Shipley Microposit 351 developer in 2 parts DI water for 20 s. The wafers are then rinsed in DI water. The developer is based on a sodium hydroxide (NaOH) solution that dissolves the exposed regions of photoresist, without attacking the unexposed regions. Figure 4-5 shows the effect of exposure and development conditions on the photoresist features. The left images show the ends of 10 μm wide IDTs, and those on the right the ends of 2.5 μm wide strips used for patterning the surface corrugations. Development times change during the tests to achieve complete development.

Condition A shows under-exposure with over-size IDTs and poor resolution of the corrugations. Condition B results in the correct feature sizes due to the correct exposure of 2.0 s with soft contact, but interference effects cause rounding of the corners and the unusual shapes at the end of the corrugation patterns. Condition C results from overexposure with a reduction in IDT finger width, more distortion, and the complete removal of the corrugation patterns in some areas. Finally, condition D shows that increasing the contact pressure by combining hard contact and vacuum contact produces accurate features of the correct size with almost no interference patterns. In this study, condition D exposure conditions are used, although the extra pressure sometimes causes problems with the mask and wafer sticking together.

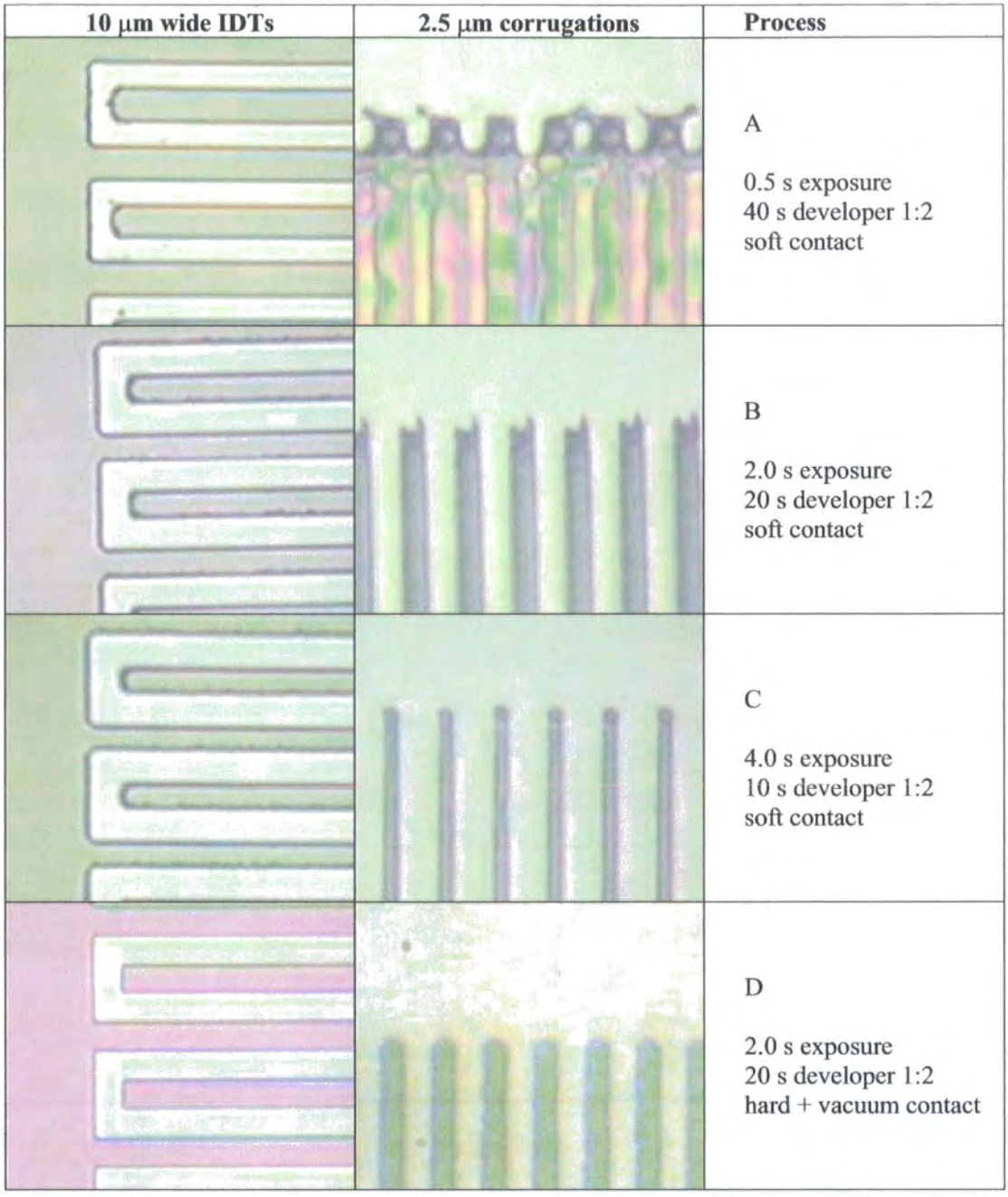

Figure 4-5. Variation in feature size with exposure time and development time (A-C), and contact method (D).

4.4 Metal deposition and patterning

4.4.1 Evaporation

Evaporation is one of the principle methods for depositing high quality thin films of metal. A high purity metal source is heated to evaporate onto a substrate, on which it condenses to form a film. The whole process takes place under a vacuum of typically

10^{-6} Torr (760 Torr = 760 mmHg = 1 atm), giving an approximate mean free path of approximately 34 m for the evaporated metal molecules to uniformly reach the substrate[1]. The vacuum also prevents contamination and oxidation of the metals at the high evaporation temperatures. Good metal adhesion requires the substrate to be clean, and for some metals with naturally poor adhesion, another metal known as a 'seed layer' is deposited first. The thickness of evaporated metal films is typically limited to less than 1 μm, otherwise internal stresses cause buckling and peeling.

Two evaporators are used for this study to evaporate Al, Cr and Au. Most Al evaporation is performed in a 12-inch thermal evaporator shown in figure 4-6. Al wire is placed in a tungsten filament or boat, positioned below the substrates and separated by a shutter. A high current through the filament melts and evaporates the Al, which rises onto the substrates once the shutter is opened. The system is pumped by a rotary-backed oil diffusion pump, with a liquid nitrogen filled cryogen trap to prevent oil vapour contaminating the chamber.

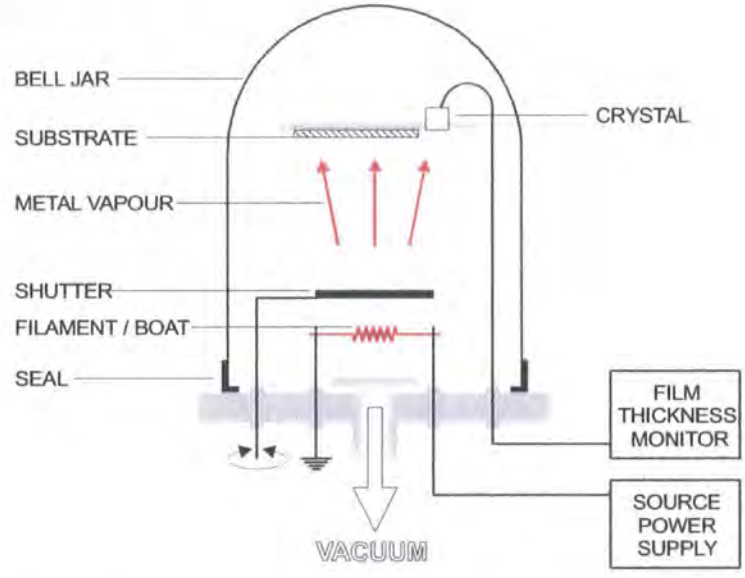

Figure 4-6. Schematic of 12-inch thermal Al evaporator.

An electron beam (e-beam) evaporator is used for evaporation of Cr and Au and some Al. The metal source is positioned in a copper water-cooled crucible as shown in figure 4-7. The source surface is heated by the e-beam, the remainder of the source

[1] The value of 34 m is for the mean free path of water vapour at 10^{-6} Torr. Obtained from Holland, L. Vacuum deposition of thin films. 1956, Chapman and Hall, p. 5.

remaining cooler due to the water cooling. The e-beam is produced from a high voltage cathode filament, with a set of magnets guiding the beam through 270° to be focused on the source. This beam path allows the filament to be protected from the evaporating metal by a shield. The evaporation system contains two identical sources allowing two metals to be consecutively evaporated without letting the system up to air. A turbo-molecular pump is used to achieve a pressure of about 10^{-6} Torr in one hour.

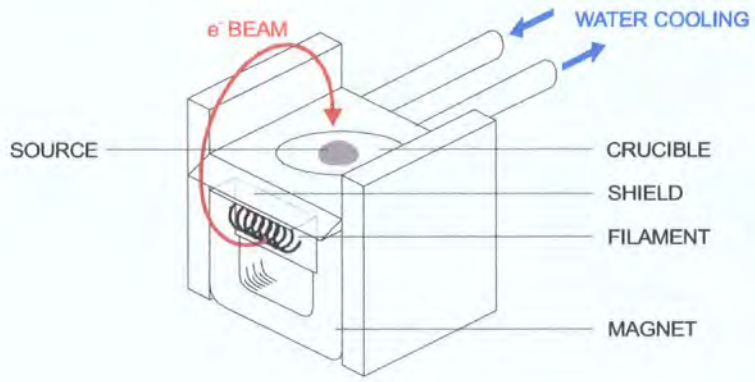

Figure 4-7. Electron beam evaporation source.

Both evaporators are equipped with a film thickness monitor consisting of a QCM positioned near the substrates. The crystal resonance shifts with the deposition of metal onto its surface. Calibration of the frequency change (with an adjustment factor for the metal density) allows the deposited thickness to be monitored.

4.4.2 Aluminium deposition and patterning

Al is used for all the IDT electrode structures in 150 nm thick layers evaporated around 30 nm min^{-1}. Layers of Al deposited early in this study using the e-beam evaporator were poor quality, with large 'blobs' of metal spitting from the source. This is caused by the large currents (>500 mA) required for Al evaporation (its high conduction grounds the e-beam very effectively) heating the entire crucible area including debris from previous evaporations. Graphite crucible liners used later in this study reduced current to approximately 150 mA, prevented spitting, and giving good quality films. The films deposited in the thermal evaporator are all good quality with no spitting or contamination.

The Al films are annealed at 490°C for 10 minutes in a tube furnace to improve the adhesion to the substrate. Annealing causes an Al oxide (Al_2O_3) layer to form at the

Al - quartz interface, creating a strong bond to the oxygen-containing quartz. The wafers are left for 10 minutes prior and after the annealing in the furnace mouth (~200°C) to reduce the probability of thermal shock cracking the quartz. Figure 4-8a shows un-annealed Al completely removed from the quartz by scratching with a probe, whereas figure 4-8b shows the improved adhesion, with the Al being scratched, but not completely removed. Sticky-tape adhesion tests peel the Al from the substrate on non-annealed samples, but show no removal on the annealed films.

(a) (b)

Figure 4-8. (a) Completely removal of the Al on the un-annealed sample and (b) only partial removal due to improved adhesion with annealing.

The Al is patterned using a photoresist mask with a standard etch recipe:

- Orthophosphoric acid (H_3PO_4) 85 %
- DI water 10 %
- Nitric acid (HNO_3) 5 %

The HNO_3 forms a surface Al oxide film, which the DI water and H_3PO_4 dissolve. Typical etch times were 4 minutes in fresh solution at room temperature, with an extra 50% once the Al was visibly etched to ensure complete removal. Increasing the solution temperature to 30°C reduces the time to around 1 minute, but with the risk of the photoresist being attacked by the warm HNO_3. At 40°C, the solution completely dissolves the photoresist mask.

The wafers are agitated by hand and repeatedly dipped in and out of the solution for the first minute to prevent the formation of H_2 bubbles [90]. These can mask the Al leaving circular spots as shown in figure 4-9. This problem is compounded by the size of the bubbles being similar to the inter-finger spacing causing many short-circuited

devices. The wafers are also wetted with DI water prior to immersion to assist the viscous etch in filling the open regions in the photoresist mask.

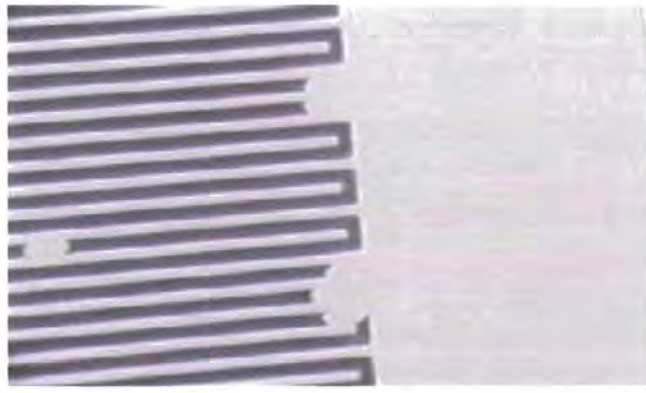

Figure 4-9. Al spots resulting from H_2 bubbles forming during Al etching, causing short-circuits.

4.4.3 Chrome and gold deposition and patterning

The deposition of Cr and Au is common for two reasons. Firstly, Cr is used as a seed layer to overcome the poor adhesion of Au. Secondly, conventional Cr etches attack photoresist making it irremovable, so a two-stage process is used where the Au is initially patterned with the photoresist mask, the photoresist removed, and then the Cr patterned using the Au mask as shown in figure 4-10.

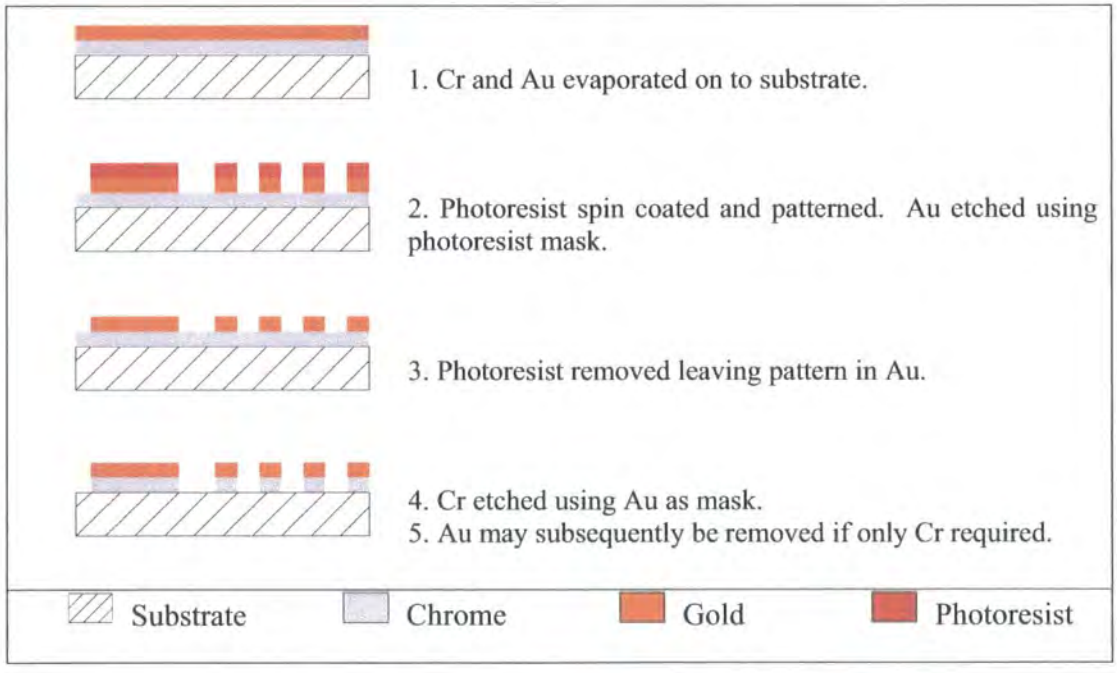

Figure 4-10. Cr - Au patterning process.

Cr-Au films are evaporated consecutively in the dual-source e-beam evaporator, preventing oxidation of the Cr between evaporations. Typical Cr layers are 5 - 10 nm thick with the Au 50 - 100 nm thick. Fine control of the e-beam current is required because Cr sublimes, and can deposit thick stressy layers with poor control.

The Cr-Au layers are used as masking layers for reactive ion etching (see later). The following etch process is used (quantities given by weight):

1 Photoresist patterning

2 Au etch: (approx 10 seconds)

- Potassium iodide (KI) 4 parts
- Iodine (I) 1 part
- DI water 8 parts

3 Photoresist strip in acetone and ultrasonic bath

4 Cr etch: (approx 10 seconds)

- DI water 8 parts
- Potassium hexacyanoferrate ($K_3Fe(CN)_6$) 2 parts
- Sodium hydroxide (NaOH) 1 part

4.5 CVD SiO_2 deposition and patterning

Chemical vapour deposition (CVD) is used in the IC industry to deposit SiO_2 or silicon nitride (Si_3N_4) for insulation between interconnect layers or for ion implantation masks, and poly-Si for interconnects. Constituent gases of the required material and a carrier gas react at the heated substrate surface in a low-pressure chamber. The reactions form a thin film on the substrate surface, where surface migration and nucleation results in conformal films with good step-coverage. The by-products of the reaction are removed through the vacuum system.

A plasma enhanced CVD process (PECVD) is used to deposit SiO_2 waveguide films between 1 and 3 μm thick. The plasma generated by an applied RF between an anode and the grounded substrate platform increases the reaction process, allowing relatively

low deposition temperatures (typically around 300 °C) and high rates. The substrate is heated from below, and gases introduced through a showerhead above the substrate. Figure 4-11 shows a schematic of the PECVD chamber, and figure 4-12 the reaction process for SiO_2 deposition using silane (SiH_4) and nitrous oxide (N_2O) constituent gases. The process can be simplified to [90]:

$$SiH_4 + 2N_2O \rightarrow SiO_2 + 2N_2 + 2H_2 \qquad (4\text{-}1)$$

The following parameters were used for the PECVD SiO_2 deposition:

- Electrode temperature: 300°C
- Operating pressure: 320 mTorr
- SiH_4 flow rate: 10 sccm
- N_2O flow rate: 200 sccm
- Plasma power: 90 W

This gives a deposition rate of approximately 27 nm/min.

Contact vias are selectively etched through the SiO_2 layers using 'pad etch':

- 40% Ammonium fluoride solution (NH_4F) 1 part
- Acetic acid ($C_2H_4O_2$) 1 part
- DI water 1 part

Etch rates of 75 nm/min were obtained, and resistive probing and optical inspection used to check for complete SiO_2 removal. S1813 photoresist hard baked at 120°C for 10 minutes is used for masking. A carbon tetrafluoride (CF_4) RIE etch is an alternative method, but long etch times and the requirement for a patterned metal mask make this undesirable.

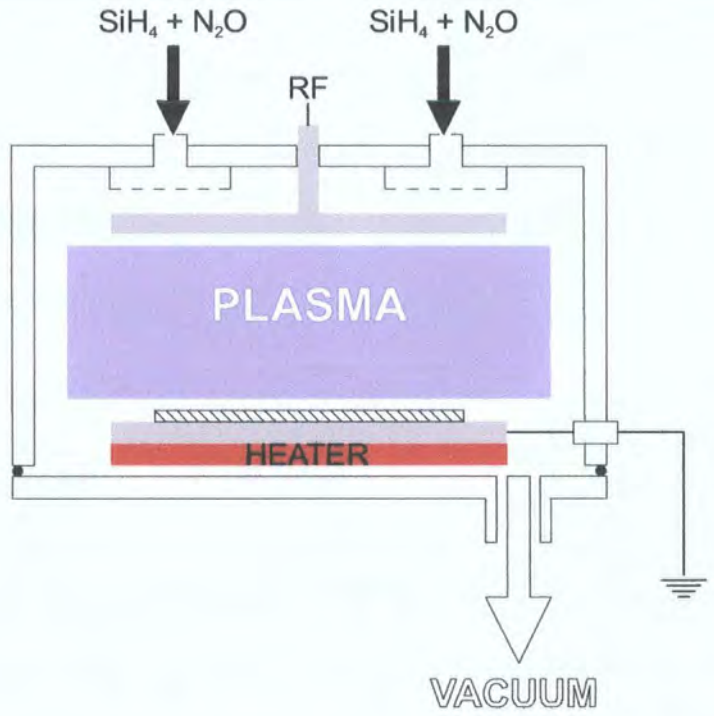

Figure 4-11. Schematic of PECVD chamber showing gas inlets and vacuum port. RF is applied between the anode and substrate.

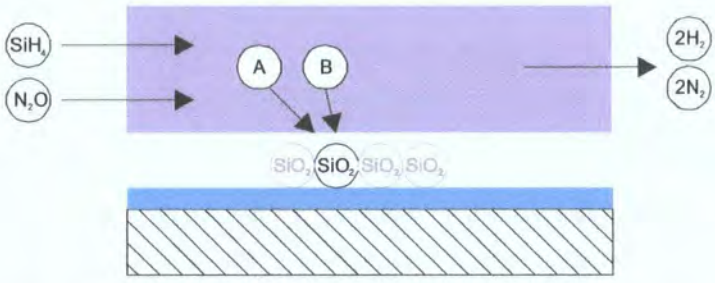

Figure 4-12. Process gases SiH_4 and N_2O react in the plasma 'A' and 'B' at the substrate surface, and migrate along the surface to nucleate forming a thin conformal film.

4.6 Polyimide deposition and patterning

HD Microsystems PI2545 polyimide is used throughout this study for the polyimide waveguide devices. All polyimides have similar cured film properties, but differ in the deposition and patterning characteristics. PI2545 was chosen primarily for its spin speed-thickness characteristics, allowing deposition of layers down to 1 μm. Other advantages are wet etch characteristics for producing contact vias, and O_2 RIE capabilities for the surface patterning.

4.6.1 Adhesion promoter

HD Microsystems VM-651 adhesion promoter is used to improve the adhesion. VM-651 is an organosilane solution, which forms a Si-O bond with an oxide forming surface, and so bonds well with quartz, PECVD SiO_2 and Al. A 0.5% solution in DI water is deposited over the wafer surface through a 0.2 μm filter and left static for 20 seconds (the activation time). The wafer is then spun dry at 3500 rpm and baked at 120°C for 1 minute on a non-vacuum hotplate.

4.6.2 Polyimide spin coating and wet-etching

The manufacturer's spin speed-thickness data is sparse, presumably due to the film thickness susceptibility to curing conditions. Figure 4-13 shows experimental film thickness measurements compared with the supplied data. HD Microsystems T9039 thinner is mixed with PI2545 20% by volume to achieve film thicknesses below 1.5 μm.

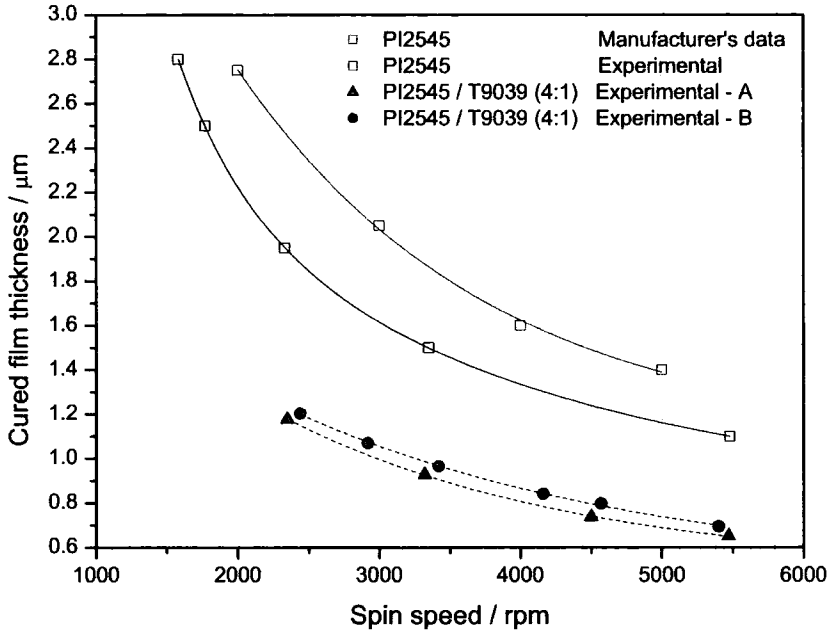

Figure 4-13. Experimentally derived spin deposition characteristics for PI2545 and thinned PI2545/T9039 compared with manufacturer's data.

The spin coating process including wet etching the contact vias is outlined below:

1. Polyimide spin coat: 500 rpm for 10 seconds followed by final speed for 45 seconds
2. 140°C vacuum hotplate low temperature cure for 2 - 6 minutes
3. Standard photoresist spin coat
4. 90°C hotplate photoresist pre-bake: 1.5 minutes (vacuum) or 15 minutes (non-vacuum)
5. Standard exposure in mask aligner
6. Development in 100% Shipley Microposit TMAH MF319 developer for 30 seconds
7. Photoresist removal in acetone using ultrasonic bath
8. Polyimide cure

4.6.3 Polyimide Curing

A simple two stage curing process is used for most of this study. Following the low temperature bake and wet etching if required, the wafers are placed on a 200°C hotplate for 30 minutes, followed by 60 minutes in the centre of a tube furnace at 350°C in a flow of 200 cc/min N_2. The furnace is switched off to cool to room temperature before wafer removal, giving a slow ramp down. Wafer size is limited to 2 inches requiring 100 mm wafers to be cut into quarters. Reproducibility is difficult due to the estimated error of ± 25°C for the inaccurate furnace temperature control.

A programmable bench top furnace was acquired for polyimide curing and used in later parts of the study. The programmable control unit enables the correct temperature ramping for correctly cured films as shown in figure 4-14.

The control thermocouple is positioned beneath the wafer boat in the tube centre, and an external thermocouple can be placed down the centre of one of the ceramic boat support arms to profile the temperature as illustrated in figure 4-15. This is used for calibration of the furnace. A spring-loaded door and quartz glass baffle enables a fairly uniform temperature profile along the tube as shown in 4-16. The central peak temperature is different to the control thermocouple due to the measurement thermocouple being positioned inside one of the ceramic rods.

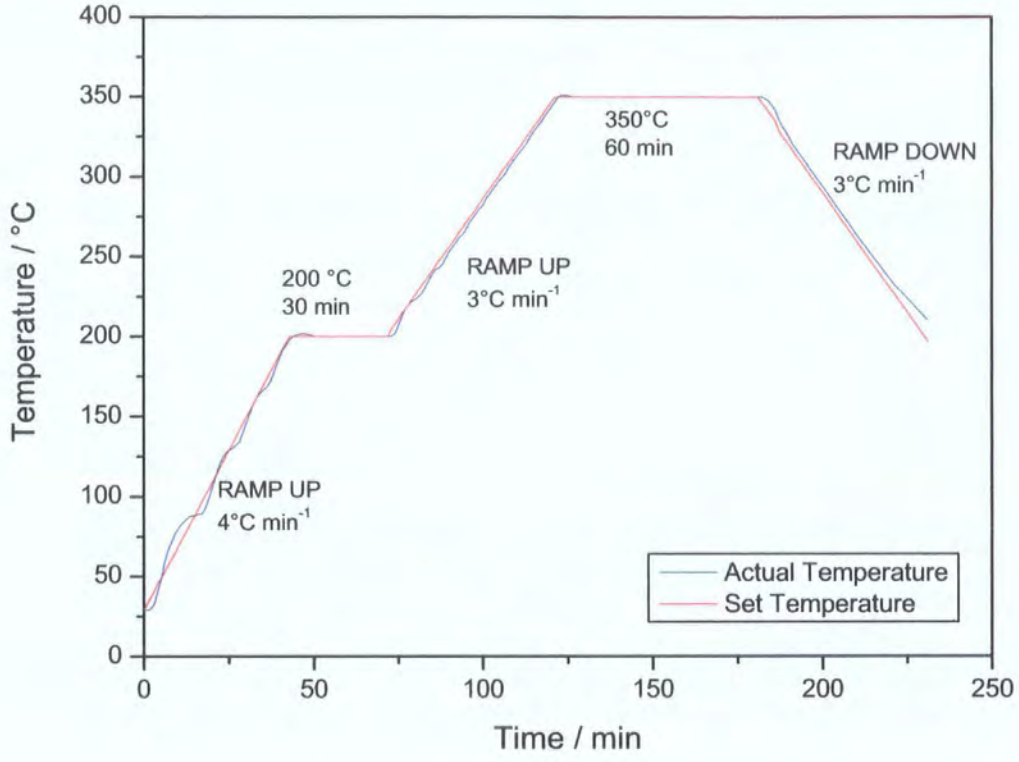

Figure 4-14. Polyimide cure temperature ramping for programmable furnace.

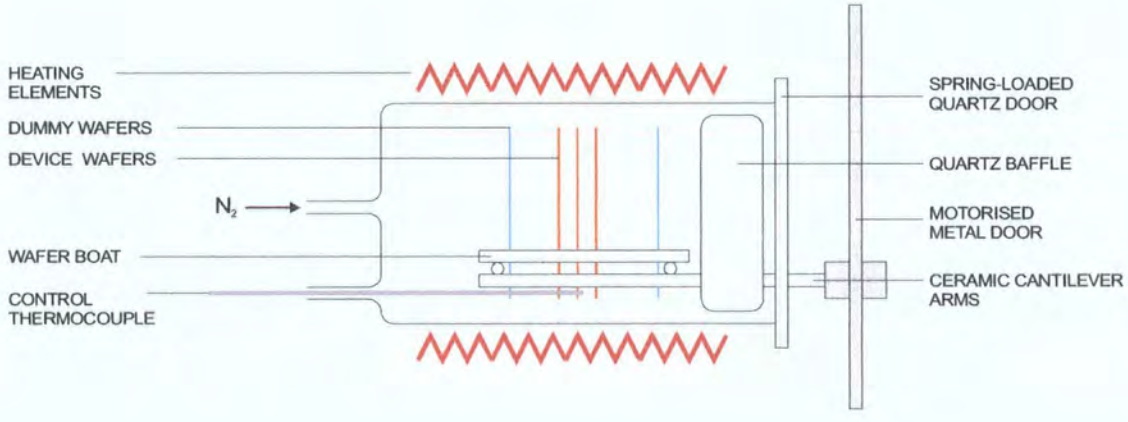

Figure 4-15. Schematic of the programmable furnace tube.

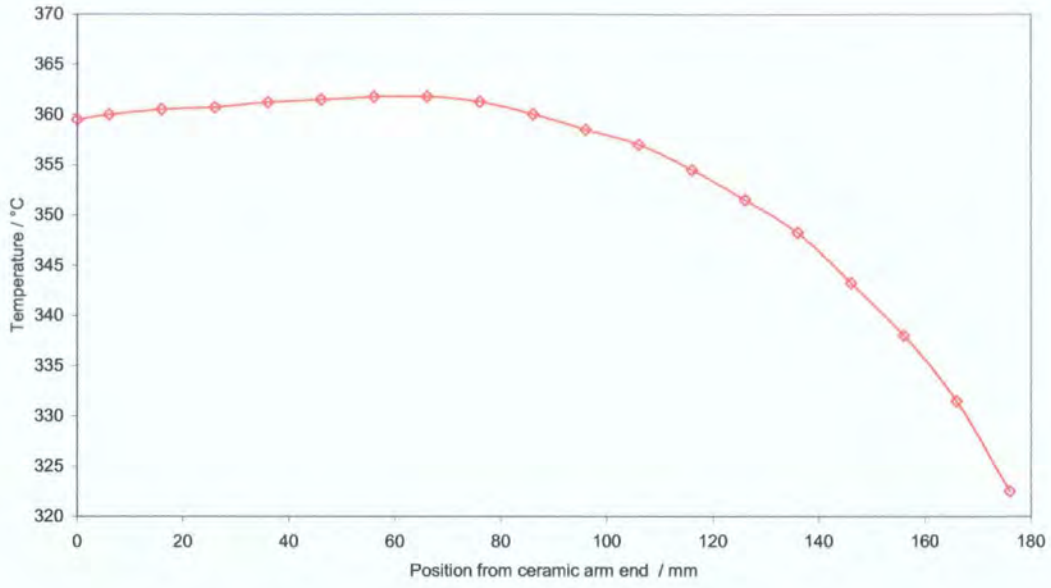

Figure 4-16. Temperature profile along the programmable furnace tube. Temperature set to 350°C.

4.7 Reactive ion etching

Dry etching with reactive ionised gases is used to overcome the isotropic nature of wet etches and their surface tension problems. Process gases are introduced into a vacuum chamber, and ionised to form a plasma around 200 mTorr. Two different plasmas are typically used; O_2 for etching organics such as photoresist, and halogen-based for non-organics like Si. In this study, O_2 was used for all organics, and CF_4 for non-organics. Their plasmas are:

$$O_2 \rightarrow 2O \tag{4-2}$$

$$CF_4 \rightarrow CF_3 + F \tag{4-3}$$

The reactive ion etcher (RIE) consists of an earthed vacuum chamber with an RF (13.56 MHz) driven substrate stage. The driven electrode area is smaller than the grounded chamber. This gives the reactive gases a strong directionality at the substrate, due to the voltage drop at the electrode being inversely proportional to its area. Figure 4-17 shows the basic components of an RIE and figure 4-18 shows the directionality of the ionised gas near the substrate.

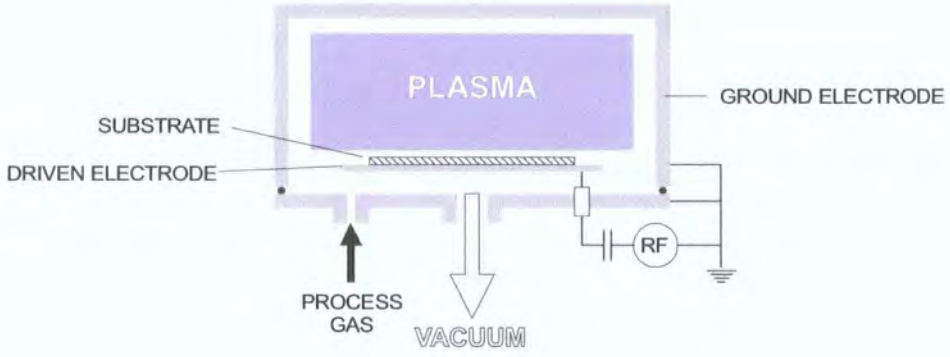

Figure 4-17. Reactive ion etcher process chamber showing large ground electrode (chamber lid) and small driven electrode (substrate stage).

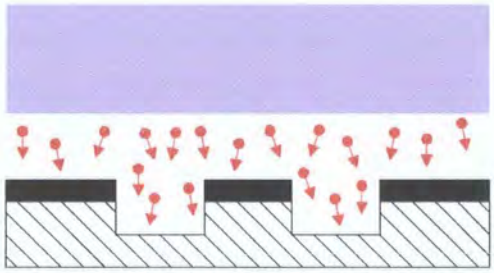

Figure 4-18. Detail of etching process. Directional ions attack the material anisotropically through a resistant mask layer (black).

A bench-top Technics RIE was used, operating around 200 - 250 mTorr, and evacuated by a rotary pump. The base pressure (around 20 mTorr) is reached in only a few minutes allowing a high throughput. The chamber is water-cooled, and the RF generated by an external HV supply.

4.7.1 Organics

An O_2 RIE etch removes the interference fringes in the photoresist pattern resulting from exposure on the Karl Suss mask aligner. The following recipe is used:

Photoresist: Interference fringe removal	
O_2 partial pressure / mTorr	200
Power / W	100
Etch time / s	90

A visual inspection checks for complete removal of the fringes. Higher power etches around 3.5 minutes are required to completely remove 1.3 μm of S1813 photoresist, so there is no risk of removing the desired pattern.

A higher power recipe is used for etching the polyimide corrugations. The following recipe gives a 0.5 μm/min etch rate:

Polyimide: Corrugation etch	
O_2 partial pressure / mTorr	200
Power / W	200

An Au mask layer is used for all polyimide patterning to prevent interference effects in the translucent polyimide during exposure from deforming the 2.5 μm corrugations. Prior tests using S1813 directly on the polyimide proved impossible for successful patterning. Adhesion tests using sticky tape show that Au has adequate adhesion to the polyimide for a single use mask layer, but further processing could cause it to peel. A Cr seed layer cannot be used on the polyimide devices due to the Cr etch attacking the Al contact pads.

4.7.2 Inorganics

Carbon tetrafluoride is used for etching PECVD SiO_2, quartz and glass during the study. The fluorine radicals created in the plasma react and etch the SiO_2. The rate of etch is partially determined by the *fluorine to carbon ratio* (F/C). For low O_2 concentrations, F/C reduces slowing the etch rate. Introducing small concentrations of O_2 forms CO or CO_2 increasing the F/C ratio giving faster etch times. An optimum value of around 20% O_2 gives the maximum SiO_2 etch rate with further increments diluting the plasma F and slowing the etch rate. Polymerisation during the etch process can cause polymer layers to be deposited on the substrate, slowing the etch rate. Higher concentrations of O_2 can be used to remove these layers.

A Cr-Au mask layer is used for the PECVD SiO_2 dry etch. Attempts at using a photoresist mask result in poor features due to exposure interference, and significant etching of the photoresist with the plasma O_2 content. The following recipe based on the RIE manufacturers recommendation is used for etching of the corrugations in

PECVD SiO_2. The recipe gave approximately 60 nm/min, resulting in etch times around 8 – 10 minutes for 0.5 μm deep corrugations. The O_2 content varies due to difficulty in striking the plasma under certain conditions and for this reason was also kept below the optimum 20%.

PECVD SiO_2: Corrugation etch	
CF_4 partial pressure / mTorr	200
O_2 partial pressure / mTorr	10 - 20
Power / W	200

4.8 Inspection

4.8.1 Scanning electron microscope

A Hitachi S2400 scanning electron microscope (SEM) is used for detailed inspection of the devices, allowing observation of the surface topology, and inspection of the corrugations including sidewall profiles. The sample devices are attached to the SEM stubs using a conductive adhesive pad, and a 10 nm layer of Au sputtered over the sample to provide a conductive surface.

4.8.2 Optical microscopes

Two microscopes are used for all optical inspection work. A high-powered top illumination Nikon with maximum magnification of 2000× is used for most inspection work, and also for taking micrograph images. The Nikon has a graduated focussing mechanism allowing depth measurements to be made with approximately 2 μm resolution.

A lower-powered Vickers microscope with a split-image system is used for measuring line widths. The image is split with a prism arrangement, and a direct readout in microns given via a mechanical drive system. The Vickers also has bottom lit illumination to allow mask inspections.

4.8.3 Profiling

A Taylor-Hobson Talystep, and Tencor Alphastep are used to measure feature profiles, layer thickness and surface roughness. Both machines trace a stylus across the sample, and measure the stylus deflection to build a cross-section of the sample. The Talystep is a manual system that outputs data to a computer. Due to the limited optics, manual levelling and stylus force adjustment, finding a feature or film edge can be difficult and many attempts can be required to get a satisfactory result. The Alphastep is a more automated system with a high-powered video camera and automatic stylus positioning and levelling, making the machine easier to use.

4.9 Device preparation

4.9.1 Dicing

The completed wafers are probed prior to dicing to check for short-circuits in defective devices, and also optically inspected. They are then scribed on the device side using a diamond scribe and a ruler, and placed device side down on a piece of dense foam with a protective wipe in-between. Considerable pressure applied along the scribe with a metal edge is used to break the wafer.

Crystalline quartz doesn't contain any cleavage planes, and the manual scribing process is only partially successful and the method's effectiveness varying between wafers. Some wafers break accurately and easily without damaging devices, whilst other identical wafers require a much greater pressure. Sometimes the scribe lines have no effect with the wafer breaking in any direction and destroying the devices. This difference of in-built stress is apparent during high temperature processing stages, with some wafers cracking in the furnace or on a hotplate.

A commercial wafer dicing company (Die Technology Ltd, UK) was approached for sawing the quartz. Unfortunately they did not have the specialist blades and attachments required for quartz, and were unsuccessful with their existing silicon equipment.

4.9.2 Wire bonding and packaging

The diced devices are fixed to the bond pad in a chip header using silver conductive paste. This enables the backside to be grounded, reducing cross talk. Ceramic and

metal tub chip headers are used, and more information on these two types is given in the chapter "Liquid sensor packaging". The metal tub type headers are used for convenience, allowing up to 4 devices to be mounted, and the ceramic headers are used for devices intended for extensive liquid testing due to the ease of sealing.

A Kulicke and Soffa ultrasonic 33 μm Au wire bonder is used for all electrical contacts. The effectiveness of the bond between the Au ball and Al contact pads is variable, particularly on the polyimide Love mode devices due to surface residue from etching the contact vias.

The wire bonds are encapsulated using either Dow Corning 732 silicone sealant or Araldite Rapid two-part epoxy, to protect them from the sample liquids. The silicone is easier to apply, but forms a cylindrical bead around the device perimeter, creating liquid traps and making cleaning difficult. The silicone flexibility also causes some wire bonds to become detached. The epoxy method produces a smooth join to the device surface and sets hard, making cleaning simple and creating a mechanically strong barrier. Figure 8-8 shows epoxy encapsulated metal tub and ceramic headers.

4.10 Electrical measurements

A HP 8743C vector network analyser (VNA) and HP 85047A S-parameter test set is used for all the electrical device measurements. The devices mounted in chip headers are connected to the VNA using a PCB-mounted socket with SMA connectors, and high frequency SMA cables are used throughout. A full two-port calibration of the VNA is made at the beginning of each test session using a HP 85033C calibration kit.

The peak frequency and insertion loss are observed by measuring the S_{21} and S_{12} transmission coefficients, which give the band-pass characteristics of a device. The parameters S_{11} and S_{22} giving the reflection coefficients at port 1 and port 2 can also be measured. The schematic in Figure 4-19 shows the four S-parameters for a two-port device such as a SAW filter. The first subscript number shows the output measurement port, and the second the activated port.

Peak-search tracer markers are selected to measure the exact values of frequency and insertion loss at the SAW peak. The maximum number of points measured in a frequency sweep for the HP 8753 C is 1601, and so a narrow frequency span is selected to encompass the peak once the approximate frequency has been determined. This is typically 500 kHz, giving a resolution of 312 Hz, which is found adequate for most

measurements. The insertion loss is measured to 0.01 dB using the same markers. The averaging facility on the VNA is used to help reduce measurement errors by averaging the response over the last 16 frequency sweeps. With 1601 data points, this takes around 15 seconds before a reading can be taken.

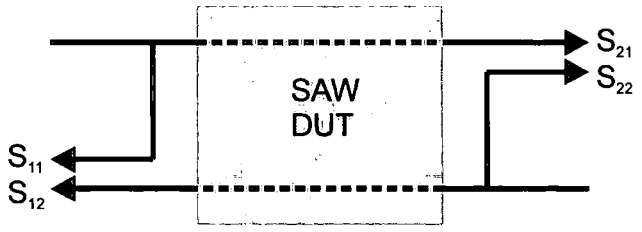

Figure 4-19. S-parameters for a two-port device.

Data transfer from the VNA to a PC is achieved using the Labview graphical interface program through a GPIB connection. The program enables the insertion loss versus frequency data to be exported to an external spreadsheet file. This is used for characterisation of the different device responses and for comparing the frequency response before and after sample loading.

4.11 Temperature measurements

Temperature response measurements are made using a home-made temperature control unit consisting of a Peltier cell, heat sink and fan. The PCB containing a socket holding the mounted device is clamped above the Peltier cell on threaded struts. A hole drilled through the base of the PCB and socket allows a 10 mm diameter by 12 mm long Al stub to act as a conduction medium between the base of the chip header and Peltier cell surface. Heat sink compound is applied to ensure adequate thermal contact. Figure 4-20 shows the assembly.

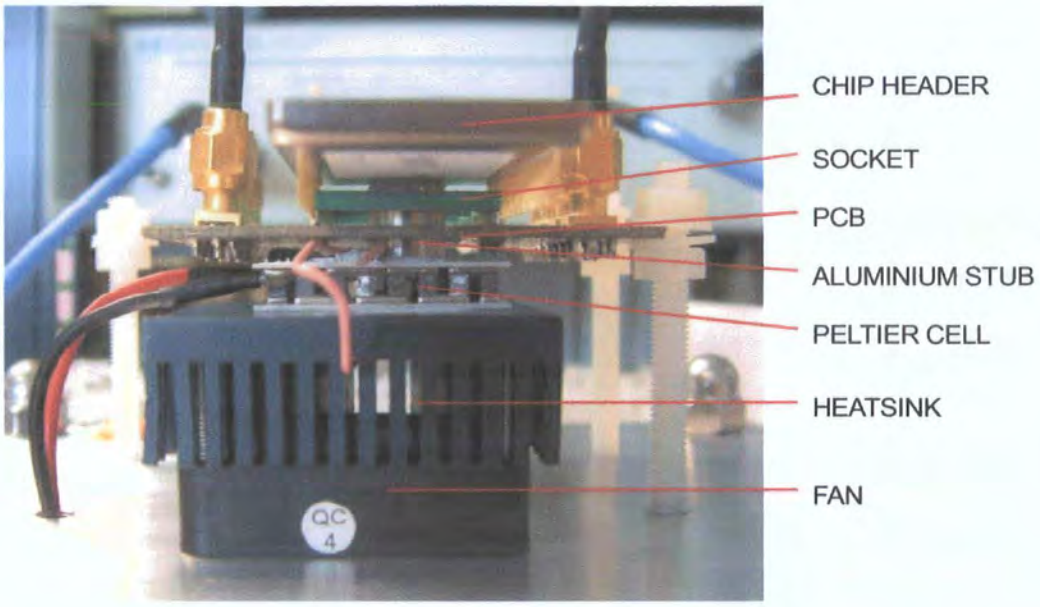

Figure 4-20. Photograph of the temperature control module.

The Peltier cell is powered by a current source switched by the relay output of a digital temperature controller. The control thermocouple is attached to the Peltier cell surface using a clip. A trial using a dummy chip and a second thermocouple is used to calibrate the difference in temperature between the sensor surface and the Peltier cell surface. The difference is negligible around room temperature, and increases at the temperature extremes. Reversing the power supply, and reversing the action of the relay enables cooling of the Peltier cell to below room temperature. Temperatures as low as –2°C are achieved although excessive heat on the lower side of the cell prevent further reductions. The upper temperature limit is approximately 90°C.

5 Device characterisation

The first part of this chapter investigates the physical structure of the devices looking at fabrication defects and their possible influence on device performance. The second section investigates the Love mode formation in different waveguide materials (SiO_2 and polyimide) and thicknesses. The influence of temperature on the device operation is also analysed.

5.1 Physical inspection

The following section presents images and data taken with the SEM and stylus profilometers to evaluate the fabrication techniques and device structure.

5.1.1 Quartz substrate

The natural seed region in quartz substrates contains defects and impurities precluding its use for devices, although the small size means wafer area loss is negligible. However, weaknesses introduced by the defects can cause stress in the wafer, inducing cracking. The seed regions on the wafers used contained many small holes through the entire wafer thickness, visible under optical and electron microscopes. The micrograph in figure 5-1 shows a typical hole about 30 μm across.

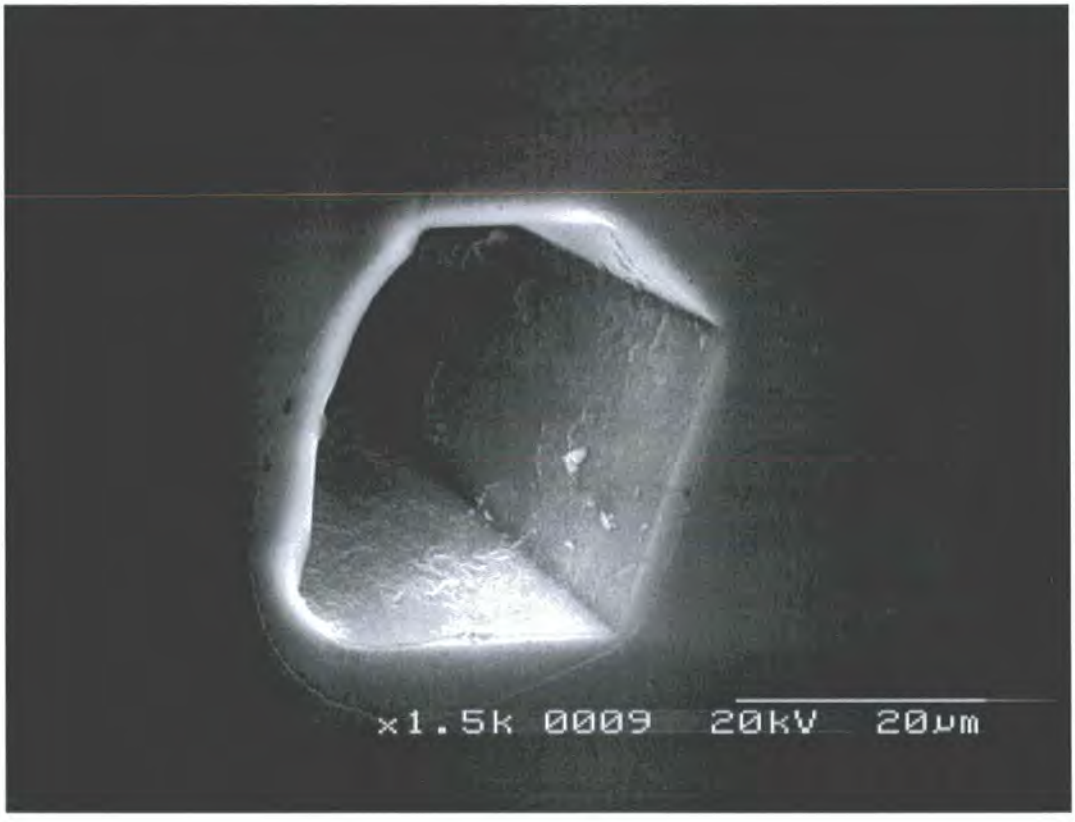

Figure 5-1. Micrograph showing seed crystal hole, with flat crystallographic planes visible. The faint line around the hole edge (passing through "×1.5 k ") is the Al electrode metallisation edge.

Stress cracking during temperature change processes was common, possibly due to holes. One cause was water or solvents remaining in the holes from wet fabrication stages, which expanded when the wafer was placed on a hotplate.

5.1.2 Polyimide waveguide devices

The four micrographs in figures 5-2 to 5-5 show the polyimide waveguide surface topology, with surface corrugations 0.5 μm deep and equal widths and spaces of 2.5 μm.

The corrugation ends in figure 5-2 have a rounded shape due to lithography limits as discussed in chapter 4. Near-vertical sidewalls and sharp external and internal corners resulting from the O_2 RIE are clearly visible, and the trough base is flat with a roughness similar to the un-etched polyimide surface. The peak shown near the right-hand end of the micron measure probably arises from contamination masking the etch process. The vertical ridges on the sidewalls are due to uneven edges in the Au mask arising from lithography limitations.

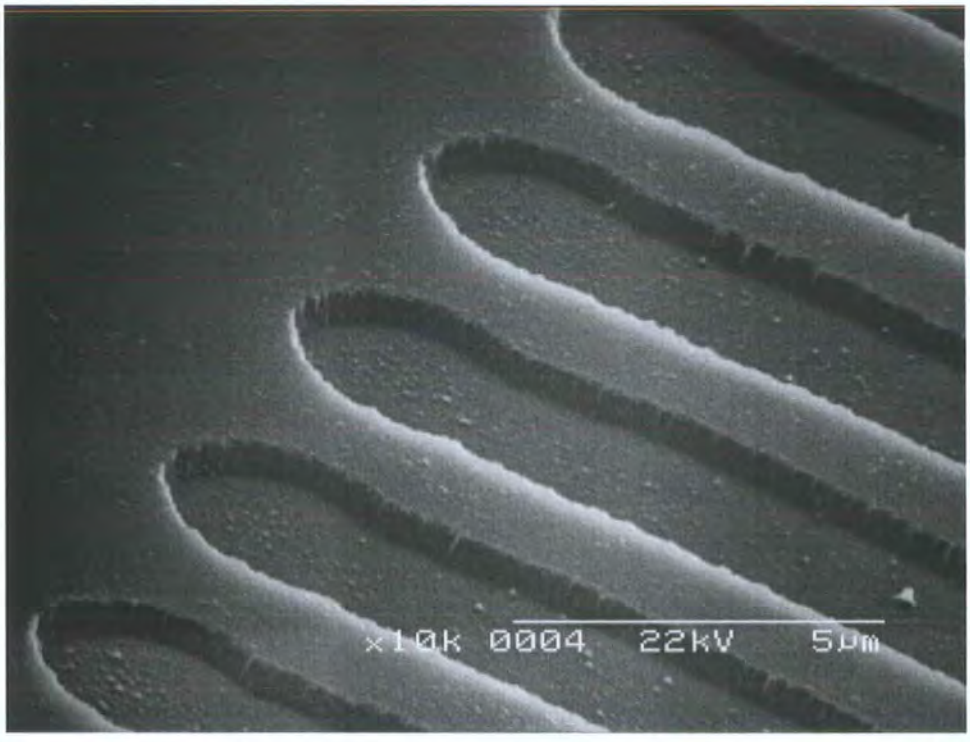

Figure 5-2. End of corrugations etched 0.5 μm into polyimide, showing vertical sidewalls and smooth trough base.

The micrograph in figure 5-3 shows the corrugations 2 mm from the device end. The near-vertical ridged sidewalls are again visible, but the etched area roughness is greater with peak-like structures protruding – some the entire corrugation depth.

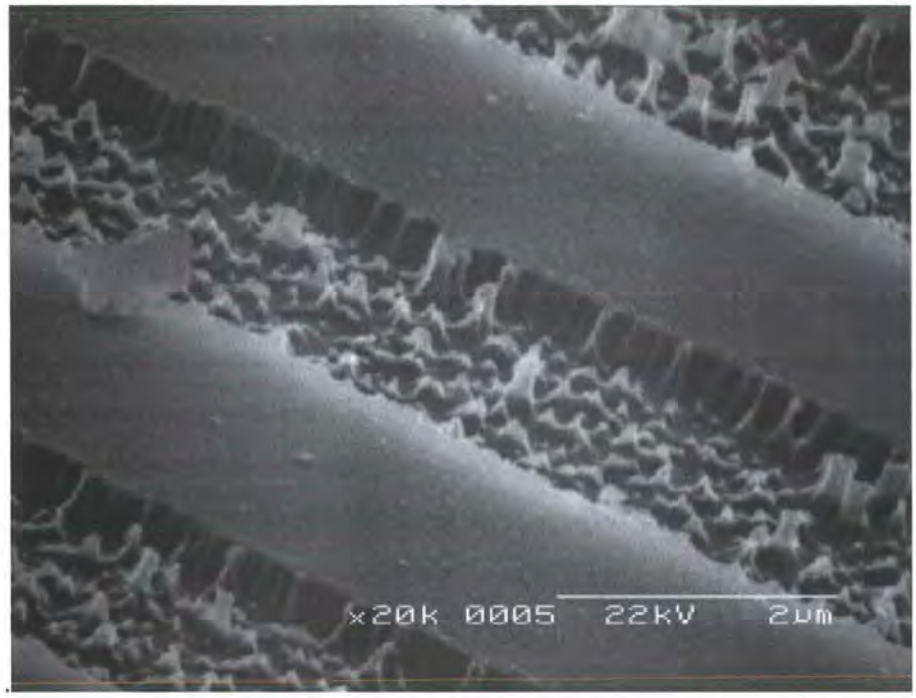

Figure 5-3. View of corrugations 2mm along the device etched 0.5 μm into polyimide, showing increased roughness.

Figures 5-4 and 5-5 show the corrugations halfway along the device with increased roughness filling the troughs with peak-like structures. The lower magnification micrograph (figure 5-5) shows the consistency of the etch roughness with a reduction in the liquid trap volume. The sharp transitions at the sidewalls are still evident.

The surface transition along the device could be due to incomplete photoresist development, the presence of photoresist scum after development, or incomplete Au mask etching, although this is unlikely due to the Au etch strength. The change along corrugations of a single device suggests that development residue is likely, with the development rinse washing the scum from one end (good etching) to the other (poor etching). The increased roughness reduces the liquid trap volume thus resulting in a lower device sensitivity. The creation of non-vertical surfaces could produce compressional waves into the main liquid body, increasing acoustic losses. Removal of the liquid from the traps and subsequent cleaning and drying would also be more difficult.

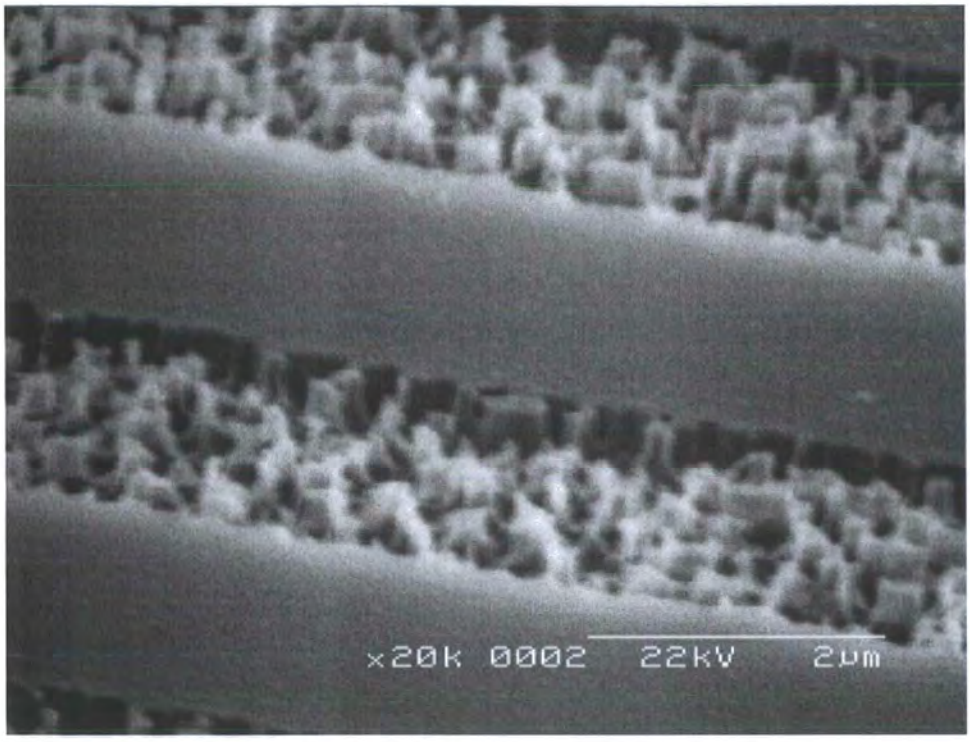

Figure 5-4. View of corrugations half way along the device etched 0.5 µm into polyimide, showing poor etch quality with peak-like structures partially filling the liquid traps.

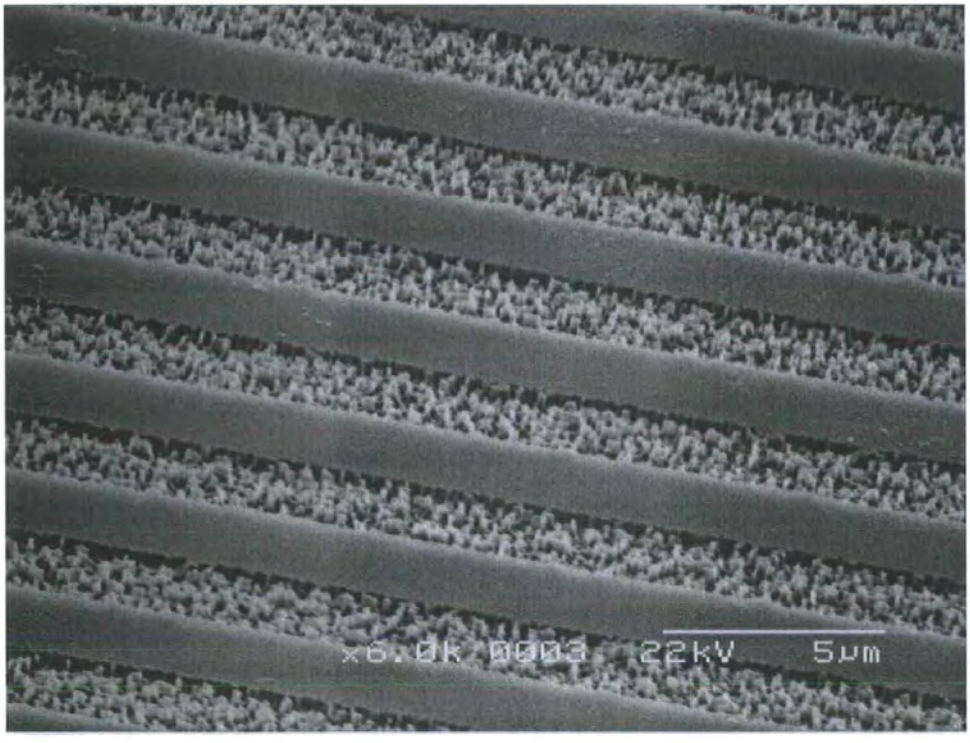

Figure 5-5. Wider view of figure 5-4 showing consistency of the poor etch process. The sharp sidewalls are still evident.

The polyimide waveguide SEM micrographs do not show the underlying IDT fingers, possibly due to the absence of sharp changes in topology. The traces in figure 5-6 show the conformal nature of the polyimide coating over the IDT fingers. They indicate an increase in the surface ridge height of Δh = 0.094 μm at h = 0.69 μm, to Δh = 0.183 μm at h = 1.20 μm, probably due to the higher spin speeds used for the thinner layers having a greater planarising effect. h is the original measured waveguide thickness, and Δh is the change in this height over the IDT finger, the height of the amplitude of the 'ripple'. The horizontal trace scales vary, but a narrowing in peak width for thicker layers is still evident.

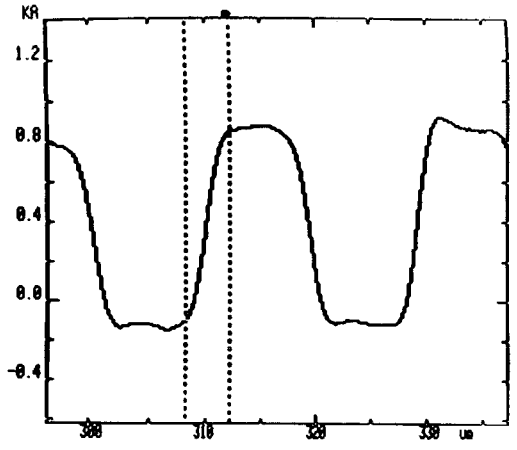

h = 0.69 μm, Δh = 0.094 μm

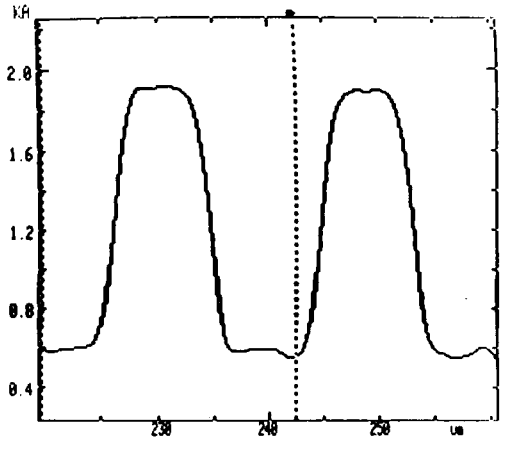

h = 0.80 μm, Δh = 0.133 μm

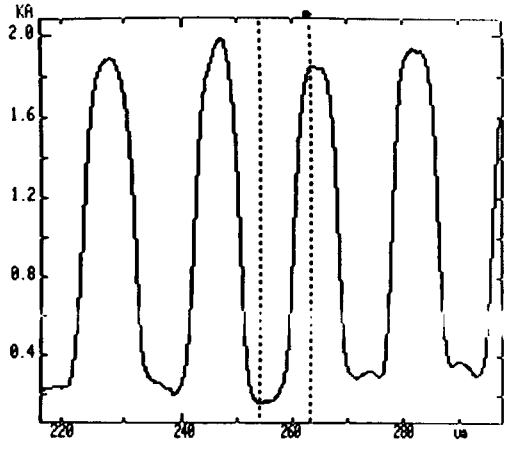

h = 1.07 μm, Δh = 0.169 μm

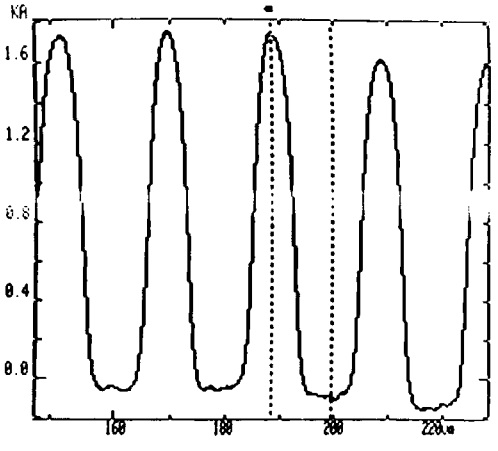

h = 1.20 μm, Δh = 0.183 μm

Figure 5-6. Surface topology of polyimide over IDT fingers measured using an Alphastep profilometer.

5.1.3 SiO_2 waveguide devices

Corrugations etched into SiO_2 waveguide layers are shown in figures 5-7 to 5-9. Figure 5-7 shows uneven corrugations with many defects due to the photoresist pattern lifting from the Au masking layer, sometimes the cause of 'tangled-ribbon' features. Whilst the etched area will remain constant, excessive trough widths could permit liquid entrainment within the traps.

Figure 5-7. Corrugations etched 0.9 µm into SiO_2, with uneven spacing due to poor photoresist adhesion, and undercut sidewalls.

Figure 5-8 shows the sidewall profile with a sharp top edge, but significant under-cutting, possibly due on this sample to over-etching to a depth of about 0.9 µm.

The conformal CVD SiO_2 deposition is evident in figure 5-9 with ridges in the waveguide layer over the underlying IDT fingers. The device shown has troughs 2.5 µm wide with 10 µm spaces. This conformal structure could have implications on the formation of the Love mode due to the periodic change in waveguide thickness. The chequer board double-trough structure could also hinder cleaning processes.

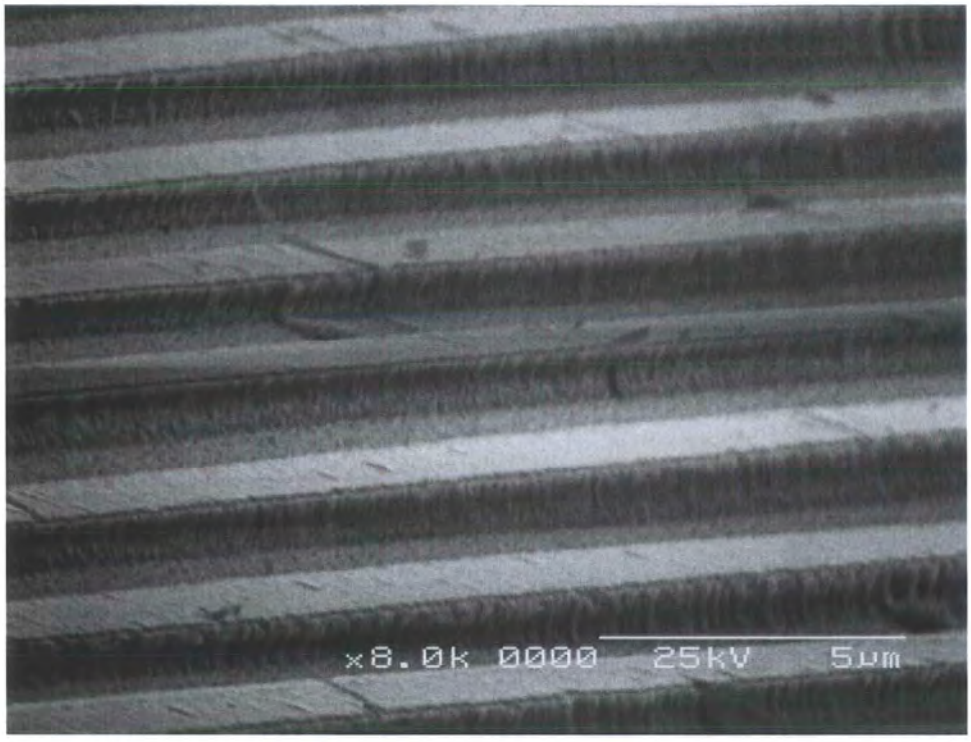

Figure 5-8. Close-up of previous image showing undercut sidewall profile.

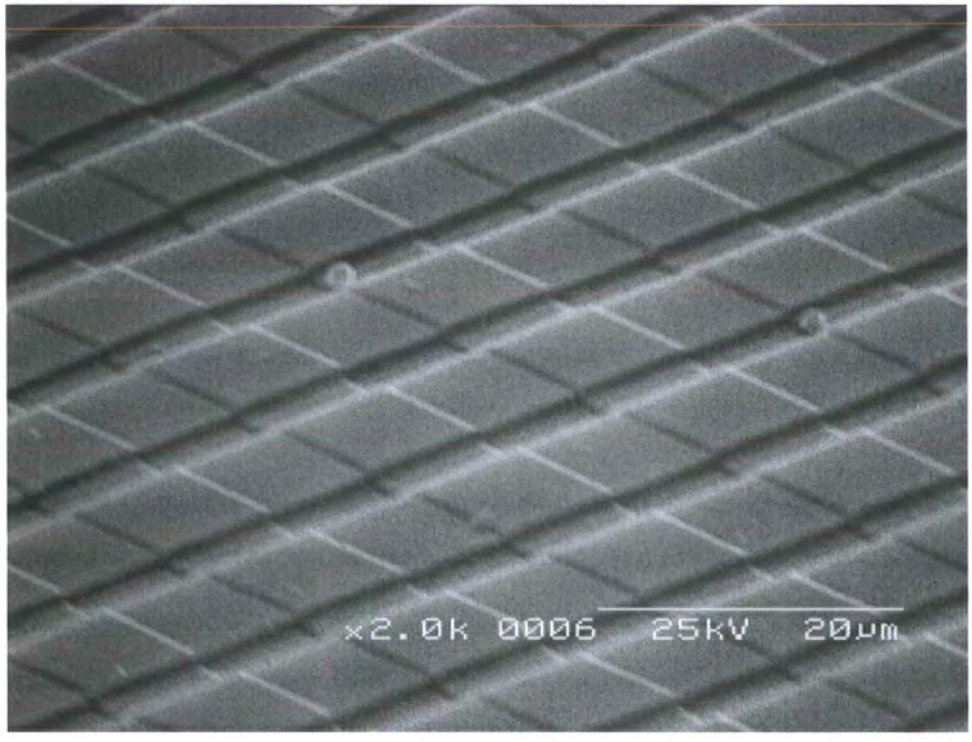

Figure 5-9. Conformal SiO_2 deposition with corrugations (0.5 µm deep) from bottom-left to top-right and the underlying IDT fingers perpendicular.

5.2 Electrical characteristics – uncoated SAW devices

5.2.1 Transducer layout

The first designs consisted of input and output transducers sharing a common grounded busbar allowing a reduction in the number of contacts to 3, or possibly 5 for a dual delay line. All subsequent devices used separate grounded busbars for the input and output transducers, with the driven sides diagonally opposite. A schematic of these two designs is shown in figure 5-10.

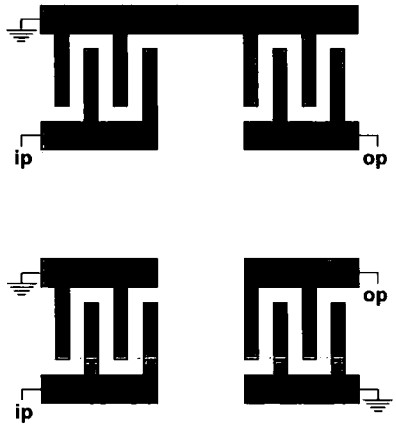

Figure 5-10. Alterative transducer layouts showing a common grounded busbar (top) and separate grounded busbars diagonally opposite (bottom).

The response from the common busbar devices shown in figures 5-12 and 5-13 was poor with no strong resonance. A 7 dB amplitude ripple at 125 MHz indicated SAW behaviour but the background level from 85 dB at 20 kHz to 20 dB at 200 MHz masked the signal. The background frequency response was similar to a high-pass RC filter, with no DC component and almost complete feedthrough approaching 200MHz.

The common busbar enabled direct electrical RF feedthrough of the capacitively coupled input signal to the output transducer. The transducer structure acted as a high-pass RC filter with the connected IDTs forming a series capacitor with a low resistance (the common busbar) to ground (see figure 5-11).

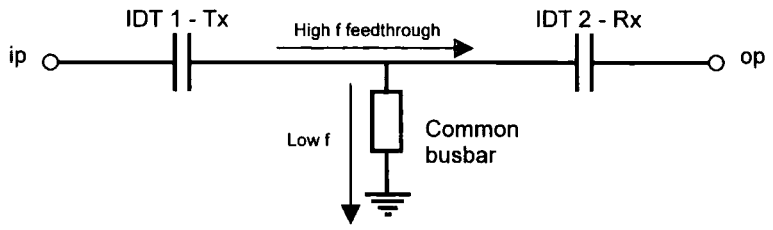

Figure 5-11. Representation of the common busbar IDT structure acting as a high-pass RC filter.

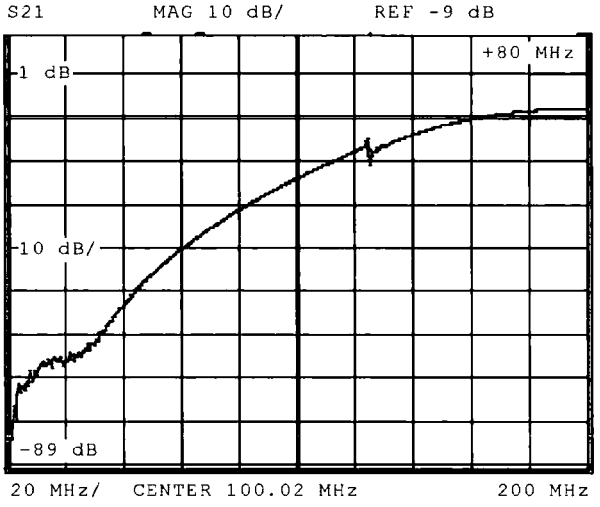

Figure 5-12. Band-pass characteristics of a common busbar delay line. The horizontal scale is 20 MHz / division and the vertical scale 10 dB / division.

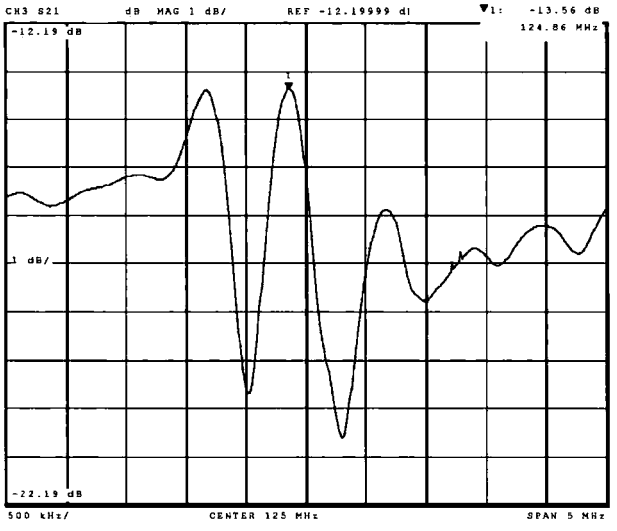

Figure 5-13. SAW ripple (≈ 7 dB amplitude) in a common busbar delay line. The horizontal scale is 500 kHz / division.

Removal of the feedthrough, initially by breaking the busbar with a scalpel, produced a strong SAW peak with 30 dB insertion loss and a lower background of approximately 55 dB. The response in figure 5-14 is from the same device as in figures 5-12 and 5-13 following busbar removal. A strong resonance peak at 124.8 MHz is shown with side lobes partially resulting from the IDT |sinc| response, and also bulk acoustic modes.

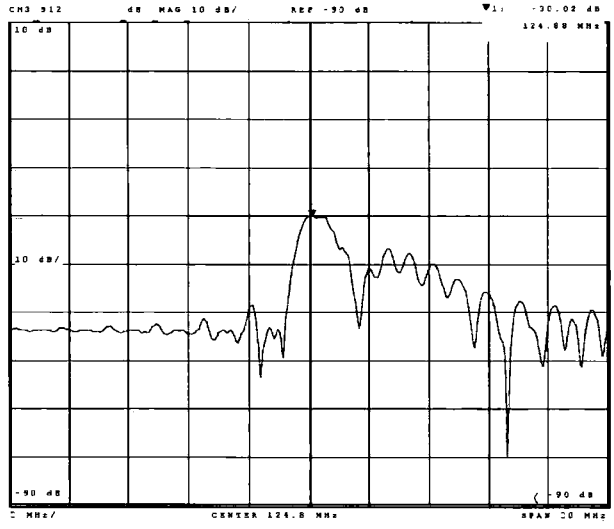

Figure 5-14. Response after common busbar removal, reducing direct RF feedthrough, and preventing RC filter – like behaviour. The horizontal scale is 2 MHz / division and the vertical 10 dB / division.

Following these results all subsequent mask sets used separate input and output IDTs with no common components, and all results presented from now are taken from such devices.

5.2.2 Interdigitated transducer design parameters

The required small sensor size necessitates both compact and efficient transducers for SAW generation. Different designs were fabricated allowing investigation of the number of finger periods in each IDT and the propagation path length between the IDTs. The transducers used in this study consist of single finger uniform IDTs with a metallisation ratio of 0.5. The wavelength is 40 μm giving finger widths and spaces of 10 μm.

Figure 5-15 shows the frequency response from four delay lines on AT-quartz. The IDTs lengths were 40 λ and 80 λ, giving a physical length of 1.6 mm and 3.2 mm

respectively. The propagation paths measured between the inside ends of the IDTs were 20 λ, 40 λ and 80 λ, giving overall delay line physical lengths between 4 mm (40 λ IDTs and 20 λ path) and 9.6 mm (80 λ IDTs and 80 λ path).

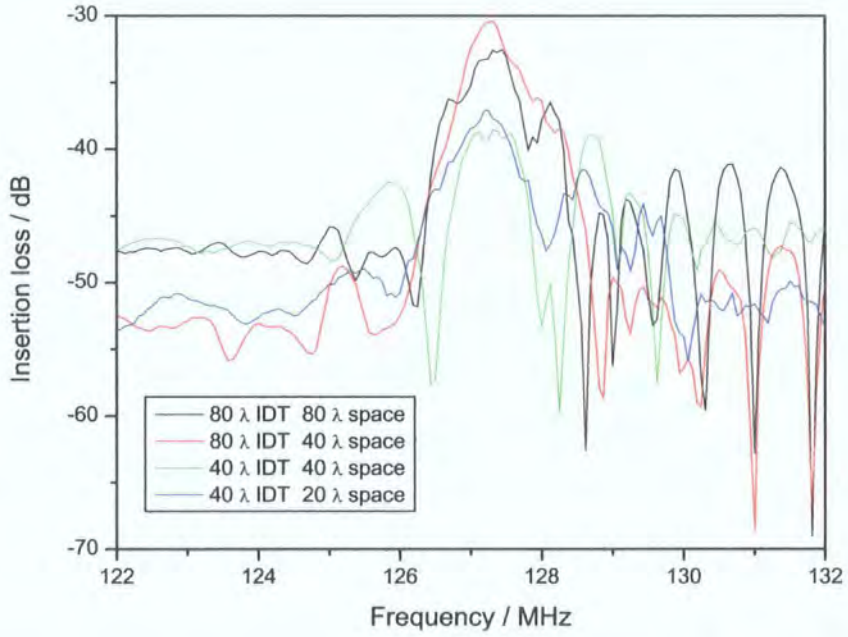

Figure 5-15. Delay line response with varying IDT and propagation path lengths. All devices are on AT-quartz substrates.

The responses show that insertion loss was proportional to the propagation path length, due to acoustic absorption and dispersion in the substrate material. The losses were 0.055 $dB\lambda^{-1}$ for the 80 λ IDT devices and 0.067 $dB\lambda^{-1}$ for the 40 λ IDT devices, giving an average propagation loss of 0.061 $dB\lambda^{-1}$. The number of periods in each IDT was inversely proportional to the insertion loss, with the 40 λ IDT delay line having a loss of 8.1 dB more than the 80 λ IDT delay line with the same propagation path length. The coupling between the transducers and the substrate was thus heavily dependent on the IDT length.

When the samples are confined to the propagation path on a sensor (such as bio-sensors), a relatively large path length is required. The nature of the density sensor operation requires the entire device surface to be loaded, thus the propagation path can be shorter. However, the path must be at least a few wavelengths long to prevent strong capacitive coupling between the input and output IDTs. The large insertion losses

arising from liquid contact make low loss devices a prerequisite. The results presented here thus indicate that both long IDTs (with many fingers) and short propagation paths are necessary. These will fundamentally limit the physical size of the sensor.

5.2.3 Substrate orientation

Love mode devices most commonly use Y-cut AT (36°) and ST (42.75°) quartz orientations as discussed in chapter 3. The lower acoustic losses arising from the increased coupling efficiency of Y-ST makes it the ubiquitous choice for liquid sensors (used in studies by Herman et al [40, 41], Gizeli et al [66, 91], Du et al [72, 85, 86] and Vellekoop et al [77, 78, 82, 83, 92]). Delay lines were fabricated on Y-AT and Y-ST to investigate the orientation effect on propagation. The frequency responses shown in figure 5-16 are from devices with 80 λ IDTs and 40 λ propagation paths.

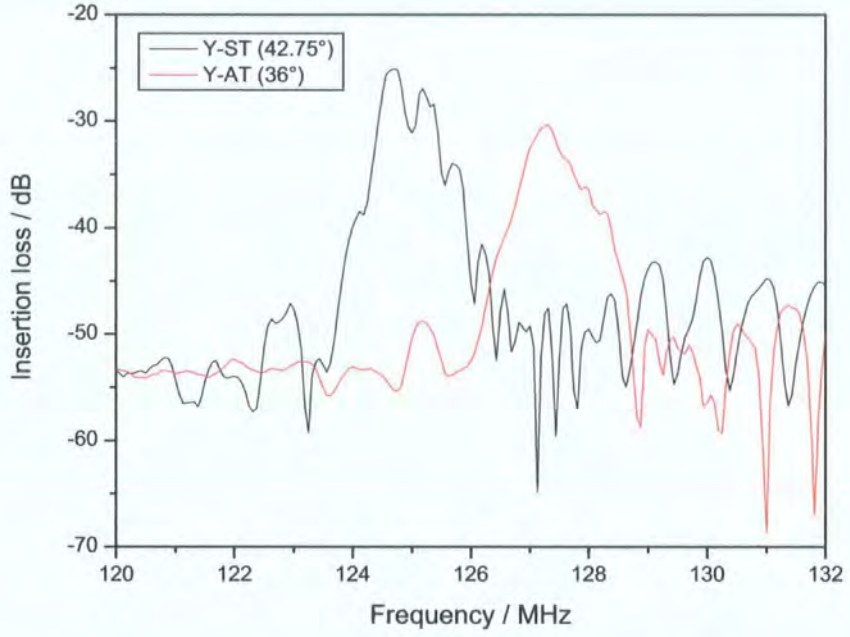

Figure 5-16. Frequency response from Y-AT and Y-ST delay lines with 80 λ IDTs and 40 λ propagation paths.

The piezoelectric and elastic components lying in the surface plane vary with orientation, thus affecting the acoustic velocity, and therefore the resonant frequency. The Y-AT peak frequency around 127.3 MHz was higher than the Y-ST of 124.7 MHz (for the highest peak) due to the increased acoustic velocity. The insertion losses were

also different at 25.08 dB for Y-ST and 30.42 dB for Y-AT, corresponding to an increase in loss for Y-AT of 3.4 times, due to its poorer coupling efficiency. This highlights the suitability of the Y-ST orientation for liquid sensors.

Multiple peaks were exhibited in the Y-ST response separated by about 500 kHz and 2 dB, whilst the Y-AT response consisted of one main peak with ripples in similar positions to the Y-ST multiple peaks. These fluctuations were initially attributed to fabrication defects (broken fingers and shorting) and poor electrical matching, but were later found to arise from reflections within the transducer causing multiple resonances. The interaction is quantified by the complex reflection coefficient of a single finger, r_s, and for Al electrodes on Y-ST quartz, is given by [106]:

$$\frac{r_s}{i} = -0.5\frac{h_m}{\lambda} \tag{5-1}$$

where h_m is the transducer metal thickness and λ the IDT period. For h_m = 150 nm and λ = 40 μm, (r_s / i) = 0.19 %, and so the cumulative reflections in a long IDT could be significant. The effect is stronger for Y-ST due to its higher coupling efficiency.

All devices discussed in this thesis from now on were fabricated on Y-ST quartz unless otherwise stated.

5.3 Polyimide waveguide Love mode characterisation

Love mode formation is dependent on the normalised waveguide thickness, h / λ, as described in chapter 3. A 40 μm transducer period was used for all devices so reference will be made only to the absolute thickness, h, in microns.

Figure 5-17 shows the responses of an uncoated delay line, and a Love mode delay line with a 0.84 μm thick polyimide waveguide. The uncoated device peak frequency was 124.70 MHz at 25 dB insertion loss, giving a substrate acoustic velocity of 4988 ms^{-1}. The uncoated device response was made up from SH-SAW and also SSBW acoustic modes. For thick substrates (assumed for 0.5 mm thick quartz supporting 40 μm λ modes) the continuum of bulk modes produces a broad frequency response typically close to, or within the peak of, the SH-SAW [93]. Interference problems between these modes can occur unless they are separated by more than the bandwidth of the received response at the IDT [88]. SH-SAW and SSBW interferences could cause

the jagged shape on the uncoated response, such as the discontinuities around 122.8 MHz and 124.2 MHz.

The polyimide-coated device response had a lower peak frequency of 123.67 MHz, and a smaller insertion loss around 16 dB. Focussing the acoustic energy into the waveguide reduces absorptive losses into the substrate and dispersion effects, enabling a more efficient energy transfer and thus lower losses. The IDT |sinc| response shape was clear in both results, with a large central lobe and smaller sidelobes.

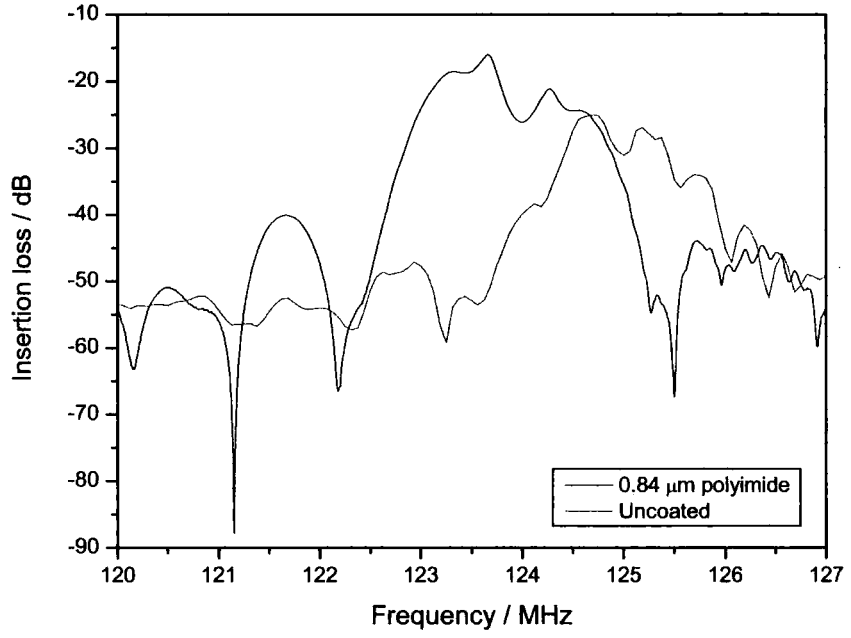

Figure 5-17. Comparison of uncoated SAW and Love mode device responses, showing a reduction in frequency and loss with the addition of a waveguide layer.

The response reproducibility from identical devices with polyimide h = 0.80 μm is shown in figure 5-18. The identically positioned multiple peaks proved that fabrication defects were not responsible. However the slight variation in the device C response could have been due to poor connections to the device or slight variations in the waveguide thickness.

The devices all produced multiple peaks; possible sources of these include poor impedance matching, internal reflections within the IDTs, and crosstalk or RF feedthrough between the IDTs. Impedance matching can be used to reduce the device

insertion loss but can introduce pass-band ripple and decrease the suppression of crosstalk leading to poor sensing capability [88]. Crosstalk ripple effects result from direct RF feedthrough due to capacitive coupling or poor grounding, interfering with the acoustic components. Reflection problems could be reduced by using split-finger IDTs and uni-directional transducers, although these were initially not possible in this study due to lithography constraints, and no experiments were subsequently made with them. Conformal polyimide coating over the IDTs (see section 5.1.2) could also have contributed to the ripples in the Love device response – the surface variations could create a double-thickness waveguide structure.

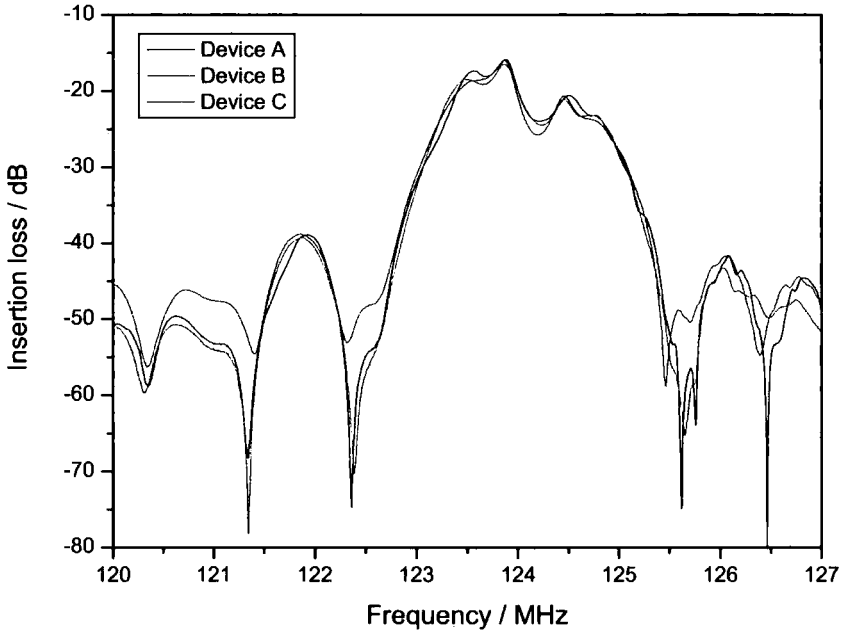

Figure 5-18. Response reproducibility from three identical delay lines with h = 0.80 μm polyimide.

Different polyimide waveguide thicknesses were deposited to investigate the Love mode dispersion characteristics. The results presented in figures 5-19 to 5-23 cover the thickness range h = 0.65 μm to h = 1.20 μm. Thinner layer coating was not possible due to the polyimide's spin-deposition characteristics, and thicker layer devices exhibited no measurable resonance.

Bandpass curves are shown for 6 different thickness polyimide waveguides in figure 5-19. The three thinnest had an insertion loss around 16 dB which increased to about

21.1 dB for h = 1.20 μm. The frequency showed a similar pattern, with a small frequency shift with increasing thickness for the thinner devices, and a larger shift down to 121.4 MHz for the thickest layer. The bandpass shape changed with increasing h, with suppression of the right hand peak increasing from 4.7 dB below the main peak for h = 0.80 μm down to 8.4 dB for h = 1.20 μm. The main peak shape also changed with the minimum insertion loss point moving from the higher to the lower frequency side.

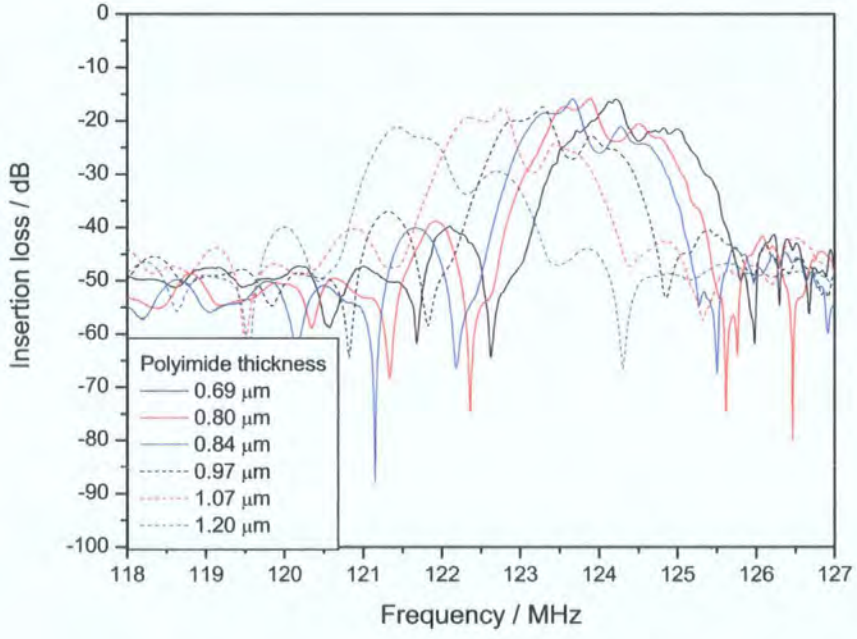

Figure 5-19. Frequency response characteristics for different polyimide waveguide thicknesses.

Peak frequency and insertion loss dependence on waveguide thickness between h = 0.69 and 1.20 μm are shown in figures 5-20 and 5-21 for device set A. These devices were all fabricated in the same batch. The lines of best fit are computer generated and act as a guide.

The peak frequency reduced with increasing waveguide thickness. The gradient was initially low, with only a small frequency shift with increasing h. This suggests a low sensitivity to mass loading. As the waveguide became thicker, the gradient became steeper giving a larger frequency shift for the same increment in h than before. This suggests a higher sensitivity to mass loading. The highest sensitivity will occur where the gradient reaches a maximum, i.e. at the point where (Δf / Δh) is a maximum. From

figure 5-19, this was for devices with h = 1.20 μm, and the trend indicates that the sensitivity will increase further for h > 1.20 μm. The optimum sensitivity will occur at $h = h_{opt}$ given by equation 3-57. Cured PI2545 polyimide has a modulus of elasticity E of 2.3 GPa (manufacturer's data), and a density of 1420 kgm^{-3}, giving a waveguide acoustic velocity $V = \sqrt{(E/\rho)}$ = 1270 ms^{-1}. These values give h_{opt} = 2.55 μm which is greater than the layers tested here. Operation at this thickness is not possible as discussed below, and thus the polyimide Love devices operate in the non-optimum frequency regime.

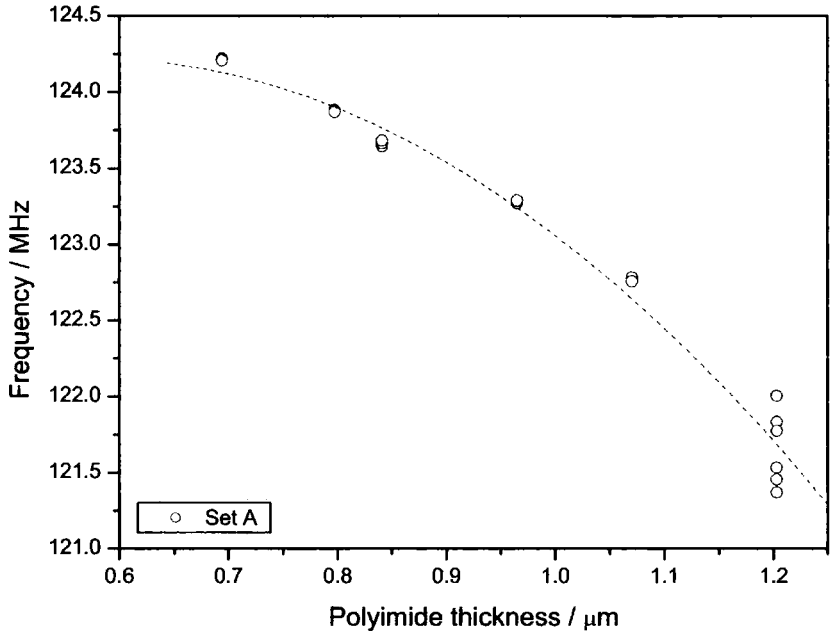

Figure 5-20. Frequency dependence on polyimide waveguide thickness for device set A.

Figure 5-21 shows a reduction in insertion loss with increasing waveguide thickness until a minimum of approximately 16 dB at h = 0.82 μm. This was the optimum thickness in terms of loss, where the Love mode is highly focussed in the waveguide resulting in minimum losses into the substrate and minimum dispersion and absorption in the polyimide. This corresponds to a normalised thickness (h / λ) = 0.021. Further increases in h resulted in dispersion of the acoustic energy throughout the extra waveguide thickness, and a corresponding increase in insertion loss. A considerable variation in frequency and loss data at h = 1.20 μm was due to poor resolution of the

high loss peak. For $h > 1.20$ μm, the insertion losses approached background levels (45 – 50 dB) preventing observation of any resonance.

The insertion loss spread for identical devices of up to 2 dB was possibly due to poor electrical contact or fabrication defects. This illustrates the suitability of frequency as a sensing mechanism: frequency is dependent on the material characteristics and dimensions, whilst insertion loss is also dependent on other non-intrinsic factors.

The results show that optimum frequency sensitivity operation is impossible due to the high insertion losses. Low insertion loss sensors are vital for operation in a liquid environment, due to additional compressional losses into the liquid. A compromise between frequency sensitivity and insertion loss is thus required, by choosing an intermediate waveguide thickness. The optimum region of operation in terms of waveguide thickness for set A was around h = 0.90 to 1.0 μm, giving improved sensitivity and negligible loss increase over the 0.82 μm low loss devices.

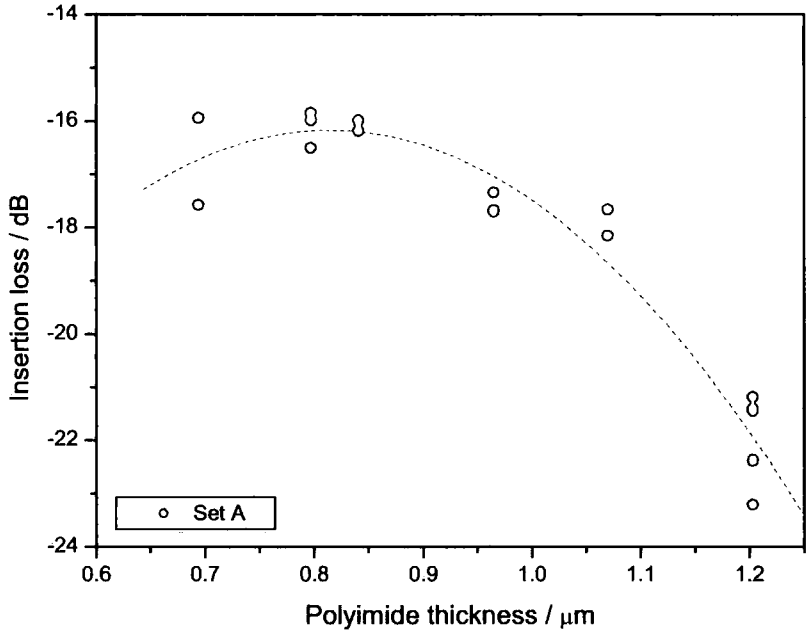

Figure 5-21. Insertion loss dependence on polyimide waveguide thickness for device set A.

The data in figures 5-22 and 5-23 show the response from a second set of devices, set B, compared with the mean results from set A. These measurements were made to check for reproducibility between different batches, and the consistent results suggest this was achieved. Polyimide's physical properties can vary with curing conditions, but

assuming the correct curing procedure is followed, the cured material properties should remain the same regardless of deposition variations. The polyimide was cured to the manufacturer's specifications cumulating in a 1-hour bake at 350°C in N_2, during which any residual solvents are removed. Variations in the solvent content when spin coating (due to incorrect thinner mixing, etc) do not affect the final film properties, just the thickness.

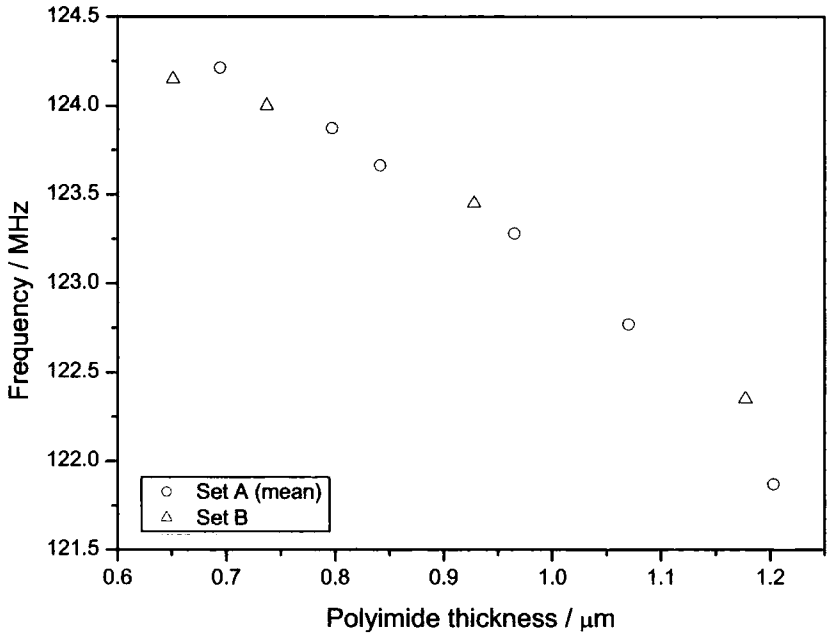

Figure 5-22. Frequency comparison between set A (mean) and set B.

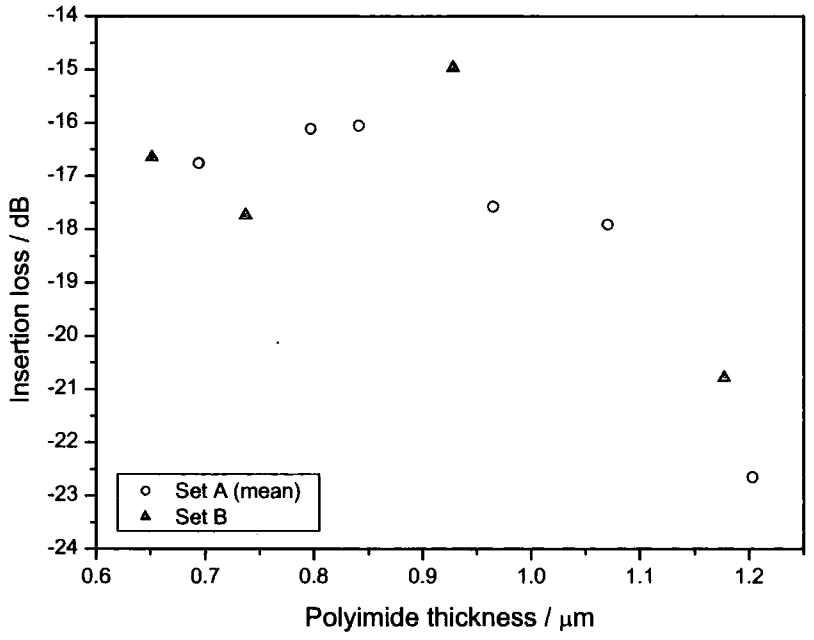

Figure 5-23. Insertion loss comparison between set A (mean) and set B.

5.4 SiO_2 waveguide Love mode characterisation

Single layer PECVD SiO_2 waveguide layers were deposited for comparison with the polyimide devices, with SiO_2 thicknesses of 0.92, 1.61 and 2.35 μm. Devices with h = 3.62 μm were also fabricated, although none of these functioned. The frequency and insertion loss dependence on SiO_2 thickness is shown in figures 5-24 and 5-25, although the poor device yield reduces the number of data points.

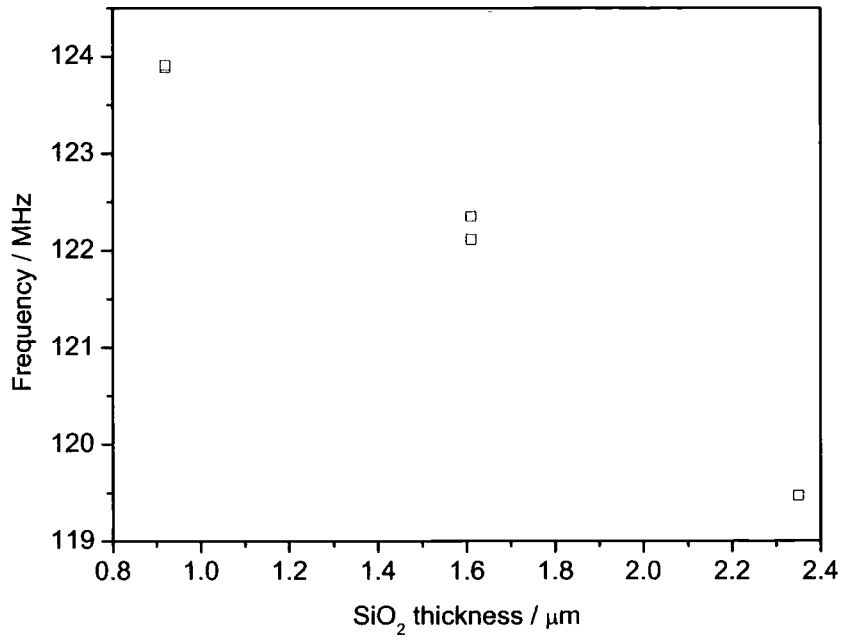

Figure 5-24. Frequency dependence on SiO_2 waveguide thickness. Data is shown for more than one device at each thickness.

The peak frequency decreased with increasing waveguide thickness from about 123.9 MHz at h = 0.92 μm to 119.5 MHz at h = 2.35 μm. Although the data is sparse, the shape suggests a steeper gradient for (Δf / Δh) for h > 2.35 μm, and thus higher sensitivities. The SiO_2 acoustic velocity is $\sqrt{(E/\rho)}$ = 2812ms^{-1} from values of E = 1.74×10^{10} GPa and ρ = 2200 kgm^{-3} [77], and the optimum thickness (in terms of frequency sensitivity) using equation 3-57 is h_{opt} = 5.7 μm. These parameters are typical although CVD SiO_2 properties change with deposition conditions as discussed in section 3.5.7.

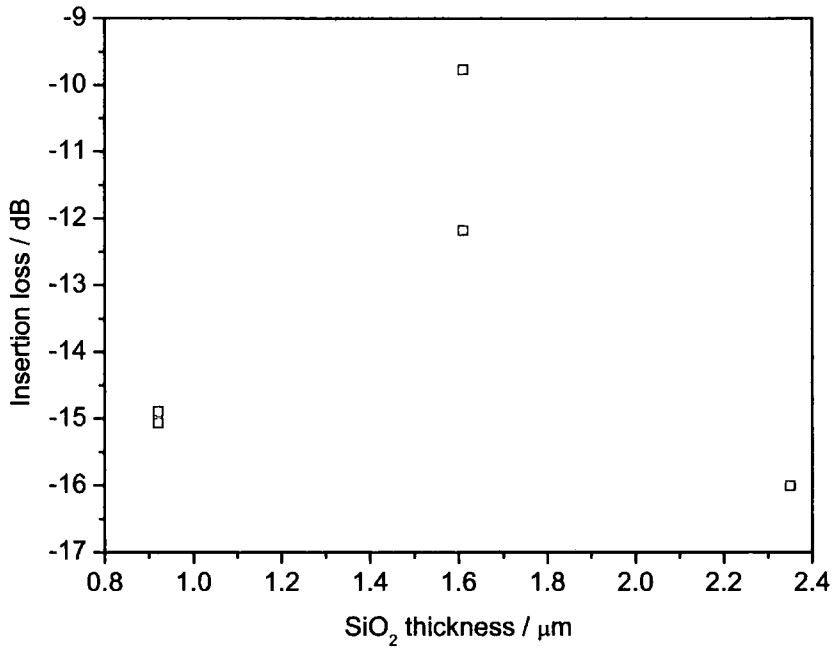

Figure 5-25. Insertion loss dependence on SiO_2 waveguide thickness. Data is shown for more than one device at each thickness.

The minimum insertion loss was 9.8 dB at h = 1.61 μm, suggesting optimum acoustic energy confinement within the SiO_2 waveguide. This value was over 6 dB stronger than for the polyimide waveguides, over 4 times the power output, highlighting the relatively low losses of glassy SiO_2 waveguide devices. The insertion losses were larger for thinner layers at 15 dB for h = 0.92 μm, and for thicker layers at 16 dB for h = 2.35 μm. Thus devices with h < 2.35 μm could offer the same insertion losses as the thinner polyimide devices. This thickness would allow practical operation, and other studies have used SiO_2 with h = 1.46 μm [77] and 2.2 μm [40, 41] for liquid sensors. Thicker layers would operate closer to the optimum sensitivity at h_{opt} = 5.7 μm, but similarly to polyimide, the dominant insertion losses prevent resonance. Deposition of thick CVD SiO_2 layers is also difficult with long deposition times and stressy layers leading to cracking and delamination. A study using sputtered SiO_2 demonstrated waveguide layers up to 7.3 μm thick, and shows the optimum experimental sensitivity to occur around h = 5.5 μm, but with intrinsic losses around 20 dB [72].

The SiO_2 waveguide device responses exhibited multiple peaks as shown in figure 5-26. The two strongest peaks were separated by 0.63 MHz and 4.5 dB, with a central 10 dB dip, and the higher-frequency peak to the right is suppressed by 6.7 dB. This response could be a result of reflections in the IDTs, which are stronger than in the polyimide due to higher reflectivity with lower acoustic absorption.

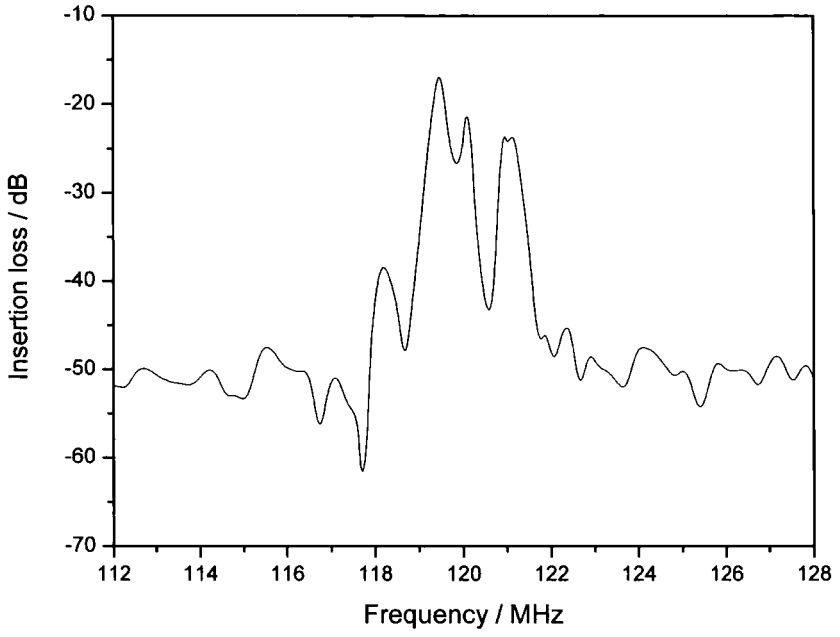

Figure 5-26. Typical response from a SiO_2 waveguide Love mode device, with $h = 2.35$ μm.

5.5 Multilayer waveguide Love mode characterisation

Multilayer waveguide structures combining the merits of different material properties were discussed in section 3.5.7, with table 3-3 giving the relative material properties.

Multilayer waveguide devices using a PECVD SiO_2 base layer and polyimide upper layer were fabricated to investigate the hybrid structure. The devices were smooth, and incorporated various material thickness combinations with h = 0.92 to 3.62 μm SiO_2 and h = 0.70 to 1.15 μm polyimide. Fabrication problems resulted in low yields without all the thickness permutations. Figures 5-27 and 5-28 show the frequency and insertion

loss dependence on waveguide material thickness. The horizontal axis denotes the polyimide thickness, and the SiO_2 thickness is defined by the data sets.

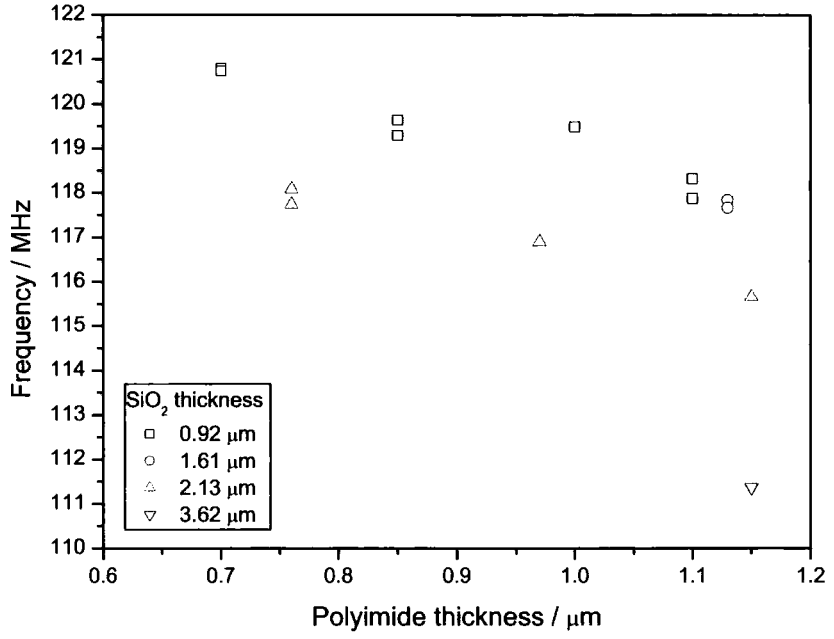

Figure 5-27. Frequency dependence on polyimide thickness (horizontal axis) and SiO_2 thickness (data sets) for multilayer devices.

The frequency decreased with increasing polyimide thickness similarly to the single layer polyimide devices (figure 5-20), and there was an additional frequency drop with increasing SiO_2 thickness. A linear interpolation of the 0.92 and 2.13 μm SiO_2 data for polyimide $h < 1.0$ μm gives a change in frequency per micron waveguide thickness of 6.78 MHz μm^{-1} for polyimide and 1.85 MHz μm^{-1} for SiO_2. This is due to stronger acoustic confinement in the polyimide and thus higher sensitivity to additional mass loading.

The insertion losses become larger with increasing polyimide thickness as shown in figure 5-28. The lowest losses are exhibited by the $h = 2.13$ μm SiO_2 devices although the limited data makes this difficult to confirm. There are no loss minima evident in the polyimide thickness range, suggesting that thinner polyimide layers are required, or that the limited data prevents observation. The results may also contain material thickness errors, due to difficulties in separating the step heights of the SiO_2 and polyimide using a stylus profilometer.

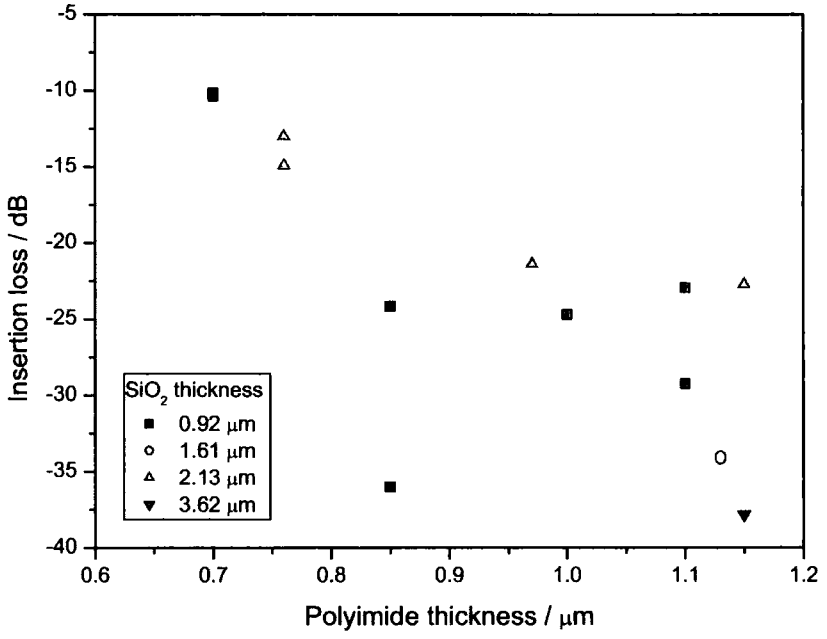

Figure 5-28. Insertion loss dependence on polyimide thickness (horizontal axis) and SiO_2 thickness (data sets) for multilayer devices.

The low intrinsic insertion losses combined with the use of a polyimide upper layer was the primary reason for investigating the multilayer structure. The 10 dB loss of the 0.92 μm SiO_2 / 0.70 μm polyimide device was a large improvement on the higher loss single layer polyimide devices, due to the partial confinement of the acoustic energy in the low loss SiO_2 layer.

5.6 Temperature dependence

Temperature independence of a crystal oscillator is important to maintain a constant and accurate resonance frequency. For example, a wristwatch quartz oscillator needs to operate at a constant frequency in temperatures which may be as low as –40°C for an Arctic explorer to +50°C for someone in direct sunlight. A cheap crystal oscillator will exhibit some variation in frequency with temperature (especially at the temperature extremes), but in standard operating conditions (cooler at night when the watch is removed, and warmer when worn during the day), the fluctuations will cancel out.

Temperature independent operation of a sensor is desirable for field use where sophisticated temperature control is not available or possible, and reduces the need for calibration. The Index Instruments refractometers incorporate sophisticated temperature control to enable RI measurements at specific temperatures. Temperature stability is therefore not a problem, but operation over a range of temperatures is necessary, requiring either temperature independence, or calibration.

The frequency dependence on temperature for a crystal oscillator is described by the temperature coefficients of frequency (TCFs). The response for SSBWs is parabolic and follows the following relation [59]:

$$\frac{\Delta f}{f_0} = TCF_1(T - T_0) + TCF_2(T - T_0)^2 \qquad (5\text{-}2)$$

Temperature independence about the central operating temperature T_0 can be achieved through choosing a cut where $TCF_1 = 0$, thus operating at the turning point, known as the turn over temperature (TOT). Standard crystal orientations are designed such that the TOT matches the required T_0 for the desired mode of oscillation, for example 25°C for a wristwatch oscillator.

5.6.1 Substrate temperature dependence

Y-AT and Y-ST orientations were developed as zero temperature coefficient substrates for Rayleigh wave (Y-AT) and bulk wave (Y-ST) oscillators. However the addition of surface waveguide layers changes their temperature dependence. Theoretical and experimental studies using various substrate rotations and different SiO_2 waveguide thicknesses found no solutions for a zero TCF using Y-ST quartz, and

only as $h / \lambda \rightarrow 0$ for Y-AT [60, 94]. Using a custom lower angle cut of Y-31°, a zero TCF was demonstrated for $h / \lambda \approx 0.11$ allowing near-optimum waveguide thickness [60]. Similar results have been demonstrated by Herrmann et al [59] using Y-30° quartz with a TOT occurring at 25°C for a waveguide thickness of $h / \lambda \approx 0.095$. Other experimental results show a change in TCF of 27 – 31 ppm°C^{-1}, with an increase in the TCF with increasing film thickness [72]. However the use of smaller angle orientations reduces the coupling efficiency giving larger insertion losses, a disadvantage for liquid sensors.

The frequency – temperature dependence is shown for uncoated Y-AT and Y-ST devices in figure 5-29. The Y-ST devices exhibited a linear temperature dependence in the range measured, with a frequency shift f-f_0 between –37.5 kHz and +206.9 kHz, giving a TCF of 27.6 ppm°C^{-1}. The Y-AT temperature dependence was more complex with a maximum around 15 – 20°C indicating a zero TCF around room temperature as expected. The Y-AT results show that temperature independent operation is almost possible between 12 and 30°C with a frequency change of only 0.04 ppm°C^{-1}. These results however are only valid for uncoated devices and not Love modes.

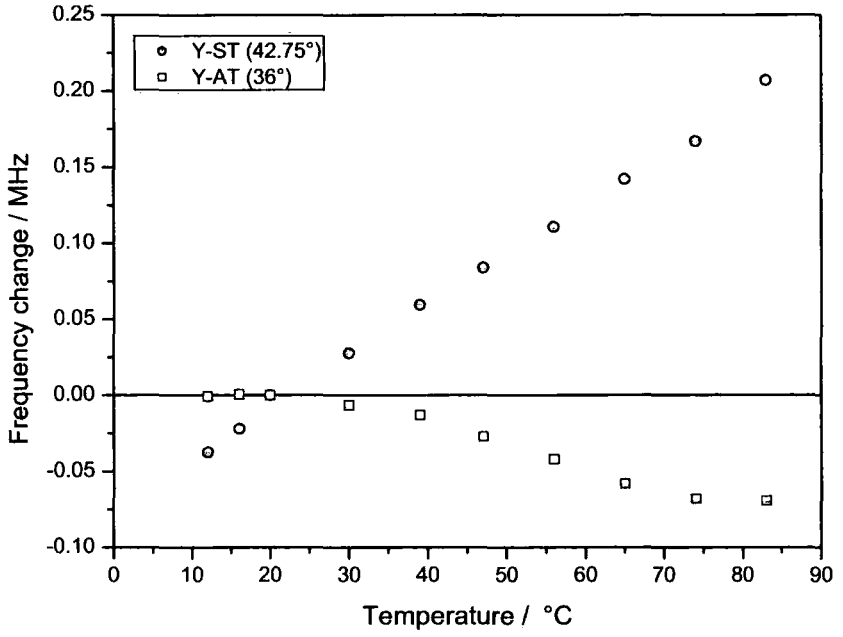

Figure 5-29. Frequency temperature dependence for Y-AT and Y-ST uncoated devices.

The insertion loss temperature dependence was similar for the two substrates as shown in figure 5-30. The Y-AT response was around 5 dB lower than for Y-ST due to the reduced coupling efficiency. Over the temperature range, the Y-ST device loss increased by 1 dB and the Y-AT increased by 0.7 dB. The low gradient around 20°C for the Y-AT device was due to the zero TCF in this region. The maxima at 20°C for the Y-ST device was probably due to the formation of condensation on the device surface (the measurements for Y-ST were started from cold) causing mass loading.

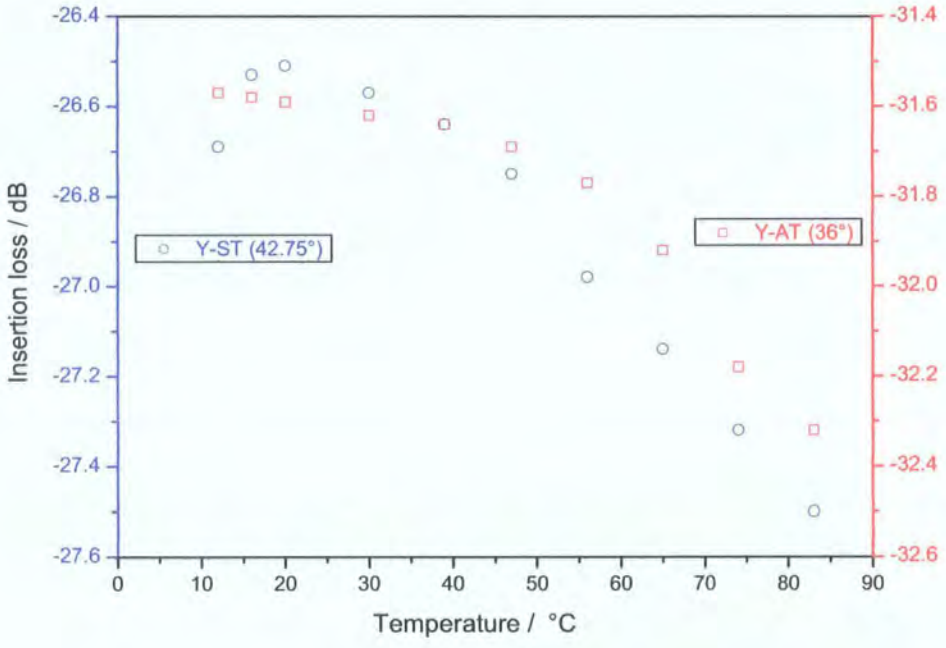

Figure 5-30. Insertion loss temperature dependence for Y-AT and Y-ST uncoated devices.

5.6.2 Waveguide temperature dependence

Figure 5-31 shows the measured responses from Y-ST Love mode devices for five different polyimide thicknesses, with the uncoated Y-ST device results shown for comparison. The thinnest polyimide waveguide device (h = 0.69 μm) had a similar temperature dependence to the Y-ST uncoated device of 30.3 ppm°C^{-1}. The change in gradient suggests a maximum (and thus TOT) at a higher temperature than tested. With an increase in h, the TCF reduced resulting in almost temperature independence for the h = 0.90 μm device, indicating operation near the TOT. Further increases in h resulted

in the TCF becoming negative and larger, giving a frequency reduction with temperature rise. For h = 1.07 μm, the TCF was –21.6 ppm°C^{-1}, a reduction in gradient at the lower temperatures suggesting the TOT maximum occurs for a lower temperature than tested. The TCF increased to –52.5 ppm°C^{-1} for h = 1.2 μm, exhibiting no gradient reduction except for the 8°C data point due to surface condensation.

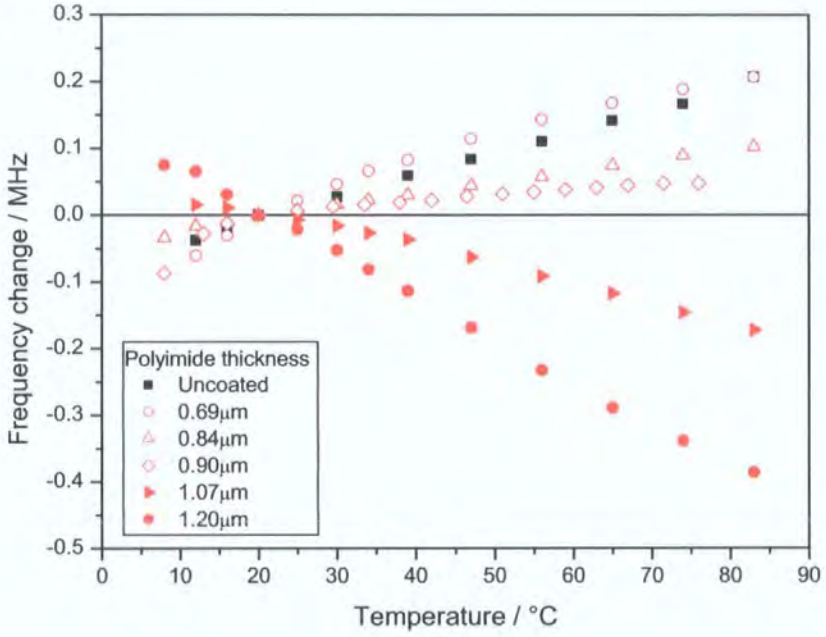

Figure 5-31. Love mode frequency temperature dependence for different polyimide thicknesses on Y-ST substrates.

The TCF values shown plotted against h in figure 5-32 are based on a linear data fits ignoring changes at the temperature extremes. The computer generated line of best fit is given to act as a guide. The reduction in TCF with increasing polyimide thickness is clear, with the best-fit line predicting a TCF = 0 for h = 0.95 μm. This highly significant result shows that temperature independent Love mode devices can be fabricated, using polyimide waveguide layers on standard quartz substrate orientations. Previous studies into Love mode temperature dependence, primarily studying SiO_2 waveguides, had shown that TCF = 0 is not possible using ST quartz, and so these results show a fundamental advantage with polyimide waveguides.

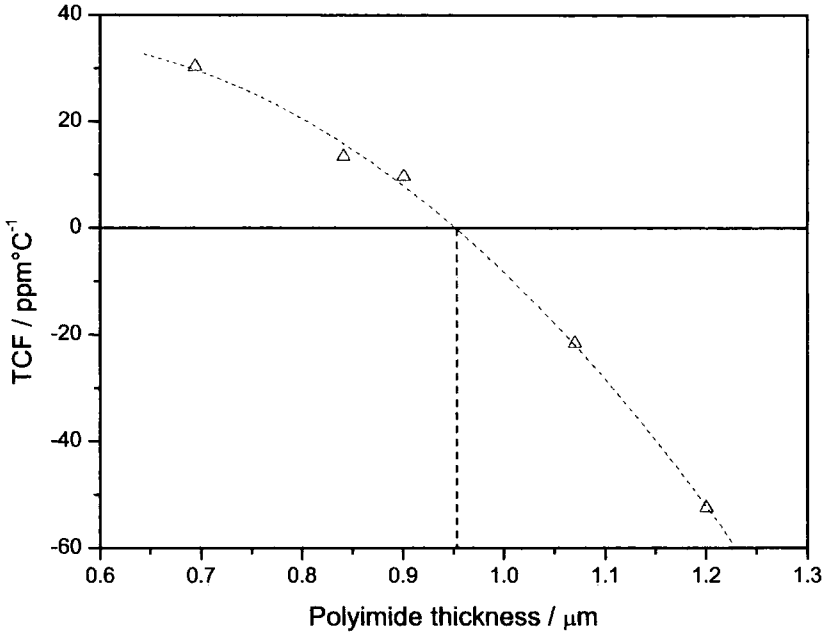

Figure 5-32. Love mode temperature coefficient of frequency (TCF) dependence on polyimide waveguide thickness.

5.6.3 Surface topology temperature dependence

The temperature responses from Love mode smooth and corrugated delay lines are shown in figure 5-33 for polyimide of h = 0.90 μm and 0.5 μm deep with corrugations 2.5 μm wide 20 μm spaced. Linear frequency changes give TCF values of 6.8 ppm°C^{-1} and 12.8 ppm°C^{-1} for the smooth and corrugated surfaces respectively.

Waveguide surface patterning clearly affects the temperature dependence, with a doubling of frequency shift shown for the corrugated device over the smooth device. This was also demonstrated by Herrmann et al where more heavily corrugated SiO_2 Love mode devices gave a larger frequency shift with increasing temperature than less corrugated devices [40]. The partial surface etching possibly reduces the effective waveguide thickness as seen by the acoustic wave. For example, the surface fraction etched 0.5 μm deep in the devices presented in figure 5-33 was 11.1%, giving an effective etch depth of 0.111 × 0.5 μm = 0.056 μm, and making the effective polyimide thickness h_{eff} = 0.85 μm. The corrugated TCF of 12.8 ppm°C^{-1} is similar to the smooth h = 0.84 μm device TCF in figure 5-31 of 13.5 ppm°C^{-1}, supporting this theory.

Similarly the 11.1 % corrugated device's peak frequency was 200 kHz higher than its smooth counterpart, and from figure 5-20 this again gives the h = 0.90 μm corrugated device the same frequency as a h = 0.84 μm smooth device.

The sharp frequency reduction at the lower temperatures was caused by surface condensation. The larger reduction for the corrugated device was due to the larger waveguide surface area and mass loading in the liquid traps in addition to the smooth device's viscous loading.

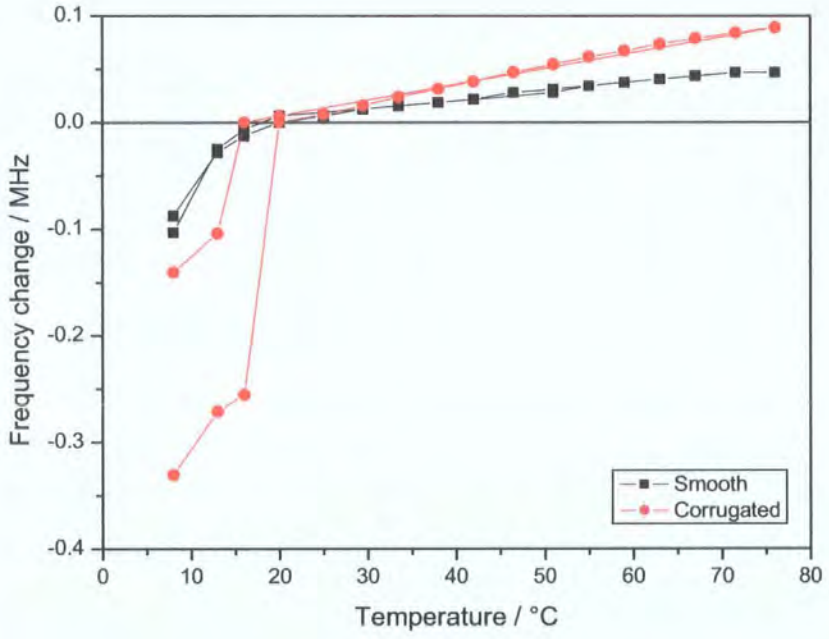

Figure 5-33. Smooth and corrugated surface temperature dependence for polyimide h = 0.90 μm on Y-ST substrates. Data is plotted for temperature ramp up and ramp down. The corrugations are 0.5 μm deep, 2.5 μm wide, and spaced by 20 μm.

5.7 Summary

SEM analysis showed that O_2 reactive ion etching produced vertical sidewall corrugations in polyimide with sharp internal and external corners. The etch quality was variable, with smooth trough bases in some regions and very rough surfaces in others, probably due to incomplete removal of development residue. The spin coating of the polyimide resulted in conformal coating producing surface ripples over IDTs of

Δh = 0.094 μm at h = 0.694 μm, to Δh = 0.183 μm at h = 1.20 μm. This may have an effect on the Love mode characteristics, and could make sample removal and surface cleaning difficult. The SiO_2 corrugations showed smooth bases with sharply defined corners, but the deeper corrugations exhibited sidewall undercutting due to etch anisotropy in the relatively low-vacuum RIE system. Conformal coating was again present over the IDTs.

The uncoated devices had peak frequencies and insertion losses of 127.3 MHz and 30.42 dB for Y-AT quartz, and 124.3 MHz and 25.08 dB for Y-ST quartz, highlighting the increased coupling efficiency with Y-ST and the resultant lower losses. Multiple peaks were present on all devices probably due to reflections within the IDTs.

The Y-AT substrate exhibited near-temperature independence of 0.04 ppm°C^{-1}, with a larger value of 27.6 ppm°C^{-1} for Y-ST. The temperature measurements from the polyimide Love mode devices showed that a zero temperature coefficient of frequency could be achieved with polyimide layers 0.95 μm thick. This is a significant advantage for polyimide waveguides with other studies showing that a zero TCF is unobtainable using SiO_2 waveguides whilst maintaining adequate coupling efficiency substrate orientations.

Deposition of a polyimide waveguide layer reduced the peak frequency and insertion losses due to focusing of the acoustic energy. The lowest loss devices had an insertion loss of 16 dB at h = 0.82 μm, and an increase in sensitivity (Δf / Δh) with increasing thickness. The optimum theoretical thickness h_{opt} = 2.55 μm was unachievable due to dominant insertion losses, and a practical optimum thickness of h = 0.90 to 1.0 μm was chosen for its combination of relatively low loss and high sensitivity. Multiple device batches showed the reproducibility of the polyimide deposition and curing, allowing identical material properties to be achieved.

Data taken from SiO_2 waveguide devices showed a change in frequency from 123.9 MHz at h = 0.92 μm to 119.5 MHz at h = 2.35 μm with a corresponding increase in (Δf / Δh). The insertion losses were lower than for polyimide, allowing operation with thicker layers closer to optimum thickness of h_{opt} = 5.7 μm. The minimum insertion loss was 9.8 dB at h = 1.61 μm, an approximately 6 dB improvement over polyimide devices. The poor device yield with thicker layers showed the possible

susceptibility of the Love mode formation to cracks and pinholes in the layer, with deposition of thick layers difficult due to defects and stress.

A minimum multilayer insertion loss of 10 dB for 0.92 μm SiO_2 and 0.70 μm polyimide was demonstrated, whilst retaining a similar (Δf / Δh) to the single layer polyimide devices. This demonstrates that partial confinement of the acoustic energy to the lower loss of SiO_2 layer reduces the overall insertion loss, allowing operation with thicker polyimide layers closer to the optimum sensitivity thickness.

6 Results and analysis of liquid sensing

This chapter presents and analyses the results from testing the devices with different liquid samples. The results are divided into different types of samples and different device sets. The significance of the high sensitivities to liquid loading obtained from polyimide waveguide layers is discussed with a view to practical use in liquid sensors. Finally the merits and limitations of the highly sensitive liquid density response are analysed.

6.1 Sensitivity

The device sensitivities were measured using DI water and IPA. Figures 6-1 and 6-2 (DI water and IPA) show the results for smooth single layer polyimide, single layer SiO_2, and multilayer devices, to compare the different structures. The waveguide thickness describes the total combined thickness for the multilayer devices, but the data is separated for each different base-layer SiO_2 thickness. The data clearly illustrate the effect of the waveguide structure and materials on the sensitivity. The results for DI water and IPA samples are similar, and the following general discussion is based on both.

The polyimide devices show highest sensitivity, and operate with the thinnest waveguide layers due to the high acoustic energy density at the film surface. Typical relative frequency shifts ($\Delta f / f$) were -0.5 – -2.0×10^{-3}, corresponding to absolute shifts of 63 – 250 kHz, with the sensitivity increasing with film thickness as discussed later.

The SiO_2 single layer devices exhibited smaller ($\Delta f / f$) of around -0.5 – -1.0×10^{-3} (63 – 125 kHz). There was no significant sensitivity variation with film thickness, and with an theoretical optimum waveguide thickness $h_{opt} \approx 6$ μm, these devices were all operating below the optimum sensitivity, where ($\Delta f / \Delta h$) is small.

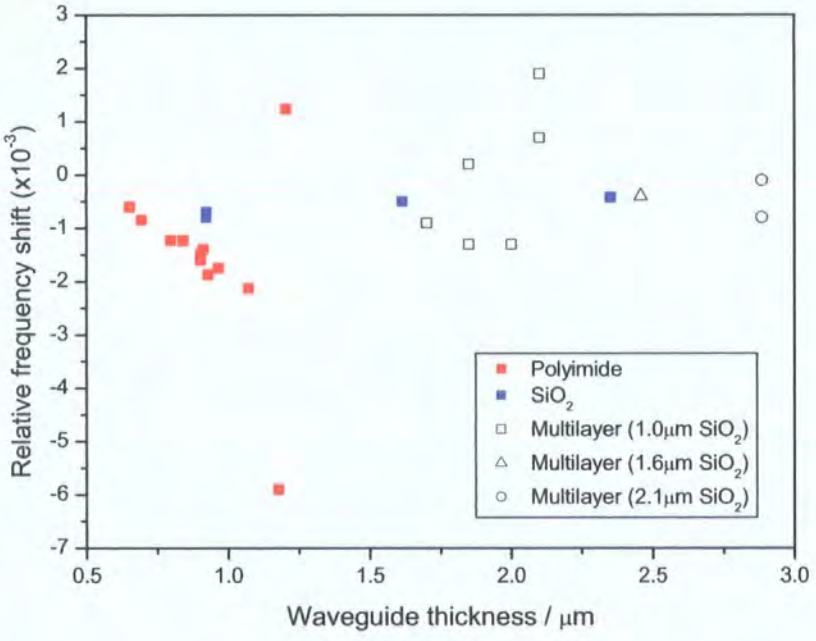

Figure 6-1. DI water sensitivity for single layer polyimide, SiO_2 and multilayer smooth waveguide devices.

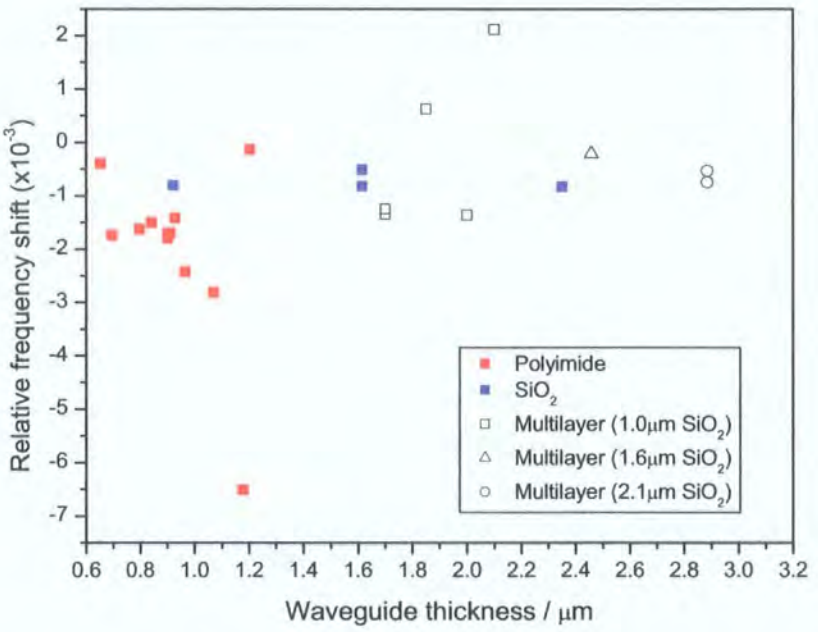

Figure 6-2. IPA sensitivity for single layer polyimide, SiO_2 and multilayer smooth waveguide devices.

The multilayer results show no patterns, and have sensitivities giving (Δf / f) of between -1.5 and +2.0×10^{-3}. The positive (Δf / f) was due to excessive insertion losses reducing the resonance peak to background levels, masking the resonance signal and making discrimination from background fluctuations difficult.

Liquid sensors ideally require high frequency sensitivity and low additional insertion losses, ΔIL, with liquid contact. Figure 6-3 shows the relation between (Δf / f) and ΔIL for the smooth devices with DI water and IPA samples. The polyimide devices had the largest sensitivity range, and generally gave relatively low additional losses, positioning them towards the top-right corner of the plot. DI water samples incurred smaller losses than IPA. The SiO_2 and multilayer devices gave relatively low sensitivities and higher ΔIL positioning them towards the bottom-left corner of the plot. The additional attenuation was around 12 dB and 14.5 dB for SiO_2 with IPA and water samples, and larger for the multilayer devices with IPA giving the largest ΔIL. It is important to remember that these results do not represent the optimum sensitivity conditions, but rather the practically measurable conditions, using a compromise between frequency and insertion loss when choosing the waveguide thickness.

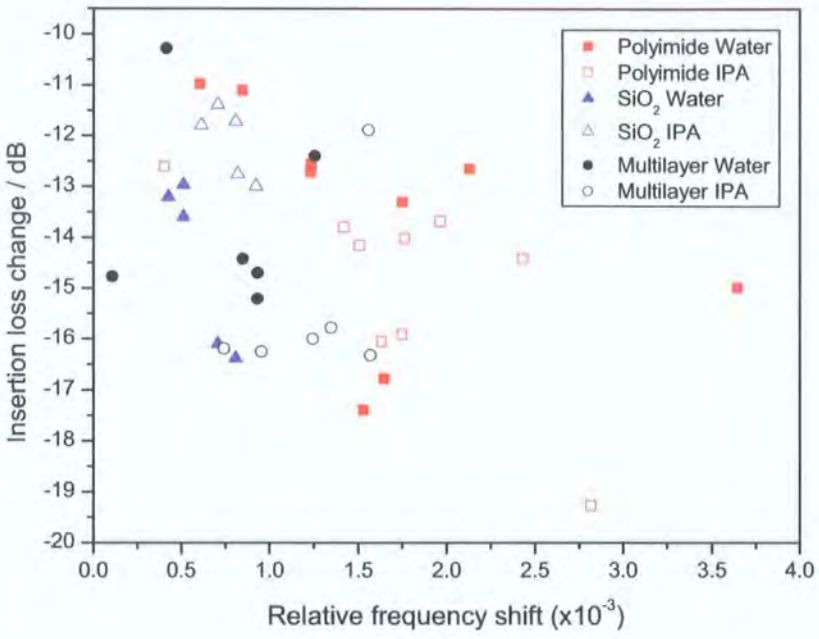

Figure 6-3. Frequency shift versus insertion loss change for DI water and IPA samples on smooth single layer polyimide and SiO_2, and multilayer waveguide devices.

The results indicate that polyimide waveguides are suitable for Love mode liquid sensors, giving higher sensitivities than SiO_2 and the multilayer structures in the measured range. Whilst having higher intrinsic insertion losses than SiO_2 and the multilayer structures, the additional losses with liquid loading are smaller, probably due to the acoustic energy's low dispersion within the waveguide, and close coupling to the substrate. The ΔIL data in figure 6-3 shows an increase with waveguide thickness (roughly proportional to $(\Delta f / f)$). This is of course in addition to the dry intrinsic loss, and thus an optimum thickness that allows high sensitivity, low intrinsic loss, and low additional loss is vital for operation in liquid environments. The change in gradient $(\Delta f / \Delta h)$ in figure 6-1 suggests the sensitivity would increase for $h > 1.20$ μm, possibly until the theoretical maximum of $h = 2.55$ μm. This was shown in the dry characterisation in section 5.3. However as previously mentioned, dominant insertion losses prevent operation for thicker layers.

Figure 6-4 shows the polyimide sensitivity as a function of h, between 0.65 and 1.20 μm, in greater detail. The IPA frequency shifts were larger than water due to the higher square root density-viscosity product of $\sqrt{(\rho\eta)} = 1.280$ $kgm^{-2}s^{-0.5}$, compared to

water's value of $\sqrt{(\rho\eta)} = 1.000\ \mathrm{kgm^{-2}s^{-0.5}}$. The frequency sensitivity increased linearly from $(\Delta f / f) = -6.0\times10^{-4}$ (water value) at $h = 0.65$ μm to $(\Delta f / f) = -2.1\times10^{-3}$ for $h = 1.07$ μm. The change in behaviour of the two thickest layers was due to dominant insertion losses almost reducing the resonance to background levels – the data points are shown to illustrate this effect.

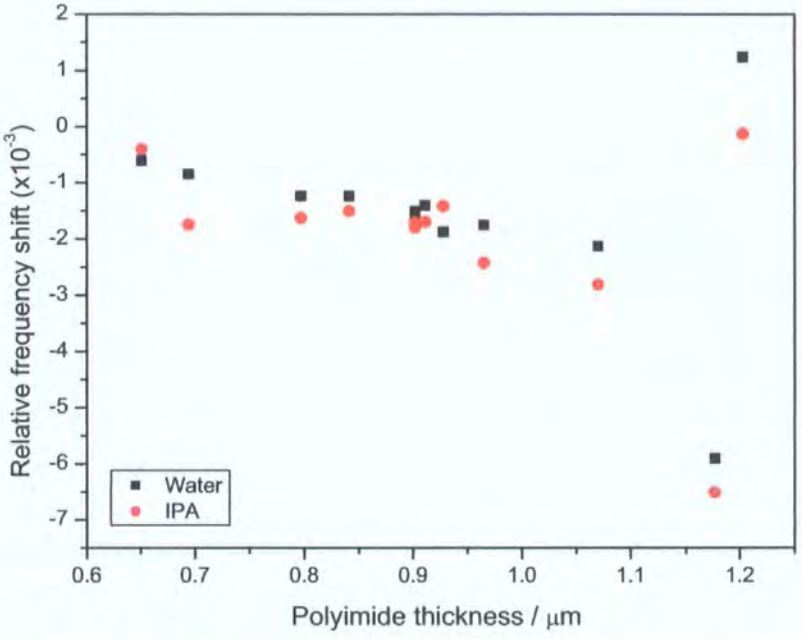

Figure 6-4. Sensitivity of polyimide devices to DI water and IPA as a function of waveguide thickness.

6.2 Corrugations

The trapping effect due to the patterned surface of the corrugated devices was investigated with IPA and DI water samples. Figure 6-5 shows the $(\Delta f / f)$ response from the smooth and corrugated surfaces. The devices all had a waveguide of $h = 0.90$ or 0.91 μm, and data is presented for multiple identical devices to check the reproducibility of the loading effect. When discussing the corrugated devices the notation *corX/Y(Z)* is used, where X is the designed trough width and Y the trough spacing, both in μm, and Z is the trough depth, usually 0.5 μm.

The corrugated devices gave larger frequency shifts than the smooth. The maximum $(\Delta f / f)$ given by the heavily corrugated devices, *cor2.5/2.5(0.5)*, was approximately twice as large as from the smooth delay line, and $(\Delta f / f)$ for the lightly corrugated

devices, *cor2.5/20(0.5)* was only slightly larger than the smooth response. This indicates that $(\Delta f / f)$ with mass loading, $(\Delta f / f)_{trapped}$, is proportional to the trap surface area, and therefore the trapped volume of liquid. The responses from the over-corrugated devices, *cor5.0/2.5(0.5)*, were smaller than for *cor2.5/2.5(0.5)*, suggesting the trapping effect is either smaller with wider troughs, or when the majority (> 50 %) of the surface area has been etched. The trough widths were all less than the compressional wavelength of water (about 12 μm at 125 MHz), and so theoretically preventing liquid entrainment within the troughs. However compressional waves could possibly form from the non-vertical sidewalls, and therefore out into the body of liquid – this would be greater with the wider troughs. The micrographs in section 5.1 show the variation in the trough profiles which could cause this. The smaller response from the *cor5.0/2.5(0.5)* devices could also have arisen from disruption to the Love mode formation with an excessively etched area, or from a smaller viscous loading effect due to only one third of the surface area contributing to viscous coupling.

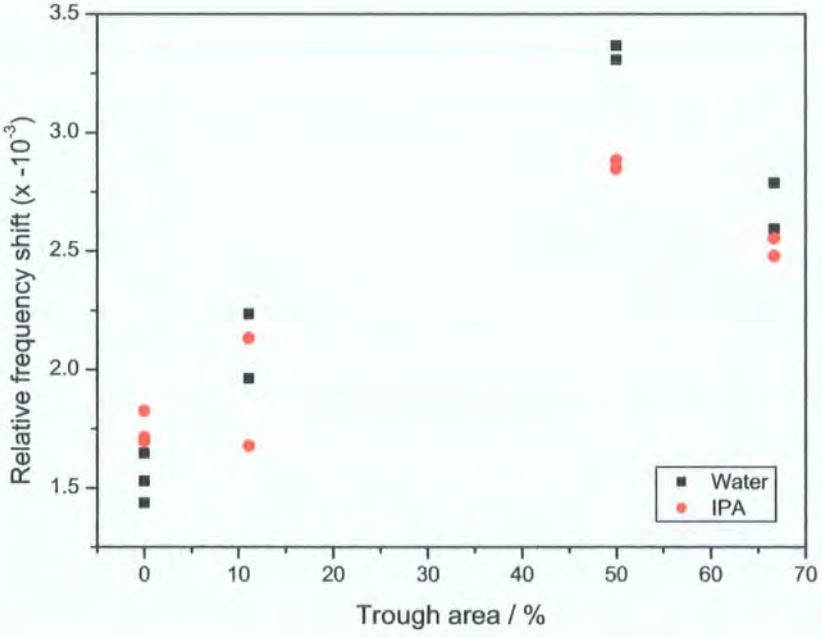

Figure 6-5. Effect of corrugations on the frequency response with DI water and IPA samples for 0.91 μm polyimide. Smooth surface – 0%. *cor2.5/20(0.5)* – 11%. *cor2.5/2.5(0.5)* – 50 %. *cor5.0/2.5(0.5)* – 67%. Three devices are shown for 0 %, and 2 devices for 11 %, 50 % and 67 % corrugations.

Figure 6-5 illustrates the two different effects of mass loading (corrugated surface) and viscous loading (smooth surface) as described by equations (3-46) and (3-49). The physical properties of water and IPA are given in table 6-1. Viscous loading on the smooth delay lines gave a larger ($\Delta f / f$) for IPA than water. This was due to the higher $\sqrt{(\rho\eta)}$ of IPA because of its relatively high viscosity. The corrugated devices gave a larger ($\Delta f / f$) with DI water due to the higher density of water. This indicates the mass loading effect due to liquid trapping, in addition to the viscous loading. The data spread for identical structures is possibly due to slight variations in the polyimide waveguide thickness. Edge bead formation during spin coating may also have caused some thickness measurement errors, and the thickness values varied across a single wafer by up to ± 0.05 μm.

Table 6-1. Properties of IPA and DI water at 20°C [18].

Property	DI Water	IPA
Density ρ / gcm^{-3}	0.998	0.780
Viscosity η / Pas	0.0010	0.0021
$\sqrt{(\rho\eta)}$ / $kgm^{-2}s^{-0.5}$	1.000	1.280

Using average values for the smooth and the *cor2.5/2.5(0.5)* delay lines, and the difference in ($\Delta f / f$) between the water and IPA results, the sensitivity of the smooth-*cor2.5/2.5(0.5)* device to liquid density was 2.9 $\mu gcm^{-3}Hz^{-1}$. This assumes that the differential response $(\Delta f / f)_{corrugated}$ - $(\Delta f / f)_{smooth}$ between the two delay lines is only dependent on the increased mass loading due to the trapped liquid.

Electrical loading of the devices due to the sample liquid's permittivities will also have affected the ($\Delta f / f$) and ΔIL responses by changing the impedance of the IDTs. The difference in permittivity between IPA ($\varepsilon_r = 18.3$) or DI water ($\varepsilon_r = 80$) and the quartz substrate ($\varepsilon_r \approx 4.5$) is large. Loading with these high permittivity samples will increase the IDT capacitance resulting in higher insertion losses. Electrical loading is evident in figure 6-6, which shows the corresponding ΔIL data for IPA and DI water loading. The ΔIL values for IPA ranged from 13.5 dB to 15.4 dB for all the devices, with a small additional increase for the corrugated devices. The values for water ranged from 16.7 dB to 22.0 dB, with a larger ΔIL additional loss with corrugation etched area.

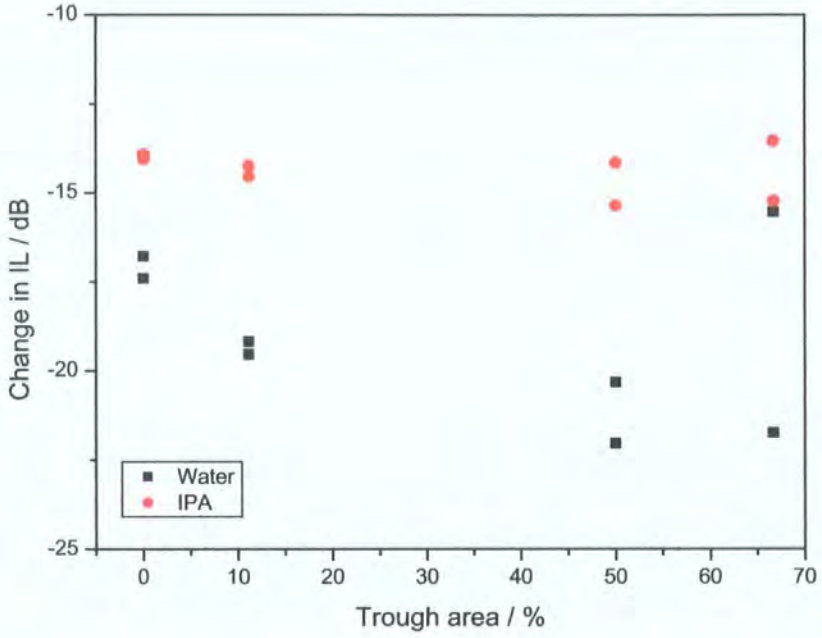

Figure 6-6. Effect of corrugations on the insertion loss change with DI water and IPA samples for 0.91 μm polyimide.

Viscous loading was clearly not dominant here since the viscosity of IPA is twice that of DI water, but water incurs greater losses. The sample liquid is closer to IDTs in proportion to the corrugation area for the corrugated structures, due to the thinner waveguide layer at the base of the troughs. For example, with the *cor2.5/2.5(0.5)* devices, half the liquid sample was separated by 0.9 μm polyimide and half by only 0.4 μm polyimide. The extra capacitive coupling to the liquid in the thinner trough areas explains the increase in insertion loss for the water results on the corrugated devices.

Dielectric waveguide layers can reduce the effect of electrical loading by acting as a buffer between the IDTs and the sample liquid. Polyimide thicknesses in excess of 8 μm are required to screen the permittivity effects of water on $LiTaO_3$ substrates, and for $h < 1$ μm, the change in IDT capacitance with thickness is large [95]. For the lower permittivity quartz used in this study, thicker polyimide waveguide layers would be required for the screening effect to be significant. Thus the overall thin layers used in this study would have had negligible screening effect, but the variation in thickness of 0.5 μm with the etched corrugations would cause a significant effect. The effective permittivity of a sample liquid ε_{eff} can be approximated taking into account a buffer layer of known thickness h / λ and permittivity ε_b [96]:

$$\varepsilon_{eff} = \varepsilon_b \frac{1+\phi e^{-2\pi h/\lambda}}{1-\phi e^{-2\pi h/\lambda}} \tag{6-1}$$

where ϕ is the normalised difference in permittivity between the buffer layer ε_b and liquid ε_l:

$$\phi = \frac{\varepsilon_l - \varepsilon_b}{\varepsilon_l + \varepsilon_b}. \tag{6-2}$$

Figures 6-7 and 6-8 show the theoretical ε_{eff} dependence on h for polyimide with $\varepsilon_b = 3.5$ (manufacturers data). Data is shown for DI water and IPA samples and for air (no sample). For large thicknesses, ε_{eff} approaches the polyimide permittivity, the layer completely shielding the IDTs from the liquid. However for small thicknesses ($h < 1$ μm) the liquid permittivity is dominant, with small changes in thickness giving a large change in ε_{eff}, and thus the capacitance of the IDTs, leading to a large impedance mismatch and an increase in capacitive loss. Considering the *cor2.5/2.5(0.5)* device, $\varepsilon_{eff} \approx 31$ for $h = 0.9$ μm, and increases to $\varepsilon_{eff} \approx 47$ for $h = 0.4$ μm. Thus ε_{eff} as seen by the IDTs can be simplified to $\varepsilon_{eff} = (0.5\times47) + (0.5\times31) = 39$. This explains the increase in insertion loss for the corrugated devices in figure 6-6.

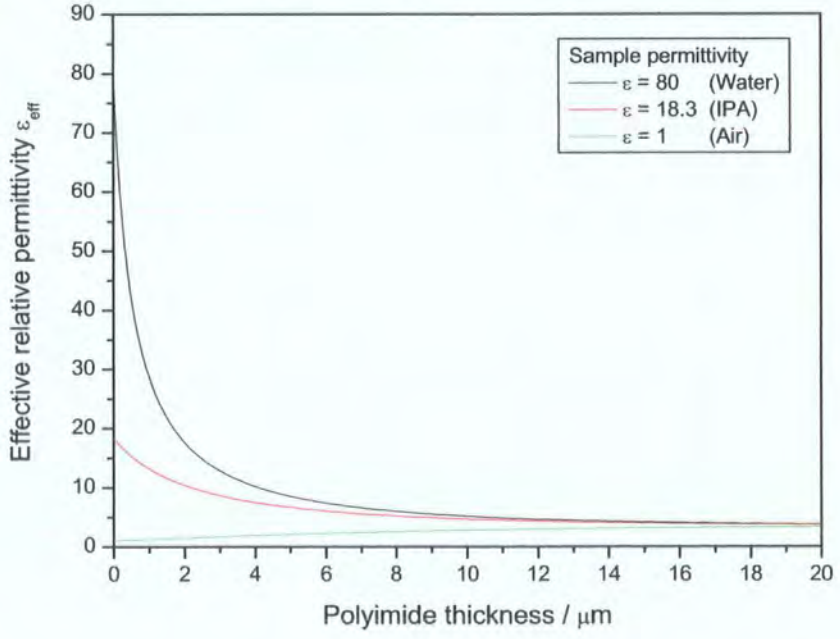

Figure 6-7. Effective permittivity ε_{eff} for polyimide waveguide layers with DI water and IPA samples, and with no sample in air.

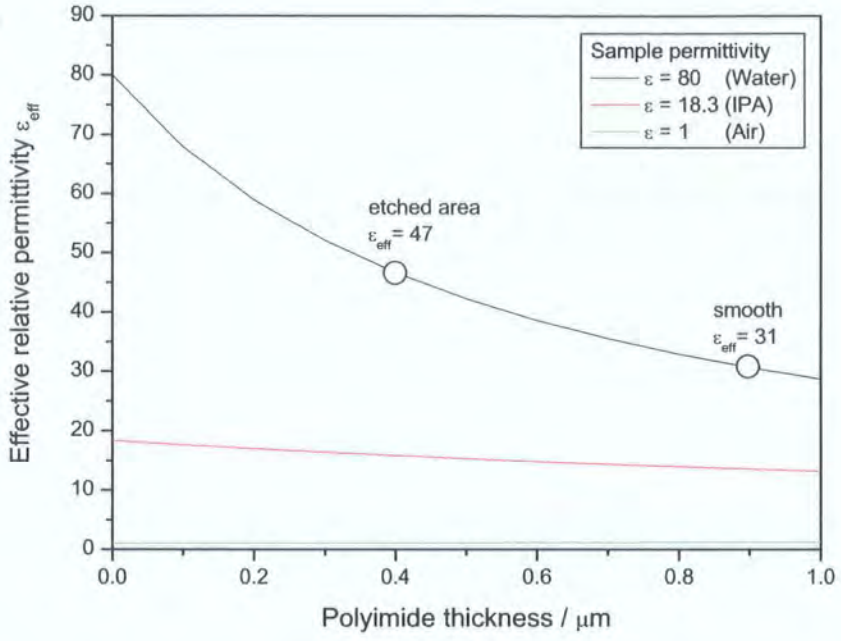

Figure 6-8. Effective permittivity ε_{eff} for polyimide waveguide layers with DI water and IPA samples, and in air. The permittivity difference between the trough regions and smooth regions is highlighted for water loading.

Studies using $LiTaO_3$ substrates show that high permittivity substrates ($\varepsilon_r \approx 48$ for $LiTaO_3$) give smaller losses in aqueous environments [96]. Reducing the permittivity difference between the substrate and sample makes the change in capacitance with sample loading smaller, thus giving lower additional insertion losses. With most liquids the permittivity is low allowing the use of quartz, but the dipole nature of water gives a high permittivity, leading to the recent work with $LiTaO_3$.

6.3 Sucrose measurements

The accurate determination of sucrose concentration (the Brix scale) is important in the sugar industry. Sugar cane's sucrose content varies independently of mass, and thus the sucrose percentage needs to be determined in another manner. Measurement of solution density and refractive index is one method of determining the Brix value, and this is potentially a large market for the combined refractometer and densitometer.

The sensors were extensively tested with ultra pure sucrose in DI water solutions, measuring the frequency shift and insertion loss changes, and calculating the difference in response between the corrugated and smooth delay lines. Sucrose concentrations of

0% to 50% were measured, with a concentration error of less than ±0.5% measured using a refractometer. The data for ρ and η were taken from standard tables [18]. Figure 6-9 shows the variation with concentration with ρ changing by 23% and η changing by 1443%, the change in η clearly acting as the dominant parameter in $\sqrt{(\rho\eta)}$.

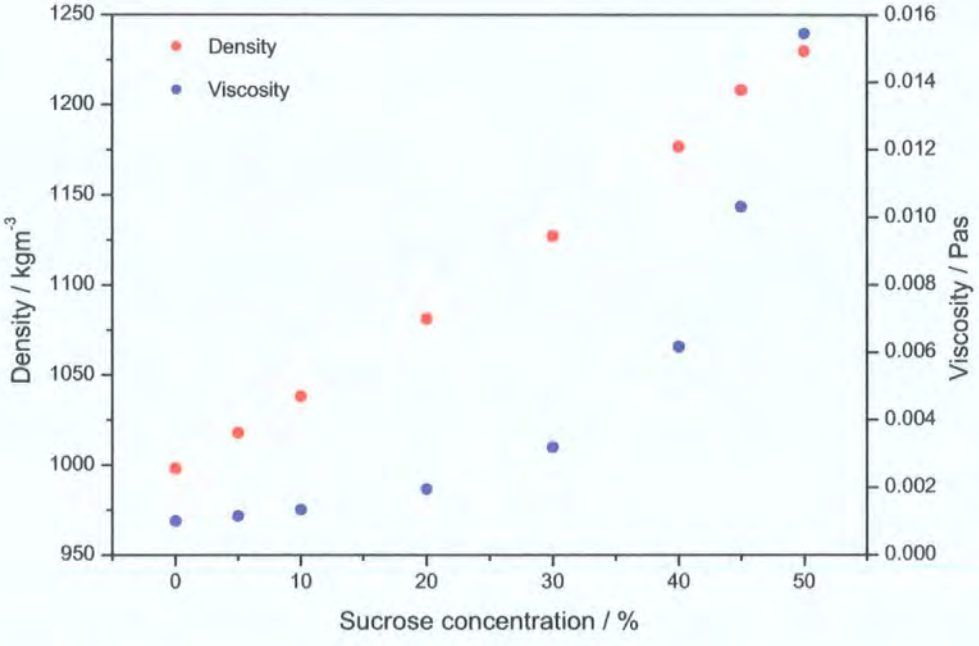

Figure 6-9. Sucrose solution density and viscosity dependence on concentration.

6.3.1 Polyimide waveguide device response

The frequency shift dependence on $\sqrt{(\rho\eta)}$ for h = 0.95 μm polyimide waveguide devices is shown in figure 6-10. The three different corrugation geometries used are given in table 6-2. Error bounds of $(\Delta f / f) = \pm 8\times10^{-5}$ are presented - these are due to measurement uncertainty based upon a 10 kHz peak-tracer fluctuation on the network analyser. This is small (and could be considered negligible) but has larger consequences on the differential results as discussed later.

The results all show a significant $(\Delta f / f)$ dependence on the sucrose concentration, or more precisely the $\sqrt{(\rho\eta)}$ product, with an increase in frequency shift (a reduction in absolute frequency) for higher sucrose concentrations. Identical responses within the errors were given by *smooth(A)* and *smooth(B)*, and the *smooth(C)* results are similar,

but with a step in (Δf / f) between 1.5 and 2 $kgm^{-2}s^{-0.5}$. The deep corrugated device responses, *cor2.5/2.5(0.5)* and *cor5.0/5.0(0.5)*, were both significantly alike with an additional relative frequency shift of approximately 1.5×10^{-3} due to the mass loading contribution from the trapped liquid in the troughs. The shallower corrugated device *cor5.0/5.0(0.25)* gave intermediate (Δf / f) values with an identical step to *smooth(C)*: these two devices formed a dual delay line on the same chip, so some experimental change (such as poor cleaning, or a loose connection) is probably the cause of the coincidental step.

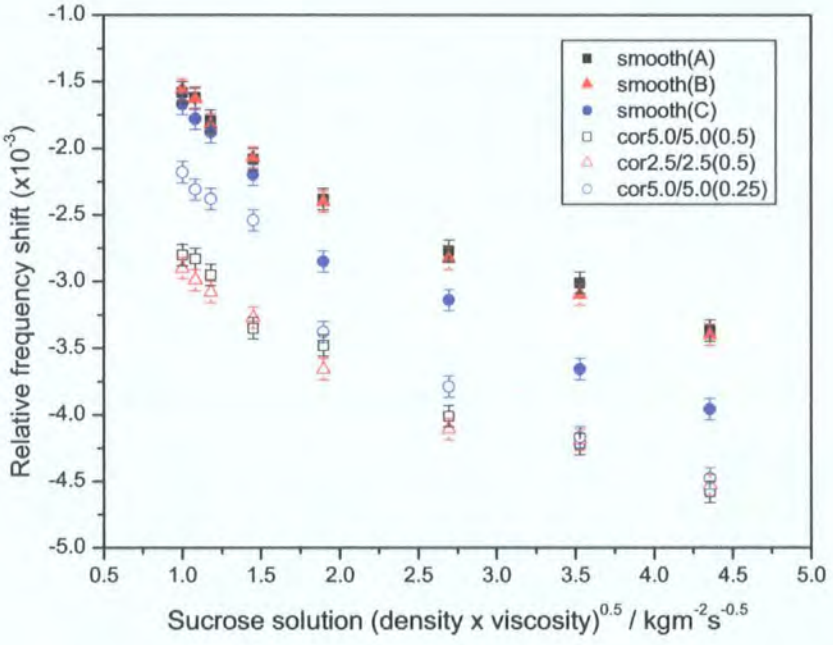

Figure 6-10. Frequency shift with increasing sucrose concentration (described in terms of density and viscosity). The error bounds are (Δf / f) = $\pm8\times10^{-5}$.

Table 6-2. Corrugation geometry of polyimide devices used with sucrose samples {values in brackets are measured values}.

Device	Trough Width / μm	Trough Space / μm	Trough depth / μm
cor2.5/2.5(0.5)	2.5 {2.3}	2.5 {2.6}	0.5
cor5.0/5.0(0.5)	5.0 {5.0}	5.0 {5.0}	0.5
cor5.0/5.0(0.25)	5.0 {4.8}	5.0 {5.2}	0.25

The insertion loss results in figure 6-11 have a similar dependence on $\sqrt{(\rho\eta)}$ with an increase in ΔIL for higher sucrose concentrations. No measurement errors are presented due to the ±0.005 dB network analyser accuracy. The ΔIL data for each surface type is less discrete than the frequency data, highlighting the susceptibility of insertion loss to factors other than purely surface loading. For example the three smooth devices cover a range of ΔIL over 3 dB, and the corrugated devices again over a similar range, with no significant gap between the sets of smooth and corrugated device data. The large ΔIL values for higher viscosity solutions (up to 30 dB extra for 50% concentration) caused excessive overall losses up to approximately 45 dB. This reduced the response peaks close to background levels, making them difficult to distinguish. For higher concentrations than 50%, the waves were completely attenuated, preventing any further measurements.

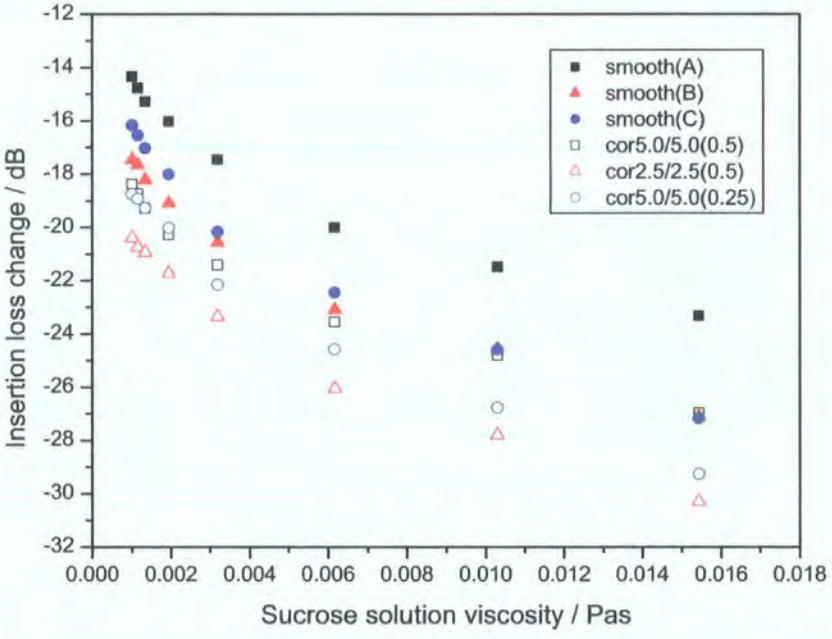

Figure 6-11. Insertion loss change with increasing sucrose concentration (in terms of viscosity).

The response for $(\Delta f / f)$ was linear for $\sqrt{(\rho\eta)} < 1.45$ kgm^{-2} s$^{-0.5}$ (corresponding to 20 % sucrose) giving a frequency sensitivity of 1.45 kgm^{-2}s$^{-0.5}$Hz^{-1} (the change in $\sqrt{(\rho\eta)}$ for a 1 Hz shift). Similarly, ΔIL was linear for $\eta < 0.0019$ Pas again corresponding to 20% sucrose concentration. With further concentration increases, the sensitivity

reduced with the change in ($\Delta f / f$) or ΔIL diminishing. This 'saturation' effect has been observed in other studies and is a characteristic response of Love mode and other acoustic sensors operating with highly viscous liquids [77, 78, 97]. The effect can be explained by the non-Newtonian behaviour of viscous liquids at high frequencies, and possibly by the inclusion of slip discontinuities at the sensor surface.

* * * * *

Newtonian Liquids: The Newtonian model assumes liquids are perfectly viscous, with a real viscosity η_0. The changes in the phase and attenuation components of the wave propagation with liquid loading are therefore directly proportional to η_0 (assuming constant ρ). The linear regions in figures 6-10 and 6-11 for $\sqrt{(\rho\eta)} < 1.45$ $kgm^{-2}s^{-0.5}$ (or $\eta < 0.0019$ Pas) are indicative of this behaviour, such that the changes in attenuation $\Delta\alpha / \beta$ and propagation $\Delta\beta / \beta$ are proportional to the sample viscosity.

Maxwellian Liquids: The physical behaviour of viscous liquids at high frequencies changes such that the viscosity becomes complex (equation (3-50) and the liquid acts visco-elastically. This behaviour is described by the relaxation time $\tau = \eta / \mu$, where μ is the high frequency shear modulus, describing the elastic behaviour. The liquid effectively acts as a spring and a damper, and does not couple perfectly viscously with the shear wave motion. For $\omega\tau = 0$, the liquid is Newtonian, but as $\omega\tau$ increases the visco-elastic effects increase until $\omega\tau \rightarrow \infty$ when the liquid behaves as an amorphous solid [98].

The inclusion of visco-elastic effects alters the response of wave propagation change to viscosity such that the effective viscosity η_0 appears smaller than the real viscosity η. The theoretical model discussed in the study by Jakoby et al illustrates how the change in attenuation $\Delta\alpha / \beta$ reaches an asymptote, and the change in phase $\Delta\beta / \beta$ reaches a maximum, then decreases again [78]. This response is partially exhibited in the sucrose results, with the sensitivities (the response gradients) $\Delta f / f / \sqrt{\rho\eta}$ and $\Delta IL / \eta$ reducing for the higher viscosity liquids. No insertion loss asymptote was reached in the experiments and presumably no frequency maximum was achieved due to a lack of data above 50% sucrose.

Interfacial slip: Another possible cause of non-linear behaviour is interfacial slip at the sensor surface and liquid interface [77, 98, 99]. The presence of a shear stress at the

substrate / liquid interface can cause a discontinuity in the shear particle velocity, resulting in slip. A slip coefficient s_l can be used to modify the surface impedance:

$$Z_{slip} = \frac{Z}{1 + s_l Z} \tag{6-3}$$

The slip factor is based on the coefficient of friction between the surface and visco-elastic liquid, and the unit mass of the liquid. As the slip factor increases, the effective surface impedance decreases. From equation (3-42), the change in the propagation components $\Delta\alpha / \beta$ and $\Delta\beta / \beta$ decreases, and thus the rate of change of ΔIL and $(\Delta f / f)$ also reduces as shown in the sucrose results. This has a similar influence on the results as the Maxwellian liquid behaviour, causing the responses to tend towards an asymptote.

The study by Kovacs et al experimentally explored the effect of slip at the interface [77]. They investigated the effect of reducing the wave power to –30 dB to reduce stress at the boundary with a highly viscous sample (100% glycerol). However they found no change in the frequency or insertion loss suggesting no change in the slip conditions.

* * * * *

The difference in $(\Delta f / f)$ between the smooth and corrugated delay lines is shown plotted against the sucrose density in figure 6-12. The error bounds are $(\Delta f / f) = \pm 1.6\times10^{-4}$, based on the compound intrinsic error arising from the 10 kHz jitter. This is significant at between 13% and 32% of the difference responses. The data for $(\Delta f / f)_{cor2.5/2.5(0.5)\text{-}smooth}$ and $(\Delta f / f)_{cor5.0/5.0(0.5)\text{-}smooth}$ coincide within the error bounds, suggesting identical sensitivities from the equal-volume liquid traps, even though different lateral dimensions were used. The responses from both devices appeared to be uniform, with no proportionality to ρ, around an average value of 1.2×10^{-3}, corresponding to an absolute frequency change difference of about 148 kHz. A similar response was given by the device using shallower troughs, with $(\Delta f / f)_{cor5.0/5.0(0.25)\text{-}smooth}$ again showing no proportionality to ρ, having an average value of approximately 5.1×10^{-4} or 63 kHz. The smaller sensitivity was due to the lower mass loading contribution with shallower, and therefore smaller volume, troughs on the corrugated delay line.

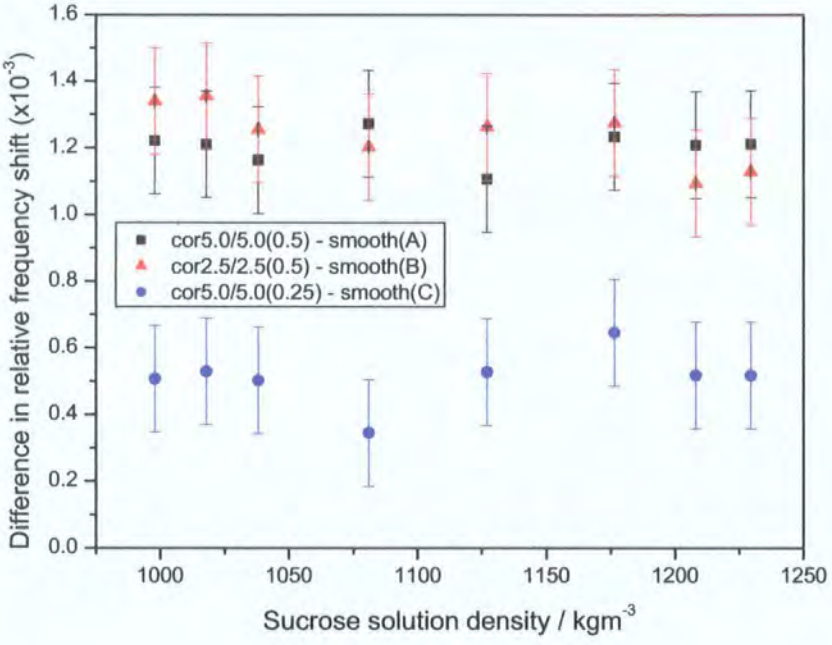

Figure 6-12. Difference in relative frequency shift between corrugated and smooth delay lines with sucrose solution density. The error bounds are $(\Delta f / f) = \pm 1.6 \times 10^{-4}$.

The results in figure 6-12 show a clear inability of the dual delay line corrugated-smooth device combinations to discriminate the sucrose solution density from the $\sqrt{(\rho\eta)}$ product by measuring the difference in relative frequency shifts. The compound measurement errors represented by the error bounds are large and could contribute to this failure. But small similarities in the trends of the data, such as the similar formations of the last 4 data points for each device combination, suggest that the results are more precise than the errors allow for. The most probable explanations are due to the relatively high sucrose solution viscosities. Firstly, the viscosities are dominant in $\sqrt{(\rho\eta)}$ as discussed in section 6.3, possibly masking changes in ρ, and preventing its discrimination. Secondly, the large viscosities resulted in high attenuation of the wave, reducing the resonance close to background levels and making accurate measurements difficult. Finally, and most likely, is the reduced sensitivity at higher viscosities arising from the non-Newtonian liquid behaviour. The change from a linear response to a reducing gradient in figures 6-10 and 6-11 almost certainly confirm the presence of the complex viscous behaviour associated with Maxwellian liquids, and this reduction in sensitivity may override any small mass loading differences.

6.3.2 SiO_2 device response

SiO_2 waveguide devices which replicate the Bosch design by Hermann et al [40, 41] were tested with sucrose solutions, with simultaneous measurements taken from polyimide waveguide devices (one smooth, and two with different corrugation geometries) for comparison. The SiO_2 waveguides were 1.61 μm thick, chosen partially for the low insertion losses as shown in figure 5-25, but also largely determined by the poor device yield and absence of functioning corrugated devices for other thicknesses.

Figure 6-13 shows the $(\Delta f / f)$ dependence on $\sqrt{(\rho\eta)}$, figure 6-14 the ΔIL dependence on η, and figure 6-15 the difference in $(\Delta f / f)$ between the smooth and corrugated delay lines plotted against ρ. A larger number of low concentration samples were measured explaining the increased number of low concentration data points. A silicone bead encapsulation method was used which made cleaning the device surfaces more difficult than the previous results which used an epoxy encapsulation, and this possibly causes the weaker trends. The 10 kHz frequency jitter measurement uncertainty is shown.

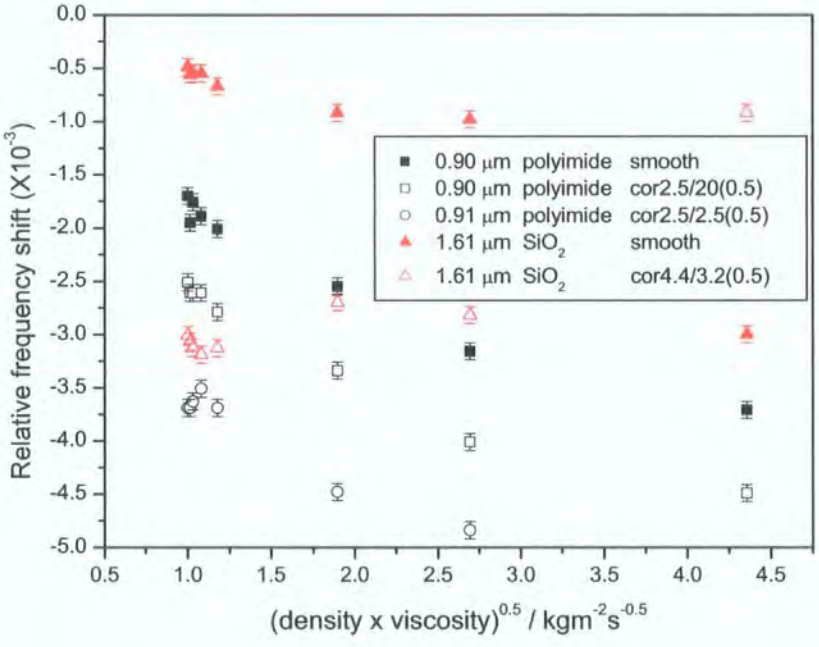

Figure 6-13. Frequency shift with increasing sucrose concentration for SiO_2 and polyimide waveguide layers. The error bounds are $(\Delta f / f) = \pm 8\times10^{-5}$.

The polyimide responses were consistent with those discussed previously and no further discussion is needed. The smooth SiO_2 waveguide devices exhibited a smaller

frequency shift than the polyimide devices, due to the thicker waveguide causing a lower surface energy density and therefore lower sensitivity as previously explained. The gradient for weaker sucrose solution concentrations is lower than the polyimide response, and the shape suggests saturation at $\sqrt{(\rho\eta)} = 1.8$ due to the Maxwellian liquid behaviour. The $(\Delta f / f)$ values for $\sqrt{(\rho\eta)} = 4.4$ were distorted due to the low signal levels making the response difficult to measure – these are still included in the results to demonstrate the measurement difficulties for high viscosity, heavily damping, liquids. The smooth SiO_2 device ΔIL values in figure 6-14 are approximately 2 dB less than for the smooth polyimide devices, due to the higher elastic modulus of SiO_2. The lower ΔIL values in addition to the 4 dB lower intrinsic losses (dry loss) of the SiO_2 devices provided an increase in power of around 6 dB over the polyimide devices, approximately four times the acoustic power. The ΔIL values do not show the same strong dependence on $\sqrt{(\rho\eta)}$ as the polyimide device responses (see figure 6-11) – this is partially due to the absence of regular data making visualisation of the trend difficult, and also due to the errors arising from sample removal and surface cleaning.

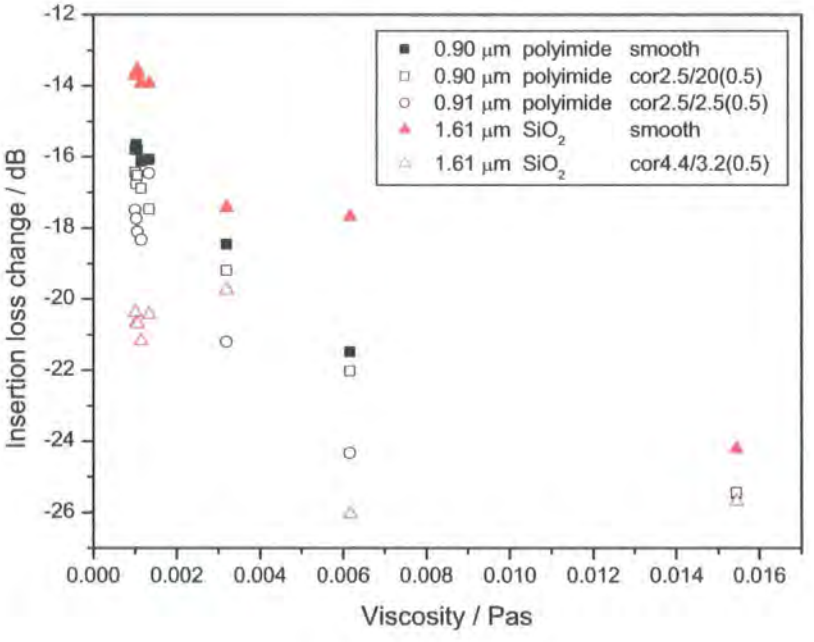

Figure 6-14. Insertion loss change with increasing sucrose concentration for SiO_2 and polyimide waveguide layers.

The corrugated SiO_2 device had 0.5 μm deep troughs 4.4 μm wide and spaced by 3.2 μm, giving 58 % etched area. The $(\Delta f / f)$ values for the lower concentrations are

comparable to the 11% corrugated polyimide responses, demonstrating again the lower sensitivity of the SiO_2 waveguide structure. For higher concentrations ($\sqrt{(\rho\eta)} > 1.8$) the frequency shifts decreased with no relation between ($\Delta f / f$) and $\sqrt{(\rho\eta)}$ visible. The corrugated SiO_2 ΔIL values were approximately 4 dB higher than for the corrugated polyimide devices, again exhibiting no dependence on $\sqrt{(\rho\eta)}$ for the higher sucrose concentrations. The increase in ΔIL for the corrugated surface was partially due to the larger volume of trapped liquid in the heavily etched surface, but the losses are still larger than the expected values of around 2 – 3 dB increase found for polyimide.

The difference in ($\Delta f / f$) between the smooth and corrugated delay lines is shown plotted against ρ in figure 6-15, with measurement uncertainty error bounds of $(\Delta f / f) = \pm 1.6 \times 10^{-4}$ included.

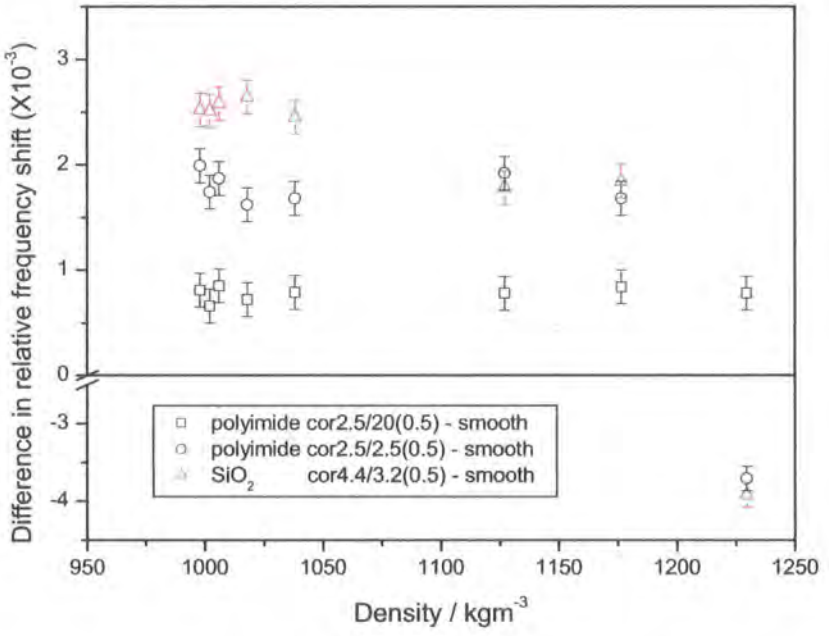

Figure 6-15. Difference in relative frequency shift between corrugated and smooth delay lines with sucrose solution density for SiO_2 and polyimide waveguide layers. The error bounds are $(\Delta f / f) = \pm 1.6 \times 10^{-4}$.

The polyimide devices showed no dependence on ρ as demonstrated earlier in figure 6-12, with a uniform response across the density range. A similar failure to discriminate ρ from $\sqrt{(\rho\eta)}$ was given by the SiO_2 devices, although a significant reduction in frequency shift difference was shown for the higher density sample. The

negative values obtained for the highest sample concentration (ρ = 1230 kgm^{-3}) represent a larger shift from the smooth delay line than the corrugated one. This was due to the high insertion losses distorting the frequency shift data presented in figure 6-13 arising from the low signal levels. Whilst these negative values can be classed as anomalies, they are actual measured data, and demonstrate the failure of Love mode sensors with highly viscous liquids due to the difficulties in tracking a highly attenuated bandpass peak. The non-linear sensitivity due to Maxwellian liquid behaviour was an added complication.

6.4 Commercial spirits and liqueurs

Potential applications for the density sensor cover a complete range of liquids, both chemicals in their pure state, and everyday 'mixtures'.

Figure 6-16 shows the (Δf / f) response to a range of different commercial spirits and liqueurs. Smooth and corrugated polyimide devices with h = 0.90 μm, and a smooth multilayer device with a 0.90 μm SiO_2 base layer and 0.69 μm polyimide upper, were used. The results are presented in ascending (Δf / f) of the *cor2.5/2.5(0.5)* corrugated device for ease of comparison.

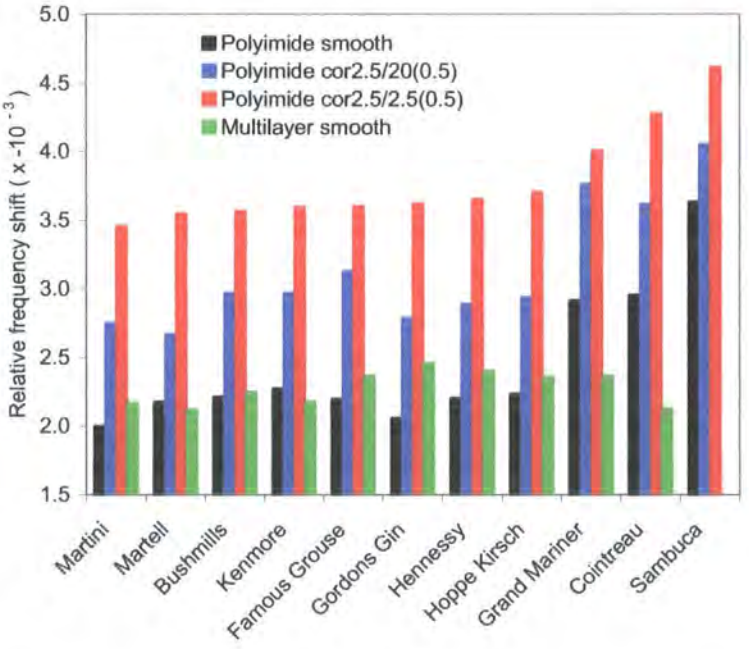

Figure 6-16. Frequency response to commercial spirits and liqueurs.

The polyimide devices demonstrated a general increase in (Δf / f) from left to the right, with Sambuca giving the largest shift. Whilst there are some anomalies, this

pattern is consistent for polyimide. The corrugated devices give the largest frequency shift due to the additional mass loading. The multilayer results are inconsistent with the polyimide responses, showing no overall trends.

The (Δf / f) data is plotted against $\sqrt{(\rho\eta)}$ in figure 6-17. The ρ and η values were measured using a slipping cone viscometer and Anton Parr densitometer. The polyimide devices exhibited increased frequency shifts with 'thicker' more viscous liquids, such as the sugary liqueurs, due to the increased viscous loading. The response is similar from all the polyimide devices, apart from the drop in frequency for *cor2.5/20(0.5)* at $\sqrt{(\rho\eta)}$ = 1.83 $kgm^{-2}s^{-0.5}$. The frequency shifts exhibited by the multilayer devices are again inconsistent with the polyimide results, except for possibly the lower $\sqrt{(\rho\eta)}$ data points.

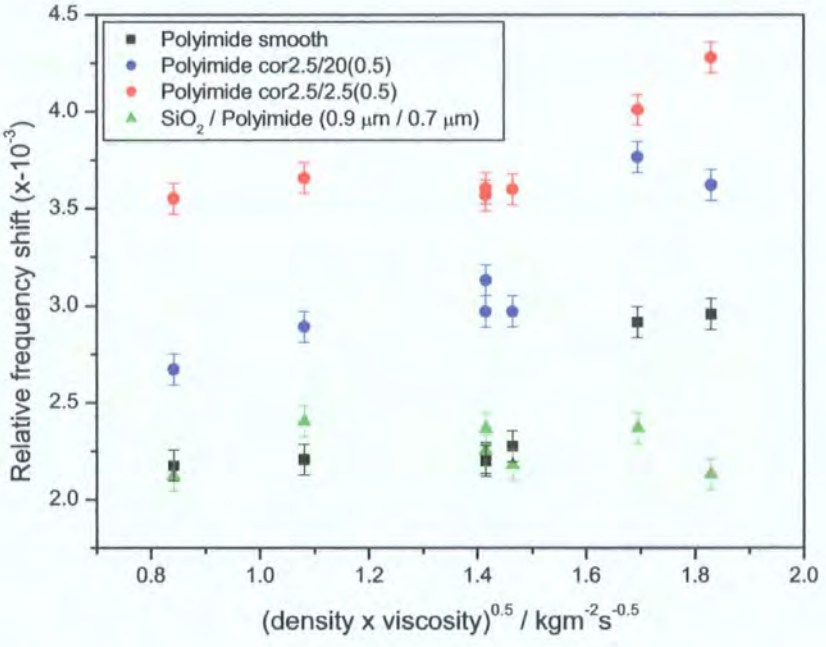

Figure 6-17. Frequency dependence on alcoholic beverage $\sqrt{(\rho\eta)}$. The error bounds are (Δf / f) = $\pm 8\times10^{-5}$.

The insertion loss increase is theoretically proportional to the liquid η, due to viscous entrainment damping the wave motion. Figure 6-18 shows the ΔIL dependence on η for the spirits and liqueurs. The ΔIL increases for the smooth and *cor2.5/20(0.5)* polyimide devices were almost identical, ranging from 18.5 dB at 0.0009 Pas to around 26 dB at 0.0067 Pas. The losses for *cor2.5/2.5(0.5)* followed the same trend with an additional 1.5 dB. These insertion losses were the additional increase with loading, and

so represent absolute values ranging between 34.5 dB and 44.5 dB. There is a general linear proportionality between ΔIL and η showing the increased damping with thicker liquids. The variation from the trend is consistent between devices, for example, three whiskies with η = 0.0021 Pas and 0.0023 Pas always fall below the trend, showing a smaller ΔIL than predicted.

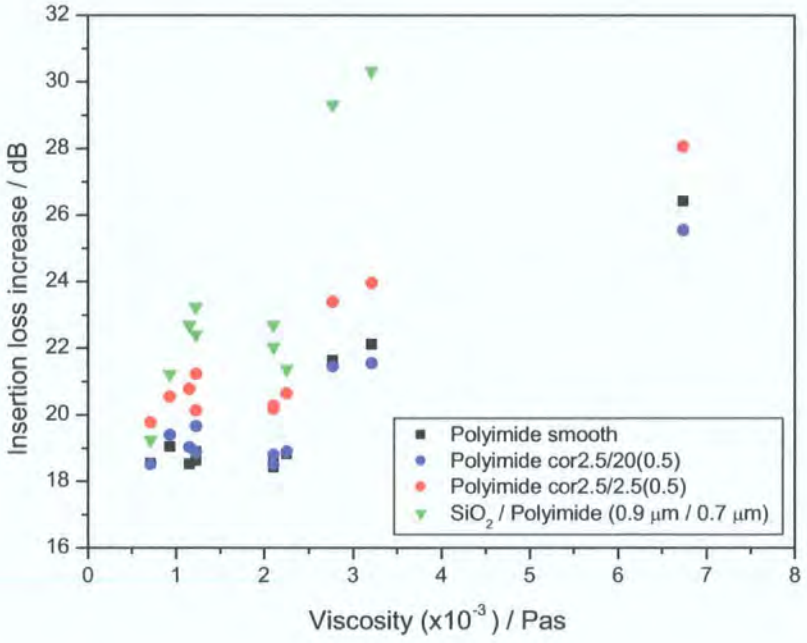

Figure 6-18. Insertion loss dependence on alcoholic beverage viscosity.

The motivation for multilayer structures was partially the expected lower insertion losses with liquid contact. However, figure 6-18 presents higher multilayer ΔIL values than the polyimide devices, ranging from 19.2 to 30.3 dB. No measurements were taken for η = 0.67 Pas due complete wave damping. Whilst the multilayer intrinsic losses were relatively low, the additional loaded losses were significantly higher, especially for the high $\sqrt{(\rho\eta)}$ samples. This can possibly be explained by a double-waveguiding effect. When dry, a large proportion of the wave is confined to the SiO_2 base layer. The lower acoustic absorption in the glassy base layer reduces the transmitted losses, giving a relatively low intrinsic loss of 10 dB (for 0.90 μm SiO_2, 0.69 μm polyimide). However loading of the surface increases the proportion of the acoustic energy confined in the polyimide. Thus the overall insertion loss is increased through viscous losses into the liquid, and additional absorption in the polyimide.

The interaction between the dual layer structure and sample liquids possibly explains the fairly uniform frequency response across the sample range. For lower $\sqrt{(\rho\eta)}$, the response shows a similar perturbation to the single layer devices. As the viscosity is increased, the increased polyimide losses reduce the acoustic power in the upper polyimide layer, resulting in the relatively unperturbed acoustic modes in the SiO_2 layer becoming dominant. This could skew the response and thus reduce the measured $(\Delta f / f)$.

Dual delay line smooth-corrugated polyimide devices were used to investigate the trapping effect and subsequent liquid density discrimination from $\sqrt{(\rho\eta)}$. The relative frequency shift differences $(\Delta f / f)_{cor2.5/20(0.5)\text{–smooth}}$ and $(\Delta f / f)_{cor2.5/2.5(0.5)\text{–smooth}}$ are shown in figure 6-19 with ρ the abscissa.

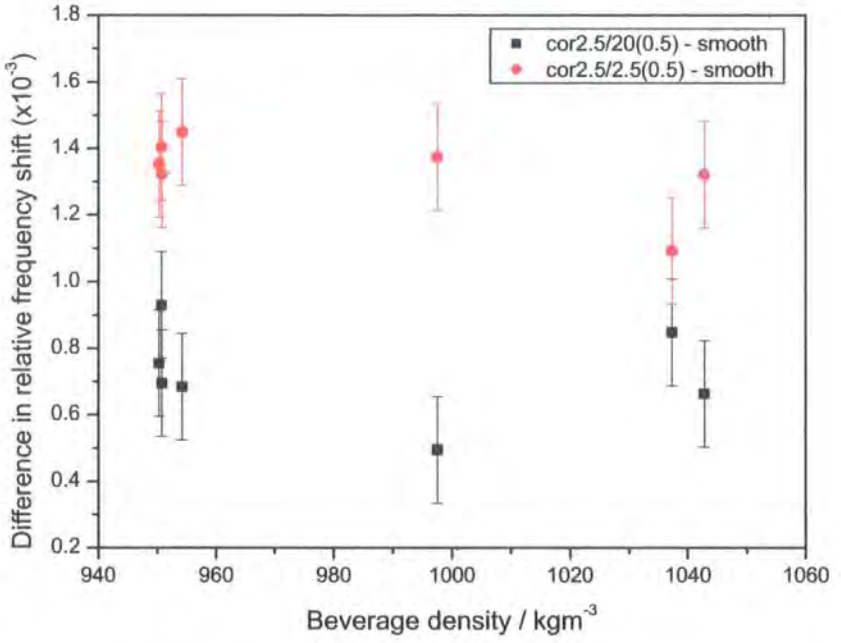

Figure 6-19. Difference in relative frequency shift between corrugated and smooth delay lines with alcoholic beverage density. The error bounds are $(\Delta f / f) = \pm 1.6\times10^{-4}$.

The measurement uncertainty in the frequency shift difference is $\pm1.6\times10^{-4}$, a compound intrinsic error arising from the 10 kHz jitter. The four data points near $\rho = 950$ kgm^{-3} are for three whiskies and a cognac, and the data near $\rho = 1000$ kgm^{-3} is for a second cognac. The data close to $\rho = 1040$ kgm^{-3} represents two orange liqueurs, which also had relatively high viscosities due to their high sugar content. The data for

the *cor2.5/2.5(0.5)*–smooth device combination, $(\Delta f / f)_{cor2.5/2.5(0.5)\text{–smooth}}$, is centred around 1.3×10^{-3} whilst the values for the less corrugated combination $(\Delta f / f)_{cor2.5/20(0.5)\text{–smooth}}$ are smaller around 0.7×10^{-3}, due to the smaller mass loading contribution. The large spread in $(\Delta f / f)_{\text{cor-smooth}}$ for similar samples is accounted for by the experimental measurement uncertainty, but the overall response for both devices was uniform with no dependence on density. The failure to discriminate density could be due to electrical loading with the sample permittivity, but is more likely due to the complex Maxwellian behaviour of viscous liquids at high frequencies, as discussed earlier in section 6.3.1.

Figure 6-20 shows $(\Delta f / f)_{cor2.5/20(0.5)\text{–smooth}}$ and $(\Delta f / f)_{cor2.5/2.5(0.5)\text{–smooth}}$ for diluted Famous Grouse and Bushmills whisky samples between $\rho = 950.8$ kg m^{-3} (0% added water) and $\rho = 966.9$ kg m^{-3} (30% added water).

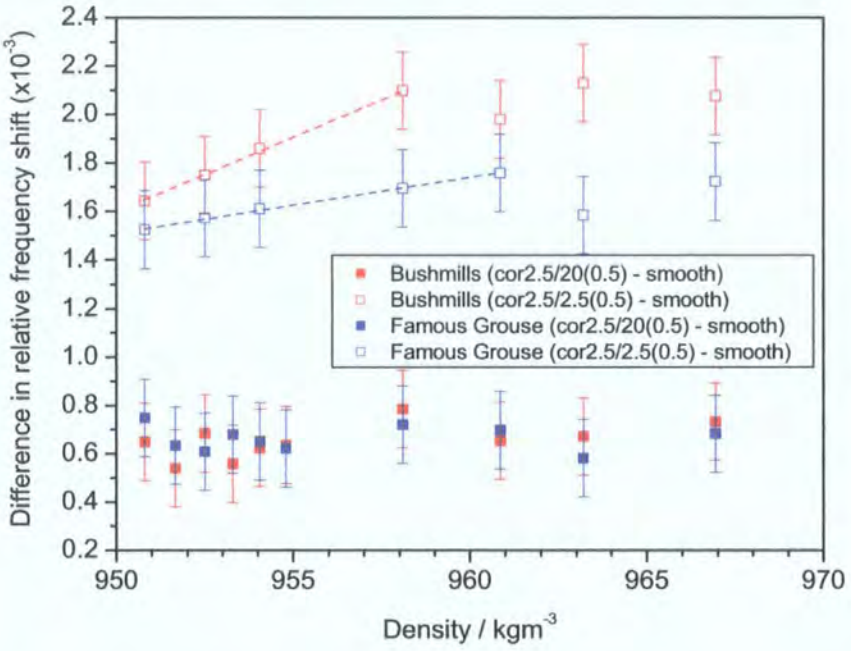

Figure 6-20. Difference in relative frequency shift between corrugated and smooth delay lines for Famous Grouse and Bushmills whisky solutions. The error bounds are $(\Delta f / f) = \pm1.6\times10^{-4}$.

The $(\Delta f / f)_{cor2.5/20(0.5)\text{–smooth}}$ device response demonstrated a similar trend for both samples, but no dependence on ρ. The errors displayed possibly suggest a uniform response, but the similarity between the two sets of data indicates that the calculated errors may be too large. This suggests that the smaller trapping effect with fewer

corrugations is insufficient to produce a measurable difference compared with the overall frequency shift. The $(\Delta f / f)_{cor2.5/2.5(0.5)\text{-smooth}}$ device response was linearly proportional to ρ for the lower concentration samples indicated by the line of best fit. A linear trend may be drawn through all the $(\Delta f / f)_{cor2.5/2.5(0.5)\text{-smooth}}$ data by including the error bounds, but the significant proportionality for the lower ρ data suggests that the response actually changes for the higher ρ. A possible explanation is that increasing the water content of whisky increased ρ, but reduced η, shown in the experiments by a reduction in frequency shift and insertion loss with increased water content. A reduction in η will cause a smaller frequency shift, but higher sensitivity due to the possible non-Newtonian behaviour of the liquid. This increased sensitivity could effectively mask the density difference response leading to the ambiguous behaviour.

These results show that for small variations in density of a single type of sample, the differential sensing effect is capable of discriminating ρ from $\sqrt{(\rho\eta)}$. The gradients of the lines give sensitivities of 0.36 $\mu gcm^{-3}Hz^{-1}$ for Famous Grouse whisky, and 0.13 $\mu gcm^{-3}Hz^{-1}$ for Bushmills whisky. To achieve a resolution comparable to the current vibrating tube densitometers of 50 μgcm^{-3}, a system frequency resolution of 387 Hz would be required for the highest sensitivity data. The sensitivity value obtained from the Bushmills data is over 16 times greater than reported by Herrmann et al for the Love mode densitometer using SiO_2 waveguide layers [40], and 700 times greater than a QCM based densitometer [34]. This highlights the large sensitivity of the thin polyimide waveguide, even when operating below the theoretical optimum sensitivity at h_{opt}.

6.5 Solvents

Different solvents were used to test for the discrimination of ρ from $\sqrt{(\rho\eta)}$. Solvents generally have low viscosities, theoretically resulting in lower ΔIL, and also have varying combinations of η and ρ unlike the aqueous based solutions where one is dependent on the other. Table 6-3 lists the solvents used.

The samples were tested on a 0.95 μm thick polyimide waveguide device incorporating a smooth and corrugated delay line on the same chip. The corrugated delay line had corrugations approximately 2.3 μm wide and spaced by 2.6 μm, etched 0.5 μm deep.

Table 6-3. Physical properties of the solvent (and DI water) samples. Values are taken from manufacturers or other published data.

Sample	ρ / kgm^{-3}	η / Pas	$\sqrt{(\rho\eta)}$ / kgm^{-2}s$^{-0.5}$
DI water	998	0.0010	0.9998
IPA	785	0.0024	1.3726
Acetone	791	0.0003	0.5031
Ethyl acetate	902	0.0004	0.6300
Amyl acetate	876	0.0038	1.8341
Ethanol	789	0.0012	0.9730
Propylene carbonate	1189	0.0028	1.8246
n-Dodecane	750	0.0014	1.0185
Diethyl malonate	1055	0.0021	1.4885

The frequency and insertion loss results from each delay line in figures 6-21 and 6-22 demonstrate no correlation between $(\Delta f / f)$ and $\sqrt{(\rho\eta)}$, or ΔIL and η.

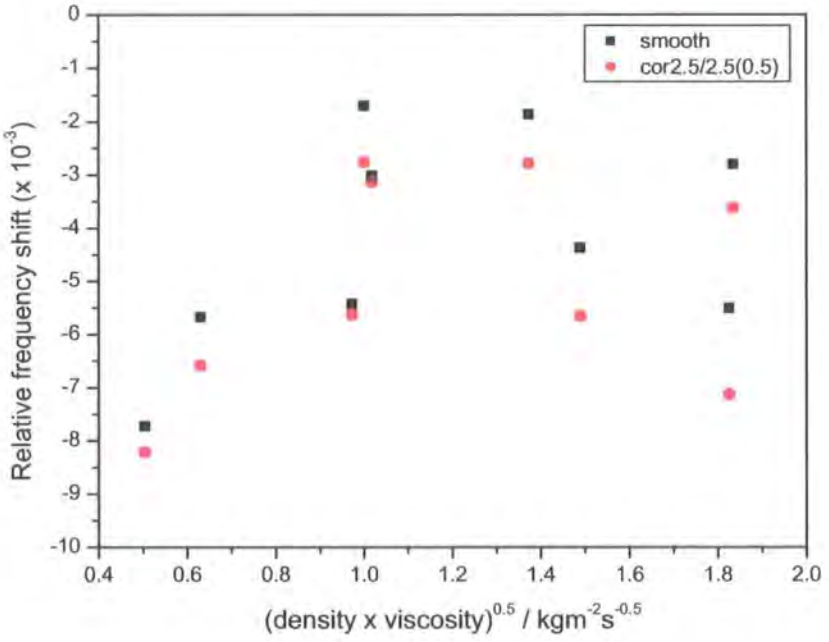

Figure 6-21. Frequency shift of smooth and corrugated polyimide devices (h = 0.95 μm) with solvent and water samples. The error bounds are $(\Delta f / f) = \pm 8\times10^{-5}$.

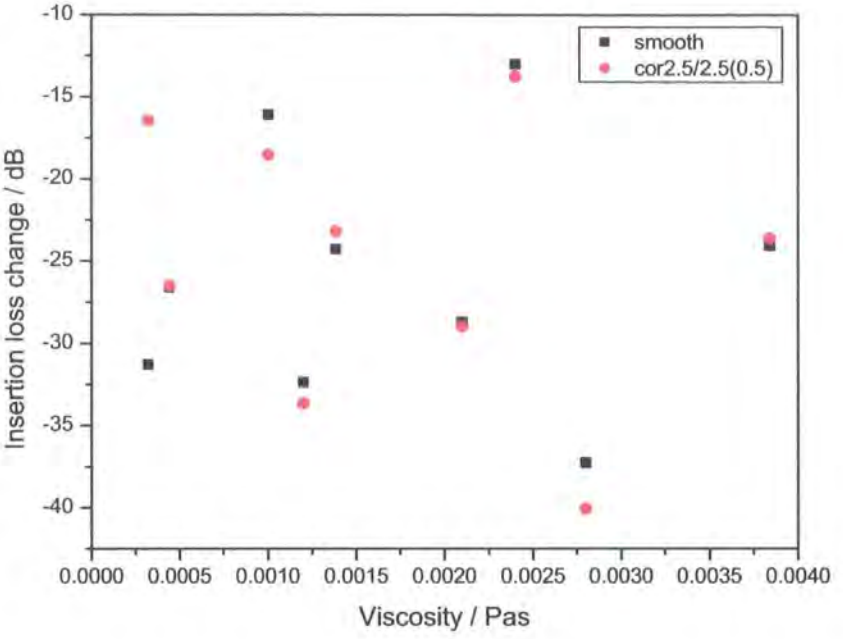

Figure 6-22. Insertion loss response of smooth and corrugated polyimide devices (h = 0.90 μm) with solvent and water samples.

Whilst the data appears random, the responses from each delay line were consistent. These results highlight the susceptibility of the acoustic mode to other non-mechanical factors, in this case probably temperature and sample permittivity. The former occurred due to evaporative cooling of the device surface: this was particularly noticeable with acetone, causing a reduction to 10°C.

Figure 6-23 shows a strong linear relation for the (Δf / f) difference between the smooth and corrugated data with sample ρ, with a correlation coefficient of R = –0.90 for the computer-generated linear regression line. The line gradient gives a sensitivity of 2.74 μgcm^{-3}Hz^{-1}. The results from three different trials spread over two days are shown in figure 6-24 for comparison, to evaluate the reproducibility of this sensitivity value. Trial 1 has a correlation R = -0.84 and a sensitivity of 2.41 μgcm^{-3}Hz^{-1}, and trial 3 has a correlation of R = -0.85 and a sensitivity of 1.93 μgcm^{-3}Hz^{-1} (the results for trial 2 are those presented in figure 6-23). The measurement uncertainty was (Δf / f) = ±1.6×10^{-5}, and whilst this allows correlation between some of the data points in the separate trials, there still remains a large overall shift, especially between trial 2 and trials 1 and 3. The errors allow for the variation in sensitivity between the trials, but

whilst the gradient gives the sensitivity (and thus ultimately the sensor resolution), the reproducibility of the absolute shift is vital to maintain accuracy.

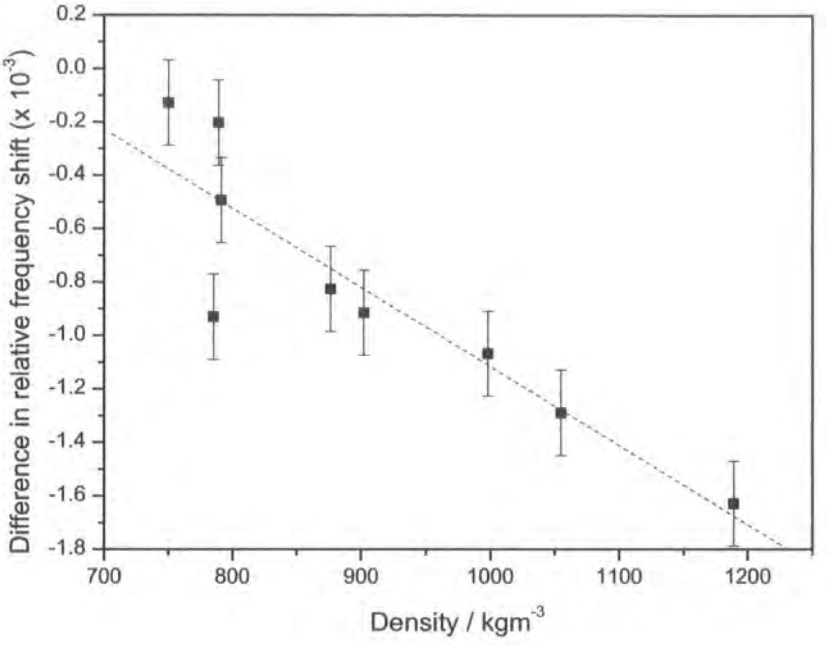

Figure 6-23. Difference in relative frequency shift between corrugated and smooth delay lines with solvent and water samples. The error bounds are $(\Delta f / f) = \pm 1.6 \times 10^{-5}$.

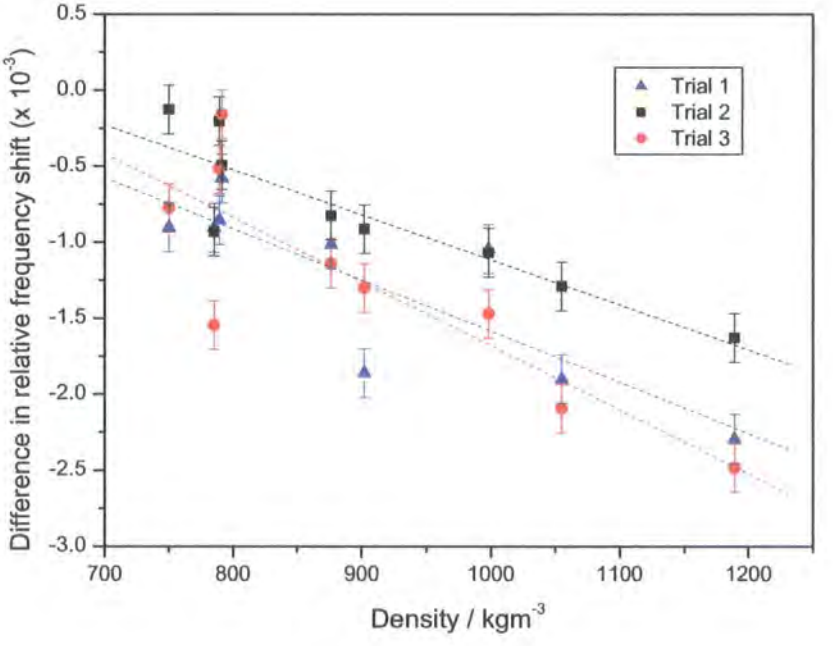

Figure 6-24. Difference in relative frequency shift between corrugated and smooth delay lines for three trials with the same device and samples. The error bounds are $(\Delta f / f) = \pm 1.6 \times 10^{-5}$.

The results clearly exhibit a strong correlation demonstrating the discrimination of ρ from $\sqrt{(\rho\eta)}$ due to the additional mass loading contribution from the trapped liquid. The variation in sensitivity can be partially accounted for by the estimated measurement uncertainty (although these may be too large as discussed earlier) but the spread of data demonstrates the inability to make a single accurate measurement. Inconsistencies could arise from a combination of sample permittivity, device temperature and surface cleaning. The effect of electrical loading by high permittivity liquids have been discussed, although the data for DI water in figure 6-24 is close to the regression line for trials 2 and 3, suggesting the differential frequency measurement could be partially removing electrical loading contribution. Considerable evaporative cooling discussed above was evident during the first trial, and the devices were given more time to stabilise for trials 2 and 3. Effective surface cleaning is vital to return the device to its intrinsic frequency between samples, and difficulties were encountered on some samples, requiring the use of intermediate cleaning liquids and a considerable stabilisation period.

6.6 Summary

Sensitivity analysis with DI water and IPA samples on the three different device structures showed the polyimide devices to be the most sensitive, with $(\Delta f / f)$ in the range -0.5 – -3.0×10^{-3}. The gradient of the frequency shifts follows the $(\Delta f / \Delta h)$ gradient presented in the previous chapter. The sensitivity from the SiO_2 layers was smaller with $(\Delta f / f)$ values around $-0.5 - -1.0 \times 10^{-3}$. The additional insertion losses due to attenuation of the wave were similar for the polyimide and SiO_2 waveguides, and so whilst the latter have a lower intrinsic loss (around 6 dB stronger), the advantages become relatively less with sample loading. The multilayer devices incorporating polyimide and SiO_2 showed a poor sensitivity response with a large range of $(\Delta f / f)$ and little relation to the waveguide thickness. The theoretical low loss advantages were not evident, with the devices spanning a large range of ΔIL comparable to the single layer devices.

Liquid loading tests on corrugated devices demonstrated an additional frequency shift proportional to the trapped liquid volume for up to a 50% trough surface area. For smooth devices the largest (Δf / f) was given by IPA due to its higher viscosity producing the largest viscous loading effect, and for the corrugated devices the largest (Δf / f) was given by DI water due to its higher density giving an additional mass loading. This showed the discrimination of density from the square root of the density-viscosity product. The insertion loss increases given by the corrugated devices were partially attributed to compressional waves being forming off non-vertical sidewalls, and also due to electrical loading with the higher permittivity DI water producing a larger ΔIL than the relatively low permittivity IPA. The reduced waveguide thickness in the etched trough areas increased this electrical loading effect by allowing stronger capacitive coupling with the IDTs.

Measurements using sucrose solutions on polyimide devices showed a strong dependence of (Δf / f) on $\sqrt{(\rho\eta)}$, and of ΔIL on η. The (Δf / f) response was linear for $\sqrt{(\rho\eta)} < 1.45$ kgm^{-2}s$^{-0.5}$ and ΔIL linear for $\eta < 0.0019$ Pas, corresponding to 20% sucrose content. The reduction in sensitivity for higher concentrations was attributed to the complex Maxwellian behaviour of high viscosity liquids at high frequencies, and possible surface-slip effects. The differential responses $(\Delta f / f)_{\text{corrugated-smooth}}$ were uniform with no dependence on ρ, probably due to the dominance of the concentration viscosity over density, and the reduction in sensitivity at higher concentrations (higher viscosities) due to Maxwellian behaviour. The corresponding results from SiO_2 waveguide devices were similar, but with lower sensitivities due to the material properties and operation with significantly thinner waveguides than theoretically required. The smooth SiO_2 ΔIL values were lower than for polyimide, but the corrugated values were much larger, negating any advantage of the lower intrinsic losses.

Sample loading with commercial spirits and liqueurs demonstrated the ability of the polyimide waveguide sensors to discriminate between different liquids. The frequency response (Δf / f) showed a weak correlation with $\sqrt{(\rho\eta)}$, and the ΔIL values showed a stronger correlation with the sample viscosity. The differential response $(\Delta f / f)_{\text{corrugated-smooth}}$ exhibited no correlation with the density producing a uniform response similar to the sucrose results. This was partially attributed to varying electrical loading between the samples, and mainly to the non-linear sensitivity over the viscosity

range. Differential frequency measurements taken of diluted whiskies demonstrated a strong correlation between $(\Delta f / f)_{\text{corrugated-smooth}}$ and density, with sensitivities of 0.36 $\mu gcm^{-3}Hz^{-1}$ obtained for Famous Grouse whisky, and 0.13 $\mu gcm^{-3}Hz^{-1}$ for Bushmills whisky.

Multilayer devices using SiO_2 base layers and polyimide upper layers were tested alongside the single layer devices in many tests. The results presented in this chapter with spirits and liqueurs combined with their characterisation from the last chapter demonstrate their inconsistencies with the other devices and inability to produce a response proportional to the sample characteristics. The main theoretical advantage of low insertion losses was annulled by the large additional loaded losses.

Measurements using a range of solvents on polyimide devices demonstrated that although the individual $(\Delta f / f)$ on $\sqrt{(\rho\eta)}$, and ΔIL on η responses showed no correlation, the differential response, $(\Delta f / f)_{\text{corrugated-smooth}}$, could still be used to discriminate the density with strong correlations up to R = -0.90 obtained. The correlations gave sensitivity values between 1.93 $\mu gcm^{-3}Hz^{-1}$ and 2.74 $\mu gcm^{-3}Hz^{-1}$, although the reproducibility of absolute values between different trials was outside the error bounds.

7 Device simulation

This chapter discusses finding suitable software for simulating SAW sensors and devices. The unusual placement after the results chapters follows the failure to find a modelling solution at the beginning of the project. The discovery of some SAW transducer simulation software near the end of the research was used to analyse the response of the fabricated devices. Details are also given into the design of some SAW resonator structures which could offer an alternative to a simple delay line.

7.1 Device modelling

Studies of Love mode sensors from the main groups discussed in this work show no evidence of prior modelling and simulation. A software modelling tool would enable verification of design ideas with the possibility of altering various parameters to simulate devices, reducing practical experimental research. Electrical simulation of the SAW could allow factors such as substrate cut and rotation, and the IDTs design to be investigated, looking at characteristics such as peak frequency, peak shape, and insertion losses. Physical modelling could be used to simulate the waveguiding effect, and the interaction with the liquid.

7.2 Microsystems simulation

A new approach to modelling software design for Microsystems Technology has been required to cover different analysis problems:

- Mechanical structures – e.g., beams, cantilevers, membranes, gears.
- Optical structures – e.g., waveguides, mirrors, photodetectors.
- Fluidic structures – e.g., turbines, pumps, channels.
- Actuation – e.g., electrostatic, piezoelectric, thermal, external loading.

Coventorware from Coventor is a leading package for the design and simulation of MST devices. The design is entered as mask layers, and a solid model constructed by defining a series of processes and materials using the mask layers, similar to physical fabrication. The model is then converted into a mesh and boundary conditions applied to define the points of actuation, and analysis. A number of solver modules using the Finite Element Analysis method (FEA), can then be used to simulate the required characteristics such as flexure, capacitance or resonance etc [100].

Coventorware was investigated for the simulation of SAW sensors, with the initial idea that the ability to model piezoelectric and fluidic devices could allow investigation of the fluid / sensor interface and the effect of the surface patterning. However, during the familiarisation of the software, it soon became apparent that there was no obvious way of modelling SAW devices. Communications with the Coventor technical support in February 2002 confirmed SAW analysis was not currently possible. Following a

conversation with Charles Dupillier (Head of Technical Support for Coventorware, Europe) it emerged that many requests had been made for a SAW simulation module, but nothing was planned due to the analysis complexity. He was also certain that no other SAW sensor simulation software existed.

7.3 Piezoelectric modelling

7.3.1 ATILA

Investigations were made into software for solving piezoelectric material simulations. ATILA, (Analysis of Transducers by the Integration of LAplace equations) from Cedrat Technologies in France was developed over 20 years ago for the French and US navies. Cedrat's agents, Magsoft Corporation, confirmed ATILA could model the separate components including fluid-solid interactions, piezoelectric actuation etc, and that SAW simulation could be possible with simplifications. A 60-day evaluation version of ATILA was started in mid-June, 2002.

ATILA can be used to model a variety of characteristics:

- Active materials with piezoelectric, magnetostrictive, electrostrictive, and shape memory characteristics, along with many other elastic materials;
- Actuation in the form of applied electrical potentials, magnetic fields and mechanical forces;
- Strong coupling between fluid and solid domains.

ATILA is structured in a similar way to Coventorware, with *Supervisor* linking together separate elements of a bottom-up design process. Familiarisation was gained through a tutorial designing an ultrasonic underwater transducer.

7.3.2 Trial simulation

A trial simulation made up from a periodic electrode structure on a piezoelectric substrate was made to examine SAW devices. A solid device model was constructed with the *Pre-flu* module by entering corner coordinates joined by edge lines. A 2-dimensional, extruded model built up in repeated elements (for periodic structures) simplified this process. ATILA then automatically constructed faces and volumes for each region, shown in figure 7-1a.

An FEA mesh was then constructed on the solid model by defining mesh nodes on the lines, followed by the faces, and finally the volumes. Wave-like structures require 3 mesh points per wavelength, but 4 mesh points were necessary due to the SAW electrodes. A relatively small mesh was used near the substrate surface, with increasing size with depth (figure 7-1b).

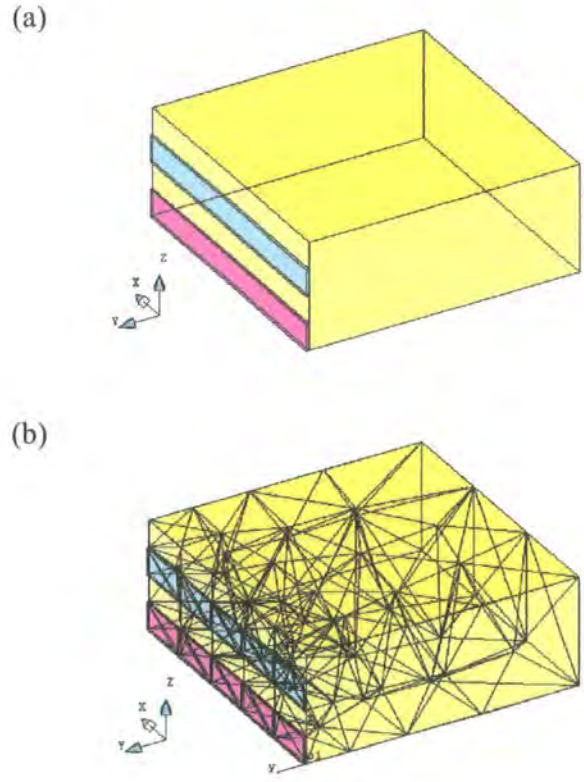

Figure 7-1. Unit structure of SAW simulation. (a) Shows the solid model with two electrodes on a piezoelectric substrate, and (b) shows the meshed model.

The meshed model was prepared for solving with the *Pre-ATI* module. Harmonic analysis was selected for the SAW structure with a frequency range of 50 – 200 MHz in 100 steps. The device unit structure was copied and transposed at this stage to include 8 complete wavelengths. Materials were chosen or input to define the model components. Quartz is included in the materials library with its complete range of piezoelectric coefficients, and was applied to the substrate region using a previously declared 'polarisation' to orientate the quartz with a rotation of 42° (ST-cut) around the x-axis. A generic 'metal' was assigned to the SAW electrode regions. Boundary conditions were finally applied, in this case a sinusoidal voltage applied to alternate electrodes.

ATILA chose the correct analysis subtype by analysing the materials and the defined boundary conditions. Each mesh node was subsequently solved at the declared frequencies. The ultrasonic transducer tutorial solving times were typically 20 minutes, but the SAW trials sometimes took in excess of 24 hours.

7.3.3 ATILA simulation results

Isotropic value parameters such as nodal displacement or potential are observed with a visual colour-coded model in *Isoval.* Alternatively, a single node may be studied in detail graphically with *ATICurve* to observe resonance modes, etc.

Figure 7-2 shows the resonant frequencies at nodes 1969 and 1999 between alternate fingers. Possible resonance modes around 132 MHz and 179 MHz with displacements of a maximum 6.752 Å may be observed. These results were unrepeatable with subsequent models having different characteristics. Figure 7-3 shows the regional displacements at 141 MHz (no expected resonance) and 179 MHz (expected resonance). The two figures are similar, and illustrate no shear displacement patterns, with the values random throughout the device ranging between ±1 nm. This was characteristic of all the visual results.

7.3.4 Conclusions on ATILA

ATILA's initial problem was the bottom–up design flow, making layout and mesh alterations time consuming. The second area of concern was with the solving times, often in excess of 24 hours for the relatively simple problem.

Throughout the trials with different SAW resonator structures, it was not possible to simulate SAW propagation with ATILA. As a result, no attempts were made to introduce the waveguide layer or liquid loading, and further use of the software was abandoned.

Finite element modelling of SAW devices is a time consuming process due to high level of complexity with many finger-pairs each acting like a point source, and the resultant displacements being made up from a superposition of the interfering components. A study by Atashbar has demonstrated FEA of SAW devices and the propagating wave using a simple single-finger pair transducer [101]. However, even for this simple model, the solving typically took a day.

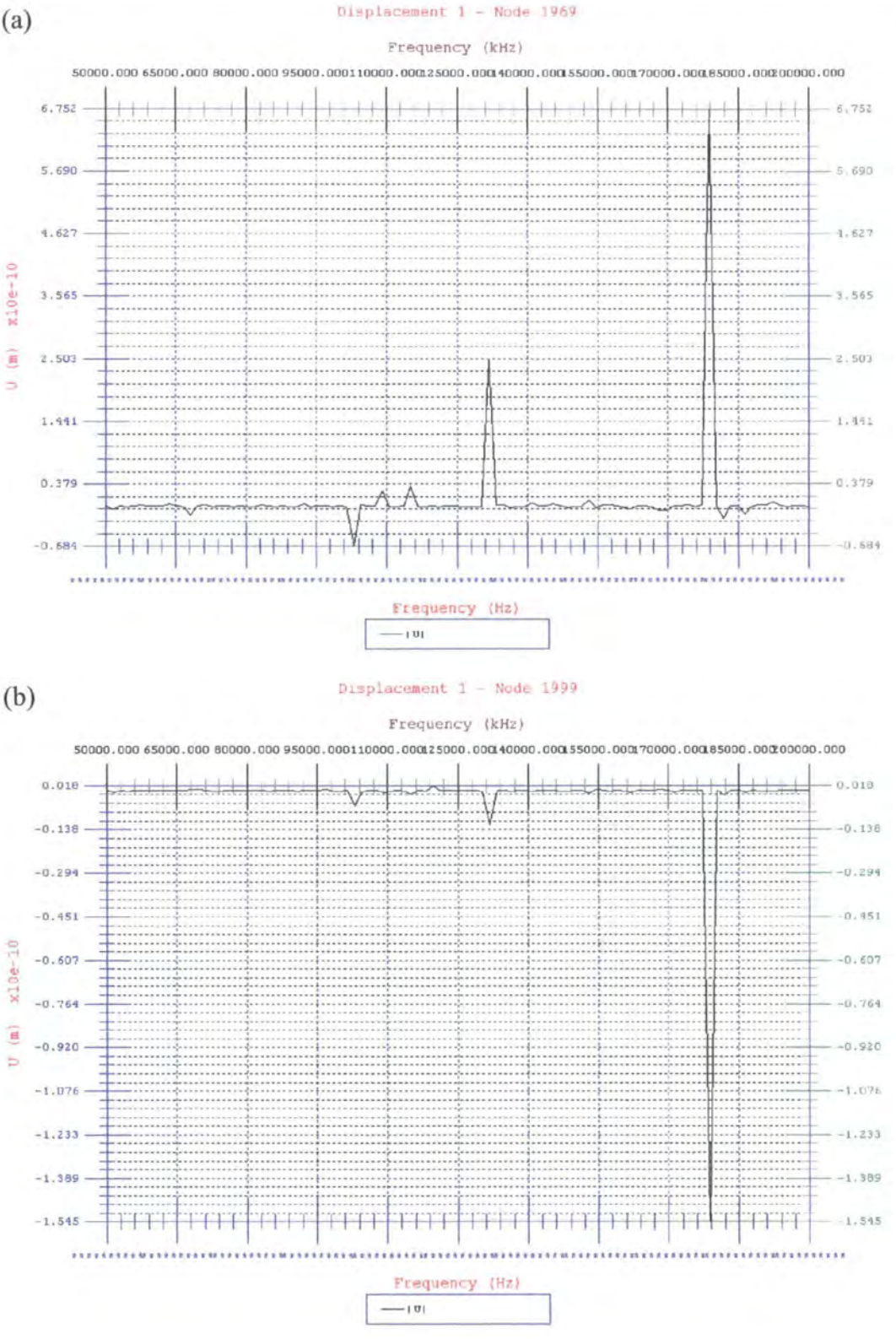

Figure 7-2. ATILA results - Resonant responses at two nodes positioned between electrode fingers.

(a)

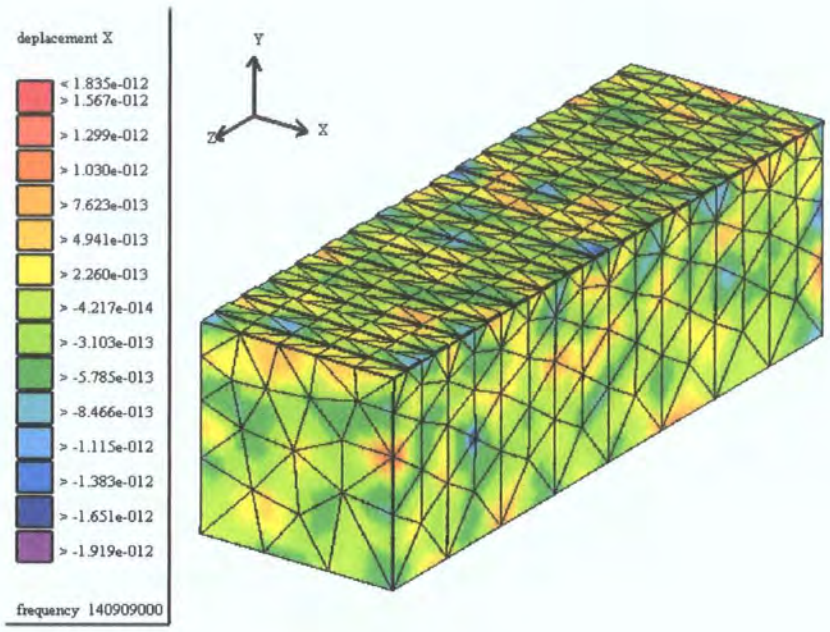

(b)

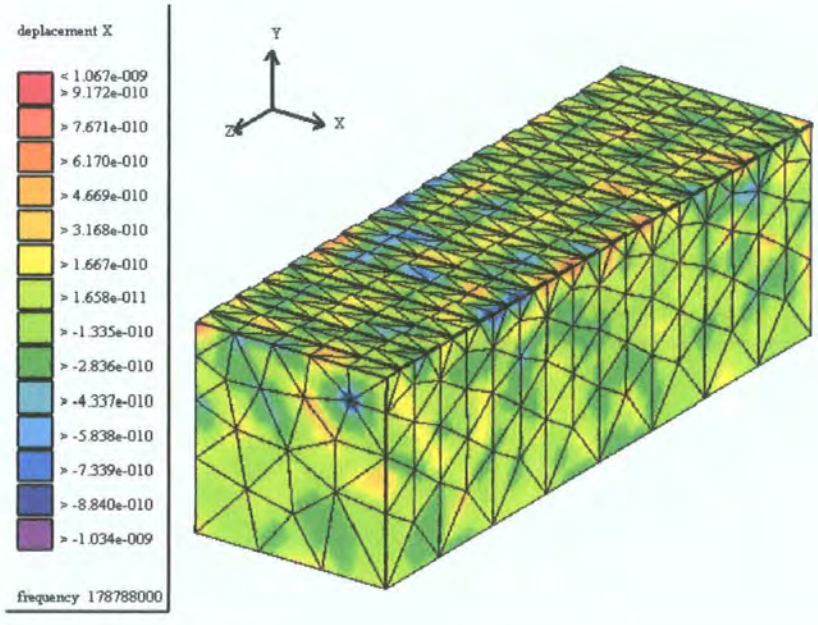

Figure 7-3. ATILA results - Regional displacements at 141 MHz and 179 MHz (note change in scales).

7.4 Electrical SAW device modelling

Following the failure in finding software in either the microsystems or piezoelectric actuator areas, a search was made into electrical characteristics modelling solutions. Two research groups working on modelling were identified: that of Ken-ya Hashimoto from Chiba University, Japan [102], and Samuel Richie from University of Central Florida, USA [103, 104]. The work from Japan appears to be based on fundamental SAW device properties, capable of modelling the acoustic velocities of materials with overlying metal transducers, and other factors such as coupling efficiency. Conversely, the research from Florida is more involved with the electrical device characteristics for filters and resonators, capable of modelling band pass properties.

Both Hashimoto and Richie were contacted for advice on the use of their software (both of which are available for free use) and the capabilities. They were also asked if they knew of any other software which may be capable of simulating the response of SAW sensors. Unfortunately no reply was received from either of them. The Richie software was downloaded from the University of Central Florida website, but there was no success in running the program, and no reply was received from a communication asking for advice.

All other references to design software lead to in-house commercial solutions from SAW filter manufacturers and developers. Following this failure to find a software solution, research into modelling was suspended in favour of experimental work.

7.5 Transducer simulation with TRES2

Following discussions with David P. Morgan, the author of [45, 105], at the IEEE Ultrasonics, Ferroelectrics and Frequency Control (UFFC) conference in August 2004, Montreal, Canada, a meeting to discuss the modelling of the transducers was arranged. The aims of this were to verify the cause of the multiple peaks in the Love device responses, and to discuss the possibility of designing a resonator structure.

A piece of software called TRES2 was written by Morgan to analyse the response of transducers on non-layered (i.e., no waveguide layer) SAW devices. The program is designed for symmetric device structures (Tx and Rx IDTs identical) with unweighted (equal length fingers) and regular IDT and reflector grating structures. It is capable of analysing a grating-transducer-transducer-grating resonator structure as shown in figure 3-16, and will give the expected frequency response and other electrical characteristics.

One main aspect of the program is the ability to analyse the transducer response including the reflectivity of the IDT fingers and gratings (obviously required for resonator simulation). The reflections are caused by the discontinuity in the surface due to the proud metal electrodes, and a similar effect can be caused by grooves. Embedding the electrode structure in a depression so that the surface remains planar is one method of reducing the effect. For the standard IDTs used in this study with two electrode fingers in each period, the reflections of each finger can add coherently producing a strong effect. By using 3 or 4 electrodes in each period (split finger IDTs) the reflections do not add coherently reducing the effect. Due to the early lithography limitations, a 2-finger structure was chosen.

The device structure is entered into the program in terms of transducer and grating geometry, substrate material, operating and analysis frequencies, and the reflectivity (r_s/i) of each finger given by equation (5-1). Using the data, the program calculates the response by analysing the P-matrix components using the coupling-of-modes (COM) equations [106]. The P-matrix method analyses transducer structures by taking into account the voltage and current at the electrical ports, and the acoustic wave amplitudes at acoustic ports, as shown in figure 7-4. 'Cascading' the matrices allows more complex structures (i.e., a whole device, or IDT) to be built up from smaller components (an IDT or single finger pair).

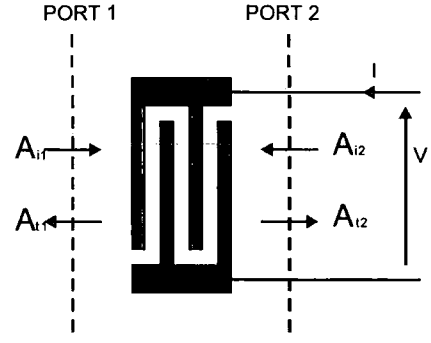

Figure 7-4. Acoustic and electrical ports on an arbitrary electrode structure.

7.5.1 Delay line simulation

Figure 7-5 shows the simulated frequency responses of a delay line with different reflection coefficients, varying from (r_s/i) = 0.0000 to (r_s/i) = 0.0200. The value of (r_s/i) = 0.0019 was calculated using the actual Al thickness evaporated of 0.15 μm and the 40 μm wavelength in equation (5-1). The IDTs contain 80 finger pairs (0.5

metallisation ratio) at 40 μm, with an aperture of 3 mm and propagation path length of 1.6 mm (40 λ). The program is designed for resonator analysis and requires a grating at each end of the device. A dummy single strip grating was input to allow the solving – this will have negligible effect on the response.

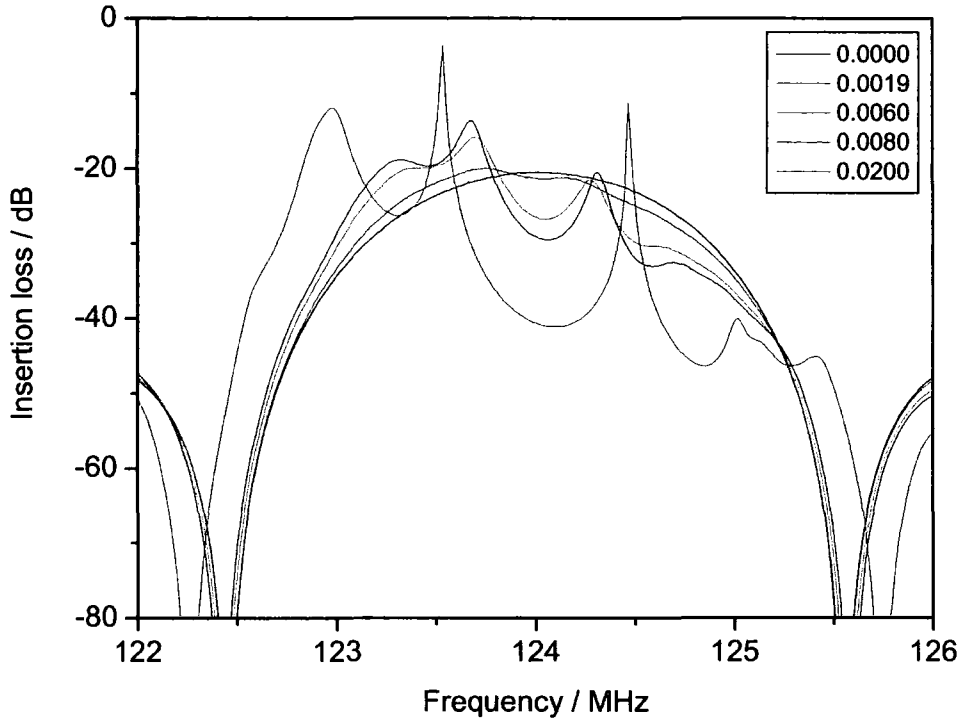

Figure 7-5. Simulated band pass shape with different reflection coefficients.

The response for zero reflection shows the idealised SAW response with a smooth |sinc| function. For the expected reflection (this is based on the metal thickness used, but no waveguide layer) of 0.0019, a 'notch' is introduced to the top of the main peak, with the shape of the peak shifting to lower frequencies. As the reflectivity increases, the notch increases producing two separate peaks, the lower frequency peak being strongest. At (r_s/i) = 0.0800, the strongest peak is at f = 124.680 MHz and 13.59 dB, and the smaller one is at 124.312 MHz and 20.34 dB, with a dip in the middle down to 29.43 dB, highlighting the strong constructive and destructive interference of the reflected waves. Further increases in (r_s/i) increase the strength and Q of the multiple peaks, and the depth of the dip. Additional peaks also form at the extremities.

Whilst the simulations are based on ST-X quartz, not ST-Y as used in the device fabrication, and the calculations do not include the effect of the waveguide layer, the responses show a remarkable similarity in both shape and magnitude to the measured results from polyimide coated Love mode devices. Figures 7-6 and 7-7 show the responses from a device with a 0.84 μm thick polyimide waveguide, alongside the simulated responses for (r_s/i) = 0.0060 and 0.0080. An important point to note is that there has been no manipulation or shifting of data, and the shapes almost exactly coincide.

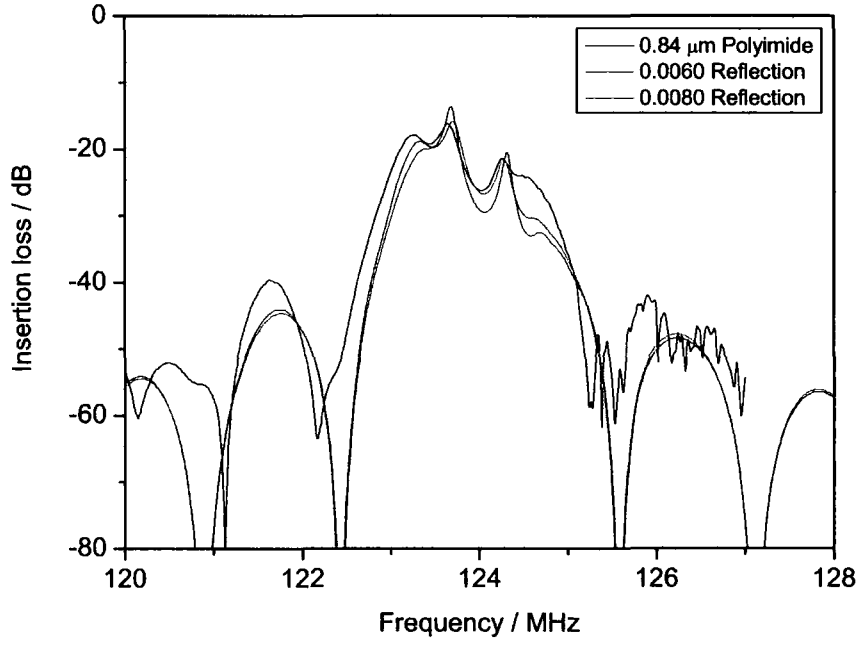

Figure 7-6. Comparison in band pass shape of 0.84 μm polyimide Love, mode device with simulated responses of 0.0060 and 0.0080 reflectivity.

The (r_s/i) = 0.0060 simulated response follows the measured response most closely with similar insertion losses for the multiple peaks and dip. Whilst the (r_s/i) = 0.0080 simulated response appears to follow less closely in terms of insertion loss, the frequency characteristics are closer to the measured response, with the difference in frequency between the two peaks of 0.632 MHz close to the actual difference of 0.621 MHz. The value for the lower reflection simulation is 0.581 MHz. The frequency is fundamental to the device structure, whereas the insertion loss can be dependent on other factors, so these results suggest that a suitable approximation of the polyimide Love-mode devices can be made using a reflection value of (r_s/i) = 0.0080.

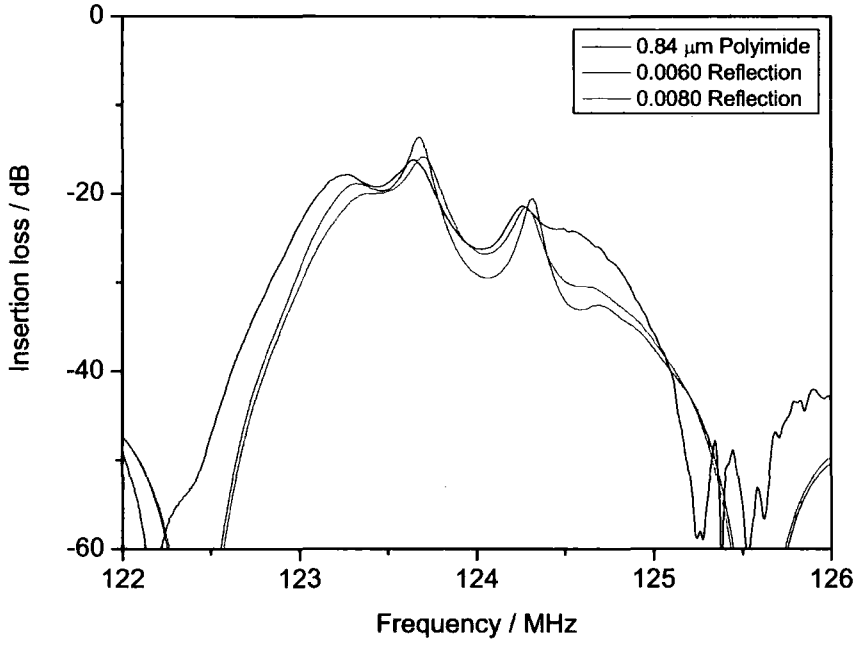

Figure 7-7. Close-up of previous figure showing the peak detail.

The significant correlation between the measured and simulated responses proves that the multiple peaks in the device are due to reflections occurring in the IDTs. The multiple peaks in the simulated devices purely arise from reflection, as shown in figure 7-5, and therefore the identical measured response is also due to reflections. These peaks will have implications on the control of the sensor requiring electronics capable of discriminating the peaks and locking on to the highest. The effect can be reduced or even removed by using split-finger IDTs that will prevent the reflections adding constructively. This was not possible for this study due to lithography limits – 4 fingers in a period gives finger widths and spaces of 5 μm, and the expected defects would greatly reduce the device yield. However, for a commercial fabrication facility, this would be possible, and an obvious design choice.

7.6 SAW Resonator sensors

One principal disadvantage with the delay line structure used in this study is the multiple peak response resulting from reflections, although this can be reduced as discussed. The main disadvantage of the delay line structure is the large insertion loss, due to acoustic losses into the liquid through the propagation path, and due to capacitive losses with high permittivity liquids.

Many Love mode delay line devices confine the liquid to the propagation path with a cell and include an electrical shielding layer. However the requirement of an open sensor precludes this solution as discussed earlier. The IDTs could be spaced closer reducing the propagation path length, and whilst this would reduce the insertion loss, reflections between the separate IDTs could become prominent, and capacitive losses would still be incurred. The use of a resonator structure would allow the reflection limitations of the current device to be exploited, reducing the propagation path length, and giving a higher-power and narrower bandwidth peak, with a larger Q.

SAW resonators can be used for sensing in an identical manner to SAW delay lines, allowing the measurement of physical changes to the substrate such as temperature or stress [58]. Gas and biological sensors using polymer films deposited on resonators have been extensively researched, although these are not always technically Love mode devices, and simply use the film for passivation and as a selective absorptive layer [107-111]. Some of these devices appear to confine the coating to the 'cavity' between the IDTs (analogous to the propagation path in a delay line), whilst others coat the entire structure. Both quartz and lithium tantalate ($LiTaO_3$) substrates were used, with most of the studies using commercially fabricated resonators operating at 380 MHz, 433 MHz, 701 MHz, and 1 GHz. The use of commercial devices was perhaps due to the complexity of designing effective resonator structures, and the higher frequencies permit reduction of the chip size, allowing a greater number of IDT fingers, and grating strips. Alternatively, the choice of device may have been due to availability, and combined research with [107, 109-111] sharing authors. Resonator liquid sensors have also been investigated using a dielectric layer for insulation of the electrodes from the liquid, thin layers (200 nm and 400 nm, $h / \lambda = 0.020$ and 0.040) of silicon nitride (Si_3N_4) [96], and 5 μm thick ($h / \lambda = 0.037$) layers of photoresist [97]. The photoresist device could be acting as a Love mode device (although no mention is made) with the film thickness the equivalent of 1.47 μm for a 40 μm wavelength. The acoustic shear velocity of Si_3N_4 is approximately 9700 ms^{-1}, higher than the $LiTaO_3$ velocity of 4135 ms^{-1} and thus this device is not acting as a Love mode, but using the layer purely for passivation [96]. The study by Nomura et al measures liquid flow properties using a dual resonator structure, with the liquid confined to the resonator cavity by a glass structure. One cavity is bare substrate, and the other uses an electrical shorting metal layer [112]. A study by Barie et al uses commercial 380 MHz resonators on $LiTaO_3$ with SiO_2 waveguide layers to produce Love mode resonator devices [113]. A value of

h / λ = 0.37 is shown for optimum mass sensitivity. This is larger than for the SiO_2 / ST-quartz delay line devices due to the $LiTaO_3$ velocity being approximately 900 ms^{-1} less than for ST-quartz.

7.6.1 Resonator design

The simplest resonator design is a two-port synchronous structure, where the reflective gratings continue the pattern of the IDTs, as shown in figure 7-8. The transducer and grating structure can be made in the same patterning stage and the continuous nature ensures that the wave velocity is the same throughout the device. The IDTs can be spaced close together because the reflections within the IDTs are synchronous with the grating reflections and contribute to the overall device response. The grating strips are spaced λ / 2 so that the Bragg condition $m\lambda = 2d \sin\theta$ is fulfilled and the waves add in phase (in this case, the incident and reflected waves are in the plane of the grating such that θ = 90 °). The reflections actually affect the IDT conductance, and skew the frequency response, and so the grating strip spacing can be increased to account for this. However, in this study we will assume a spacing of λ / 2 for simplification. A metallisation ratio of 0.5 is also assumed.

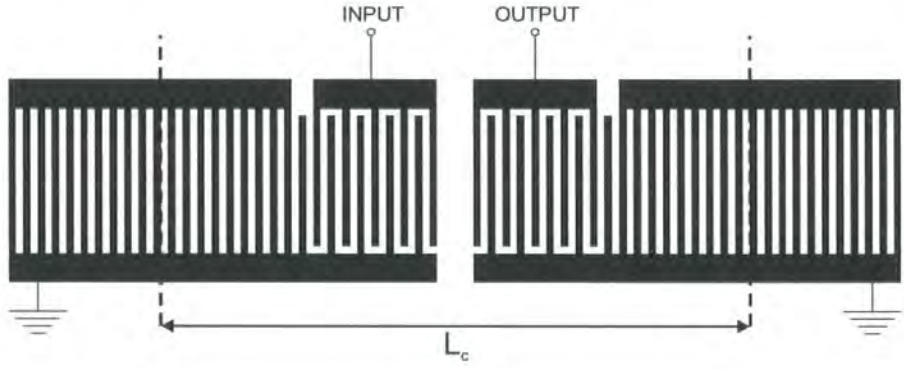

Figure 7-8. Synchronous resonator structure.

The critical design parameter for the resonator is the cavity length L_c. This depends on the effective point in the gratings where the wave is reflected, and the central spacing between the IDTs. The gratings typically act as a localised mirror at strip number $1/(2|r_s|)$ such that the gratings have to contain at least this number of strips for resonance [114]. This factor affects L_c in terms of complete wavelengths.

The spacing between the IDTs is crucial to the device response in terms of fractions of a wavelength. This parameter depends on many factors, and even with sophisticated

modelling techniques, successful design is a matter of trial and error. Common industrial practice is to make experimental masks containing a large range of different device designs, and testing them all for the desired response. This spacing affects the cavity phase change of a complete 'round trip' θ_c and thus the frequency and power of the resonance.

The study by Andle et al investigated resonators on $LiTaO_3$, using central spacings of 5, 49, and 99 λ, with fractional changes at each length [96]. Due to propagation losses, they found the 5 λ spacing regime the most suitable. Variations in the central spacing of 0.1 λ between 4.5 and 5.0 λ were made. Devices with 4.7 to 4.9 λ gave the strongest peaks, and the 4.7 λ and 4.8 λ devices gave the highest sensitivity to liquid loading. The theoretical study by Yantchev et al based on AT-quartz investigated the effect of central spacing on insertion loss, Q, and side-lobe suppression [115]. It found that optimum insertion losses occurred for a length ($n\lambda$ / 2). With a decrease in length to ($n\lambda$ / 2) - (λ /32), the Q reduced and side lobe suppression increased, and an increase in length to ($n\lambda$ / 2) + (λ /32) caused an increase in Q and reduction in side lobe suppression with a value of ($n\lambda$ / 2) + (λ /16) giving two identical power peaks. An experimental study by the same group investigated the effect of polymer coating thickness on the devices, and found an increase in insertion loss with (h / λ), but no change in side-lobe suppression [111]. For thick layers, a secondary resonance peak was observed at a higher frequency than the main peak, causing additional degradation of the main response.

7.6.2 Resonator modelling

TRES2 was used to model some simple synchronous resonator structures on ST-X quartz. A value of (r_s /i) = 0.0080 was chosen based on the previous analysis of the delay lines, and all simulations were made around a central frequency of 124 MHz. Variations in IDT length, grating length, and central cavity length were made. The latter dimension was varied around a central value of 5 λ in 0.1 λ steps.

Figure 7-9 shows the resonator response with varying IDT lengths from 10 periods in each IDT (21 fingers) to 40 periods (81 fingers). The basic response consists of a SAW delay line |sinc| - like trace with a sharp peak in the central lobe from the constructive interference of the reflections. This is an extreme extension of the delay line simulations in figure 7-5. The change with IDT length is similar to the delay lines,

with an approximate increase in power of 12 dB for a doubling in periods. The central lobe also narrows proportionally to the number of periods, but importantly, the resonance peak keeps the same Q, as this is largely dependent on the grating length, and not the IDTs.

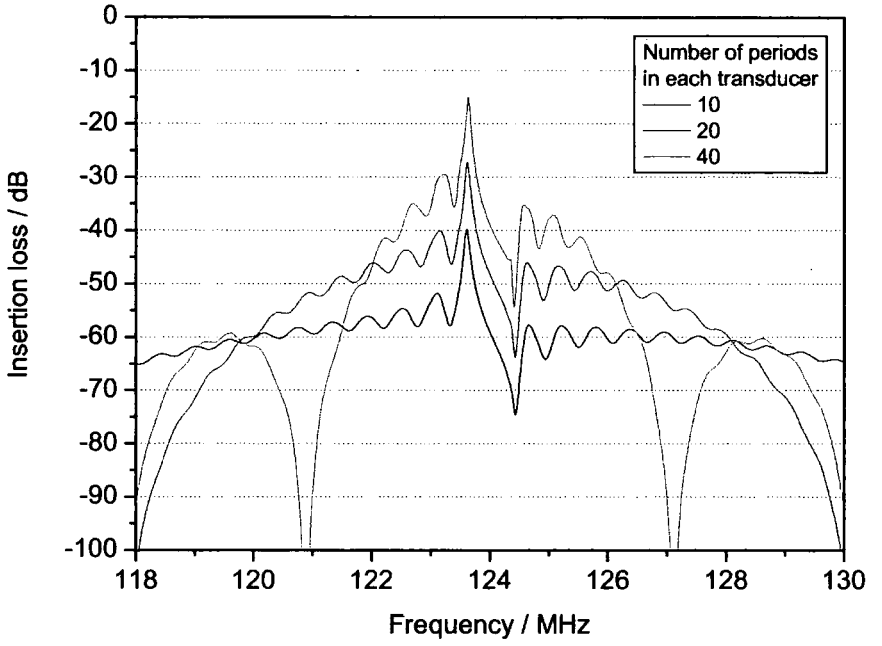

Figure 7-9. Simulated resonator response with variations in IDT length reflective grating length, 5.0 λ central spacing and 200 strips in each grating.

The increased reflection with larger gratings is illustrated in figure 7-10 for 40 period IDTs. The strength of the peak increases from 20.9 dB insertion loss with 100 strips to 8.5 dB with 400 strips. This highlights the need for long reflective gratings, with devices often having 10 times as many strips in each grating as periods in the IDTs. A disadvantage of this is an increase in device size – for example a device with 40 IDT periods and 400 strip grating, and a 5 λ central gap, will have an overall length of 19.4 mm for $\lambda = 40$ μm. The resonance Q increases with number of grating strips, but the spread in frequency between the main peak and side lobe reduces, increasing the chance of frequency hopping when acting as an oscillator.

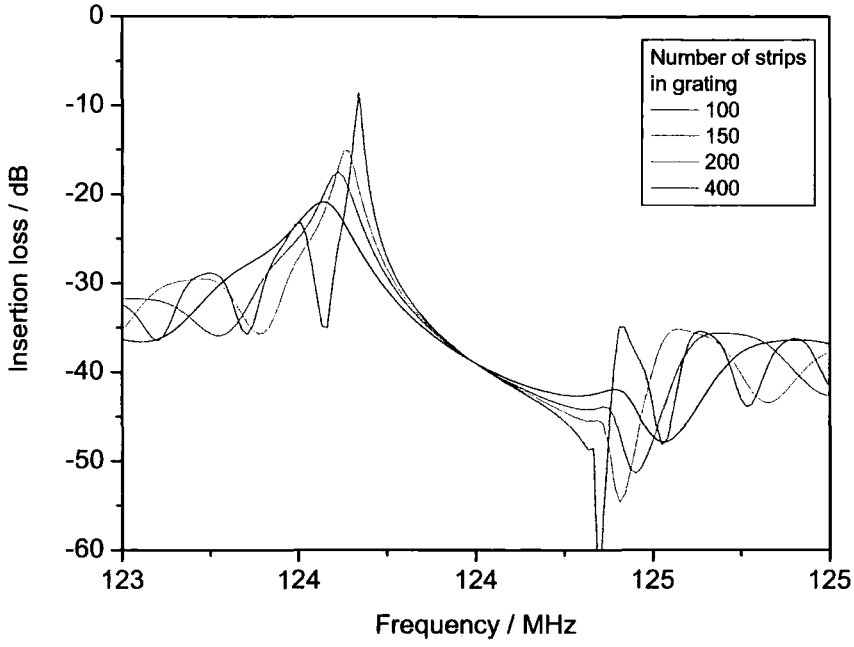

Figure 7-10. Simulated resonator response with variations in number of grating strips, 5.0 λ central spacing and 40 periods in each IDT.

The importance of the exact cavity length to allow constructive interference of the reflected waves is illustrated in figure 7-11. The simulated devices all consist of 40 period IDTs and 200 strips in each grating. This gives an overall length of 11.4 mm at $\lambda = 40$ μm. There are two sets of almost identical responses with a $\lambda / 2$ cycle. The minimum insertion loss is given by a 4.8 (or 5.3 λ) spacing, similar to that in reference [96] using a similar modelling technique, but on $LiTaO_3$. The insertion loss is approximately 10 dB compared with the minimum delay line value of about 16 dB (based on a polyimide thickness of 0.85 μm). This value also gives maximum side lobe suppression.

These simulations indicate the type of response that may be achievable using a simple synchronous design. However, the actual measured response will depend on many other parameters such as metallisation thickness, polyimide thickness, and most importantly, substrate orientation, and would require the fabrication of many design variations to find the optimum dimensions.

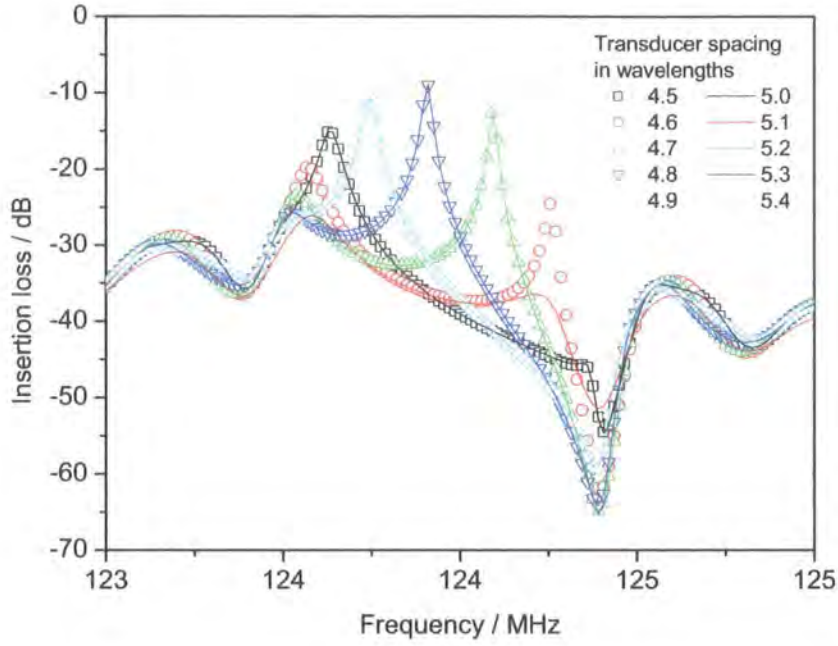

Figure 7-11. Simulated resonator response with variations in cavity length, 40 period IDTs and 200 strips in each grating.

The merits of using $LiTaO_3$ for aqueous liquids due to its high permittivity have already been discussed, with a reduction in loaded insertion loss due to the smaller change in impedance mismatch than when using quartz. The devices also have a lower intrinsic insertion loss, due to the greater coupling efficiency between the electrical excitation and the excited acoustic wave. The increased coupling efficiency increases the reflection coefficient (r_s / i) to 4 times the value for quartz, resulting in a stronger resonant response [96]. Figure 7-12 shows the simulated responses from identical synchronous resonators on ST-X quartz and $LiTaO_3$. The increased acoustic power in the latter is evident with a 0 dB peak insertion loss around 20 dB higher than for ST-X quartz. However the increased coupling efficiency also results in a lower Q due to the larger bandwidth. The side lobe suppression for this particular design is also poor at 3 dB compared with 14.4 for ST-X quartz.

The study by Andle et al shows small increases in insertion loss with liquid loading, with a typical value of 2 dB increase for a liquid of $\sqrt{(\rho\eta)} = 1$, i.e., water (assuming no electrical loading) [96]. With an intrinsic insertion loss of 6 dB, this would give a loaded loss of only 8 dB, compared to the values in the order of 30 dB for the polyimide

Love mode delay lines presented in this study. This is a clear improvement. Conference results presented by Rapp [116] demonstrated a $LiTaO_3$ based resonator operating at 433 MHz with an intrinsic insertion loss of about 2 – 3 dB, and aqueous solution loaded losses of about 6 dB. These results were obtained with the sample covering the entire device surface, highlighting the increased coupling efficiency and reduced electrical loading of $LiTaO_3$.

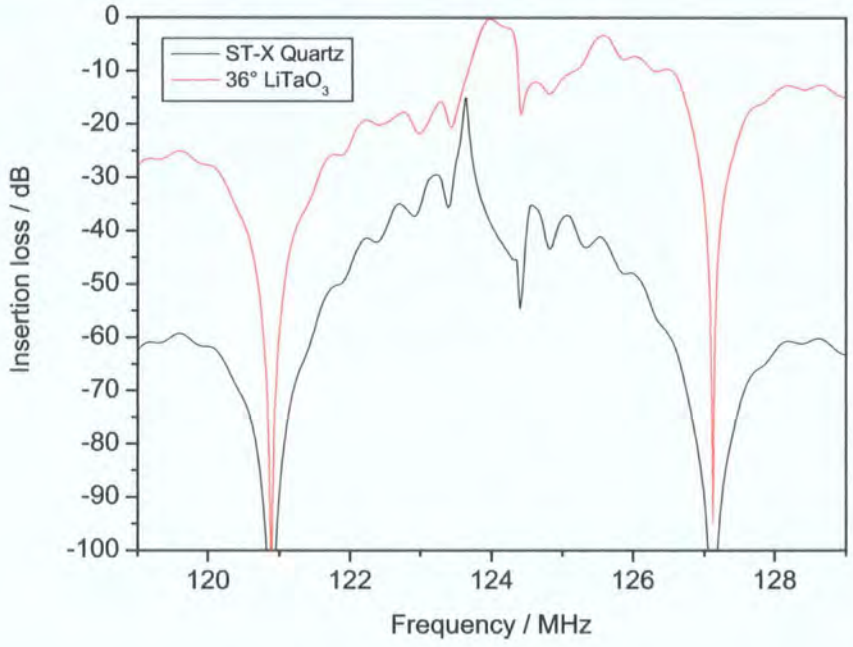

Figure 7-12. Resonator frequency response for identical transducer structures on ST quartz and $LiTaO_3$, 40 period IDTs and 200 strips in each grating.

7.6.3 Resonator conclusions

The brief discussion and simulations presented here show the potential of a synchronous resonator structure for the basis of a Love mode liquid density sensor, replacing the simple delay line structure. The limitations of the single-pass delay line structure in terms of large liquid contact area and reflection problems can be made use of in a synchronous resonator design, in which the IDT reflections are advantageous, and the propagation path can be almost removed.

A disadvantage with a resonator is the increased size. The optimum design presented here (figure 7-13) has 40 period IDTs and 400 strip gratings, with a central cavity length of 4.8 λ. This gives a peak insertion loss of 0.9 dB, a high Q of 13000, comparable to the values in [115], and 24 dB side lobe suppression. The overall length of 19.4 mm at λ = 40 μm is twice the size of a delay line structure. The main loss advantages in the resonators are due to the grating lengths, which are the largest part of the devices, and reductions in IDT length and centre cavity length would be negligible.

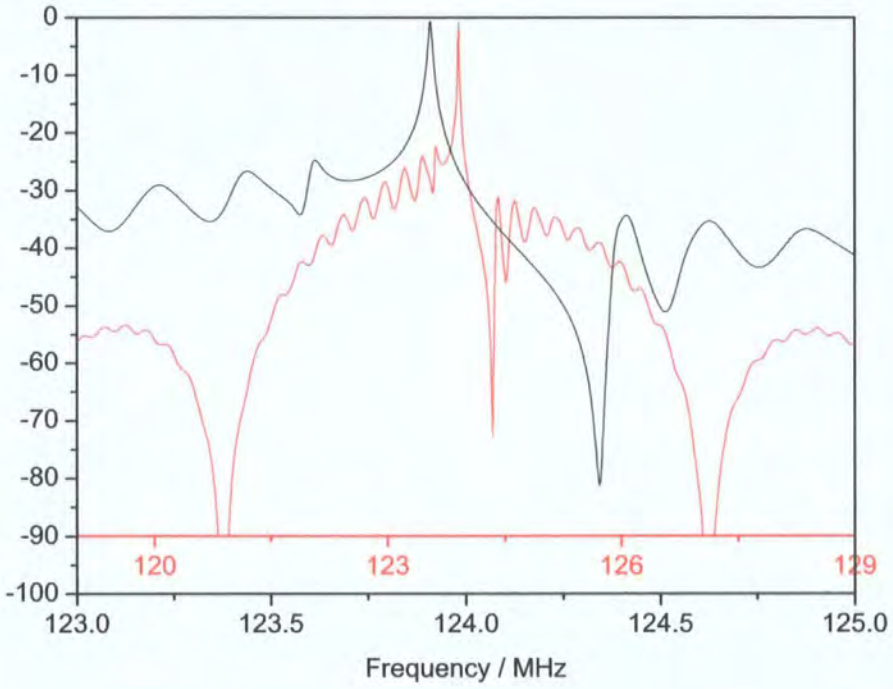

Figure 7-13. Optimum resonator design on ST-X quartz, with 40 period IDTs, 400 strip gratings and a 4.8 λ central cavity length.

The simplest method of retaining the optimum device characteristic would be to reduce the wavelength (increase the frequency) to 250 MHz for example, thus halving the device size. The resonators presented in other studies range between 380 MHz and 1 GHz, presumably partially because of the size limitations. This would however decrease the minimum feature size to between 3.3 and 1.25 μm, beyond the practical capabilities of the fabrication facilities available for this study, and also requiring much thinner waveguide layers.

8 Liquid sensor packaging

This chapter outlines the unusual requirements for the packaging of the liquid density sensor, and some possible solutions. A brief description of current electronics packaging technology is given followed by modification ideas. A prototype package is presented, as well as a description of a design improvement, with both designs allowing the sensor to be positioned in the sample chamber. Finally some recent advances in packaging technology are discussed which could offer a practical commercial route.

8.1 Packaging requirements for sensors

An important element in the development of a microsystems device or sensor is the final packaging which can often pose unusual requirements. Some devices require hermetically sealed cavity packages or controlled environments. These can help reduce problems with stiction in membrane devices such as RF variable capacitors and MEMS accelerometers, and protect small micromachined components [117-119]. Other devices require open packaging allowing the sensor chip to interact with the outside environment. Examples include gas sensors, fingerprint sensors, and liquid sensors. For some devices, the main requirement may be the ability to house a large chip area.

In addition to the chip requirements, the package itself will have complex specifications, including factors such as shape, size and materials. These are important, because unlike ICs which are normally placed on a PCB in a container, the sensor packages are used in-situ, such as an oil sensor in a combustion engine, a gas sensor in an exhaust, or a fingerprint sensor on a security device.

At the start of this study, no commercial packaging solutions suitable for the density sensor application could be found. The requirement of a large open chip surface combined with sealed contacts, backside lead-outs, and small overall dimensions precluded all existing solutions. For this reason, research started looking at adapting existing electronics chip headers, and at complete custom units.

8.2 Electronics packaging

The packaging methods for ICs are well established with a large range of off-the-shelf products. These seal the chip with electrical feedthroughs allowing contact with an external circuit and protection from the outside environment. Materials are often used which allow heat transfer to keep the IC cool. The principle package styles are moulded plastic, cast ceramic, and metal can. The moulded plastic packages are based on a sheet metal lead frame that is cut or etched to create the electrical feedthroughs. At the manufacturing stage, the 'legs' are all connected allowing batch processing. The ICs are bonded to the die-pad and wire bonds made between the chip contact pads and the feedthroughs. The entire device is then moulded in a plastic case and the frame cut to produce the separate components. Figure 8-1 illustrates the method.

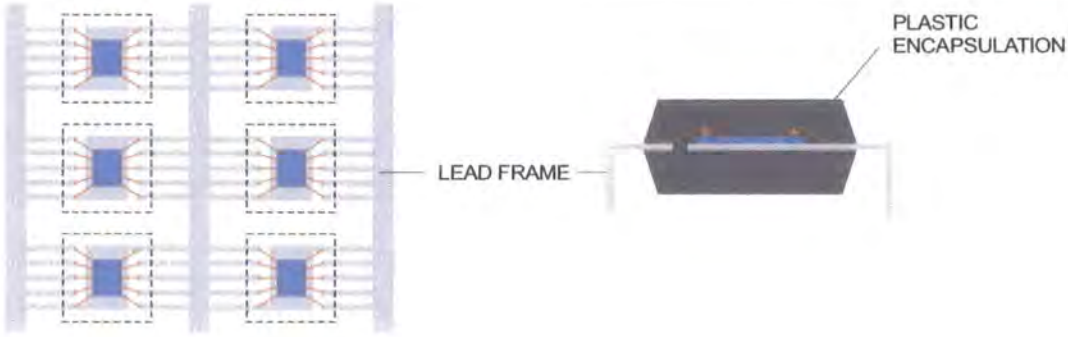

Figure 8-1. Plastic moulded packages. The diagram on the left shows the dies wire bonded to the lead frame before encapsulation and the cross section on the right shows the finished package.

The ceramic headers are made from a cast ceramic base into which the chip is placed and wire bonded (figure 8-2). Au is deposited and patterned part way through the casting process to create the electrical feedthroughs and internal and external contacts. A metal lid is sealed over the top using a solder bead or electron-beam weld. This allows an open cavity (unlike the moulded plastic package) in which the environment can be defined (e.g. low humidity, vacuum, nitrogen), making them suitable for crystal oscillators, etc.

Figure 8-2. Ceramic package cross-section.

Metal can type packages are made from a metal base with electrical wire feedthroughs using insulating collars, and a metal tank lid sealed to the top (figure 8-3). They are familiar as the single transistor package, and are used extensively for discrete component packaging, crystal oscillators and other high frequency components.

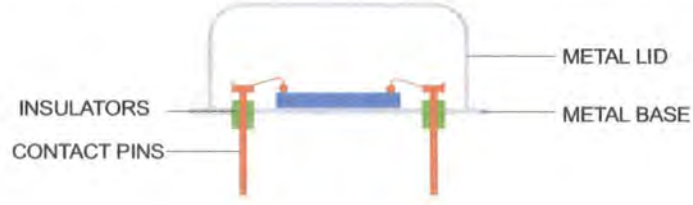

Figure 8-3. Metal can package cross-section.

Some of these designs are suitable for microsystems packaging either with or without alteration. The unusual requirements of the liquid density sensor preclude all these designs in their present form.

8.3 Liquid density sensor package requirements

The two distinct areas which need to be considered for the liquid density sensor are the requirements of the actual sensor chip, and the specifications which will allow the package to be integrated into the sample chamber.

Firstly, the packaging of the chip has the following basic requirements:

- A large open area over the delay line structures for liquid contact.
- Ability to house a large die of approximately 10 mm square.
- Adequate number of electrical contacts for SAW operation.
- Protection of the electrical contacts, both physically and electrically.
- Smooth sealing to the chip surface to allow effective cleaning and prevent sample contamination.
- Resistance to a large range of chemicals.

Secondly, the package needs to be integrated into the existing refractometer sample chamber as shown in figures 8-4 and 8-5. The chamber consists of a stainless steel bowl with a 12 mm diameter hole at the bottom under which is bonded the sapphire prism forming the window. The edges of the hole are chamfered to allow effective cleaning preventing any sharp internal corners from trapping the sample. A Dow Corning epoxy (DC 730) is used to bond the prism to the stainless steel, the adhesive being resistant to most chemicals. A thin layer of adhesive ensures that a minimal gap exists between the two components, preventing liquid trapping. All the refractometers have some form of lid over the sample chamber made of stainless steel or Delrin plastic, with a stub that protrudes and spreads the liquid over the window. The dimensions are such that the gap between the window and the stub is typically 0.5 mm. This enables accurate operation of the refractometer, although larger dimensions may also be used. The type of lid varies, allowing features such as in line measurements with inlet and outlet ports in the lid, and sample temperature control with a heater in the stub.

Figure 8-4. Refractometer sample chamber. The stainless steel bowl with the central window region is positioned towards the bottom of the picture, and the lid with the central stub is in the vertical open position. The UK one-penny coin has a diameter of 20 mm for comparison.

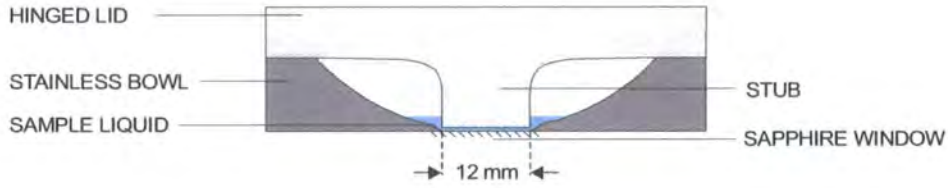

Figure 8-5. Cross-section of sample chamber, showing stainless bowl, lid and stub, window and sample liquid.

The proposed position for the liquid density sensor is on the end of the stub, allowing the sensor surface to spread the sample liquid over the window. The design of the stainless bowl and window area is unchangeable, largely due to the availability and cost of the sapphire prisms for the window, but the lid design is easily altered with few restrictions.

Positioning of the sensor in the lid gives the following packaging requirements:

- The open chip surface needs to be close to the surface of the package to allow close proximity to the window.

- The package needs to be small (and preferably circular) to allow location towards to bottom of the chamber.
- The exterior of the package needs to be smooth for cleaning and contamination control.

The combination of specifications gives some unusual packaging problems: the chip area is large, but needs to be in a small package – ideally the package would not be much larger than the sensor die. Most importantly, the die surface needs to be prominent, but with a sealing mechanism to protect the electrical contacts from the liquids. Finally, the die will probably be square, but the package circular – this instantly makes the package outline larger than the die.

8.4 Initial ideas

8.4.1 Modifying conventional headers

Initial investigations into packaging were based on using a standard ceramic header package, and sealing the wire bonds. Figures 8-6 and 8-7 show two proposed methods to achieve this. The first uses a machined metal lid with a lip sealed to the chip surface using a silicone adhesive. This protects the wire bonds from the sample liquids and would be robust. However, the lid would have to be custom made, and correct assembly of the package ensuring effective sealing would be time consuming and expensive. The internal corner by the adhesive could be difficult to clean and the depth of the sensor surface from the top of the package would be dependent on the lid design and underlying electrical contacts.

Figure 8-6. Method of sealing electrical contacts using a metal lid and ceramic base. The ceramic package is based on the electrical header illustrated in figure 8-2.

An alternative method is to use a sealant or epoxy to encapsulate the wire bonds as shown in figure 8-7. Correct choice of sealant viscosity would allow controllable deposition around the chip over the wire bonds to seal the die edge, without 'slumping' and covering the sensor surface. Curing of the sealant would produce a smooth surface and a continuous join to the chip surface preventing any cavities or corners that may trap the samples. This method would be robust if the correct chemical resistant sealants can be obtained. The sealing would be more effective than the metal lid method and cheaper to achieve, and the depth of the chip surface from the top of the package reduced.

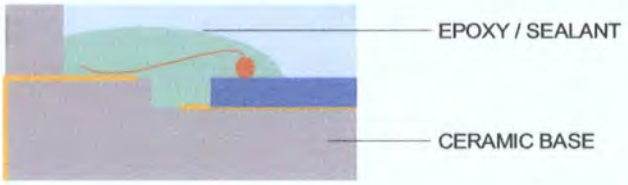

Figure 8-7. Alternative method of sealing using sealant or epoxy.

Many of the test samples used the encapsulation method, proving the practical operation of the devices and ease of cleaning. 'Araldite Rapid' epoxy was used – a two-component household adhesive designed for quick curing at room temperature. The five-minute work time allowed the epoxy to be dropped around the edge of the die over the wire bonds, and to slump over the edge of the chip, creating a smooth join without covering the entire surface. The photos in figure 8-8 show the encapsulated devices.

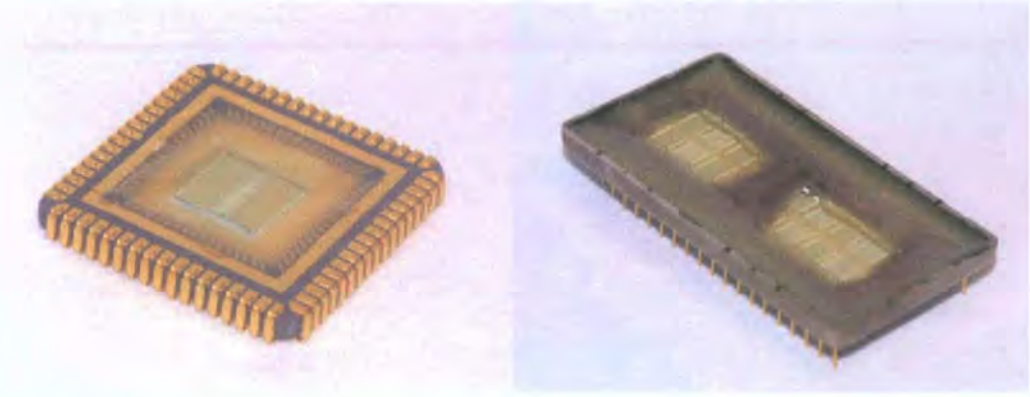

Figure 8-8. Encapsulated test devices using a Kyocera ceramic header (left), and a metal 'bath-tub' header (right). Araldite Rapid epoxy has been used for encapsulation.

Sealing of conventional electronic headers could offer a practical package for the liquid density sensor, if suitably sized and shaped headers can be sourced. One major problem is with the size of the sensor die. Large complex ICs require a large number of pins and thus the packages suitable for the large sensor die have a large pin count, which increases the outside dimensions of the package.

8.4.2 Backside contacts

To fulfil the requirement of prominent chip surface and small outline, an arrangement with electrical through-wafer interconnects (ETWI) would be advantageous. This reduces the need for topside sealing, topside protrusions (the wire bonds), and potentially a reduction of the package size to the sensor die dimensions. The two aspects of fabricating such an assembly are the production of contact vias through the quartz substrate, and the package design.

Producing a contact via through the quartz first requires a hole through the substrate and subsequently an electrical contact. The hole could be produced using a variety of drilling techniques including mechanical drilling and ultrasonic drilling, both available commercially, and laser drilling [120]. Alternatively, dry etching using CF_4 [121-123] or SF_6 based plasmas [124], and wet etch techniques using buffered hydrofluoric acid (HF and NH_4F) [121, 125], or a combination of both, could be used. The slow dry etch rates of less than 100 nm / min for CF_4 and 600 nm / min for SF_6 give long etch times of 14 hours or more, making plasma etching very slow. Wet etch rates of up to 530 nm / min [125] are also slow and crystallographic, thus a direct via through an ST or AT quartz wafer would not be possible.

Many of the drilling techniques are established on glass substrates for micro fluidic devices, but not quartz. Drilling could induce cracking or stress in the substrate due to the brittle nature of quartz. If the holes were produced before any device fabrication, the weakened substrate may not withstand further processing steps, reducing yield. By producing the holes at the final stage, the expected failure would again reduce the yield of the completed devices making drilling disadvantageous. Some of the etching techniques are established for the fabrication of quartz resonators, and could be used as a final fabrication step. However the etch rates are very slow, and suitable masking material would need to be used to mask and protect the device. Neither method is ideal for producing the vias.

Electrical feed-throughs can be electroplated metal, such as copper [126, 127] as outlined in figure 8-9. A metal seed would be sputtered or evaporated over the backside of the wafer covering the base and sidewalls of the holes, and a photoresist mask patterned to define the areas to be plated. Subsequent removal of the photoresist and un-plated seed layer would leave the electrical contacts through the wafer, which could be soldered, epoxied or wire-bonded to the header.

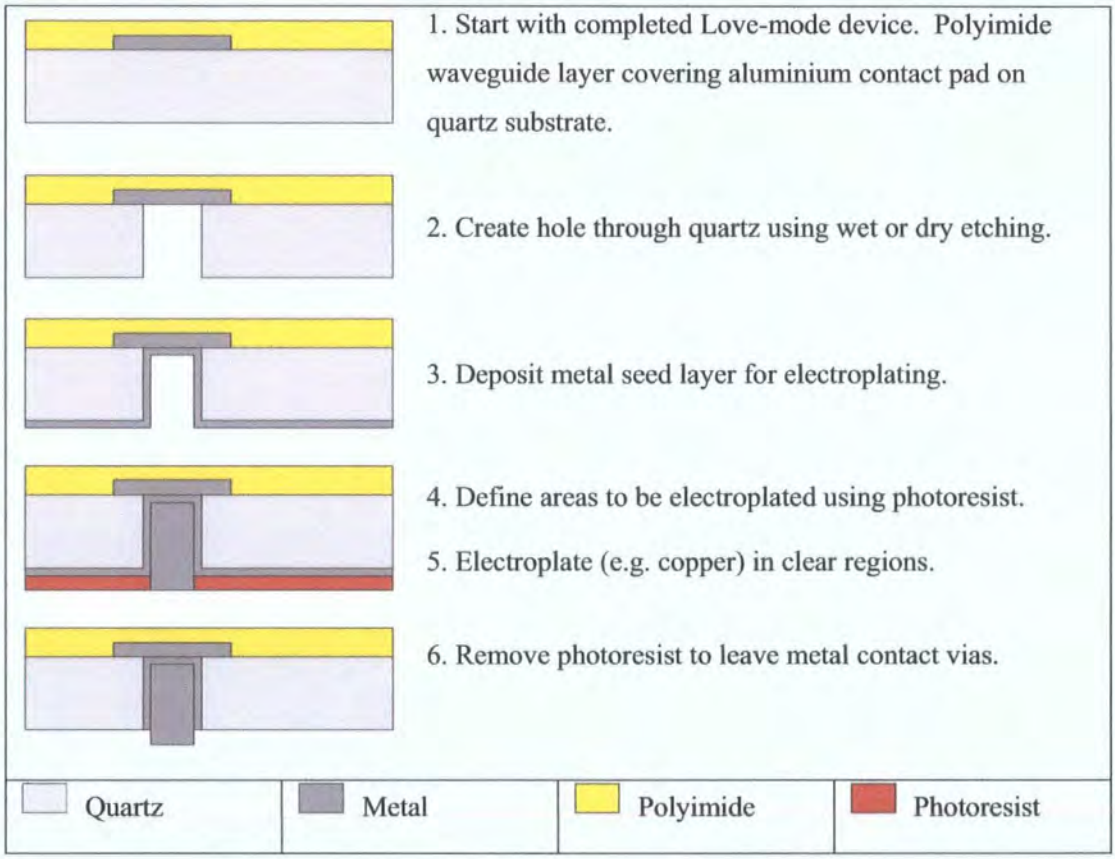

Figure 8-9. Basic process to produce contact vias through substrate using etching and electroplating.

The chip header for the ETWI approach could be converted from conventional electronic packages, or be custom made. A conventional ceramic SMD package, as discussed earlier and illustrated in figure 8-2, could be used upside-down with a hole machined into the base. The sensor die could then be bonded inside the base (using the hole as the sample area) or outside the base (using the hole for wire-bonding through) as illustrated in figures 8-10 and 8-11. The latter solution would allow the header outline to be the same size (or even smaller) than the die and place the sensor surface at the top

of the assembly. Both of these methods would be simple to assemble and make use of the wide variety of stock SMD ceramic packages, reducing the cost.

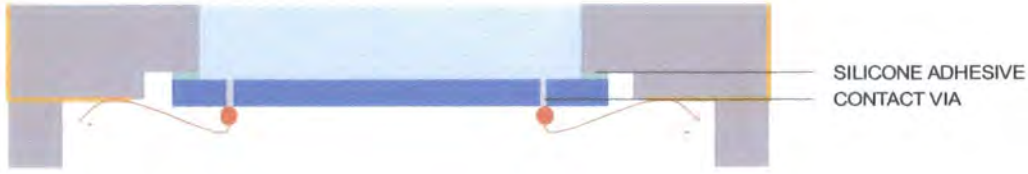

Figure 8-10. Backside contact arrangement using SMD ceramic header upside down with sensor die inside. The hole through the header base (now top) allows sample contact.

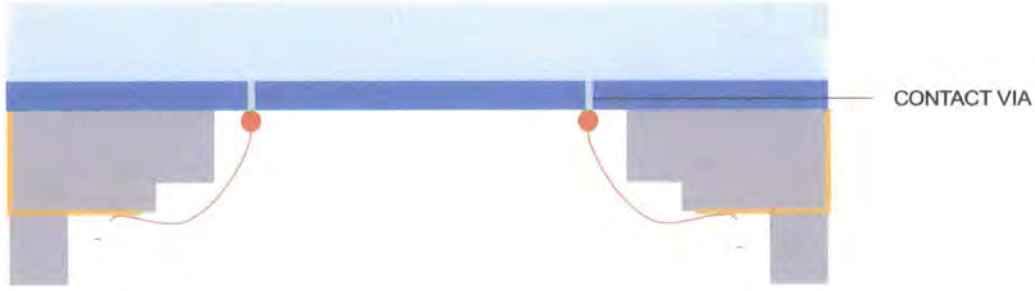

Figure 8-11. Backside contact arrangement using SMD ceramic header upside down with sensor die bonded to outside. The hole through the header allows wire bonds to be made to the die. The outline of the header and die can be identical.

Following discussions with Kyocera, an alternative method was discussed using ball grid array (BGA) ceramic headers. These consist of a thin plate of ceramic with pins on the reverse that feed through to solder bumps on the topside. The die (with contact vias correctly spaced) is placed on the BGA and heated to melt the solder to the contacts. The packages can be defined in the ceramic plate by perforations similar to a postage stamp, and 'snapped off'. This could facilitate the fabrication of many-sided packages (e.g., an octagon) that would fit lower into the refractometer sample chamber, although the sensor die would have to be similarly shaped.

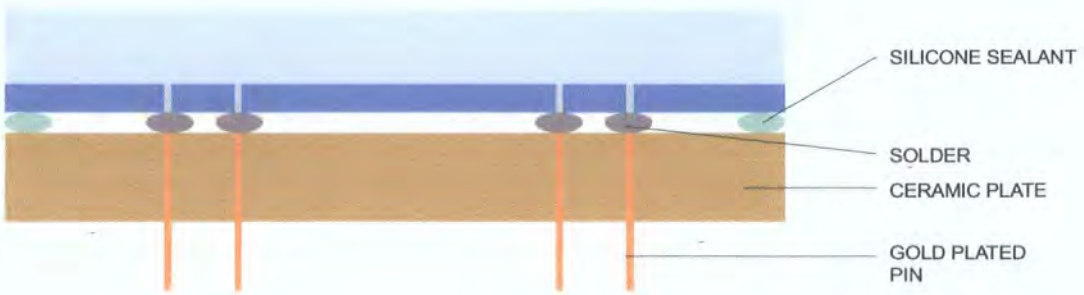

Figure 8-12. Ball Grid Array (BGA) type package. Contacts made between die and Au plated pins with solder.

A packaging method using backside die contacts offers the advantages of a small outline, simple sealing, prominent sensor surface, and simple assembly using conventional techniques. These factors would enable the sensor to integrate well into the existing refractometer allowing positioning of the sensor surface close to the chamber window. However the production of contact vias in quartz wafers, although feasible, is difficult due to the fragility of the material and this would potentially reduce the device yield. Via fabrication using etch techniques would be slow, increasing the fabrication time and cost, and the device would have to be suitably protected from the etch process.

8.5 Prototype package

A prototype package was built to demonstrate positioning the sensor surface within the chamber close to the window surface. A cylindrical machined Delrin casing containing 8 spring-loaded pins houses the sensor die, which is glued in a recess in the top. A patterned PCB which may be epoxied, (using a product such as Ablestick conductive epoxy), or soldered to the die contacts, forms the top of the package, and makes contact with the spring-loaded pins. A hole in the centre of the PCB allows liquid contact with the sensor. The rim of the package is 18 mm diameter, allowing the surface of the die (with standard thickness PCB of 1.5 mm) to be positioned 3 mm from the window. Figure 8-13 shows the basic construction principle. The photos in figures 8-14 and 8-15 show the component parts and the dry-assembled package in position in the refractometer sample chamber.

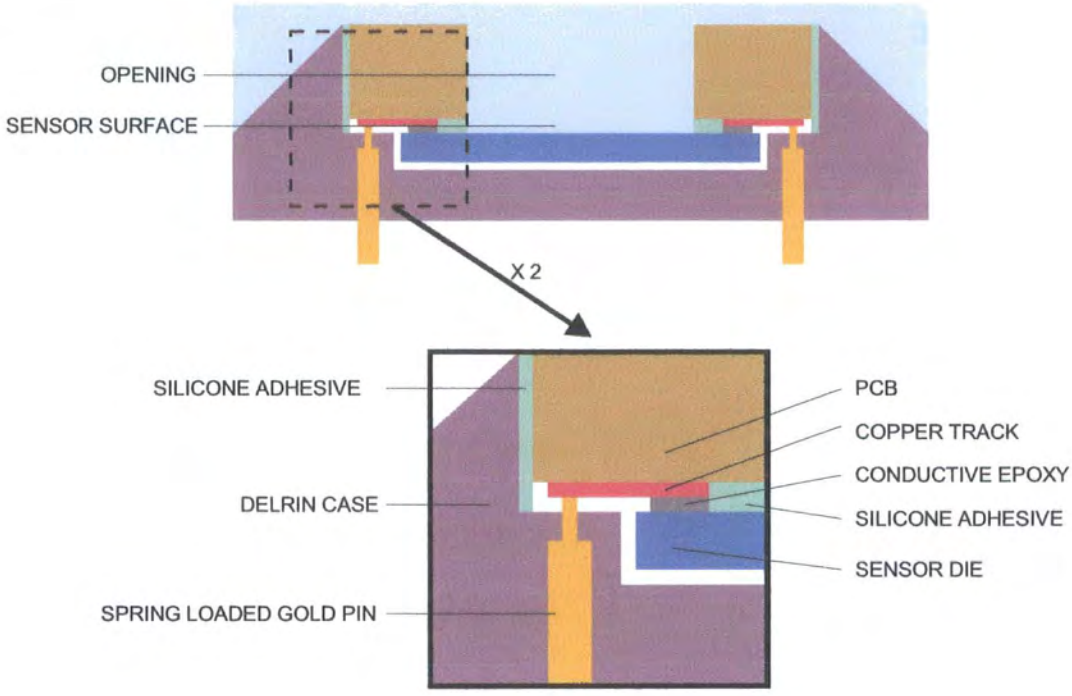

Figure 8-13. Cross-section schematic of prototype package. The detail shows the electrical contact method and liquid sealing.

Figure 8-14. Component parts of prototype package. The sensor die is positioned in the case, surrounded by 8 spring-loaded pins. The copper tracks on the PCB allow contact between the pins and contact pads on the die.

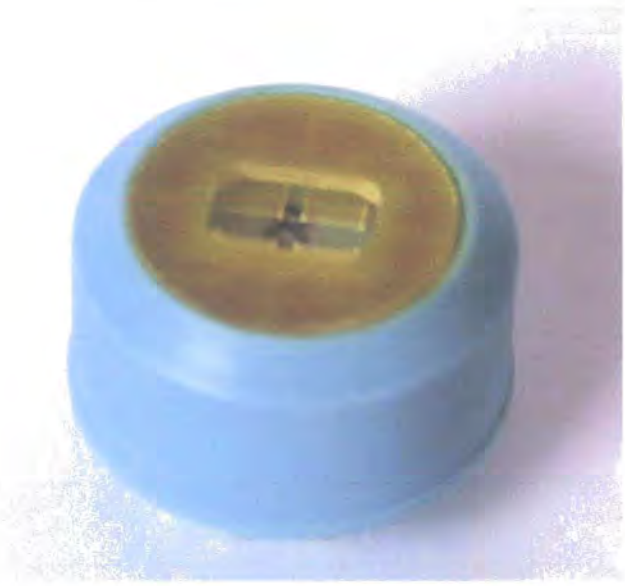

Figure 8-15. All parts in position showing the open chip area.

Figure 8-16. Prototype package in sample chamber. The pins would locate in a socket in the lid.

The prototype showed that a small custom-built package mounted on a custom lid could allow a sensor to be positioned low in the sample chamber within close proximity of the window. The 3 mm gap achieved, although not the optimum 0.5 mm, was practical for small sample size refractometer operation, confirmed by independent tests at Index Instruments with dummy sensor dies. However it was expected that the confined open area on the chip would not fill with liquid when the chamber lid is brought down due to the formation of an air bubble in the cavity. Removing the sample and cleaning the sensor with the deep cavity would also be difficult.

Final assembly of the package proved difficult, preventing the production of a working sample. The sensor die has to (a) be sealed around the hole perimeter on the PCB with a silicone adhesive, and (b) be electrically connected with conductive epoxy at the contact pads, in one process. Accurate deposition of the conductive epoxy and silicone sealant within the small dimensions (the area for the silicone seal was only 1 mm wide, adjacent to the contact pads) proved impossible with manual dispensing. Also, due to the small length between the IDTs and the contact pads, the sealant would partially cover the IDTs, attenuating the wave. However, these problems could be overcome by altering the sensor layout.

8.6 Flexible PCB Package

The complex assembly of the first package, and the expected operational difficulties in filling and cleaning the chip surface led to a design proposal incorporating flexible PCBs. These are made up from copper or gold tracks patterned on a polyimide substrate, and can be built up into multilayer structures. The PCBs are used as a contact mechanism, soldered or epoxied onto the sensor contact pads, and bent around the edge of the chip to the back, where they could be attached to a socket. The entire assembly is then either moulded into a package, or sealed into a machined case. By contacting opposite sides of the die, a smooth surface on other two edges is left for filling and cleaning. Figure 8-17 gives an impression of the package shape, showing the protection of the PCBs on opposite sides, and a smooth join to the die surface on the other sides. The sensor would be orientated with the corrugations (and thus wave propagation) aligned such that the surface could be easily cleaned, as shown in the figure.

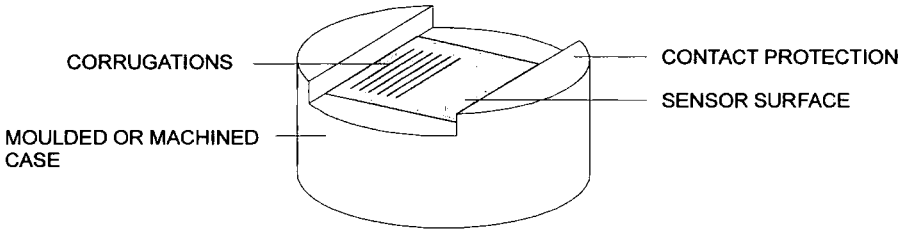

Figure 8-17. The proposed shape of a package incorporating flexible PCBs. The contacts are sealed under the protected covers. The chip surface (shaded area) can be easily cleaned with a continuous surface at each end of the delay lines. The corrugations (indicated by lines in the picture) are also aligned in this direction.

Figure 8-18 shows a cross section of the proposed package, and figure 8-19 a plan view, with one side shown with no contact protection, and the other side shaded to indicate the raised protective region. The schematics show how the flexible PCBs are soldered to opposite sides of the die, then become narrower and bend around to the backside. By reducing the width of the PCBs, the overall diameter of the package can be reduced so that it is only slightly larger than the die's diagonal dimension. A machined package is shown in the two schematics with a silicone seal between the parts and the sensor surface. However, the package could be injection moulded around the die-PCB combination, whilst protecting the sensor surface, to produce a sealed assembly.

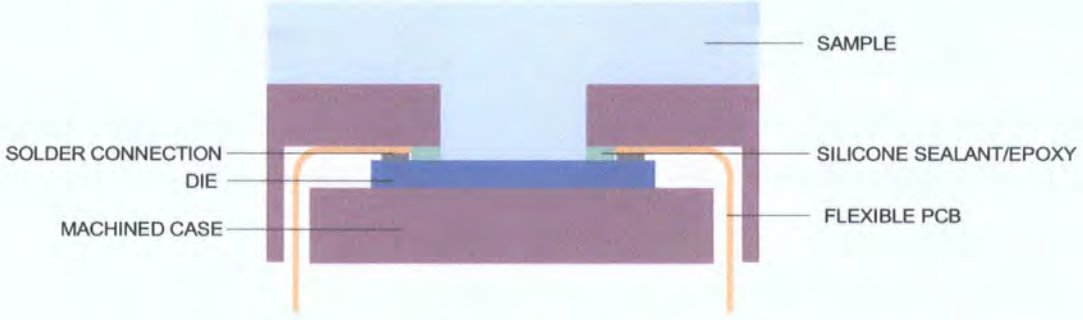

Figure 8-18. Cross section through flexible PCB package. A machined case with silicone sealant is illustrated, although a moulded case could be used.

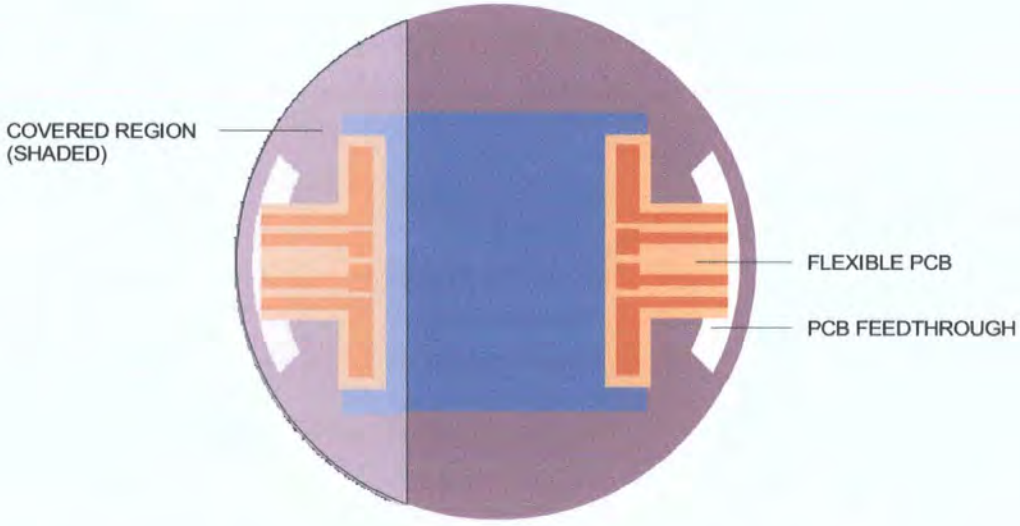

Figure 8-19. Plan view of package. The right side is shown at sensor surface level and the shading on the left shows the raised protective region. The PCBs become narrower for the lead-outs.

Sample flexible PCBs obtained from Hallmark Electronics Ltd [128] showed that a dual layer PCB with two layers of metal would enable a suitable small curvature. The dual layer structure would allow both the electrical contacts for the sensor, and a crosshatch RF shield to reduce interference and noise. Additionally, impedance matching circuitry could be incorporated on the PCBs within the package. Contacts to the end of the PCBs could be made with a commercially available connector embedded in the package allowing the entire assembly to be located in a socket.

Whilst preliminary drawings were made of the flexible PCB package in conjunction with the PCB suppliers, no devices were built. This was due to new requirements in the sensing industry leading to the development of commercial open cavity packaging.

8.7 Commercial packaging solutions

Almost all SAW sensors for liquid applications reported are at a research stage, or used in the research environment, and no commercial packages were found at the start of this study. The devices are often housed in home-made, relatively complex packages and are not suitable for incorporating into a commercial instrument. Many of the sensors reported use a liquid cell sealed to the surface of the chip, either made out of metal or plastic with an inlet and outlet, bonded to the path between the transducers as described earlier, although this is more to reduce the electrical loading of the wave.

However more recent developments into sensor packaging have resulted in some commercially developed solutions.

8.7.1 Oil dipstick sensor

Research at the Fraunhofer Institute for Solid State Technology initially used a liquid cell for research into liquid SAW sensors as shown in figure 8-20 [88]. A Perspex cell containing inlet and outlet ports is clamped above the surface of the SAW device with a rubber seal. This research led to the development of a SAW viscometer dipstick for incorporation into internal combustion engines for oil quality measurements [129, 130]. The SAW device has encapsulated wire bonds and is completely sealed around the edges as shown in the photo in figure 8-21. The main aspects of large open chip surface and encapsulation are ideally suited for the liquid density sensor, allowing immersion into the sample liquid.

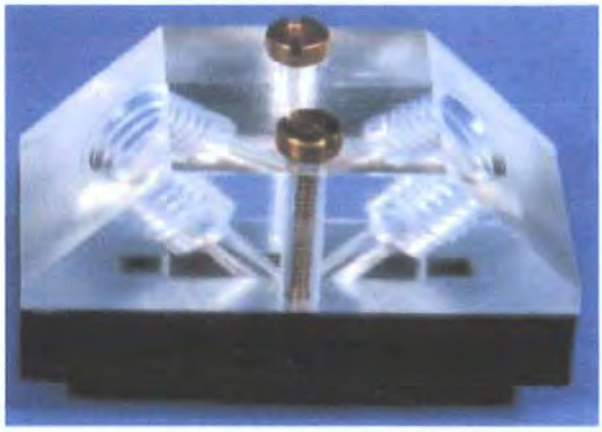

Figure 8-20. Perspex liquid cell clamped to the surface of a SAW sensor. The SAW device is dark, with the inlet and outlets directed at the propagation path between the IDTs [88, 130].

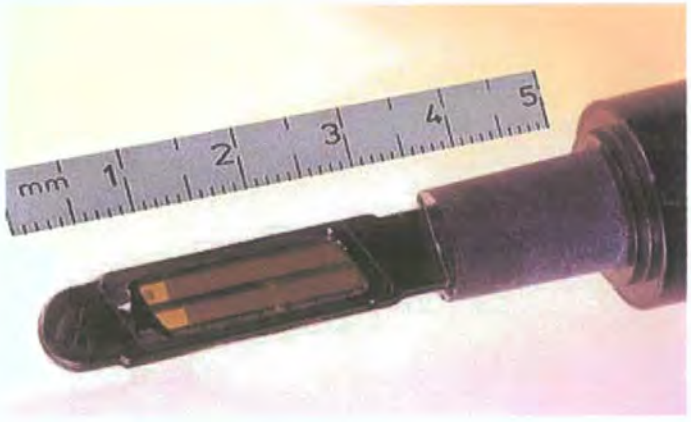

Figure 8-21. Dip-stick viscometer using a SAW device for oil quality measurements [129].

8.7.2 Fingerprint sensors

The development and large market for fingerprint sensors has necessitated the development of new packaging solutions, resulting in recent patents [131, 132]. The chips require a large open surface (~10 mm × 10 mm) to allow finger contact, and the surface needs to be prominent with a minimal recess. A robust method of edge sealing around the open region is vital to protect the electrical contacts from physical damage, chemical damage from finger grease (and other substances which may be on the finger) and from cleaning solutions and processes. The overall package dimensions are not much larger than the sensor die resulting in a compact assembly. Figure 8-22 shows

views of two sensors manufactured by UPEK Inc, and are typical of other manufacturers.

Figure 8-22. Fingerprint sensors manufactured by UPEK Inc. The large open sensor surface is orange / yellow, encapsulated in the black moulded package. Electrical contacts are on the reverse of the package.

The early patent from the Harris Corporation describing a complete sensor system gives two solutions for packaging [131]. Schematics are given for a sealed-lid type package with a bead of sealant, similar to figure 8-6, and also for a moulded encapsulated package based on a standard lead frame/plastic package. Both of these are given as potential solutions, although there is no evidence of actual fabrication or processes and techniques. The later patent from AuthenTec [132] is based solely on packaging, and describes a process using plastic moulded package technology to produce an enclosure leaving the surface of an chip exposed. The wire-bonded die and lead frame are placed in a mould, which clamps to the surface of the die defining the exposed region. The mould incorporates a "bleed-through retention channel" positioned inwardly from the lip of the opening, such that the encapsulation spreads over a small proportion of the chip surface to the channel to control the encapsulant migration, as shown in figure 8-23.

The characteristics of the fingerprint sensor packages are identical to those required for the liquid density sensor. Their development has arisen due to the increased demand from the security industry, and a very similar technology could be suitable for liquid sensors. However, the large range of packages and designs differing between manufacturers, combined with the sensor manufacturer's patents in packaging solutions, suggests that the packaging process is in-house and not by a third-party die packaging specialist.

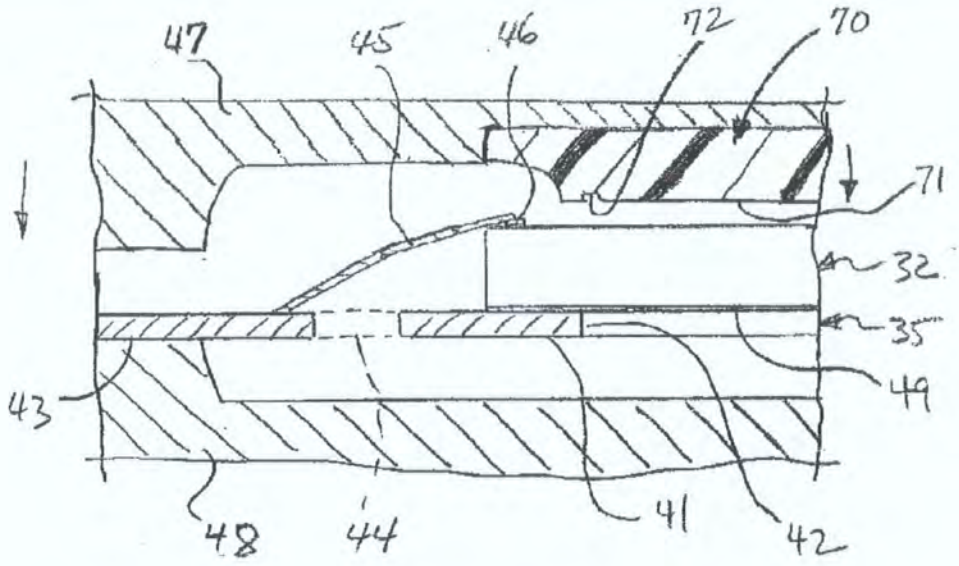

32 – die
35,41,43 – lead frame
45 – wire bond
47 – top mould
48 – bottom mould
70 – mould protrusion
71 – IC contact surface
72 – bleed-through retention channel

Figure 8-23. Packaging encapsulation method patented by AuthenTec [132].

A number of fingerprint sensor manufacturers were approached for information on the packaging. Information was requested on methods and processes, and if third party packaging specialists were used. Whilst it was explicitly stated that the market was smaller and very different to the security field, unfortunately no replies were received.

8.7.3 Open cavity liquid sensor package

Investigations into fingerprint sensor package specialists led to the research into liquid electrical property sensors by Eggers et al [133]. The liquid sensor is shown in figure 8-24 sealed in an open cavity moulded package, by the European Semiconductor Assembly (Eurasem BV). This packaging process was patented in 1999 for optoelectronic device encapsulation [134] but can equally well be used for liquid sensors as this study shows.

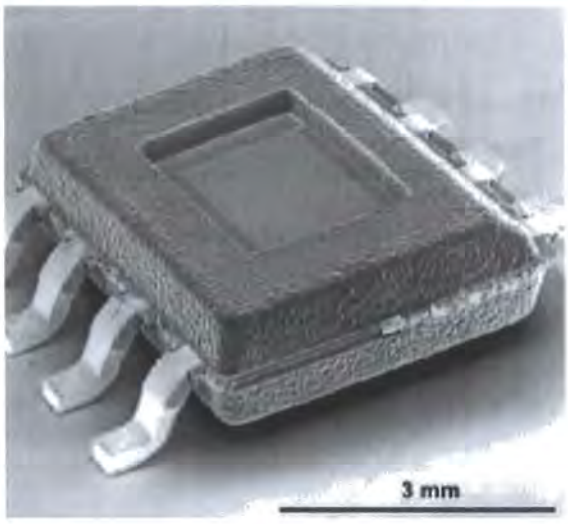

Figure 8-24. Liquid sensor in an open cavity sealed package by Eurasem [133].

The package is produced based on the standard plastic encapsulation technique. The chip is first bonded to the lead frame and electrical connections made. A standard base mould is used and a top mould with a hole over the open area. A soft deformable bung (silicone gel is mentioned in the patent) is brought through the hole and pressed to the chip surface before injection moulding. After partial cure, the moulds are all removed, leaving the clear chip surface with a smooth join around the edge of the opening. Figure 8-25 shows a cross section through the completed package, although the optical window is obviously not required for liquid sensing applications.

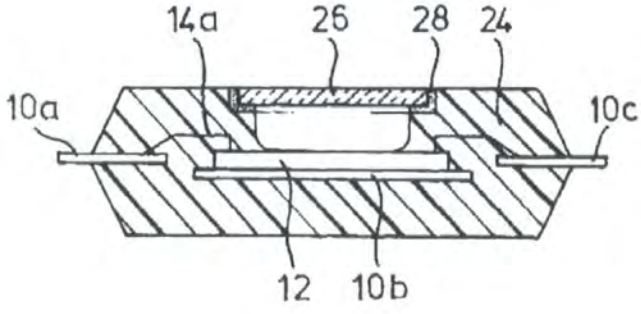

10a,b,c – lead frame
12 – die
14a – wire bond
24 - encapsulant
26 – optical window (not applicable)
28 – sealant (not applicable)

Figure 8-25. Cross section through Eurasem open cavity package [134]. Note the smooth rounded join at the cavity periphery.

This package offers many advantages over the others presented here in that it is based on a standard cheap IC encapsulation process with minor alterations. Due to this, a variety of standard package sizes and shapes could be used as a basis, allowing the optimum size for integration into the refractometer to be chosen. The electrical contacts onto the die are well encapsulated, not relying on a sealed edge to keep the liquid out as with many of the other designs discussed. This encapsulation would also make the device withstand physical handling (when cleaning, etc) and be resistant to any harsh environment (the packages are specified to withstand a range of chemicals and temperatures). The edge of the encapsulation is smooth due to the soft mould bung, which would make cleaning the surface easier with no sharp internal corners. The sensor surface is only recessed by around 0.3 mm (estimated from figure 8-24), which would also assist with cleaning and sample filling, as well as allowing closer positioning to the refractometer window, providing the lateral dimensions allow. A desirable alteration would be the extending of the open region to the ends of the package giving a clear run for cleaning and sample filling. Extending the moulding bung, and perhaps using a longer die with bare regions at each end could presumably achieve this, although forming the ends of the package would be more complex, requiring more extensive changes to the moulds, and therefore be more expensive.

Eurasem BV were contacted about the possible use of the package for the liquid density sensor, but no reply was received from the initial request or a follow up. Possible reasons could include the package style no longer being produced or perhaps the small scale of the density sensor project. They do however market the company as being a specialist in MEMS packaging.

At the same time, Mintech UK (Interconnect and Test Division) were approached with a view to reproducing the Eurasem style package. Mintech are part of a group of companies operating in the UK working on the back-end processing of electronics devices, for large and small-scale projects. Initial design ideas and requirements were presented to Mintech along with the existing commercial solutions. Whilst they do not currently have the facilities to produce an open cavity package, they suggested that an adaptation of their prototyping process could produce such a device.

8.8 Summary

At the start of this study, it quickly became clear that the final packaging of the liquid sensor would be a major aspect, with the requirement of a small compact package

capable of holding a large die with an open surface, suitable for immersion into a range of liquids.

Adaptation of existing electronics packaging using either a sealed lid or encapsulation to protect the contacts could be a viable option. The latter was used for many of the test sensors and proved a reliable method of sealing. However the fabrication of the package is a manual process and inconsistent, and the resulting packages with the currently available headers were too large for integration into the refractometer. Alternative designs using backside contacts reduce the external size and complexity of the packages by moving all the electrical contacts to the rear of the die. The simplification of the sealing process and smaller external size are desirable but the added complexity and cost of making contact vias through the brittle quartz substrate make this an undesirable option at present.

The lack of a commercially available solution led to the development of the prototype package, to demonstrate the possibility of producing a small sealed enclosure capable of being positioned inside the refractometer sample chamber. The assembly of the device proved impossible although design changes could simplify the process. The proposal to use flexible PCBs as a contact mechanism reduces the size and complexity of the assembly and also offers the option of including screening and/or matching circuitry. This could be a viable option for a custom-built package, but as with any intricate custom-built assembly, this will increase the final sensor cost and fabrication time. Reliability could also be an issue.

The fingerprint sensor market has created a new need for open cavity packages, and the expanding market has made the development of a simple solution possible. The types of packages offered by the fingerprint sensor companies are suitable for the liquid sensor, and whilst not available as a commercial process, they can be replicated by making changes to the plastic moulded packages used for electronics. This offers the most suitable route for the liquid density sensor, offering a small sealed package with a large open chip area, which can be immersed in liquids and is robust for cleaning purposes.

9 Conclusions

9.1 Initial aims

The initial aim of this study was to investigate liquid density sensing techniques, and research a sensor for incorporation into a refractometer with a sensitivity and resolution comparable to a stand-alone instrument from the current market leaders, Anton Parr. A Love mode based liquid density sensor fulfilled the requirements, exhibiting high sensitivity, small size, and robustness, whilst being simple and cheap to fabricate.

Previous studies into Love mode devices since the early work by Gizeli et. al [66, 79] have extensively investigated Love mode sensors using both SiO_2 polymer waveguide layers, and with typically a small range of samples. One of the aims of this study was to investigate the practicalities of Love mode devices as sensors in a commercial multi-use environment, by testing with a wide range of liquid samples, and discovering limitations. The liquid loading results presented in this study are a select sample chosen to represent the findings.

9.2 Results

The results show that Love mode devices using polyimide waveguide layers can be made to operate with a high sensitivity and relatively low insertion losses with layers 0.90 to 1.0 μm thick. The sensitivity increased with thickness, but so did the insertion loss, and so a compromise was required due to excessive losses preventing operation around the theoretical optimum sensitivity regime predicted at 2.55 μm.

Liquid loading results for the smooth polyimide devices exhibited viscous loading with a frequency shift proportional to the square root of the density-viscosity product $\sqrt{(\rho\eta)}$. The corrugated polyimide devices showed an additional mass loading effect with a further frequency shift proportional to the trap volume (up to 50% etched area), but with larger insertion losses possibly due to compressional losses into the liquid. Discrimination of ρ from $\sqrt{(\rho\eta)}$ using the difference in frequency shift between the two delay lines gave sensitivities of 0.36 $\mu gcm^{-3}Hz^{-1}$ and 0.13 $\mu gcm^{-3}Hz^{-1}$ for diluted whisky samples, a state of the art value over 16 times greater than the sensitivity of the SiO_2 Love mode devices presented by Herrmann et. al [40, 41]. This highlights the high sensitivities achievable by using a thin polyimide layer with low acoustic shear velocity. Larger values of between 1.93 $\mu gcm^{-3}Hz^{-1}$ and 2.74 $\mu gcm^{-3}Hz^{-1}$ were obtained from the solvent samples indicating the frequency response dependence on other liquid characteristics in addition to density and viscosity. The frequency results from sucrose

solutions gave no correlation with ρ, probably due to excessive damping introducing measurement errors, and from the reduced sensitivity for more viscous solutions with complex Maxwellian behaviour.

Temperature measurements with different thickness polyimide layers indicated a temperature independent frequency response for layers 0.95 μm thick, coinciding with optimum operation thickness. Previous studies investigating SiO_2 waveguides and alternative crystal cuts proposed that temperature independent Love-mode operation is not possible. The use of polyimide would allow the sensors to be operated in a field environment with minimal temperature calibration and control.

The SiO_2 waveguide layer devices showed similar responses to the polyimide devices, but with lower sensitivities. Preliminary multilayer devices incorporating both SiO_2 and polyimide were designed to exploit the merits of low insertion loss (SiO_2) and high sensitivity (polyimide). They exhibited low intrinsic losses around 10 dB, but no proportional response to different samples, and with inconsistent results to the single layer devices. The insertion losses were also comparable to the polyimide devices giving no advantage.

9.3 Limitations

The results highlight the high sensitivity achievable with Love mode devices using polyimide, and also the discrimination of ρ from $\sqrt{(\rho\eta)}$ using the dual delay line smooth-corrugated structure. However they also illustrate the limitations of Love mode devices, some that are fundamental, and some that may be surmountable with further work.

The variations in sensitivity with different types of liquids, and inconsistent responses for different liquids with similar physical characteristics, show that the sensor is susceptible to other factors such as the electrical permittivity of the sample. Methods of reducing the electrical loading have been discussed, but they introduce further impracticalities such as increased capacitance of the transducers leading to higher insertion losses, and the introduction of a cell structure reducing the feasibility of the sensor for the refractometer application.

The devices showed that the frequency sensitivity was proportional to $\sqrt{(\rho\eta)}$ up to $\sqrt{(\rho\eta)} = 1.45\ kgm^{-2}s^{-0.5}$, the Newtonian range of the liquid with no relaxation effects. For higher values of $\sqrt{(\rho\eta)}$, the sensitivity reduces to almost zero, due to the complex

Maxwellian behaviour of viscous liquids at high frequencies, with relaxation behaviour reducing the effective viscosity. This reduction in sensitivity probably prevents the discrimination of ρ from $\sqrt{(\rho\eta)}$ for higher viscosity liquids, shown by the diluted whisky responses. The large loaded insertion losses approaching 40 to 45 dB for more viscous liquids, combined with the reduced sensitivity, also increase the measurement errors with a poorly defined peak frequency.

These findings suggest that Love mode devices are suited for high sensitivity measurements on relatively low viscosity liquids (< 0.002 Pas for sucrose), where the response is previously known with extensive calibration. They are thus ideally suited to bio-sensing or gas-sensing applications where they monitor concentrations of a single sample, which produces a known response. For the purposes of liquid sensing, they are suitable for process monitoring and analysis of single sample types, for example in line monitoring of a product, or quality analysis. In addition to this, they could act as highly sensitive on-off discrete sensors, for example, an automotive oil quality detector which warns when the engine oil needs changing.

9.4 Integration into refractometer

The two significant aspects of integrating the sensor into the refractometer are the sensor packaging and control.

The various custom packaging methods discussed illustrate potential solutions, allowing an open sensor surface with encapsulated electrical connections. The designs based on existing electronics chip headers are largely dependent on the availability of suitable products which will allow a large chip area with minimum overall dimensions. Epoxy encapsulation of wire bonds on commercial SMD ceramic type headers proved effective allowing ease of cleaning and offering robust protection. The two designs based on a machined housing and either spring-loaded pins or flexible PCB enable close positioning of the sensor surface to the refractometer window. However they are complex to assemble, and potentially fragile. The most suitable solution is based on the new type of packages developed for finger print sensors and optical devices. These are available from commercial packaging companies and would offer the most compact and robust solution. Adaptation of existing processes using a prototype process would also enable a choice of package formats with different connection mechanisms.

Due to the immaturity of the sensors and extensive measurement problems with high insertion losses, the electronics development has largely been underdeveloped in this study, although some parallel investigations have been made into potential solutions including phase locked loops and more simple oscillator feedback circuits. Some early work identified PLL ICs operating at 120 MHz which could have been ideal, but these were withdrawn by the manufacturer early in the project timescale. The rapid development of communications and the quest for ever higher frequencies causes this short product lifecycle with lack of similar frequency replacements.

The limiting factors of the current sensor design are the large losses of up to 45 dB and the multiple peaks, which prevent oscillation and lock-on. A complete control package requires the frequency detection of the Love mode, mixing circuitry to calculate the relative frequency shifts, and further signal processing with calibration tables to enable a direct density read-out. This could be relatively simple for a sensor designed for a specific range and type of liquids, but the variations in response will make this more complex for a multi-purpose sensor.

9.5 Future work

The sensing characteristics of the delay line Love mode devices show potential for high sensitivity density sensing, albeit with restrictions on the range and types of samples. However they are heavily limited by losses which affect the measurement errors, and control methods, with a network analyser currently the only suitable measurement method. The resonator design proposed in the simulation discussion potentially offers the best route to reducing insertion losses and increasing the device Q allowing measurements of more viscous liquids, and control with simple electronics systems. Further improvements could also be made using lithium tantalate substrates, reducing the electrical loading with aqueous samples, and improving insertion losses through a stronger piezoelectric coupling coefficient.

Appendices

A. Publications and conference presentations..... 216

B. Dispersion – transverse resonance..... 217

C. Bulk waves in SAW devices..... 219

D. Fresnel's equations..... 220

A Publications and conference presentations

Conference presentations and papers:

a. Turton, A, Bhattacharyya, D and Wood, D. Love-mode surface acoustic wave liquid sensors using a polyimide waveguide layer. *Proceedings of the 2004 IEEE International Frequency Control Symposium and Exposition.* 24–27 August, 2004. Montreal, Canada. p. 250–256.

b. Turton, A, Bhattacharyya, D and Wood, D. High sensitivity Love-mode liquid density sensors. *Eurosensors XVIII. Digest of Technical Papers.* 13–15 September, 2004. Rome, Italy. p. 474-475.

c. Turton, A, Bhattacharyya, D and Wood, D. High sensitivity liquid density sensors using Love-mode acoustic waves. *Advanced Sensors and Instrumentation Systems for the Food and Beverage Industries.* 15 December 2004. London, UK.

Journal papers

1. Turton, A, Bhattacharyya, D and Wood, D. High sensitivity Love-mode liquid density sensors. *Sensors and actuators A-Physical.* 2005. **123-124**: p. 267-273.
2. Turton, A, Bhattacharyya, D and Wood, D. Liquid density analysis of sucrose and alcoholic beverages using polyimide guided Love-mode acoustic wave sensors. *Measurement Science and Technology. IOP.* **17**. 2006: p. 257-263
3. Grancharov, G, Khosravi, E, Wood, D, Turton, A and Kataky, R. Individually addressable recessed gold microelectrode arrays with monolayers of thio-cyclodextrin nanocavities. *Analyst*, 2005, **130**: p. 1351-1357.

B Dispersion – transverse resonance

The dispersion relation for an arbitrary wave can be derived by substituting chosen wave solutions into the wave equation:

$$\nabla^2 \upsilon - \frac{1}{V^2}\frac{\partial^2 \upsilon}{\partial t^2} = 0 \qquad \text{(B-1)}$$

where V is the wave velocity and υ the waveform. Consider a transverse resonance waveguide (figure B-1) where a wave is confined to a plate of thickness h, and propagates in the z-direction with a longitudinal wavevector k_z and transverse wavevector k_t.

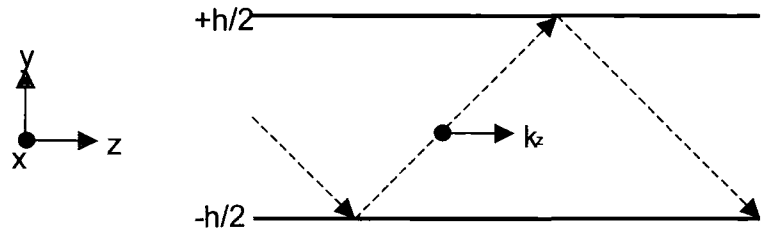

Figure B-1. Shear wave on a plate of thickness h reflecting off upper and lower boundaries.

The waveform does not change in the x-direction and thus the wave equation becomes:

$$\frac{\partial^2 \upsilon_x}{\partial y^2} + \frac{\partial^2 \upsilon_x}{\partial z^2} - \frac{1}{V^2}\frac{\partial^2 \upsilon_x}{\partial t^2} = 0 \qquad \text{(B-2)}$$

By taking the waveform $\upsilon(z,t) = A \exp i(k_z z - \omega t)$, and substituting into (B-2) we get:

$$\frac{\partial^2 \upsilon_x}{\partial y^2} - \upsilon\left(k_z^2 - \frac{\omega^2}{V^2}\right) = 0 \qquad \text{(B-3)}$$

A general form for υ_x $(-h/2 < y < h/2)$ is:

$$\upsilon_x(y) = B\cos(k_t y) + B\sin(k_t y) \qquad \text{(B-4)}$$

The solution of this when put into (B-3) gives the relation:

$$k_t^2 = \left(\frac{\omega}{V}\right)^2 - k_z^2 \tag{B-5}$$

For the wave to propagate without losses, the phase shift during each round trip of $2h$ must be a multiple of 2π. We get the transverse resonance condition:

$$k_t = \frac{n\pi}{h} \tag{B-6}$$

where n is the mode number (0,1,2,3,...). Substituting (B-6) into (B-5):

$$k_z^2 + \left(\frac{n\pi}{h}\right)^2 = \left(\frac{\omega}{V}\right)^2 \tag{B-7}$$

This describes the wave mode frequency and velocity in terms of transverse wavevector k_t and propagation constant k_z.

C Bulk waves in SAW devices

Crystal oscillations in SAW devices are typically within one wavelength of the surface, but bulk oscillations may also exist. In some situations these are considered as surface waves, such as Surface Skimming Bulk Waves (SSBW). These occur when the IDTs have poor coupling to a SAW mode, but generate bulk waves which follow the surface [45].

We can consider the generation of a bulk wave from IDT fingers of wavelength L as shown in figure C-1, where the wave is generated at an angle θ into the substrate.

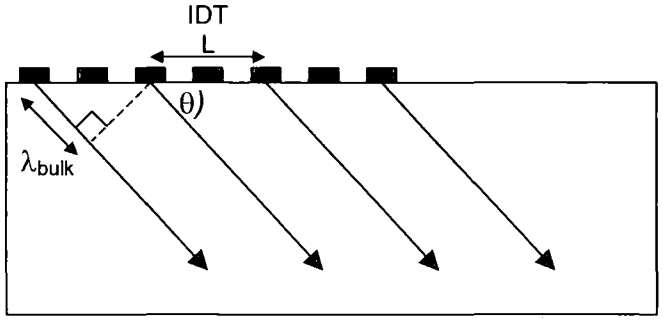

Figure C-1 Propagation of bulk waves into substrate from multiple point sources.

When the condition $\lambda_{bulk} = L\cos\theta$ is met, the individual bulk waves will add constructively and propagate through the substrate. If the velocity of the bulk wave is V_b, the frequency dependence is given by (C-1):

$$f_b = \frac{V_b(\theta)}{L\cos\theta} \qquad \text{(C-1)}$$

A cut-off frequency occurs with $\theta = 0$, and as $\theta \rightarrow \pi/2$, f_b approaches infinity. The bulk wave velocity is greater than the SAW velocity, thus bulk waves have higher frequencies than the corresponding SAWs. Roughening the substrate backside reduces large θ mode propagation, leaving SSBW modes with $\theta \rightarrow 0$ at $f_c = V_b / L$, which are often close to the SAW frequency causing a superposition of SAW and SSBW response.

D Fresnel's equations

Fresnel's equations evaluate the reflected and transmitted wave coefficients for waves incident on a boundary of two materials with different physical properties.

$$\Gamma = \frac{\upsilon_{xR}}{\upsilon_{xI}} = \frac{Z_s \cos\theta_s - Z'_s \cos\theta'_s}{Z_s \cos\theta_s + Z'_s \cos\theta'_s} \quad \text{(D-1)}$$

$$T = \frac{\upsilon_{xT}}{\upsilon_{xI}} = \frac{2Z_s \cos\theta_s}{Z_s \cos\theta_s + Z'_s \cos\theta'_s} \quad \text{(D-2)}$$

where υ_{xI}, υ_{xR}, and υ_{xT} are the incident, reflected and transmitted waves, Z_s and Z'_s the shear acoustic impedance in the waveguide and substrate, and θ and θ' the reflected and transmitted angles.

References

1. Feynman, R. There's Plenty of Room at the Bottom. *Journal of Microelectromechanical Systems*, 1992. **1**(1): p. 60-66.

2. Bardeen, J and Brattain, W H. The Transistor, a Semiconductor Triode. *Physical Review*, 1947. **74**(2): p. 230-231.

3. Shockley, W. The Theory of p-n Junction in Semiconductors and p-n Junction Transistors. *Bell System Technical Journal*, 1949. **28**: p. 485.

4. Kahng, D and Atalla, M M. Silicon-Silicon Dioxide Surface Device. *IRE Device Research Conference*. 1960. Pittsburgh, USA.

5. Kilby, J S. Texas Instruments Inc. Miniaturized electronic circuits. 1964, US3138743.

6. Silicon Research Areas - EUV Lithography. 2005, Intel, http://www.intel.com/research/silicon/lithography.htm.

7. Peterson, K. Silicon as a Mechanical Material. *Proceedings IEEE*, 1982. **70**(5): p. 420 - 457.

8. Tufte, O N, Chapman, P W and Long, D. Silicon Diffused-element Piezoresistive Diaphragms. *Journal of Applied Physics*, 1962. **33**: p. 3322.

9. Bassous, E, Taub, H H and Kuhn, L. Ink jet printing nozzle arrays etched in silicon. *Applied Physics Letters*, 1977. **31**(2): p. 135-137.

10. Madou, M. Fundamentals of Microfabrication. 1 ed. 1997, Florida: CRC Press.

11. Market analysis for microsystems 1996 - 2002. 1998, NEXUS.

12. Market analysis for microsystems II 2000 - 2005. 2002, NEXUS.

13. The RF MEMS Market 2002 - 2007. 2002, Wicht Technologie Consulting, http://www.wtc-consult.de/download/rfmems/rfabstra.pdf.

14. Boyd, J. Epson Using MEMS to Create Advanced Inkjet Heads for POS Printers. 2004, Seiko Epson Corporation, http://www.epson.co.jp/e/newsroom/tech_news/tnl0302single.pdf.

15. Boyd, J. Epson Printers Attain New Heights in Color Management. 2004, Seiko Epson Corporation, http://www.epson.co.jp/e/newsroom/tech_news/tnl0411single.pdf.

16. HP Reports Fourth Quarter 2004 Results - News release. 2004, Hewlett Packard, http://www.hp.com/hpinfo/investor/financials/quarters/2004/q4.pdf.

17. Annual report 2003. 2003, Robert Bosch GmbH, http://www.bosch.com/en/download/GB2003_EN.pdf.

18. Handbook of Chemistry and Physics. 83 ed, ed. Lide, D R. 2002: CRC Press.

19. Wood, D. An Analysis Of The Techniques Available For A Microsystem to Measure Fluid Density. 2001, School of Engineering, University of Durham, UK.

20. Stemme, G. Resonant silicon sensors. *Journal of Micromechanics and Microengineering*, 1991. **1**(2): p. 113-125.

21. McClements, D J and Fairley, P. Ultrasonic pulse echo reflectometer. *Ultrasonics*, 1991. **29**(1): p. 58-62.

22. Puttmer, A, Hauptmann, P and Henning, B. Ultrasonic density sensor for liquids. *IEEE Transactions on Ultrasonics, Ferroelectrics and Frequency Control*, 2000. **47**(1): p. 85-92.

23. Shih, W Y, Li, X P, Gu, H M, Shih, W H and Aksay, I A. Simultaneous liquid viscosity and density determination with piezoelectric unimorph cantilevers. *Journal of Applied Physics*, 2001. **89**(2): p. 1497-1505.

24. Oden, P I, Chen, G Y, Steele, R A, Warmack, R J and Thundat, T. Viscous drag measurements utilizing microfabricated cantilevers. *Applied Physics Letters*, 1996. **68**(26): p. 3814-3816.

25. Enoksson, P, Stemme, G and Stemme, E. Silicon tube structures for a fluid-density sensor. *Sensors and Actuators A-Physical*, 1996. **54**(1-3): p. 558-562.

26. Enoksson, P, Stemme, G and Stemme, E. Vibration modes of a resonant silicon tube density sensor. *Journal of Microelectromechanical Systems*, 1996. **5**(1): p. 39-44.

27. Enoksson, P. Novel Resonant Micromachined Silicon Devices for Fluid Applications. PhD. 1997. Royal Institute of Technology, Stockholm.

28. Corman, T, Enoksson, P, Noren, K and Stemme, G. A low-pressure encapsulated resonant fluid density sensor with feedback control electronics. *Measurement Science & Technology*, 2000. **11**(3): p. 205-211.

29. Sparks, D, Massoud-Ansari, S, Straayer, M, Smith, R, Schneider, R, Cripe, J, Zhang, Y and Meng, G. A Density / Specific Gravity Meter Based on Silicon Microtube Technology. *Proceedings Sensors Expo*. 25 September, 2002. Boston, USA. p. 171-176.

30. Westberg, D, Paul, O, Andersson, G and Baltes, H. A CMOS-compatible fluid density sensor. *Journal of Micromechanics and Microengineering*, 1997. **7**(3): p. 253-255.

31. Westberg, D, Paul, O, Andersson, G I and Baltes, H. A CMOS-compatible device for fluid density measurements fabricated by sacrificial aluminium etching. *Sensors and Actuators A-Physical*, 1999. **73**(3): p. 243-251.

32. Sauerbrey, G. Verwendung Von Schwingquarzen Zur Wagung Dunner Schichten Und Zur Mikrowagung. *Zeitschrift Fur Physik*, 1959. **155**(2): p. 206-222.

33. Kanazawa, K K and Gordon, J G. Frequency of a Quartz Microbalance in Contact with Liquid. *Analytical Chemistry*, 1985. **57**(8): p. 1770-1771.

34. Martin, S J, Wessendorf, K O, Gebert, C T, Frye, G C, Cernosek, R W, Casaus, L and Mitchell, M A. Measuring liquid properties with smooth- and textured-surface resonators. *IEEE International Frequency Control Symposium*. 2-4 June, 1993. Salt Lake City, USA. p. 603-608.

35. Martin, S J, Wiczer, J J, Cernosek, R W, Frye, G C, Gebert, C T, Casaus, L and Mitchell, M A. Sandia National Laboratories. Quartz resonator fluid density and viscosity monitor. 1998, US5798452.

36. White, R M and Wenzel, S W. Fluid Loading of a Lamb-Wave Sensor. *Applied Physics Letters*, 1988. **52**(20): p. 1653-1655.

37. Martin, S J, Ricco, A J, Niemczyk, T M and Frye, G C. Characterization of SH Acoustic Plate Mode Liquid Sensors. *Sensors and Actuators*, 1989. **20**(3): p. 253-268.

38. Martin, B A, Wenzel, S W and White, R M. Viscosity and Density Sensing with Ultrasonic Plate Waves. *Sensors and Actuators A-Physical*, 1990. **22**(1-3): p. 704-708.

39. Bender, F, Dahint, R, Josse, F, Grunze, M and Vschickfus, M. Mass Sensitivity of Acoustic Plate Mode Liquid Sensors on Zx- $LiNbO_3$. *Journal of the Acoustical Society of America*, 1994. **95**(3): p. 1386-1389.

40. Herrmann, F, Hahn, D and Buttgenbach, S. Separate determination of liquid density and viscosity with sagittally corrugated Love-mode sensors. *Sensors and Actuators A-Physical*, 1999. **78**(2-3): p. 99-107.

41. Herrmann, F, Hahn, D and Buttgenbach, S. Separation of density and viscosity influence on liquid-loaded surface acoustic wave devices. *Applied Physics Letters*, 1999. **74**(22): p. 3410-3412.

42. Hahn, D and Gottfried, F. Bosch GmbH Robert. Sensor array and method for determining the density and viscosity of a liquid. 2000, WO0026658.

43. Herrmann, F, Hahn, D and Gottfried, F. Robert Bosch GmbH. Sensor array and method for determining the density and viscosity of a liquid. 2003, US6543274.

44. Rayleigh, J W S. On waves propagating along the plane surface of an elastic solid. *Proceedings - London Mathematical Society*, 1885. **17**(4): p. 4-11.

45. Morgan, D P. Surface-Wave Devices for Signal Processing. Studies in Electrical and Electronic Engineering. Vol. 19. 1991, Amsterdam: Elsevier.

46. White, R M and Voltmer, F W. Direct Piezoelectric Coupling To Surface Elastic Waves. *Applied Physics Letters*, 1965. **7**(L12): p. 314.

47. Cady, W G. Piezoelectricity. 1 ed. International Series in Pure and Applied Physics, ed. DuBridge, L A. 1946, New York: McGraw-Hill.

48. Balazik, R. Quartz Crystal. United States Geological Survey, http://minerals.usgs.gov/minerals/pubs/commodity/silica/810495.pdf.

49. Bragg, L and Claringbull, G F. Crystal Structures of Minerals. 1965: G Bell and Sons.

50. Ward, R W. The Constants Of Alpha Quartz. *14th Piezoelectric Devices Conference and Exhibition*. 15-17 September, 1992. Kansas, USA.

51. Hydrothermal Growth of Quartz - Technical Brief. 1999, Sawyer Research Products Inc.

52. D'Amico, A and Verona, E. Saw Sensors. *Sensors and Actuators*, 1989. **17**(1-2): p. 55-66.

53. Buff, W. SAW Sensors. *Sensors and Actuators A-Physical*, 1992. **30**(1-2): p. 117-121.

54. Scholl, G, Schmidt, F and Wolff, U. Surface acoustic wave devices for sensor applications. *Physica Status Solidi A-Applied Research*, 2001. **185**(1): p. 47-58.

55. Cole, P H and Vaughan, R. Electronic surveillance system. 1972, US3706094.

56. Hartmann, C S. A global SAW ID tag with large data capacity. *IEEE Ultrasonics Symposium*. 2002. Munich, Germany. **1**: p. 65-69.

57. Varadan, V V, Varadan, V K, Bao, X Q, Ramanathan, S and Piscotty, D. Wireless passive IDT strain microsensor. *Smart Materials & Structures*, 1997. **6**(6): p. 745-751.

58. Buff, W, Klett, S, Rusko, M, Ehrenpfordt, J and Goroli, M. Passive remote sensing for temperature and pressure using SAW resonator devices. *IEEE Transactions on Ultrasonics, Ferroelectrics and Frequency Control*, 1998. **45**(5): p. 1388-1392.

59. Herrmann, F and Buttgenbach, S. Temperature-compensated shear-horizontal surface acoustic waves in layered quartz/SiO_2-Structures. *Physica Status Solidi A-Applied Research*, 1998. **170**(2): p. R3-R4.

60. Jakoby, B, Bastemeijer, J and Vellekoop, M J. Temperature-compensated Love-wave sensors on quartz substrates. *Sensors and Actuators A-Physical*, 2000. **82**(1-3): p. 83-88.

61. Lonsdale, A and Lonsdale, B. Method and apparatus for measuring strain. 1996, US5585571.

62. Wohltjen, H. Mechanism of Operation and Design Considerations for Surface Acoustic-Wave Device Vapor Sensors. *Sensors and Actuators*, 1984. **5**(4): p. 307-325.

63. Venema, A, Nieuwkoop, E, Vellekoop, M J, Nieuwenhuizen, M S and Barendsz, A W. Design Aspects of Saw Gas Sensors. *Sensors and Actuators*, 1986. **10**(1-2): p. 47-64.

64. Caliendo, C, Verardi, P, Verona, E, D'Amico, A, Di Natale, C, Saggio, G, Serafini, M, Paolesse, R and Huq, S E. Advances in SAW-based gas sensors. *Smart Materials & Structures*, 1997. **6**(6): p. 689-699.

65. Shigematsu, T and Kurosawa, M K. Miniaturized SAW motor with 100 MHz driving frequency. *IEEE Micro Electro Mechanical Systems*. 25-29 January, 2004. Maastricht, Netherlands. p. 482- 485.

66. Gizeli, E, Stevenson, A C, Goddard, N J and Lowe, C R. A Novel Love-Plate Acoustic Sensor Utilizing Polymer Overlayers. *IEEE Transactions on Ultrasonics Ferroelectrics and Frequency Control*, 1992. **39**(5): p. 657-659.

67. Auld, B A. Acoustic Fields and Waves in Solids. 2nd ed. Vol. 2. 1990: Krieger.

68. McHale, G, Martin, F and Newton, M I. Mass sensitivity of acoustic wave devices from group and phase velocity measurements. *Journal of Applied Physics*, 2002. **92**(6): p. 3368-3373.

69. McHale, G, Newton, M I, Martin, F, Gizeli, E and Melzak, K A. Resonant conditions for Love wave guiding layer thickness. *Applied Physics Letters*, 2001. **79**(21): p. 3542-3543.

70. Newton, M I, McHale, G and Martin, F. Experimental study of Love wave devices with thick guiding layers. *Sensors and Actuators A-Physical*, 2004. **109**(3): p. 180-185.

71. Kovacs, G and Venema, A. Theoretical Comparison of Sensitivities of Acoustic Shear-Wave Modes for (Bio)Chemical Sensing in Liquids. *Applied Physics Letters*, 1992. **61**(6): p. 639-641.

72. Du, J, Harding, G L, Ogilvy, J A, Dencher, P R and Lake, M. A study of Love-wave acoustic sensors. *Sensors and Actuators A-Physical*, 1996. **56**(3): p. 211-219.

73. McHale, G. Generalized concept of shear horizontal acoustic plate mode and Love wave sensors. *Measurement Science & Technology*, 2003. **14**(11): p. 1847-1853.

74. Nishikawa, T, Tani, A and Takeuchi, C. Sh-Type Surface Acoustic-Waves on Rotated Y-Cut Quartz. *Fujitsu Scientific & Technical Journal*, 1981. **17**(4): p. 99-113.

75. Herrmann, F, Weihnacht, M and Buttgenbach, S. Properties of shear-horizontal surface acoustic waves in different layered quartz-SiO_2 structures. *Ultrasonics*, 1999. **37**(5): p. 335-341.

76. Wang, Z, Cheeke, J D N and Jen, C K. Sensitivity Analysis for Love Mode Acoustic Gravimetric Sensors. *Applied Physics Letters*, 1994. **64**(22): p. 2940-2942.

77. Kovacs, G, Vellekoop, M J, Haueis, R, Lubking, G W and Venema, A. A Love Wave Sensor for (Bio)Chemical Sensing in Liquids. *Sensors and Actuators A-Physical*, 1994. **43**(1-3): p. 38-43.

78. Jakoby, B and Vellekoop, M J. Viscosity sensing using a Love-wave device. *Sensors and Actuators A-Physical*, 1998. **68**(1-3): p. 275-281.

79. Gizeli, E, Goddard, N J, Lowe, C R and Stevenson, A C. A Love plate biosensor utilising a polymer layer. *Sensors and Actuators B-Chemical*, 1992. **6**(1-3): p. 131-137.

80. Bender, F, Cernosek, R W and Josse, F. Love-wave biosensors using cross-linked polymer waveguides on $LiTaO_3$ substrates. *Electronics Letters*, 2000. **36**(19): p. 1672-1673.

81. Josse, F, Bender, F and Cernosek, R W. Guided shear horizontal surface acoustic wave sensors for chemical and biochemical detection in liquids. *Analytical Chemistry*, 2001. **73**(24): p. 5937-5944.

82. Jakoby, B and Vellekoop, M J. Analysis and optimization of Love wave liquid sensors. *IEEE Transactions on Ultrasonics Ferroelectrics and Frequency Control*, 1998. **45**(5): p. 1293-1302.

83. Jakoby, B, Venema, A and Vellekoop, M J. Design of Love wave sensor devices for the operation in liquid environments. *IEEE Ultrasonics Symposium*. 5-8 October, 1997. Toronto, Canada. **1**: p. 375-379.

84. Vellekoop, N J, Jakoby, B and Bastemeijer, J. A Love-wave ice detector. *IEEE Ultrasonics Symposium*. 17-20 October, 1999. Lake Tahoe, USA. **1**: p. 453-456.

85. Du, J and Harding, G L. A multilayer structure for Love-mode acoustic sensors. *Sensors and Actuators A-Physical*, 1998. **65**(2-3): p. 152-159.

86. Harding, G L and Du, J. Design and properties of quartz-based Love wave acoustic sensors incorporating silicon dioxide and PMMA guiding layers. *Smart Materials & Structures*, 1997. **6**(6): p. 716-720.

87. Herrmann, F, Weihnacht, M and Buttgenbach, S. Properties of sensors based on shear-horizontal surface acoustic waves in $LiTaO_3/SiO_2$ and quartz/SiO_2 structures. *IEEE Transactions on Ultrasonics, Ferroelectrics and Frequency Control*, 2001. **48**(1): p. 268-273.

88. Leidl, A, Oberlack, I, Schaber, U, Mader, B and Drost, S. Surface acoustic wave devices and applications in liquid sensing. *Smart Materials & Structures*, 1997. **6**(6): p. 680-688.

89. Young, M. Development and experimental analysis of a micromachined resonant gyroscope. Ph.D. 1999. University of Durham, Durham, UK.

90. Wolf, S and Tauber, R N. Process Technology. Silicon Processing for the VLSI Era. Vol. 1. 1986, California: Lattice Press.

91. Gizeli, E. Design considerations for the acoustic waveguide biosensor. *Smart Materials & Structures*, 1997. **6**(6): p. 700-706.

92. Jakoby, B and Vellekoop, M J. Properties of Love waves: applications in sensors. *Smart Materials & Structures*, 1997. **6**(6): p. 668-679.

93. Lee, D L. Excitation and Detection of Surface Skimming Bulk Waves on Rotated Y-Cut Quartz. *IEEE Transactions on Sonics and Ultrasonics*, 1980. **27**(1): p. 22-30.

94. Jakoby, B and Vellekoop, M J. Reducing the temperature sensitivity of Love-wave sensors. *IEEE Ultrasonics Symposium*. 5-8 October, 1998. Sendai, Japan: IEEE. **1**: p. 447-450.

95. Branch, D W and Brozik, S M. Low-level detection of a *Bacillus anthracis* simulant using Love-wave biosensors on 36° YX $LiTaO_3$. *Biosensors and Bioelectronics*, 2004. **19**(8): p. 849-859.

96. Andle, J C, French, L A, Jr. and Vetelino, J F. Theoretical and experimental results on two-port resonators fabricated on 36 degrees lithium tantalate. *IEEE International Frequency Control Symposium*. 27-29 May, 1998. California, USA. p. 861-866.

97. Nomura, T, Yasuda, T and Furukawa, S. One-port surface acoustic wave resonator for sensing in liquids. *IEEE Ultrasonics Symposium*. 20-23 October, 1992. Tuscon, USA. **1**: p. 299-302.

98. McHale, G, Newton, M I, Banerjee, M K and Cowen, J A. Acoustic wave-liquid interactions. *Materials Science & Engineering C-Biomimetic and Supramolecular Systems*, 2000. **12**(1-2): p. 17-22.

99. McHale, G, Lucklum, R, Newton, M I and Cowen, J A. Influence of viscoelasticity and interfacial slip on acoustic wave sensors. *Journal of Applied Physics*, 2000. **88**(12): p. 7304-7312.

100. Gallant, A J and Wood, D. The modelling and fabrication of widely tunable capacitors. *Journal of Micromechanics and Microengineering*, 2003. **13**(4): p. S178-S182.

101. Atashbar, M Z, Bazuin, B J, Simpeh, M, Banerji, D and Krishnamurthy, S. 3-Dimensional finite-element simulation of acoustic wave propagation of SAW metallic thin film gas sensors. *Eurosensors XVIII - Digest of Technical Papers*. 13 - 15 September, 2004. Rome, Italy. p. 700-701.

102. Hashimoto, K and Yamaguchi, M. Free software products for simulation and design of surface acoustic wave and surface transverse wave devices. *IEEE International Frequency Control Symposium*. 5-7 June, 1996. Honolulu, USA. p. 300-306.

103. Malocha, D C, Richie, S M and Abbott, B P. Methods of computer aided analysis and design for surface acoustic wave devices. *IEEE Ultrasonics Symposium*. 2-5 October, 1988. Chicago, USA. p. 11-21.

104. Richie, S M, Abbott, B P and Malocha, D C. Description and Development of a SAW Filter CAD System. *IEEE Transactions on Microwave Theory and Techniques*, 1988. **36**(2): p. 456.

105. Morgan, D P, Surface Acoustic Wave Devices and Applications, in Key Papers on Surface Acoustic Wave Passive Interdigital Devices. Morgan, D, Editor. 1976, IEE. p. 2-12.

106. Morgan, D P, Ch. 6. Surface Acoustic Wave Devices, in Handbook of RF/Microwave Components and Engineering. Chang, K, Editor. 2003, Wiley.

107. Rapp, M, Barie, N, Stier, S and Ache, H J. Optimization of an analytical SAW microsystem for organic gas detection. *IEEE Ultrasonics Symposium*. 7-10 November, 1995. Seattle, USA. **1**: p. 477-480.

108. Enguang, D, Guanping, F, Zhenhua, H and Dafu, C. Organic vapor sensors based on SAW resonator and organic films. *IEEE Transactions on Ultrasonics, Ferroelectrics and Frequency Control*, 1997. **44**(2): p. 309-314.

109. Barie, N, Rapp, M, Sigrist, H and Ache, H J. Covalent photolinker-mediated immobilization of an intermediate dextran layer to polymer-coated surfaces for biosensing applications. *Biosensors and Bioelectronics*, 1998. **13**(7-8): p. 855-860.

110. Avramov, I D, Rapp, M, Kurosawa, S, Krawczak, P and Radeva, E I. Gas sensitivity comparison of polymer coated SAW and STW resonators operating at the same acoustic wave length. *IEEE Sensors Journal*, 2002. **2**(3): p. 150-159.

111. Yantchev, V M, Strashilov, V L, Rapp, M, Stahl, U and Avramov, I D. Theoretical and experimental mass-sensitivity analysis of polymer-coated SAW and STW resonators for gas sensing applications. *IEEE Sensors Journal*, 2002. **2**(4): p. 307-313.

112. Nomura, T, Saitoh, A and Horikoshi, Y. Measurement of acoustic properties of liquid using liquid flow SH-SAW sensor system. *Sensors and Actuators B-Chemical*, 2001. **76**: p. 69-73.

113. Barie, N, Wessa, T, Bruns, M and Rapp, M. Love waves in SiO_2 layers on STW-resonators based on $LiTaO_3$. *Talanta*, 2004. **62**(1): p. 71-79.

114. Morgan, D P. A Survey of SAW Resonators. *VNIISIMS Jubilee Conference*. 8-11 June, 2004. Alexandrov, Russia.

115. Yantchev, V M and Strashilov, V L. Coupling-of-modes analysis of STW resonators including loss mechanism. *IEEE Transactions on Ultrasonics, Ferroelectrics and Frequency Control*, 2002. **49**(3): p. 331-336.

116. Lange, K, Blass, G, Voigt, A, Rapp, M and Hansjosten, E. Packaging of surface acoustic wave (SAW) based biosensors: An important issue for future biomedical applications. Presentation FC2-H-4. *IEEE International Ultrasonics, Ferroelectrics, and Frequency Control 50th Anniversary Joint Conference*. 24-27 August, 2004. Montreal, Canada.

117. Tilmans, H A C, Van de Peer, M D J and Beyne, E. The indent reflow sealing (IRS) technique - A method for the fabrication of sealed cavities for MEMS devices. *Journal of Microelectromechanical Systems*, 2000. **9**(2): p. 206-217.

118. Witvrouw, A, Tilmans, H A C and De Wolf, I. Materials issues in the processing, the operation and the reliability of MEMS. *Microelectronic Engineering*, 2004. **76**(1-4): p. 245-257.

119. Gallant, A J and Wood, D. Surface Micromachined Membranes for Wafer Level Packaging. *Micromechanics Europe*. 5-7 September, 2004. Leuven, Belgium. p. 163-166.

120. Hwang, D J, Choi, T Y and Grigoropoulos, C P. Liquid-assisted femtosecond laser drilling of straight and three-dimensional microchannels in glass. *Applied Physics A-Materials Science & Processing*, 2004. **79**(3): p. 605-612.

121. Danel, J S and Delapierre, G. Quartz: a material for microdevices. *Journal of Micromechanics and Microengineering*, 1991. **1**(4): p. 187.

122. Leech, P W. Reactive ion etching of quartz and silica-based glasses in CF_4/CHF_3 plasmas. *Vacuum*, 1999. **55**(3-4): p. 191-196.

123. Zeze, D A, Forrest, R D, Carey, J D, Cox, D C, Robertson, I D, Weiss, B L and Silva, S R P. Reactive ion etching of quartz and Pyrex for microelectronic applications. *Journal of Applied Physics*, 2002. **92**(7): p. 3624-3629.

124. Li, X H, Abe, T and Esashi, M. Deep reactive ion etching of Pyrex glass using SF_6 plasma. *Sensors and Actuators A-Physical*, 2001. **87**(3): p. 139-145.

125. Rangsten, P, Hedlund, C, Katardjiev, I V and Backlund, Y. Etch rates of crystallographic planes in Z -cut quartz - experiments and simulation. *Journal of Micromechanics and Microengineering*, 1998. **8**(1): p. 1-6.

126. Nguyen, N T, Boellaard, E, Pham, N P, Kutchoukov, V G, Craciun, G and Sarro, P M. Through-wafer copper electroplating for three-dimensional interconnects. *Journal of Micromechanics and Microengineering*, 2002. **12**(4): p. 395-399.

127. Kim, B H, Kim, H C, Chun, K, Ki, J and Tak, Y. Cantilever-type microelectromechanical systems probe card with through-wafer interconnects for fine pitch and high-speed testing. *Japanese Journal of Applied Physics Part 1-Regular Papers Short Notes & Review Papers*, 2004. **43**(6B): p. 3877-3881.

128. Hallmark Electronics Ltd, Hallmark House, Loomer Road, Chesterton, Newcastle under Lyme, ST5 7LA, UK.

129. Fast analysis of used hydrocarbons, particularly motor oil. 2004, Fraunhofer IZM, http://www.izm-m.fraunhofer.de/en/index/thedepartments_n400001abteilungen_a/thedepartments_n40001fabteilungen_a/thedepartments_n4000e1abteilungen_a/thedepartments_n4000e9abteilungen_a/thedepartments_n4000e9abteilungen_a.html.

130. Sensoren für Viskosität, Dielektrizitätszahl und Leitfähigkeit. 2002, Fraunhofer IZM, http://www.izm-m.fhg.de/files/fraunhofer2/3_sensor_fuer_visko_-d.pdf.

131. Setlak, D R, McCalley, K W, Wilson, S D, Hewitt, C L and Van Vonno, N W. Harris Corporation. Enhanced security fingerprint sensor package and related methods. 1999, US5956415.

132. Weber, P O and Salatino, M. Hestia Technologies Inc, Authentec Inc. Integrated circuit package including opening exposing portion of an IC. 2003, US6667439.

133. Eggers, T, Dobrinski, H, van Dommelen, I, Lüdtke, O, Nebeling, A, Raben, J and Wüllner, D. Open-cavity moulding technique for fluid sensor applications. *Workshop on MEMS Sensor Packaging*. 20-21 March, 2003. Copenhagen, Denmark.

134. Kaldenberg, P J. European Semiconductor Assembly. Method for encapsulating an integrated semi-conductor circuit. 1999, US5897338.